

59
COPIES

NATIONAL AERONAUTICS AND SPACE ADMINISTRATION

Space Programs Summary 37-43, Vol. III

The Deep Space Network

For the Period November 1 to December 31, 1966

JET PROPULSION LABORATORY
CALIFORNIA INSTITUTE OF TECHNOLOGY
PASADENA, CALIFORNIA

January 31, 1967

FACILITY FORM 602	N 67-19870	
	(ACCESSION NUMBER)	(THRU)
	156	1
	(PAGES)	(CODE)
	CR-82940	07
	(NASA CR OR TMX OR AD NUMBER)	(CATEGORY)

NATIONAL AERONAUTICS AND SPACE ADMINISTRATION

Space Programs Summary 37-43, Vol. III

The Deep Space Network

For the Period November 1 to December 31, 1966

JET PROPULSION LABORATORY
CALIFORNIA INSTITUTE OF TECHNOLOGY
PASADENA, CALIFORNIA

January 31, 1967

SPACE PROGRAMS SUMMARY 37-43, VOL. III

Copyright © 1967

Jet Propulsion Laboratory
California Institute of Technology

Prepared Under Contract No. NAS 7-100
National Aeronautics & Space Administration

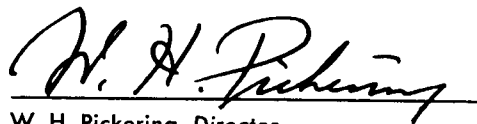
Preface

The Space Programs Summary is a six-volume bimonthly publication designed to report on JPL space exploration programs and related supporting research and advanced development projects. The titles of all volumes of the Space Programs Summary are:

- Vol. I. *The Lunar Program* (Confidential)
- Vol. II. *The Planetary-Interplanetary Program* (Confidential)
- Vol. III. *The Deep Space Network* (Unclassified)
- Vol. IV. *Supporting Research and Advanced Development* (Unclassified)
- Vol. V. *Supporting Research and Advanced Development* (Confidential)
- Vol. VI. *Space Exploration Programs and Space Sciences* (Unclassified)

The Space Programs Summary, Vol. VI, consists of: an unclassified digest of appropriate material from Vols. I, II, and III; an original presentation of the JPL quality assurance and reliability efforts, and the environmental- and dynamic-testing facility-development activities; and a reprint of the space science instrumentation studies of Vols. I and II.

Approved by:



W. H. Pickering, Director

Jet Propulsion Laboratory

Contents

I. Introduction	1
II. Tracking and Navigational Accuracy Analysis	3
A. DSN Inherent Accuracy Project	
<i>T. W. Hamilton and D. W. Trask</i>	3
B. Tracking Station Locations as Determined by Radio Tracking Data: Comparison of Results Obtained From Combined <i>Ranger</i> Block III Missions and From Baker-Nunn Optical Data	
<i>C. J. Vegas and D. W. Trask</i>	3
C. The Introduction of Range Data Into the Data Compression Scheme	
<i>J. D. Anderson</i>	18
D. <i>Lunar Orbiter</i> Ranging Data: Initial Results	
<i>W. L. Sjogren and J. D. Mulholland</i>	24
E. Theoretical Basis for the Double Precision Orbit Determination Program: VI. Angular Observables	
<i>T. D. Moyer</i>	28
F. <i>Pioneer</i> Project Support	
<i>D. W. Curkendall and R. L. Matsch</i>	37
G. Definition and Analysis of the Tracking Data System	
<i>L. W. Miller</i>	39
References	49
III. Communications Research and Development	51
A. Low Noise Receivers: Microwave Maser Development	
<i>R. C. Clauss</i>	51
B. Frequency Generation and Control: Atomic Hydrogen Frequency Standard	
<i>W. H. Higa</i>	52
C. Efficient Antenna Systems: Refrigerated Transmission Line Study	
<i>P. D. Potter</i>	53
D. Improved RF Calibration Techniques: Precision Insertion Loss Measurement of WR 430 Aluminum Waveguide Test Section	
<i>C. T. Stelzried and T. Y. Otoshi</i>	54
E. Efficient Antenna Systems: X-Band Cone Receiving System Description and Calibration	
<i>T. Y. Otoshi and C. T. Stelzried</i>	56
F. Efficient Antenna Systems: X-Band Gain Measurements	
<i>D. A. Bathker</i>	61
G. Efficient Antenna Systems: System Noise Temperature as a Function of Meteorological Conditions	
<i>P. D. Potter</i>	63
H. Efficient Antenna Systems: Effect of Wind and Elevation Angle Upon Antenna Gain	
<i>P. D. Potter</i>	69
I. Digital Communication and Tracking: Design of Lock Detectors	
<i>R. Tausworthe</i>	71
J. Digital Communication and Tracking: An Experimental Study of the First-Slip Statistics of the Second-Order Phase-Locked Loop	
<i>D. Sanger and R. Tausworthe</i>	76

Contents (contd)

K. Ultra-Stable Oscillators: Hydrogen Maser Frequency Standard	
<i>R. Syndor</i>	80
L. Frequency Generation and Control: Digital Frequency and Phase Meter	
<i>W. F. Gillmore, Jr.</i>	84
M. Frequency Generation and Control: Mariner Venus 67 Ranging	
<i>G. U. Barbani</i>	90
N. Time-Synchronization System	
<i>W. S. Baumgartner, J. R. Smith, M. F. Easterling, R. E. Arnold, E. R. Caro, T. Sato,</i> <i>M. Kron, R. C. Coffin, W. L. Martin, and R.F. Emerson</i>	92
References	106
IV. Communications Development Engineering	108
A. High Power Transmitter Development: 400-kw Klystron	
<i>C. P. Wiggins</i>	108
B. High Power Transmitter Development: A Controlled 20-kw Power Source	
<i>E. J. Finnegan</i>	111
C. 100-kHz Module Development	
<i>R. B. Crow</i>	112
D. Mariner IV Subcarrier Signal Evaluation Near Threshold	
<i>N. A. Burow</i>	116
V. Facility Engineering and Operations	120
A. Flight Project Support	
<i>J. Orbison</i>	120
B. Facility Construction and Equipment Installation	
<i>J. Orbison</i>	121
C. DSIF Station Control and Data Equipment	
<i>W. Frey, R. Flanders, G. Jenkins, A. Burke, and H. Baugh</i>	123
D. Venus DSS Operations	
<i>M. A. Gregg, E. B. Jackson, and A. L. Price</i>	124
E. Systems Reliability and Availability Study for SFOF Power Design	
<i>D. C. Card</i>	126
VI. Operations Programming	131
A. SFOF Conversion Project: Surveyor and Lunar Orbiter Mission-Dependent Software	
<i>H. Alcorn</i>	131
B. DSIF Monitoring Programming: Interim Version (IMP)	
<i>I. Urban</i>	143
C. Antenna-Pointing Subsystem Phase I Computer Program for 210-Ft Antenna	
<i>R. Rovello</i>	144
D. PDP-7 Symbolic Assembler (BLAP)	
<i>P. Poulson</i>	145
E. Bit-String Data Processing Procedure	
<i>M. Seamons</i>	146
F. Symbolic Tape Update Program	
<i>Truman Cox</i>	148

I. Introduction

The Deep Space Network (DSN), established by the NASA Office of Tracking and Data Acquisition, is under the system management and technical direction of JPL. The DSN is responsible for two-way communications with unmanned spacecraft travelling from approximately 10,000 miles from Earth to interplanetary distances. Tracking and data-handling equipment to support these missions is provided. Present facilities permit simultaneous control of a newly launched spacecraft and a second one already in flight. In preparation for the increased number of U.S. activities in space, a capability is being developed for simultaneous control of either two newly launched spacecraft plus two in flight, or four spacecraft in flight. Advanced communications techniques are being implemented to make possible obtaining data from, and tracking spacecraft to, planets as far out in space as Jupiter.

The DSN is distinct from other NASA networks such as the Space Tracking and Data Acquisition Network (STADAN), which tracks Earth-orbiting scientific and communication satellites, and the Manned Space Flight Network (MSFN), which tracks the manned spacecraft of the *Gemini* and *Apollo* programs.

The DSN supports, or has supported, the following NASA space exploration projects: (1) *Ranger*, *Surveyor*, *Mariner*, and *Voyager* Projects of JPL; (2) *Lunar Orbiter* Project of the Langley Research Center; (3) *Pioneer* Project of the Ames Research Center, and (4) *Apollo* Project of the Manned Spacecraft Center (as backup to the Manned Space Flight Network). The main elements of the network are: the Deep Space Instrumentation Facility (DSIF), with space communications and tracking stations located around the world; the Ground Communi-

cations System (GCS), which provides communications between all elements of the DSN; and the JPL Space Flight Operations Facility (SFOF), the command and control center.

The DSIF tracking stations are situated such that three stations may be selected approximately 120 deg apart in longitude in order that a spacecraft in or near the ecliptic plane is always within the field of view of at least one of the selected ground antennas. The DSIF stations are:

Deep Space Communication Complex (DSCC)	Deep Space Station (DSS)	DSS serial designation
Goldstone	Pioneer	11
	Echo	12
	Venus	13
	Mars	14
Canberra	Woomera	41
	Tidbinbilla	42
	Booroomba ²	43
	Johannesburg	51
Madrid ¹	Robledo	61
	Cebreros ²	62
	Rio Cofio ²	63
	Cape Kennedy (Spacecraft Monitoring)	71
	Ascension Island (Spacecraft Guidance and Command)	72
¹ Planned. ² Station not yet authorized. ³ Station not yet operational.		

JPL operates the U.S. stations and the Ascension Island Station. The overseas stations are normally staffed and operated by government agencies of the respective countries, with the assistance of U.S. support personnel.

The Cape Kennedy Station supports spacecraft final checkout prior to launch, verifies compatibility between the DSN and the flight spacecraft, measures spacecraft frequencies during countdown, and provides telemetry reception from lift-off to local horizon. The other DSIF stations obtain angular position, velocity (doppler), and distance (range) data for the spacecraft, and provide command control to (up-link), and data reception from (down-link), the spacecraft. Large antennas, low noise phase-lock receiving systems, and high-power transmitters are utilized. The 85-ft diam antennas have gains of 53 db at 2300 MHz, with a system temperature of 55°K, making possible the receipt of significant data rates at distances as far as the planet Mars. To improve the data rate and distance capability, a 210-ft diam antenna has been built at DSS 14, and two additional antennas of this size are planned for installation at overseas stations.

In their present configuration all stations, with the exception of Johannesburg, are full S-band stations. The Johannesburg receiver has the capability for L- to S-band conversion.

It is the policy of the DSN to continuously conduct research and development of new components and systems and to engineer them into the network to maintain a state-of-the-art capability. Therefore, the Goldstone stations are also used for extensive investigation of space tracking and telecommunications techniques, establishment of DSIF/spacecraft compatibility, and development of new DSIF hardware and software. New DSIF-system equipment is installed and tested at the Goldstone DSCC

before being accepted for system-wide integration into the DSIF. After acceptance for general use, it is classed as Goldstone Duplicate Standard (GSDS) equipment, thus standardizing the design and operation of identical items throughout the system.

The GCS consists of voice, teletype, and high-speed data circuits provided by the NASA World-Wide Communications Network between each overseas station, the Cape Kennedy Station, and the SFOF. Voice, teletype, high-speed data, and video circuits between the SFOF and the Goldstone stations are provided by a DSN microwave link. The NASA Communications Network is a global network consisting of more than 100,000 route mi and 450,000 circuit mi, interconnecting 89 stations of which 34 are overseas in 18 foreign countries. It is entirely operationally oriented and comprises those circuits, terminals, and switching equipments interconnecting tracking and data acquisition stations with, for example, mission control, project control, and computing centers. Circuits used exclusively for administrative purposes are not included.

During the support of a spacecraft, the entire DSN operation is controlled by the SFOF. All spacecraft command, data processing, and data analysis can be accomplished within this facility. The SFOF, located in a three-story building at JPL, utilizes operations control consoles, status and operations displays, computers, and data-processing equipment for the analysis of spacecraft performance and space science experiments, and communications facilities to control space flight operations. This control is accomplished by generating trajectories and orbits, command and control data from tracking and telemetry data received from the DSIF in near-real time. The SFOF also reduces the telemetry, tracking, command, and station performance data recorded by the DSIF into engineering and scientific information for analysis and use by scientific experimenters and spacecraft engineers.

II. Tracking and Navigational Accuracy Analysis

A. DSN Inherent Accuracy Project, T. W. Hamilton and D. W. Trask

The DSN Inherent Accuracy Project was formally established by the DSN Executive Committee in July 1965. The objectives of the Project are:

- (1) Determination (and verification) of the inherent accuracy of the DSN as a radio navigation instrument for lunar and planetary missions.
- (2) Formulation of designs and plans for refining this accuracy to its practical limits.

Achievement of these goals is the joint responsibility of the Telecommunications Division (33) and the Systems Division (31) of JPL. To this end, regular monthly meetings are held to coordinate and initiate relevant activities. The Project leader and his assistant (from Divisions 31 and 33, respectively) report to the DSN Executive Committee, and are authorized to task Project members to (1) conduct analyses of proposed experiments, (2) prepare reports on current work, and (3) write descriptions of proposed experiments. The Project is further authorized to deal directly with those flight projects using the DSN regarding data-gathering procedures that bear on inherent accuracy.

The various data types and tracking modes provided by the DSIF in support of lunar and planetary missions are discussed in SPS 37-39, Vol. III, pp. 6-8.

Technical work directly related to the Inherent Accuracy Project was presented in SPS 37-38, Vol. III, and in subsequent issues, and is continued in the following sections of this volume.

B. Tracking Station Locations as Determined by Radio Tracking Data: Comparison of Results Obtained From Combined Ranger Block III Missions and From Baker-Nunn Optical Data, C. J. Vegos and D. W. Trask

1. Introduction

The determination of tracking station locations within the DSIF is discussed. The combined determinations from the four *Ranger* Block III missions using DSIF radio tracking data are described and compared with results obtained from Baker-Nunn photographic observations. These two tracking systems are completely independent, and different methods are used for the analysis.

Three deep space stations within the DSIF are considered: DSS 12 (Echo, Goldstone, California), DSS 41 (Woomera, Australia), and DSS 51 (Johannesburg, South Africa). The Baker-Nunn observations pertain to three Smithsonian Astrophysical Observatory (SAO) stations which are located in Organ Pass, New Mexico; Olifantsfontein, South Africa; and Woomera, Australia. Land-survey results are used to derive the DSS locations from the Baker-Nunn determinations of the SAO stations.

The following discussion reviews the Baker-Nunn results as reported by SAO and the JPL results from individual missions. Next, the method of statistically combining the DSS location determinations from the individual missions is described, and these combined solutions are compared with those derived by SAO and with land-survey results. In general, a high degree of internal consistency exists among the individual *Ranger* solutions. Also, the agreement between the combined *Ranger* and the SAO solutions is encouraging in light of the quoted statistics and the independence of the data from the two tracking systems.

Finally, the limitations of the combined *Ranger* analysis are described. These limitations include the omission of ionospheric effects as well as uncertainties in the timing relationships and the Earth-Moon ephemeris.

2. Results From the Baker-Nunn Cameras¹

The coordinates of the astrophysical observing stations adopted for the Standard Earth² were obtained by combining dynamical and geometrical methods of satellite geodesy (Ref. 2). Table 1 gives the values of these coordinates, referred to as C.5.

Table 1. C.5 coordinates of astrophysical observing stations

Station	X, km	Y, km	Z, km
01—Organ Pass, New Mexico	—1535.761	—5167.003	3401.046
02—Olifantsfontein, South Africa	5056.134	2716.489	—2775.820
03—Woomera, Australia	—3983.756	3743.107	—3275.598

These coordinates pertain to a reference system that approximates as closely as possible an ideal geocentric terrestrial system; i.e., the Z-axis is oriented in the direction of the mean pole 1900–1905, and the Y-axis in the direction of the meridian of the "Mean Observatory." Strictly speaking, the X-axis is directed toward the meridian 75°03'55"94 east of the U.S. Naval Observatory, since the definition of Universal Time One (UT1) was based on the U.S. Naval Observatory's time determination.

¹The authors are indebted to G. Veis of SAO for permission to include this section which is abstracted from Ref. 1.

²In May 1966, during the 7th COSPAR International Space Science Symposium in Vienna, the Smithsonian Astrophysical Observatory presented the results of an analysis of several thousand Baker-Nunn observations to determine the best set of geodetic parameters from satellite observations. The results, known as the Smithsonian Standard Earth, will be published in the *COSPAR Proceedings* and, in a much more detailed form, by SAO.

The uncertainty in the definition of this system is about 10 m for the geocentricity, 0".2 for the directions of the axes, and a few parts per million for the scale. It must be emphasized that the scale in this case is defined by the adopted value of

$$GM_{\oplus} = 398,603.2 \text{ km}^3/\text{sec}^2$$

where GM_{\oplus} is the gravitational constant of the Earth, since only directions (not distances) were introduced in the solution. The semimajor axes of the orbits were determined from the measured periods using the above-mentioned adopted value of GM_{\oplus} . The accuracy with which the coordinates of the Baker-Nunn cameras are determined is estimated to be ± 15 m.

Each of the three DSIF stations is located in an area with a reliable triangulation network. In each of the same areas and within each of the same triangulations is also one of three of the astrophysical observing stations; namely, New Mexico (SAO 01), South Africa (SAO 02), and Australia (SAO 03).

Both the DSIF and the astrophysical observing stations have been connected to local triangulations, which in turn are connected to major geodetic systems (or datums). Thus, Goldstone (DSS 12) and New Mexico (SAO 01) are connected to the North American Datum (NAD); Johannesburg (DSS 51) and South Africa (SAO 02) to the Arc Datum (ARC); and Woomera (DSS 41) and Australia (SAO 03) to the Central Datum (CEN). Table 2 gives the geodetic coordinates of the stations in the respective datums.

Table 2. Geodetic coordinates

Datum	Station		Latitude ϕ	Longitude $\lambda_{(E)}$	h (from MSL), m	H (from ellipsoid), m
	DSS	SAO				
NAD	12	01	35°17'59".850	243°11'43".414	988.93	972
			32°25'24".56	253°26'51".17	1651.33	1648
ARC	51	02	—25°53'21".156	27°41'08".520	1398.1	1405
			—25°57'33".85	28°14'53".91	1544.1	1544
CEN	41	03	—31°22'59".363	136°53'10".161	151.56	137
			—31°06'07".27	136°46'58".74	162.5	162

Since each pair of DSIF and astrophysical observing stations is connected to the same datum, the relative positions of the two stations are known from ground survey. These relative positions are best expressed in terms of differences of their Cartesian geodetic coordinates, which,

assuming the rigor of the geodetic systems, must be invariants of any terrestrial coordinate transformation.

A typical triangulation is estimated to provide coordinates with an accuracy of 10^{-5} . The distances between DSS 12 and SAO 01, DSS 51 and SAO 02, and DSS 41 and SAO 03 are 990, 60, and 30 km, respectively. Accordingly, the relative positions can be expected to be accurate to 10, 1, and 1 m, respectively.

Table 3 gives the coordinate differences and their estimated uncertainties.

Table 3. Coordinate differences and uncertainties

Stations	ΔX , km	ΔY , km	ΔZ , km	σ , m
DSS 12 — SAO 01	— 814.705	+ 515.014	+ 264.583	10
DSS 51 — SAO 02	+ 29.331	— 48.258	+ 7.056	1
DSS 41 — SAO 03	+ 5.075	— 18.235	— 26.645	1

The C.5 set of coordinates determined by SAO for the astrophysical observing stations is based on a scale defined by that adopted for the solution value of $GM_{\oplus} = 398,603.2 \text{ km}^3/\text{sec}^2$. However, the JPL results based on *Rangers VI, VII, VIII, and IX*, and *Mariner IV* give the following value (Ref. 3):

$$GM_{\oplus} = 398,601.2 \pm 1.0 \text{ km}^3/\text{sec}^2$$

The new value corresponds to a relative reduction of $-(5.00 \pm 2.50) \times 10^{-6}$ from the value adopted by SAO for the Standard-Earth solution.

Since the scale of the orbits was determined from the semimajor axis, which in turn was determined from Kepler's third law, a change in GM_{\oplus} will introduce a change in the semimajor axes and thus in the coordinates of the camera stations (since they were determined only by angular measurements) by an appropriate scale factor.

We have

$$\frac{da}{a} = \frac{1}{3} \frac{dGM_{\oplus}}{GM_{\oplus}}$$

and thus the scale defined with the C.5 system should be reduced by a factor of $-(1.7 \pm 0.8) \times 10^{-6}$; that is, the C.5 coordinates should be multiplied by a factor

$$0.9999983 \pm 0.0000008$$

The new coordinates of the astrophysical observing stations are identified as the S.5 system. On the basis of the S.5 coordinates of SAO 01, 02, 03 and the ground-survey results of Table 3, the coordinates for DSS 12, 51, and 41 are derived (Table 4).

Table 4. Coordinates for DSIF stations

DSS	X, km	Y, km	Z, km	σ , m	r_s , km	λ , deg
12	— 2350.464	— 4651.981	+ 3665.624	± 18	5212.064	243.19431
51	+ 5085.457	2668.227	— 2768.760	± 15	5742.936	27.685002
41	— 3978.675	3724.866	— 3302.238	± 15	5450.182	136.88701

The given values for σ are based on a ± 15 -m uncertainty for the S.5 coordinates of the astrophysical observing stations and the uncertainty of the ground survey.

With the values given in Table 4, the distance off the spin axis r_s and longitude of the DSIF stations in the S.5 system can be compared with the directly measured values of JPL (but reduced to the mean pole of 1900–1905).

3. Results From DSIF Radio Tracking

This section discusses the results obtained when the tracking information from the *Ranger* Block III missions (*Ranger VI* through *Ranger IX*) is combined. All four flights were tracked continuously from injection to impact on the lunar surface by the use of three deep space stations; namely, DSS 12 (Echo, Goldstone, California), DSS 41 (Woomera, Australia), and DSS 51 (Johannesburg, South Africa). Only two-way doppler was used during postflight analysis because the information content of the angle data also obtained during the missions is completely overshadowed by that provided by the two-way doppler. A summary of the data used and the analysis performed for the *Ranger* missions is contained in Ref. 3, and a detailed description of the *immediate* postflight analysis for the individual *Ranger* Block III missions is given in Refs. 4–7. This report will concentrate on the statistical combinations of these results and the associated limitations.

It has been shown by Hamilton and Melbourne (SPS 37-39, Vol. III, pp. 18–23)³ that the information content of a single pass (horizon to horizon of a single DSS) of

³For the simplified case of a distant probe whose α , δ , and \dot{r} are essentially constant over the whole pass.

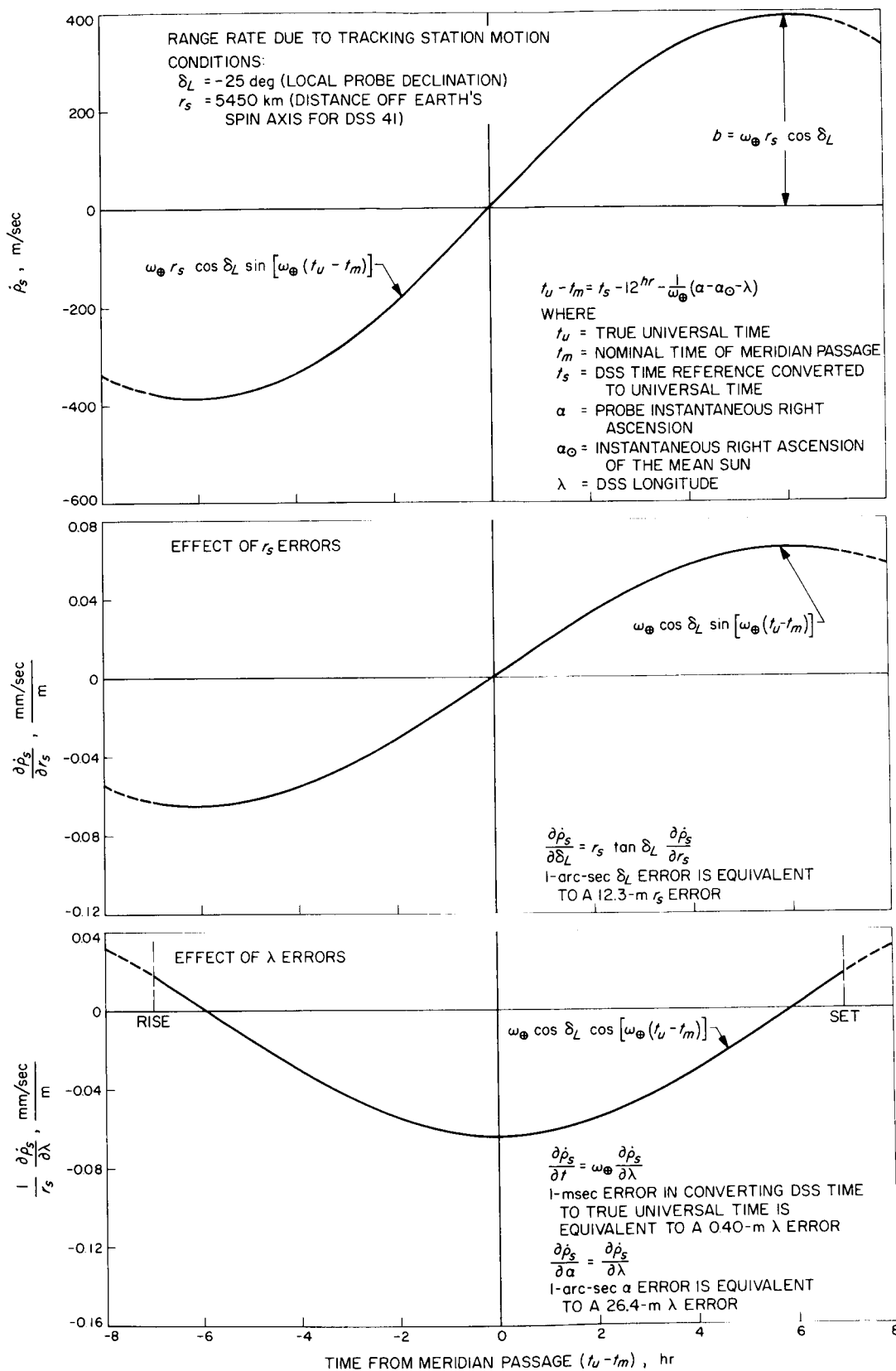


Fig. 1. Sensitivity of range rate to DSS location

doppler can be compressed into three parameters (a, b, c); namely,

$$\left. \begin{aligned} a &= \dot{r} \\ b &= \omega r_s \cos \delta \\ c &= (\alpha - \lambda - \omega \xi) \end{aligned} \right\} \quad (1)$$

where

\dot{r} = probe geocentric radial velocity

ω = Earth spin rate

δ = probe declination

α = probe right ascension

ξ = error in converting the time reference at the DSS to true universal time.

The relative tracking station-probe range rate $\Delta \dot{r}_s$ due to the daily rotational motion of the Earth is shown in Fig. 1 along with the sensitivity of $\Delta \dot{r}_s$ to errors in station coordinates. The doppler tracking data are primarily sensitive to the distance⁴ of the tracking station off the Earth's spin axis r_s and the longitude λ of the tracking station. Changes in the station location parallel to the Earth's spin axis Z have little effect on the doppler data;

⁴For convenience, this report quotes distances in meters, although the true unit is the light meter (i.e., the distance the electromagnetic signal travels in a unit time is the basic unit of length in the "radio tracking world"). Throughout the JPL analysis, lengths (in meters) depend on the adopted value of $c = 299792.5$ km/sec.

i.e., the tracking station is essentially located on the surface of a cylinder as illustrated in Fig. 2. Notice that b of Eq. (1) represents the amplitude of $\Delta \dot{r}_s$ while c is a measure of the time of meridian passage. It can be seen from Eq. (1) and from Fig. 1 that station location errors ($\epsilon_{r_s}, \epsilon_\lambda$) are highly correlated with probe angular position errors ($\epsilon_\alpha, \epsilon_\delta$), and that timing errors directly affect the solution for λ by an amount $\omega \xi$. In general, r_s and longitude differences are the better determined DSS coordinates. Longitude differences are not affected by timing errors common to the DSS or by errors in α . However, as will be discussed in Section 4, inadequacies in accounting for the ionosphere affect all the coordinates.

The determinations for the three DSS locations from each of the *Ranger* Block III missions are shown in Table 5 together with the ET-UTC and UT1-UTC assumed during the analysis⁵. These results refer to the instantaneous axis of rotation of the Earth. The station coordinates must be converted to a common reference pole before they can be properly statistically combined. The mean pole of 1900-1905 was chosen, as defined in Ref. 8. The conversion formula is as follows:

$$\Delta r_s = -r_{s0} \tan \phi_0 (x \cos \lambda_0 - y \sin \lambda_0)$$

$$\Delta \lambda = \tan \phi_0 (x \sin \lambda_0 + y \cos \lambda_0)$$

$$\Delta Z = r_{s0} (x \cos \lambda_0 - y \sin \lambda_0)$$

where

$r_s = r_{s0} + \Delta r_s$, $r_s \rightarrow \lambda \rightarrow Z$, and the subscript 0 refers to the mean pole of 1900-1905 while the nonsubscripted quantities are referenced to the instantaneous pole.

x, y = angular coordinates of instantaneous pole relative to the 1900-1905 mean pole; x is measured south along the 1900-1905 meridian of zero longitude, and y is measured south along the 90° W meridian of 1900-1905.

The changes to DSS locations due to pole wandering are shown in Table 6 along with the x, y values obtained from Ref. 8.

The station location coordinates estimated from the *Ranger* data appear to be internally consistent. As an

⁵A discussion of the role of Ephemeris Time (ET), Universal Time Coordinated (UTC), and Universal Time One (UT1) as it pertains to processing DSIF tracking data is given in SPS 37-39, Vol. III, pp. 7-17.

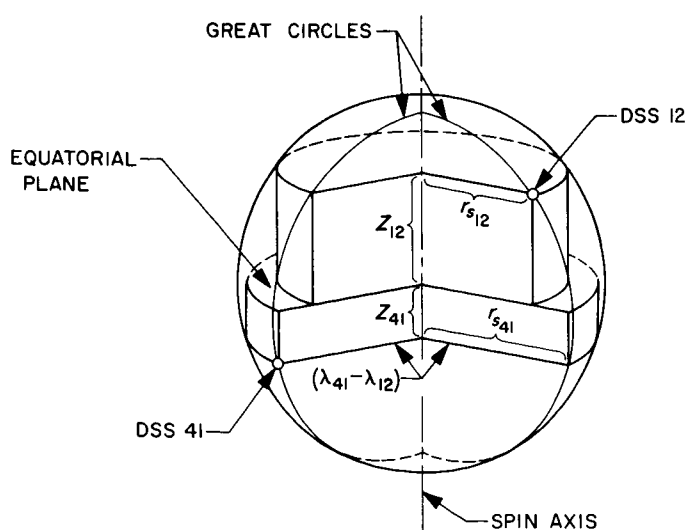


Fig. 2. Station coordinate system

Table 5. Results of Ranger Block III missions referenced to instantaneous Earth pole

DSS	Source	Mission dates								ET—UTC, sec	UT1—UTC, ms	Probe declination, ^a deg	Coordinates referenced to instantaneous pole		
		Launch				Impact							<i>r</i> , km	λ , deg	Z, km
		Y	M	D	H	Y	M	D	H						
12	Ranger VI	64	01	30	16	64	02	02	09	35.201	— 112	1.92	5212.0334	243.19478	3665.4459
	Ranger VII	64	07	28	17	64	07	31	13	35.538	— 119	7.46	5212.0361	243.19497	3665.4491
	Ranger VIII	65	02	17	17	65	02	20	09	35.940	— 49	— 7.39	5212.0392	243.19460	3665.4455
	Ranger IX	65	03	21	21	65	03	24	14	36.015	+ 19	— 24.52	5212.0468	243.19492	3665.4473
	Combined Rangers												5212.0363	243.19465	3665.4480
41	Ranger VI												5450.2121	136.88776	— 3302.3088
	Ranger VII												5450.1866	136.88805	— 3302.3460
	Ranger VIII												5450.2017	136.88761	— 3302.3600
	Ranger IX												5450.2232	136.88806	— 3302.3598
	Combined Rangers												5450.2012	136.88770	— 3302.3470
51	Ranger VI												5742.9171	27.685673	— 2768.7305
	Ranger VII												5742.9234	27.685827	— 2768.7148
	Ranger VIII												5742.9332	27.685515	— 2768.7298
	Ranger IX												5742.9570	27.685802	— 2768.7245
	Combined Rangers												5742.9302	27.685529	— 2768.7172

^aProbe geocentric declination at encounter.

^aProbe geocentric declination at encounter.

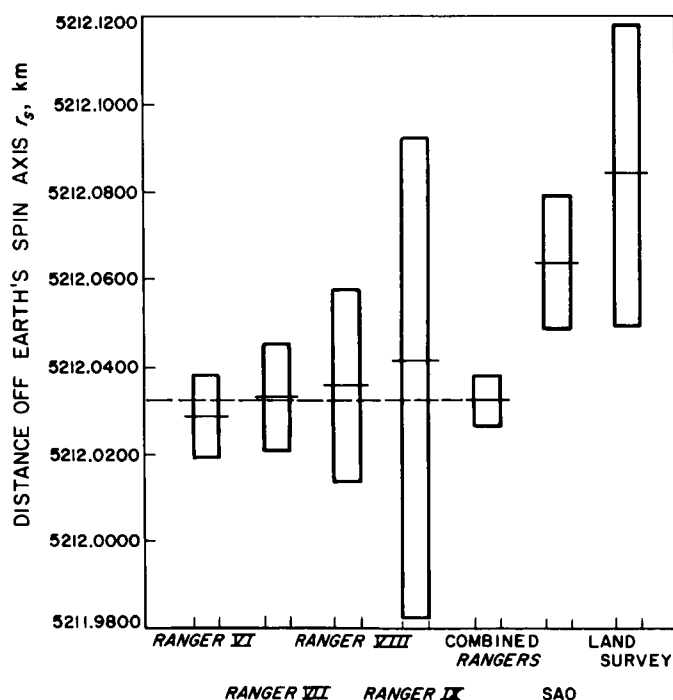


Fig. 3. Distance off Earth's spin axis for DSS 12 referenced to 1900-1905 pole

example, the r_s solutions shown in Fig. 3 for DSS 12 fall within 9 m of the mean, while σ_{r_s} varies from 10 m (Ranger VI) to 58 m (Ranger IX). Similarly, as illustrated in Fig. 4, a maximum deviation of 22 m from the mean occurs for the DSS 12 longitude solutions, while σ_λ varies from 45 m (Ranger IV) to 82 m (Ranger VIII). As previously noted, Table 7 shows that the longitude differences are better determined than the absolute longitude. The case of $\lambda_{12} - \lambda_{41}$ is displayed in Fig. 5, where an 11-m variation from the mean exists, while $\lambda_{51} - \lambda_{12}$ (as shown in Fig. 6) all fall within 5 m of the mean. The statistics for longitude differences are also smaller than for absolute longitude and vary from 13 to 23 m.

The postflight analysis for each of the Ranger Block III missions used the values labeled "old survey" in Table 6 as *a priori* information. The nominal standard deviations associated with these *a priori* coordinates are 500 m in both the r_s and the λ direction and 100 m along Z.^a Little, if any, information about the Z coordinate is contained

^aAlthough no significance is attached to the Z solution from the combined Ranger analysis, it will turn out that $\sigma_Z \approx 50$ m. This is simply a consequence of combining the four flights, each with an *a priori* uncertainty of 100 m on Z.

Table 6. DSS locations referenced to 1900-1905 pole

DSS	Source	Corrections to 1900-1905 pole					Coordinates referenced to 1900-1905 pole					
		x, arc sec	y, arc sec	Δr , m	$\Delta \lambda$, m	ΔZ , m	r, km	σ_r , m	λ , deg	σ_λ , m	Z, km	σ_z , m
12	Ranger VI	-0.198	0.206	-4.8	2.0	6.8	5212.0286	9.5	243.19480	64.2	3665.4527	99.8
	Ranger VII	0.240	0.305	-2.6	-7.0	4.7	5212.0335	12.3	243.19490	56.2	3665.4538	99.9
	Ranger VIII	-0.148	0.135	-3.3	1.0	4.7	5212.0359	21.5	243.19461	81.9	3665.4502	99.7
	Ranger IX	-0.188	0.254	-5.5	1.0	7.9	5212.0413	58.2	243.19493	45.0	3665.4552	99.9
	Combined Rangers						5212.0319	5.8	243.19483	20.8	3665.4534	49.9
	SAO						5212.0635	15.0	243.19431	15.0	3665.6243	15.0
	Old land survey						5212.2054		243.19539		3665.4476	
	Current land survey ^a						5212.0836		243.19487		3665.6757	
41	Ranger VI			0.1	5.0	0.2	5450.2122	39.6	136.88781	67.1	-3302.3086	86.7
	Ranger VII			-6.2	1.0	-10.2	5450.1804	33.4	136.88806	60.6	-3302.3562	99.2
	Ranger VIII			0.2	3.0	0.3	5450.2019	19.9	136.88764	80.9	-3302.3597	95.9
	Ranger IX			-0.5	5.0	-0.9	5450.2227	55.1	136.88811	49.7	-3302.3607	99.8
	Combined Rangers						5450.1987	8.6	136.88790	21.2	-3302.3334	45.4
	SAO						5450.1820	15.0	136.88701	15.0	-3302.2384	15.0
	Old land survey						5450.1884		136.88617		-3302.3586	
	Current land survey						5450.1629		136.88614		-3302.3397	
51	Ranger VI			-3.6	-1.2	-7.5	5742.9135	19.7	27.685661	69.4	-2768.7380	93.0
	Ranger VII			0.9	-5.1	1.9	5742.9243	25.5	27.685776	61.3	-2768.7129	98.8
	Ranger VIII			-2.5	-0.7	-5.4	5742.9307	22.3	27.685508	85.2	-2768.7352	90.5
	Ranger IX			-3.8	-1.2	-8.0	5742.9532	56.7	27.685784	49.5	-2768.7325	97.2
	Combined Rangers						5742.9265	8.5	27.685682	22.2	-2768.7317	46.3
	SAO						5742.9360	15.0	27.685002	15.0	-2768.7604	15.0
	Old land survey						5742.9900		27.685588		-2768.7013	
	Current land survey						5742.9707		27.685858		-2768.7198	

^aSee Ref. 11.

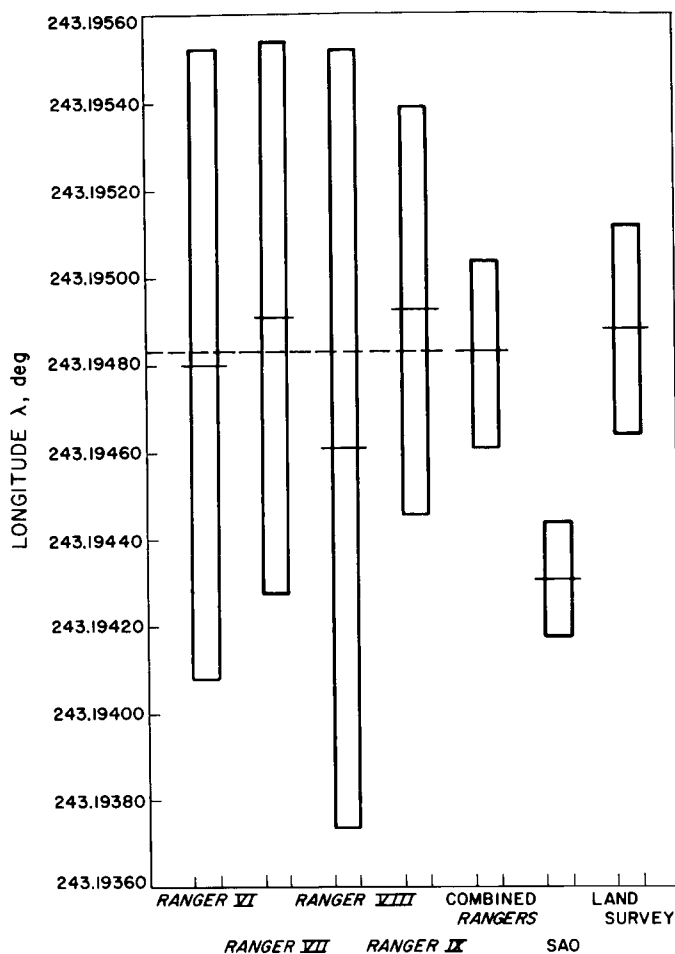


Fig. 4. Longitude for DSS 12 referenced to 1900-1905 pole

in the *Ranger* tracking data. Conversely, the results of this analysis are not sensitive to the *a priori* choice of the *Z* coordinate.

The statistical combination of the DSS locations utilize the covariance matrices and solution vectors of the individual flights as follows: The variations in the two-way doppler z_i associated with the i th experiment are given by

$$\delta z_i = A_i \delta q_i + B_i \delta a$$

where

z_i = doppler data from the i th probe where i = *Rangers* VI through IX

q_i = parameters unique to each mission; i.e., position and velocity vector for each probe plus the Earth-Moon ephemeris scale factor

a = parameters common to all the missions; i.e., DSS locations, mass of the Earth, and mass of the Moon

$$A_i = \frac{\partial z_i}{\partial q_i}$$

$$B_i = \frac{\partial z_i}{\partial a}$$

$\delta()$ = variation in ($$)

*This method is described by J. D. Anderson in JPL Interoffice Technical Memorandum 312-284, *Average of Least Squares Parameter Estimates Over Several Experiments*, March 12, 1963.

Table 7. Longitude differences referenced to 1900-1905 pole

Source	Longitude differences			Source	Standard deviations, m		
	$\lambda_{12} - \lambda_{41}$	$\lambda_{41} - \lambda_{51}$	$\lambda_{51} - \lambda_{12}$		$\lambda_{12} - \lambda_{41}$	$\lambda_{41} - \lambda_{51}$	$\lambda_{51} - \lambda_{12}$
Combined <i>Rangers</i> , deg	106.30693	109.20217	-215.50910	Combined <i>Rangers</i>	7.9	7.8	7.9
<i>Ranger</i> VI minus combined <i>Rangers</i>	6 m	-7 m	1 m	<i>Ranger</i> VI	21.4	22.3	18.8
<i>Ranger</i> VII minus combined <i>Rangers</i>	-9 m	7 m	2 m	<i>Ranger</i> VII	23.2	22.5	18.2
<i>Ranger</i> VIII minus combined <i>Rangers</i>	4 m	-9 m	5 m	<i>Ranger</i> VIII	14.3	14.0	16.5
<i>Ranger</i> IX minus combined <i>Rangers</i>	-11 m	11 m	0	<i>Ranger</i> IX	16.3	12.8	15.3

1 m ~ 10^{-5} deg.

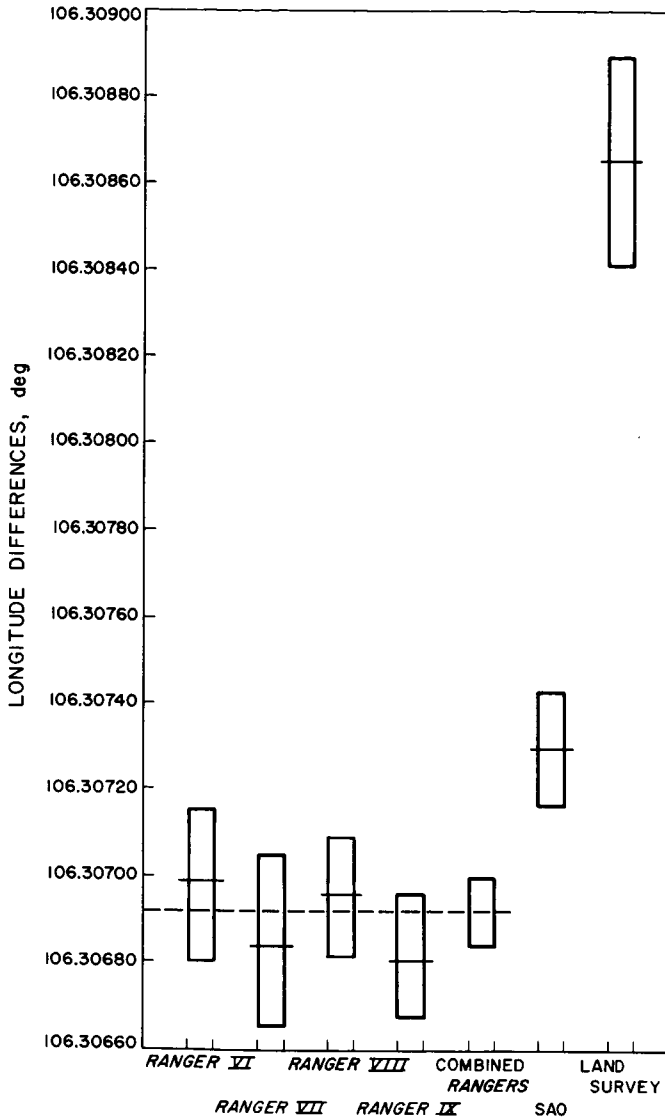


Fig. 5. DSS 12 longitude minus DSS 41 longitude referenced to 1900–1905 pole

The normal matrix J that results from the least-square formulation of the orbit determination program is used in the following partitioned form:

$$J_i = \begin{pmatrix} L_i & X_i \\ X_i^T & K_i \end{pmatrix} = \begin{pmatrix} A_i^T W_i A_i & A_i^T W_i B_i \\ B_i^T W_i A_i & B_i^T W_i B_i \end{pmatrix} \quad (2)$$

where J_i is obtained from each mission and W_i is the weighting matrix for the doppler data. Next designate the least-squares estimates of the parameters for the i th experiment by \tilde{q}_i and \tilde{a}_i and form differences between the \tilde{a}_i and some standard value of a (e.g., $a = \tilde{a}_1$), where

$$\delta \tilde{a}_i = \tilde{a}_i - a \quad (3)$$

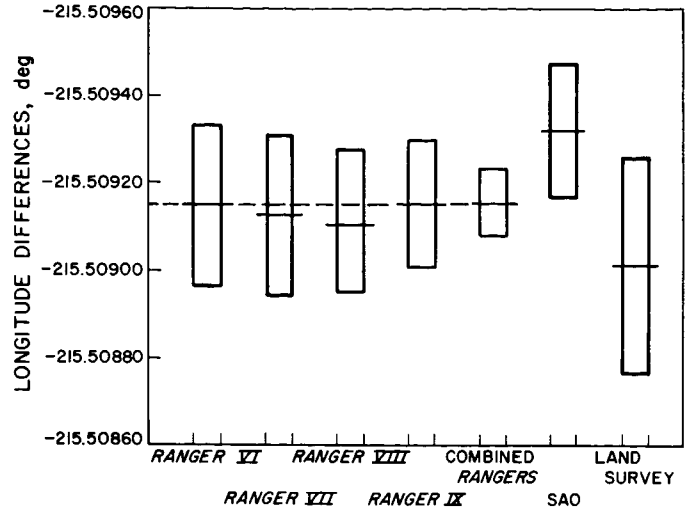


Fig. 6. DSS 12 longitude minus DSS 51 longitude referenced to 1900–1905 pole

Finally, for each experiment, form the matrix

$$M_i = K_i - X_i^T L_i^{-1} X_i \quad (4)$$

where, of course, J_i must be nonsingular.

Then the least-squares estimate a^* of a over all of the data z_1, z_2, \dots, z_n is given by

$$a^* = a + \delta a^* \quad (5)$$

where

$$\delta a^* = \left(\sum_{i=1}^n M_i \right)^{-1} \sum_{i=1}^n M_i \delta \tilde{a}_i \quad (6)$$

The covariance matrix of δa^* is given by

$$\left(\sum_{i=1}^n M_i \right)^{-1}$$

The above procedure was programmed⁸ to accept the standard double-precision J matrix punched output of the JPL single precision orbit determination program (SPODP)⁹ which is described in Refs. 9 and 10.

Notice that although the masses of the Earth (GM_\oplus) and Moon (GM_\lrcorner) are included as common parameters in the combined analysis, the Earth–Moon ephemeris scale factor (REM) is not. That is, the constraint that matches

⁸By Paul Muller, JPL Section 312.

⁹Although SPODP is a single precision program, it accumulates the normal matrix in double precision.

the calculated period of the Moon with the observed period, namely,

$$REM = 86.315745 (GM_{\oplus} + GM_{\zeta})^{1/2}$$

is not applied because the statistics associated with REM are competitive with the quality of the lunar ephemeris. Therefore, REM , which is determined independently, is left unconstrained to compensate for ephemeris errors.

The resultant standard deviations¹⁰ and correlation matrix are shown in Table 8. Notice the independence of

¹⁰All statistics quoted in this report are standard deviations unless otherwise noted.

r_s and λ with Z as shown by the covariance matrix in Table 8 ($\rho_{r_s, Z}, \rho_{\lambda, Z} < 0.09$). The only significant correlation among station locations exists between absolute longitudes ($\rho_{\lambda_i, \lambda_j} \approx 0.9$). This can be anticipated from the high correlation of each DSS longitude with the probe right ascension, as indicated in Eq. 1. In Table 9, the DSS combined locations are compared with the SAO results and with the latest survey (Ref. 11). Also, a comparison of the individual *Ranger* missions, the combined *Ranger*, and the SAO is illustrated for $r_{s_{12}}$ in Fig. 3, for λ_{12} in Fig. 4, for $\lambda_{12} - \lambda_{41}$ in Fig. 5, and for $\lambda_{51} - \lambda_{12}$ in Fig. 6. In general, the JPL-SAO comparison is more favorable than the JPL-survey comparison. In particular, survey longitude differences involving DSS 41 disagree with both JPL and SAO values from 143 to 194 m.

Table 8. Correlation matrix on combined *Rangers* referenced to 1900-1905 pole

Standard deviation			Correlation coefficients												
			GM_{\oplus}	G^A	GM_{ζ}	$r_{s_{12}}$	λ_{12}	Z_{12}	$r_{s_{41}}$	λ_{41}	Z_{41}	$r_{s_{51}}$	λ_{51}	Z_{51}	
GM_{\oplus}	0.370	km ³ /sec ²	1.000	0.112	0.070	-0.052	0.033	-0.024	0.054	-0.069	0.094	0.358	-0.062	-0.148	
G	0.146	—				-0.113	-0.029	-0.054	0	0.004	-0.039	0.012	0	-0.041	-0.011
GM_{ζ}	0.074	km ³ /sec ²				1.000	-0.036	0.641	0.007	-0.166	0.671	0.036	-0.154	0.658	-0.038
$r_{s_{12}}$	5.8	m				1.000	-0.334	-0.012	0.252	-0.357	-0.047	0.196	-0.396	0.045	
λ_{12}	20.8	m				1.000	0.026	-0.294	0.929	0.059	-0.224	0.934	-0.077		
Z_{12}	49.9	m				1.000	-0.021	0.007	0.008	-0.020	0.006	0.010			
$r_{s_{41}}$	8.6	m				1.000	-0.341	0.044	0.361	-0.298	-0.013				
λ_{41}	21.2	m				1.000	0.087	-0.267	0.937	-0.055					
Z_{41}	45.4	m				1.000	0.003	0.054	0.054						
$r_{s_{51}}$	8.5	m				1.000	-0.291	0.016							
λ_{51}	22.2	m	1.000	-0.034											
Z_{51}	46.3	m	1.000												

*Solar pressure constant.

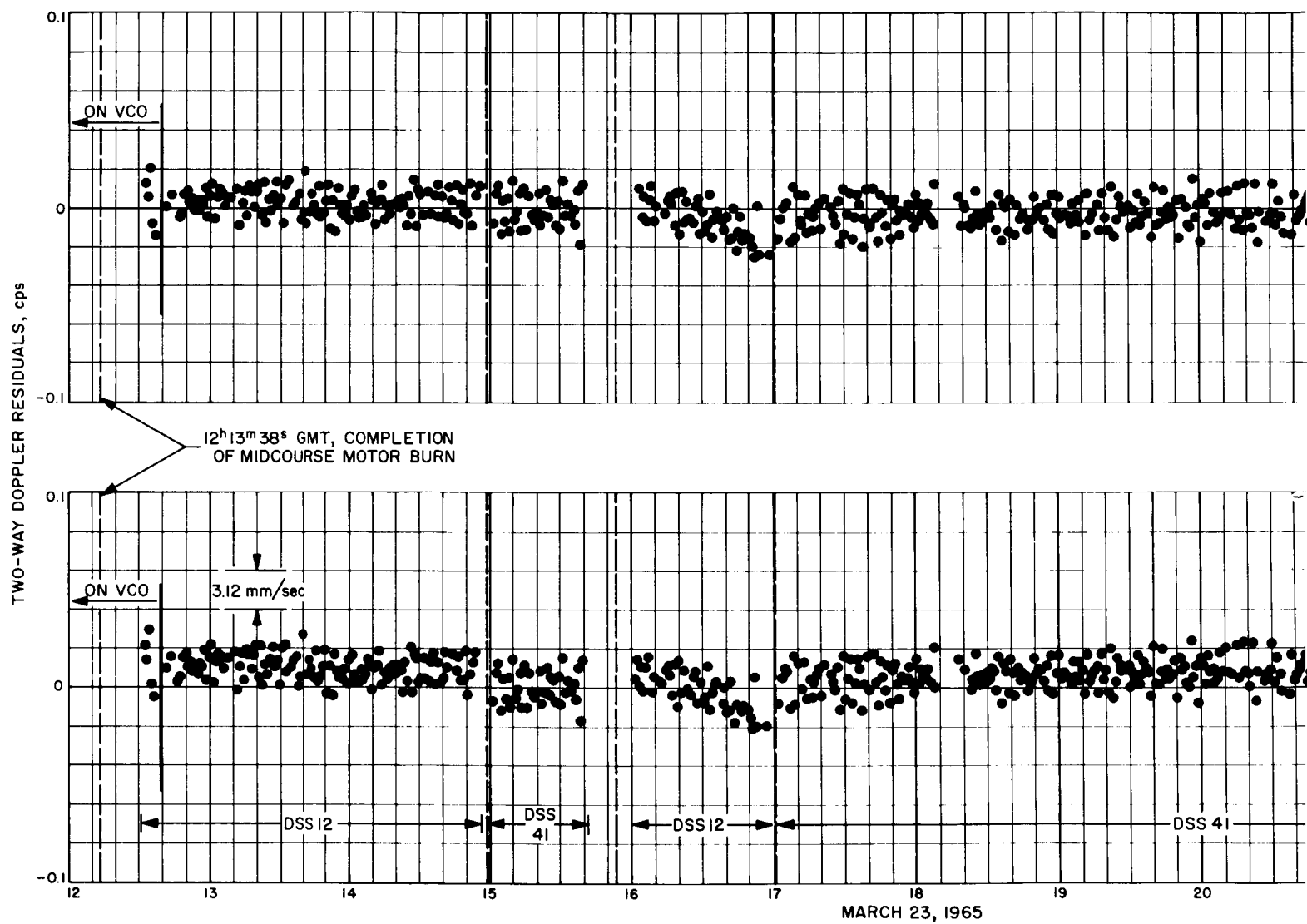
^ASolar pressure constant.

Table 9. Comparison of r_s and λ differences for DSS locations referenced to 1900-1905 pole

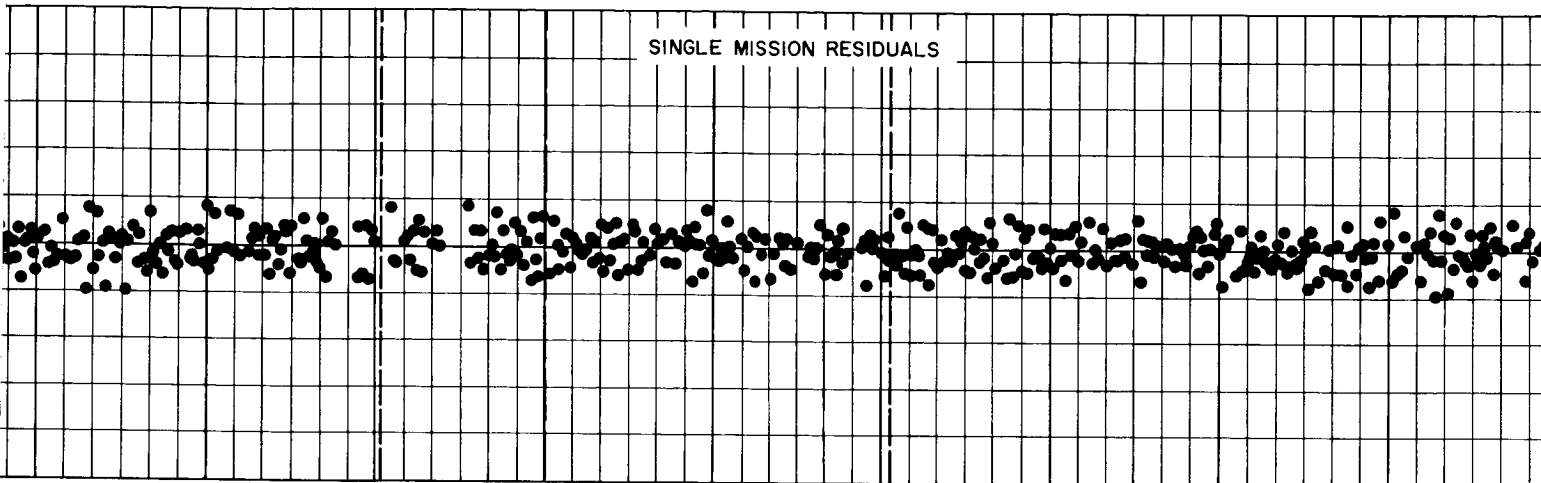
Item	Combined <i>Rangers</i>	SAO	Land survey	Combined <i>Rangers</i> minus land survey, m ^a	SAO minus land survey, m ^a	Combined <i>Rangers</i> minus SAO, m ^a
$r_{s_{12}}$, km	5212.0319	5212.0635	5212.0836	- 51.7	- 20.1	- 31.6
$r_{s_{41}}$, km	5450.1987	5450.1820	5450.1629	35.8	19.1	16.7
$r_{s_{51}}$, km	5742.9265	5742.9360	5742.9707	- 44.2	- 34.7	- 9.5
λ_{12} , deg	243.19483	243.19431	243.19487	- 4	- 56	52
λ_{41} , deg	136.88790	136.88701	136.88614	176	87	89
λ_{51} , deg	27.685682	27.685002	27.685858	- 17.6	- 85.6	68
$\lambda_{12} - \lambda_{41}$, deg	106.30693 ^b	106.30730	106.30873	- 180	- 143	- 37
$\lambda_{41} - \lambda_{51}$, deg	109.20222 ^b	109.20201	109.20028	194	173	21
$\lambda_{51} - \lambda_{12}$, deg	- 215.50915 ^b	- 215.50931	- 215.50901	- 14	- 30	16

^a1 m \sim 10⁻⁶ deg.

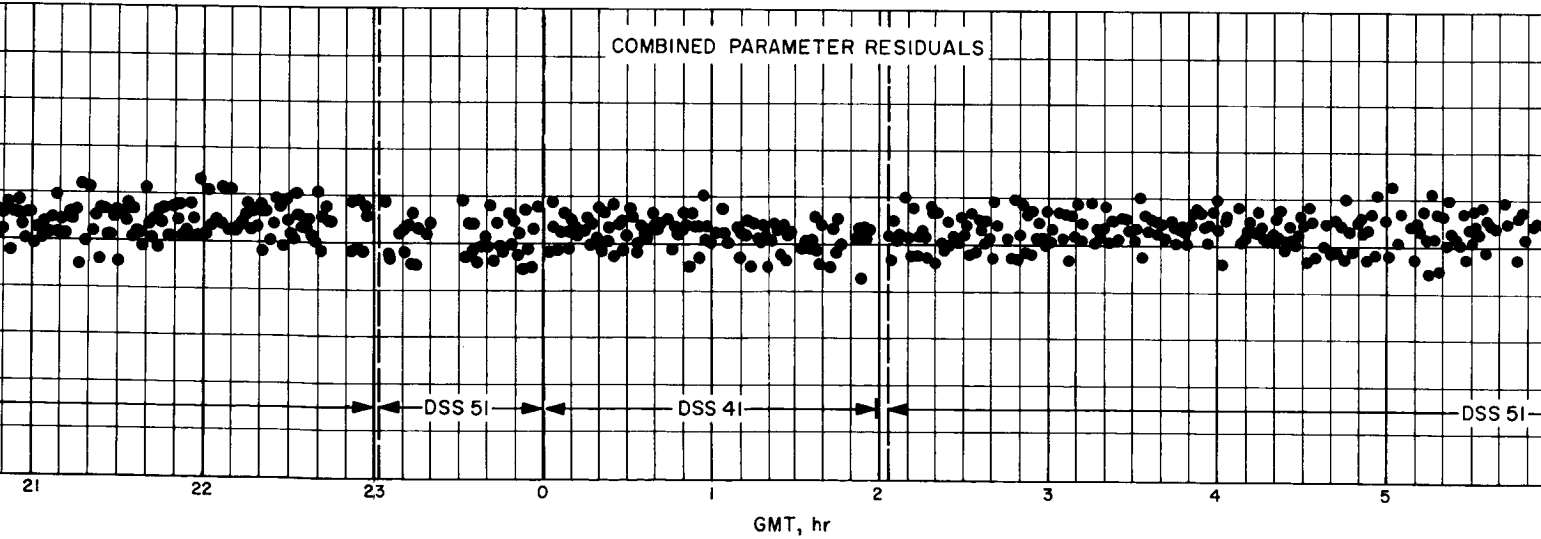
^bThe standard deviation for these differences is 8 m.



SINGLE MISSION RESIDUALS



COMBINED PARAMETER RESIDUALS



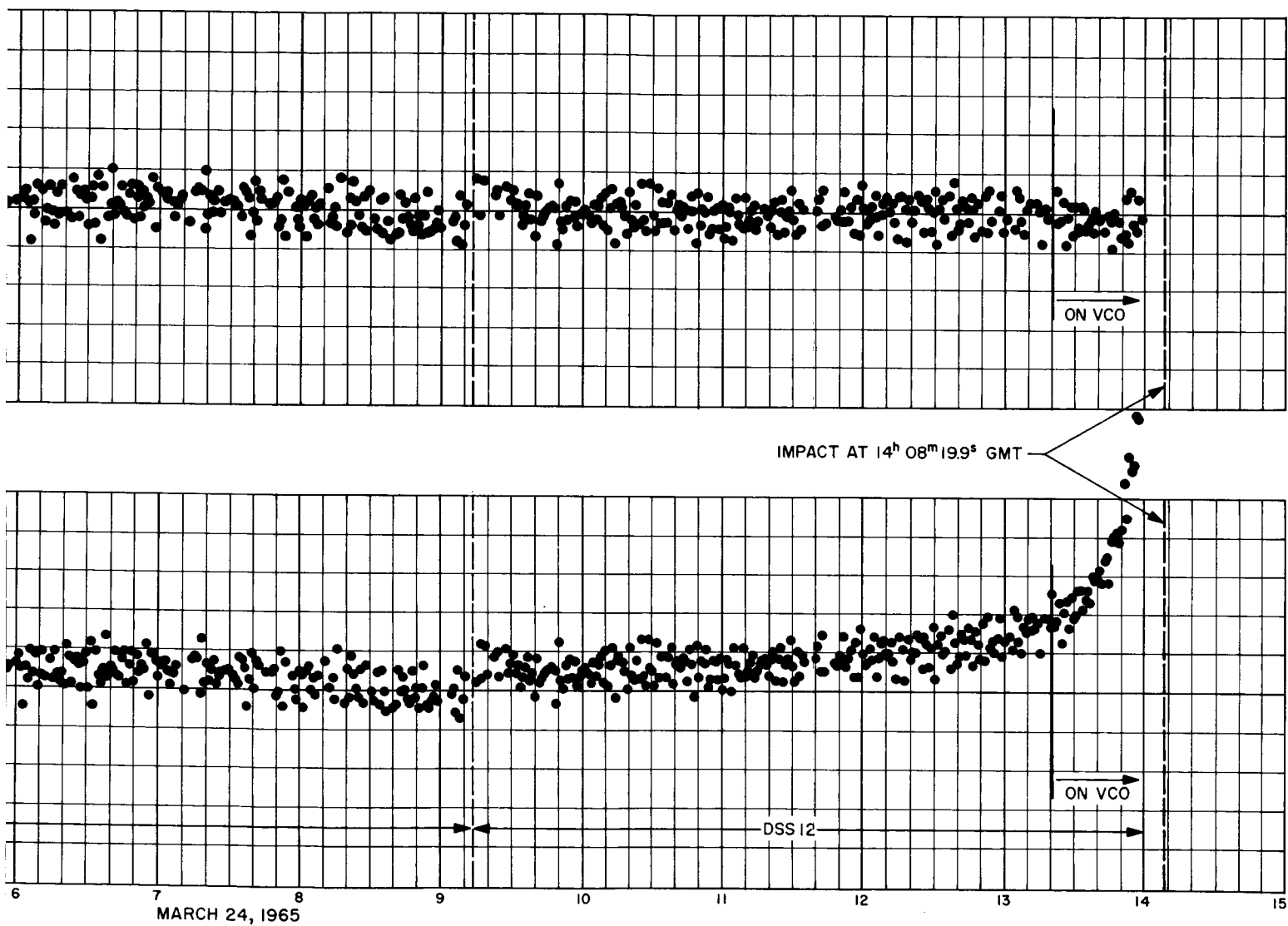


Fig. 7. Ranger IX two-way doppler residual comparison

It is encouraging to notice that the independently determined JPL-SAO values for r_s agree to within 31 m and the longitude differences agree to within 37 m, even though the quoted 1- σ statistics are somewhat smaller than this; i.e., the JPL analysis claims 8 m (1 σ) for longitude differences. However, the JPL statistics are known to be optimistic to the extent that they do not include uncertainties in the effects of the ionosphere, the Earth-Moon ephemeris (except for a scale factor), and in certain timing relationships. These model inadequacies are discussed further in the next section.

The degree to which the computed tracking data agrees with the observed tracking data is illustrated in Fig. 7. Two cases are presented for *Ranger IX* postmidcourse data: the residuals which result from the best fit to the *Ranger IX* data (single mission *Ranger IX* residuals), and the residuals based on the parameters (common and unique) derived from the combined *Ranger* analysis (combined mission *Ranger IX* residuals). The common parameters a , which include the DSS locations, mass of the Earth, and mass of the Moon, are those obtained from Eq. (6). The remaining parameters, i.e., the unique parameters q_i for the *Ranger IX* mission, which include the position and velocity of *Ranger IX* shortly after the midcourse maneuver plus the Earth-Moon ephemeris scale factor, are computed as follows:

$$q_i^* - q_i = L_i^{-1} X_i (\delta a_i - \delta a^*)$$

where

q_i^* is the new estimate of the unique (state vector) parameters for the *Ranger IX* mission

q_i are the unique parameters from least-squares fit for the *Ranger IX* mission

L_i , X_i , δa_i and δa^* are defined in Eqs. 2, 3, and 6, respectively.

The single-mission residuals represent the best obtainable when given the software model of the universe used for the analysis. Although the visible noise on a residual plot, such as Fig. 7, may not include all the data error (low frequency noise may be partially absorbed by a false solution vector), the high frequency noise caused, for example, by transmitter instability, doppler counter quantization error, and phase jitter is evident. It is interesting to note that doppler counter quantization error¹¹ is the major contributor to the visible noise. This source contributes

1.1 mm/sec of a standard deviation of 1.3 mm/sec for the combined errors¹².

Although the combined parameters are optimum when taken over the set of *Ranger* Block III missions, they are not optimum in the sense of a single mission. Except for the region near the Moon, this is primarily reflected by biases (generally less than 1.6 mm/sec) in the combined mission *Ranger IX* residuals of Fig. 7. The solution vectors derived from a single mission may to some extent fit out model inadequacies. However, this freedom is generally not available to the combined solution. Therefore, the relatively large deviation in the combined mission *Ranger IX* residuals starting at 1 hr and 10 min prior to impact is to be expected, in light of the extreme sensitivity of the tracking data near the Moon to small changes in the probe orbital parameters and certain physical constants. However, the general behavior of the combined mission *Ranger IX* residuals is encouraging and lends confidence to the method of analysis employed in combining the *Ranger* Block III results to obtain a best estimate for the DSS locations based on radio tracking data.

It should be pointed out that although the postmaneuver residual plots are a simple extension of the combined *Ranger* analysis performed for this report, this is not true of the premaneuver plots. That is, the premaneuver data are processed and mapped forward through the midcourse maneuver and used as *a priori* information for processing the postmaneuver data. This results in a best estimate of the probe coordinates and the physical constants at the postmidcourse maneuver epoch. However, the best estimate of the probe coordinates before the maneuver is not obtained. To obtain these coordinates, the reverse procedure (as done in Refs. 4 through 7) must be followed; i.e., process the postmaneuver data, map backward through the midcourse maneuver and use as *a priori* information for processing the premaneuver data. Although the physical constant solutions are identical (within numerical noise limitations) regardless of the order of processing the tracking data, both series of runs must be made if the best estimate of the probe coordinates on both sides of the midcourse maneuver are desired. The analysis reported here dealt only with the runs that yielded the postmaneuver probe coordinates.

¹¹The doppler is continuously counted and sampled once a minute. The data used in Fig. 7 are obtained by differencing successive samples and dividing by the count time. The resulting "normalized" range difference can have a quantization error as large as one cycle/count time or 156 mm/60 sec.

¹²For elevation angles greater than 17 deg and excluding the last pass of DSS 12 data.

4. Limitations

Of the above-mentioned items, the effect of charged particles (ionosphere) on the doppler signal is the most severe, especially for longitude differences. There has been no correction made for this effect, which is illustrated in Fig. 8 for the L-band system used during the *Ranger* Block III missions. The dashed line indicates the behavior of range errors for a portion of the *Ranger IX* mission. The spacecraft rises on the horizon of DSS 41 a little before midnight (when the density of charged particles in the ionosphere is near a minimum) and 14 hr later sets at noon (when the charged particle density is an order of magnitude greater than at the start of the pass). This may result in an error in r_s from 5 to 10 m and in λ from 10 to 20 m. The Sun-Earth probe geometry is similar (third-quarter Moon) for the four *Ranger* Block III missions, and therefore the JPL solutions for r_s and λ will tend to be biased from the true values. However, the longitude (and r_s) solutions will deviate from the bias because the tracking pattern, the spacecraft declination (and hence the DSS view periods), and the solar activity (which affects the number of charged particles in the ionosphere) are not the same during each mission.

The difference in the extent to which DSS 12 and DSS 41 were affected during the *Ranger IX* mission is

illustrated in Fig. 8. The large negative declination (-24.5 deg) of the probe results in a 4.8 hr shorter view period for DSS 12 ($\phi_c = +35.1$ deg) than for DSS 41 ($\phi_c = -31.2$ deg), where ϕ is the geocentric latitude. The greatest concentration of charged particles generally occurs at 3 p.m. local time and the minimum concentration at 3 a.m. With its shorter view period, DSS 12 typically viewed the probe from 1:05 to 10:20 a.m. local time, while DSS 41 viewed from 10:40 p.m. to 0:40 p.m. local time the next day. This means, as can be seen in Fig. 8, that DSS 41 viewed the probe through a higher concentration of charged particles during the ends of its view period than did DSS 12. Such variations among deep space stations during a mission, plus the above-mentioned differences from mission to mission, will cause variations from 5 to 15 m in the solutions for longitude differences.

Inaccuracies in the Earth-Moon ephemeris are probably the next largest error source. Near impact the probe trajectory is strongly influenced by the presence of the Moon; i.e., the SPODP essentially determines the orbit of the probe with respect to the Moon. The lunar ephemeris errors (Moon with respect to Earth) are generally conceded to be on the order of 1 km, 1σ . As seen from Eq. 1, for a spacecraft "tied" to the Moon, a 1-km error in lunar longitude will result in a 16-m error in DSS longitude (but

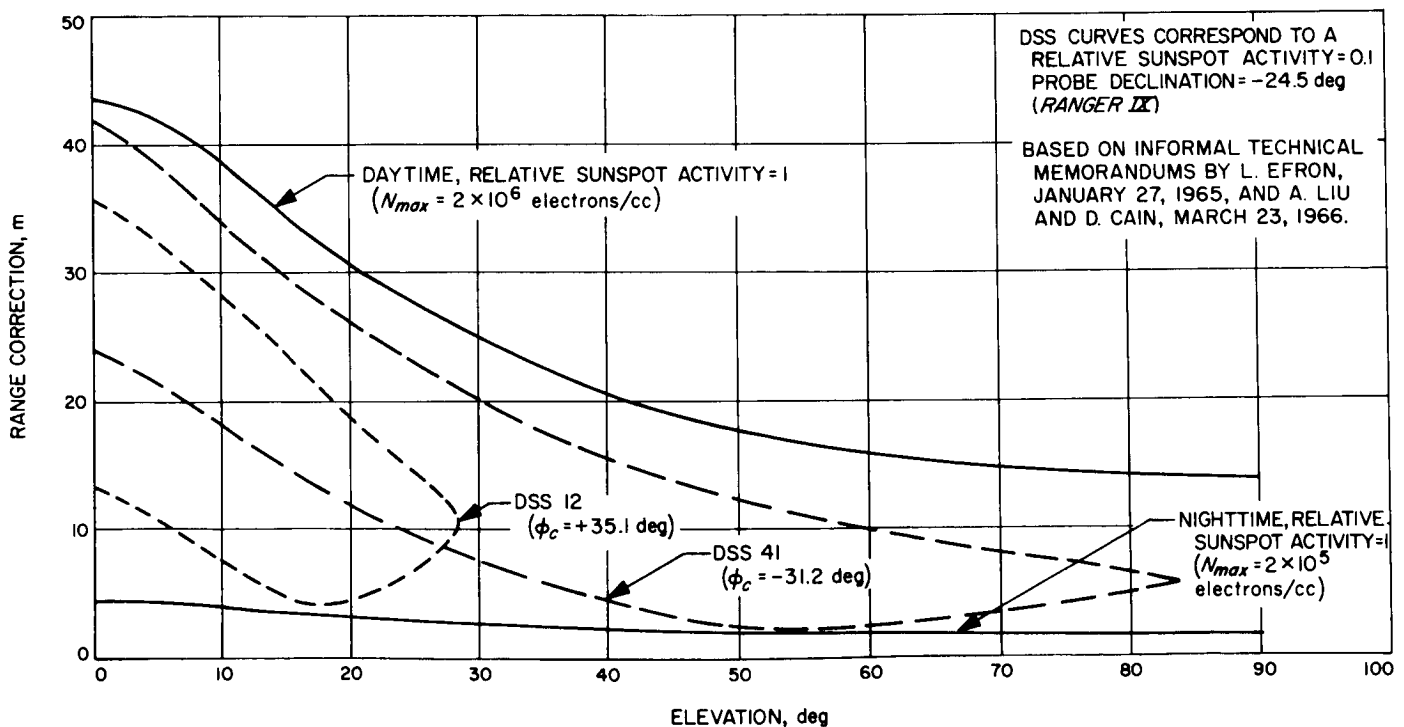
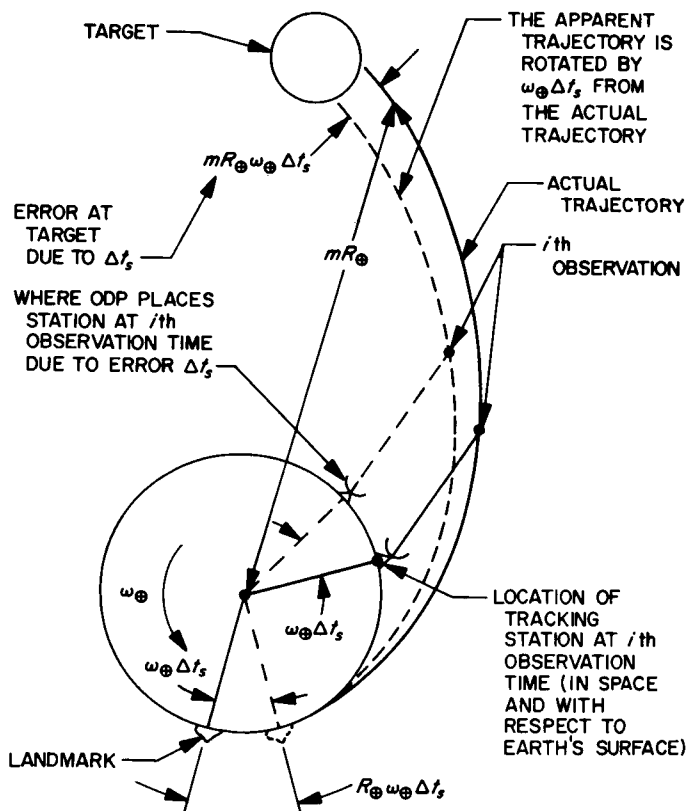


Fig. 8. Effect of ionosphere on range measurements (DSIF L-band system, $f = 960$ MHz)

no error in relative DSS longitudes). Also, an error in lunar latitude will be reflected in an r_s error proportional to $\tan \delta$, which for *Ranger IX* ($\delta = -24.5$ deg) is 6 m.

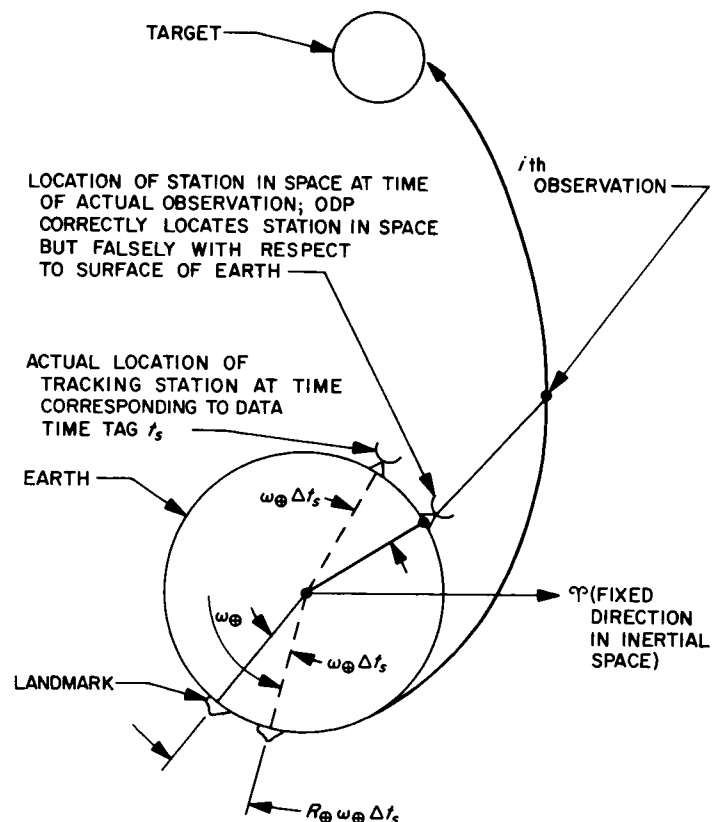
In addition, the station-location solutions are sensitive to the timing relationships assumed in the orbit determination process, as indicated by Eq. 1 (illustrated in Fig. 9). At the start of a mission, an error in either station longitude or station time will cause a compensating rotation of the spacecraft orbit in space. That is, even if station time is assumed to be perfectly known, the station longitude cannot be determined, and vice versa. However, if the station times are perfectly known, *relative* station longitudes can be determined or, conversely, an error

between the two station clocks will cause an error in the relative longitudes. For the deep space stations (located $\sim \pm 35$ -deg latitude), a 1-sec time error results in a 400-m longitude error. As the spacecraft approaches the Moon, the orbit becomes determined in space (i.e., the right ascension of the probe \approx the right ascension of the Moon) and the absolute station longitude is determined if the station time is known with respect to ET (defines location of the Moon in space) and UT (defines the rotational orientation of the Earth). A more complete description of the role these time systems play in the orbit determination process and the likely errors among these time systems is discussed in SPS 37-39, Vol. III, pp. 7-17.



CASE 1. ASSUME THAT:

- (1) STATION LOCATION IS PERFECTLY KNOWN AND FIXED WITH RESPECT TO THE EARTH
- (2) NO *A PRIORI* KNOWLEDGE OF SPACECRAFT TRAJECTORY
- (3) ONLY NEAR-EARTH TRACKING DATA IS PROCESSED (i.e., THE EARTH IS THE ONLY EFFECTIVE ATTRACTING BODY)



CASE 2. ASSUME THAT:

- (1) SPACECRAFT TRAJECTORY IS PERFECTLY KNOWN
- (2) STATION LOCATION IS INCLUDED IN THE ODP SOLUTION VECTOR

Fig. 9. Effect of an error Δt_s in UT1 - t_s

It should be remembered that the statistics quoted in Table 7 do not include errors due to charged particles, ephemeris errors, or timing inaccuracies. The actual statistics of the combined *Ranger* analysis are probably on the order of $\sigma_{r_s} \sim 15$ m, $\sigma_\lambda \sim 30$ m, and $\sigma_{\lambda_i - \lambda_j} \sim 15$ m.

A more detailed discussion of limitations and future plans is contained in Ref. 3. Significant progress is being made in handling the timing problems and developing a better Earth-Moon ephemeris (SPS 37-42, Vol. IV, pp. 2-5). The next-generation orbit determination program currently under development (SPS 37-38, Vol. III, pp. 24-26 and subsequent issues of Vol. III) will automatically include the pole-wandering motion and will apply corrections for charged particles. It is anticipated that further refinements in the postflight processing of existing tracking data will produce DSS location determinations approaching 1 m in r_s and λ . At the conclusion of the *Ranger* Block III missions, the DSIF was converted from L-band to S-band, which is only one-sixth as sensitive to the ionosphere. Use of this S-band data may allow these 1-m goals to be exceeded.

5. Conclusions

Radio tracking of deep-space probes provides a powerful means of determining certain coordinates of the tracking stations. In particular, longitude differences between tracking stations and the distance off the Earth's spin axis are the best determined coordinates; absolute longitudes can also be determined for lunar missions if the probe has been sufficiently influenced by the lunar gravitational field. Thus, the probe's right ascension (and consequently absolute station longitude) is derived from the *known* right ascension of the Moon.

The results from the individual *Ranger* Block III missions exhibit a high degree of internal consistency. As an example, r_s solutions fall within 9 m of the mean for DSS 12, and longitude differences fall within 11 m of the mean for DSS 12 minus DSS 41 and 5 m of the mean for DSS 51 minus DSS 12. In all cases, the individual results are within a standard deviation of the mean.

It is felt that $\sigma_{r_s} = 15$ m, $\sigma_\lambda = 30$ m, and $\sigma_{\lambda_i - \lambda_j} = 15$ m are realistic statistics to associate with the combined *Ranger* solutions when known limitations of the analysis are taken into account. These limitations include omission of ionospheric effects as well as uncertainties in the timing relationships and the Earth-Moon ephemeris that are not accounted for in the statistical model.

The agreement between the JPL and SAO results varies from 10 to 32 m in r_s and from 16 to 37 m in relative station longitudes. This is encouraging considering the quoted statistics and the independence of the tracking data and the associated analysis of the two tracking systems.

It is anticipated that DSS location determinations on the order of 1 m in r_s and λ will be obtainable with further refinements in the post-postflight processing of radio tracking data.

C. The Introduction of Range Data Into the Data Compression Scheme, J. D. Anderson

1. Introduction

In SPS 37-39, Vol. III, pp. 18-23, Hamilton and Melbourne derive a physically meaningful set of three parameters which characterize a single pass of doppler data from a spacecraft at a great distance from the Earth. For this problem, a great distance is defined such that a first-order expansion of the doppler formula is valid in terms of quantities that are of the order of the Earth's dimension divided by the distance to the spacecraft. The purpose here is to extend the analysis to a single pass of range and doppler data under the same conditions. This is necessary for the anticipated compression of the *Mariner* Venus 67 and *Mariner* Mars 1969 data; however, the *Mariner II* and *Mariner IV* data consist of doppler measurements only, and the data compression can proceed without analysis of the range information.

The noise on the doppler data is represented by random range-rate errors of zero mean with standard deviation $\sigma_{\dot{r}}$, and the range noise is also random with zero mean and standard deviation σ_r . In this article, neither the effect of treating the doppler errors as white range noise, as done by Curkendall (SPS 37-40, Vol. III), nor the effect of a small unknown acceleration, as done by Nishimura (SPS 37-41, Vol. IV), are considered.

The addition of range data to a single pass of data causes the number of parameters characterizing the pass to increase from three to four, the new parameter being closely related to the geocentric distance, and the statistical correlation in the four parameters conveniently separates into only two nonzero correlations. Thus, as in the case of doppler data only, which resulted in one nonzero correlation among the three parameters, it is possible to obtain analytical expressions for the covariance matrix of the compression parameters and to analytically investigate

the statistical properties of the parameter's determination as a function of the fraction of a full pass of data. Also, the statistical properties of the determination can be expressed as a function of the relative accuracies in the range and doppler systems.

2. Approximation to Range and Range Rate

The geocentric position of the spacecraft is given by the vector \mathbf{r} with components $x = r \cos \delta \cos \alpha$, $y = r \cos \delta \sin \alpha$, and $z = r \sin \delta$ referred to the true equator and equinox of date. Similarly, the geocentric station location is given by the vector \mathbf{R} with components $X = R \cos \phi \cos \theta$, $Y = R \cos \phi \sin \theta$, and $Z = r \sin \phi$ in the same coordinate system. Then the topocentric position of the spacecraft is given by the range vector $\boldsymbol{\rho}$, where

$$\boldsymbol{\rho} = \mathbf{r} - \mathbf{R} \quad (1)$$

and the range ρ is simply the magnitude of $\boldsymbol{\rho}$.

$$\rho^2 = \boldsymbol{\rho} \cdot \boldsymbol{\rho} = r^2 - 2\mathbf{r} \cdot \mathbf{R} + R^2 \quad (2)$$

The scalar product of \mathbf{r} and \mathbf{R} is equal to $rR(\sin \delta \sin \phi + \cos \delta \cos \phi \cos H)$ with the hour angle H defined by $H = \theta - \alpha$. Thus, the range can be expressed in the form

$$\rho = r [1 - 2\mu (\sin \delta \sin \phi + \cos \delta \cos \phi \cos H) + \mu^2]^{1/2} \quad (3)$$

where $\mu = R/r$ is a small quantity for a distant spacecraft. Now, analogous to the expansion carried out by Hamilton and Melbourne, terms of the order μ^2 and higher are neglected in the computation of the observable, and the expression for range that will be used in this analysis of data compression is

$$\rho = r - R \cos(\delta - \phi) + R(1 - \cos H) \cos \delta \cos \phi + O(\mu^2) \quad (4)$$

The expression for range rate $\dot{\rho}$, equivalent to that used by Hamilton and Melbourne, can be derived by differentiating Eq. (4) and by neglecting the rates $\dot{\alpha}$ and $\dot{\delta}$ in the geocentric right ascension and declination:

$$\dot{\rho} = \dot{r} + R \omega \cos \delta \cos \phi \sin H \quad (5)$$

The four compression parameters (a, b, c, d) for range and range-rate data are identified with constants in

Eqs. (4) and (5), such that

$$\rho = d + b [1 - \cos(\omega t + c)] + at \quad (6)^{13}$$

$$\dot{\rho} = a + b\omega \sin(\omega t + c) \quad (7)$$

where

$$a = \dot{r}_0$$

$$b = R \cos \phi \cos \delta$$

$$c = H_0$$

$$d = r_0 - R \cos(\delta - \phi)$$

The time argument t is measured from an epoch t_0 at which $H = H_0$. In practice, t_0 is selected, before the data compression is accomplished, as the best *a priori* estimate of the time of zero hour angle when the spacecraft is on the station's meridian. Then a nonzero determination of H_0 from the raw range and doppler data can be interpreted as the time t_m of meridian crossing as measured from the fixed time t_0 . The appropriate formula is

$$c = -\omega t_m \approx 0 \quad (8)$$

It should be noted that the definitions of b and c used here differ in their exact form from those used by Hamilton and Melbourne, but they are expressions of the same quantities. For comparison purposes, call the Hamilton-Melbourne set of parameters a', b', c' . Then the relation to the a, b, c set used here is

$$\left. \begin{aligned} a' &= a \\ b' &= b\omega \cos c \approx b\omega \\ c' &= b\omega \sin c \approx bc\omega \end{aligned} \right\} \quad (9)$$

3. Regression Analysis

A statistical analysis of the determination of a, b, c , and d from a single pass of range and doppler data depends on a linearization of Eqs. (6) and (7).

$$\Delta \rho = \Delta d + (1 - \cos H) \Delta b + b \sin H \Delta c + \frac{H - c}{\omega} \Delta a \quad (10)$$

$$\Delta \dot{\rho} = \Delta a + \omega \sin H \Delta b + b\omega \cos H \Delta c \quad (11)$$

¹³The author wishes to thank D. W. Curkendall for pointing out the significant sensitivity of range to the parameter a .

Now, as in Hamilton and Melbourne's article, assume that tracking occurs symmetrically about the meridian crossing with the half-width of the pass given by ψ . Then the inverse covariance matrix J_p on a , b , c , and d from the range data is given by

$$J_p = \begin{bmatrix} \frac{1}{3} \frac{\psi^2}{\omega^2} & 0 & \frac{b}{\omega} \left(\frac{\sin \psi}{\psi} - \cos \psi \right) & 0 \\ 0 & \frac{3}{2} - \frac{2 \sin \psi}{\psi} + \frac{\sin 2\psi}{4\psi} & 0 & 1 - \frac{\sin \psi}{\psi} \\ \frac{b}{\omega} \left(\frac{\sin \psi}{\psi} - \cos \psi \right) & 0 & \frac{1}{2} b^2 \left(1 - \frac{\sin 2\psi}{2\psi} \right) & 0 \\ 0 & 1 - \frac{\sin \psi}{\psi} & 0 & 1 \end{bmatrix} \frac{N}{\sigma_p^2}$$

and the similar matrix for range rate is

$$J_{\dot{p}} = \begin{bmatrix} 1 & 0 & b\omega \frac{\sin \psi}{\psi} & 0 \\ 0 & \frac{1}{2} \omega^2 \left(1 - \frac{\sin 2\psi}{2\psi} \right) & 0 & 0 \\ b\omega \frac{\sin \psi}{\psi} & 0 & \frac{1}{2} b^2 \omega^2 \left(1 + \frac{\sin 2\psi}{2\psi} \right) & 0 \\ 0 & 0 & 0 & 0 \end{bmatrix} \frac{N}{\sigma_{\dot{p}}^2}$$

The combined inverse covariance matrix is $J = J_p + J_{\dot{p}}$ under the assumption that the range and doppler data are not correlated. Fortunately, when the two types of data are combined, there are only two correlations between the four compression parameters. The first correlation, ρ_{ac} , is given by

$$\rho_{ac} = - \frac{j_{13}}{(j_{11} j_{33})^{1/2}} \quad (12)$$

and the second, ρ_{bd} , by

$$\rho_{bd} = - \frac{j_{24}}{(j_{22} j_{44})^{1/2}} \quad (13)$$

where j_{ij} is the element in the i th row and j th column of the matrix J . Thus,

$$\rho_{ac} = - \frac{2^{1/2}}{\left(1 + \frac{1}{3} l \psi^2 \right)^{1/2}} \left[(1 + l) \frac{\sin \psi}{\psi} - l \cos \psi \right] \left[(1 + l) + (1 - l) \frac{\sin 2\psi}{2\psi} \right]^{-1/2} \quad (14)$$

$$\rho_{bd} = - (2l)^{1/2} \left(1 - \frac{\sin \psi}{\psi} \right) \left[1 + 3l - 4l \frac{\sin \psi}{\psi} + (l - 1) \frac{\sin 2\psi}{2\psi} \right]^{-1/2} \quad (15)$$

where l reflects the relative accuracy of the range and range-rate data:

$$l = \left(\frac{\sigma_p}{\omega \sigma_r} \right)^2 \quad (16)$$

A representative value for l with data from the DSIF is between one-fourth and unity.

The variances on the four compression parameters can be found from an analytical inversion of J which is easily accomplished because of its separation into two 2×2 matrices.

$$\sigma_a^2 = \frac{1}{(1 - \rho_{ac}^2)} \left(1 + \frac{1}{3} l \psi^2 \right)^{-1} \frac{\sigma_p^2}{N} \quad (17)$$

$$\sigma_b^2 = \frac{2}{\omega^2 (1 - \rho_{bd}^2)} \left[1 + 3l - 4l \frac{\sin \psi}{\psi} - (1 - l) \frac{\sin 2\psi}{2\psi} \right]^{-1} \frac{\sigma_p^2}{N} \quad (18)$$

$$\sigma_c^2 = \frac{2}{b^2 \omega^2 (1 - \rho_{ac}^2)} \left[1 + l + (1 - l) \frac{\sin 2\psi}{2\psi} \right]^{-1} \frac{\sigma_p^2}{N} \quad (19)$$

$$\sigma_d^2 = \frac{1}{\omega^2 l (1 - \rho_{bd}^2)} \frac{\sigma_p^2}{N} \quad (20)$$

4. Numerical Results

Three cases are considered for the evaluation of the variances on a , b , c , and d .

CASE 1: $l = 0$ (doppler data only)

$$\rho_{ac} = -2^{1/2} \frac{\sin \psi}{\psi} \left(1 + \frac{\sin 2\psi}{2\psi} \right)^{-1/2}$$

$$\rho_{bd} = 0$$

$$\sigma_a^2 = \frac{1}{(1 - \rho_{ac}^2)} \frac{\sigma_p^2}{N}$$

$$\sigma_b^2 = \frac{2}{\omega^2} \left(1 - \frac{\sin 2\psi}{2\psi} \right)^{-1} \frac{\sigma_p^2}{N}$$

$$\sigma_c^2 = \frac{2}{b^2 \omega^2 (1 - \rho_{ac}^2)} \left(1 + \frac{\sin 2\psi}{2\psi} \right)^{-1} \frac{\sigma_p^2}{N}$$

$$\sigma_d^2 = \infty$$

CASE 2: $l = 1$ (range and doppler data)

$$\rho_{ac} = \frac{\cos \psi - 2 \frac{\sin \psi}{\psi}}{\left(1 + \frac{1}{3} \psi^2 \right)^{1/2}}$$

$$\rho_{bd} = -\frac{1}{2^{1/2}} \left(1 - \frac{\sin \psi}{\psi} \right)^{1/2}$$

$$\sigma_a^2 = \frac{1}{(1 - \rho_{ac}^2) \left(1 + \frac{1}{3} \psi^2 \right)} \frac{\sigma_p^2}{N}$$

$$\sigma_b^2 = \frac{1}{2 \omega^2 (1 - \rho_{bd}^2)} \left(1 - \frac{\sin \psi}{\psi} \right)^{-1} \frac{\sigma_p^2}{N}$$

$$\sigma_c^2 = \frac{1}{b^2 \omega^2 (1 - \rho_{ac}^2)} \frac{\sigma_p^2}{N}$$

$$\sigma_d^2 = \frac{1}{\omega^2 (1 - \rho_{bd}^2)} \frac{\sigma_p^2}{N}$$

CASE 3: $l = \infty$ (range data only)

$$\rho_{ac} = -\frac{6^{1/2}}{\psi} \left(\frac{\sin \psi}{\psi} - \cos \psi \right) \left(1 - \frac{\sin 2\psi}{2\psi} \right)^{-1/2}$$

$$\rho_{bd} = -2^{1/2} \left(1 - \frac{\sin \psi}{\psi} \right) \left(3 - 4 \frac{\sin \psi}{\psi} + \frac{\sin 2\psi}{2\psi} \right)^{-1/2}$$

$$\sigma_a^2 = \frac{3 \omega^2}{(1 - \rho_{ac}^2) \psi^2} \frac{\sigma_p^2}{N}$$

$$\sigma_b^2 = \frac{2}{(1 - \rho_{bd}^2)} \left(3 - 4 \frac{\sin \psi}{\psi} + \frac{\sin 2\psi}{2\psi} \right)^{-1} \frac{\sigma_p^2}{N}$$

$$\sigma_c^2 = \frac{2}{b^2 (1 - \rho_{ac}^2)} \left(1 - \frac{\sin 2\psi}{2\psi} \right)^{-1} \frac{\sigma_p^2}{N}$$

$$\sigma_d^2 = \frac{1}{(1 - \rho_{bd}^2)} \frac{\sigma_p^2}{N}$$

Figs. 10-15 show the behavior of the correlations and standard deviations for the three cases as a function of the half-width of the pass ψ . The precision σ_p in the range-rate data and the sample interval are chosen the same as in Hamilton and Melbourne's study; as a result, the curves given here for $l = 0$ are the same as those given in their article (SPS 37-39, Vol. III, p. 21, Fig. 16). The representa-

tion of the combined range and doppler data by a value of unity for l implies (by Eq. 16) that the precision σ_p in a range measurement is given by $\sigma_p = \omega^{-1} \dot{\sigma}_p$. Thus, the complete set of numerical values used in the construction of Figs. 10-15 is

$$\sigma_p = 13.75 \text{ m}$$

$$\sigma_p = 0.001 \text{ m/sec}$$

$$\omega = 7.272 \times 10^{-5} \text{ rad/sec}$$

$$N = 1 \text{ sample/min}$$

5. Conclusions

It is evident from the curves that doppler data alone can determine a , b , and c to their ultimate precision without the introduction of range.

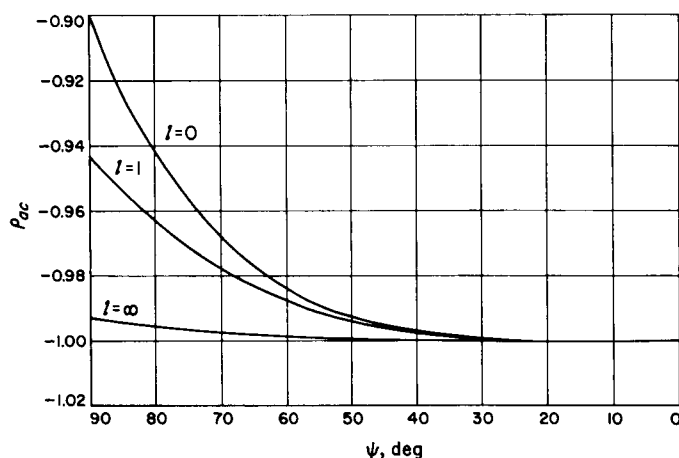


Fig. 10. Correlation of a and c as a function of ψ

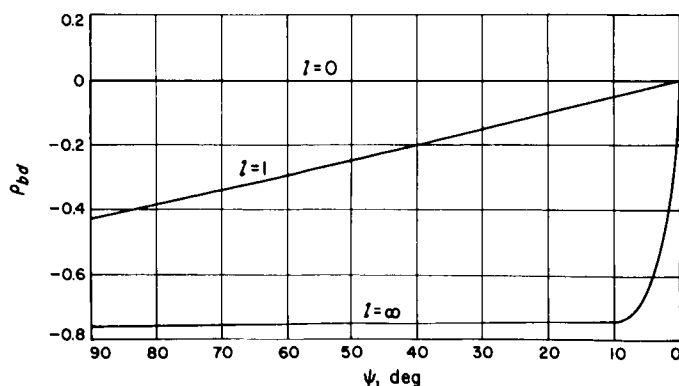


Fig. 11. Correlation of b and d as a function of ψ

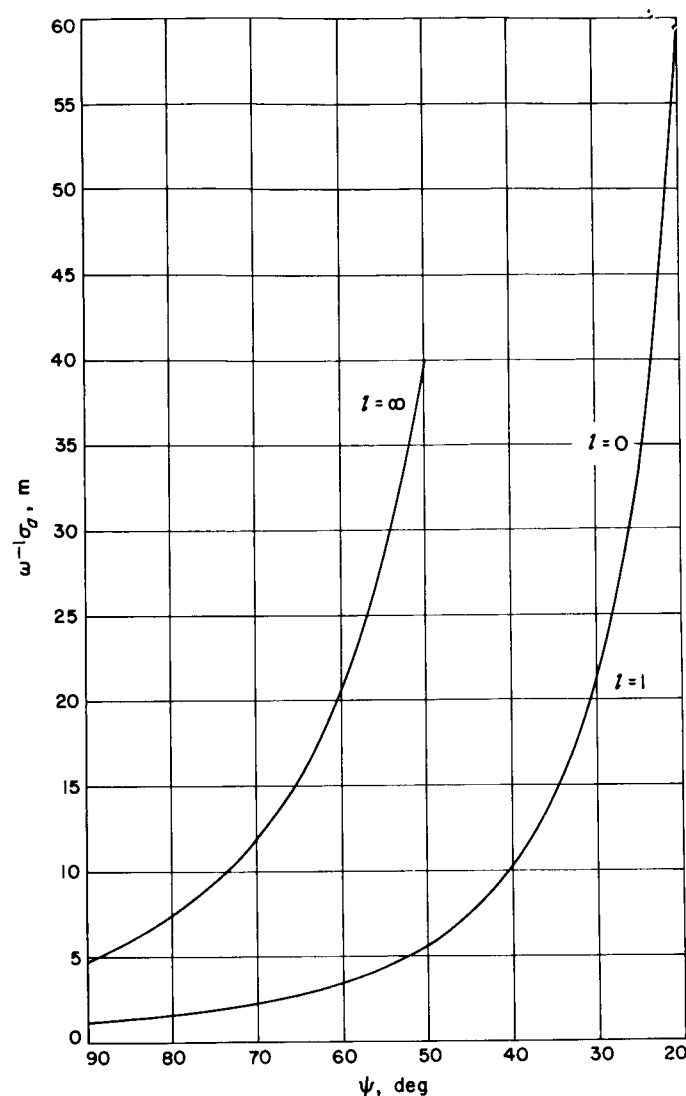


Fig. 12. Uncertainty in a as a function of ψ

Also, there is nothing unexpected in the result that the parameter d , essentially geocentric range, can be determined from the range data and that the introduction of doppler data results in only a slight improvement. The importance of Fig. 15 is that the improvement in σ_d as a function of ψ is nothing more than a $1/N^{1/2}$ effect, and the accuracy for range and doppler data is very close to $\sigma_p/N^{1/2}$. Of course, the improvement for $l=1$ occurs because the correlation ρ_{bd} , which is about -0.75 for the range-only case, is reduced appreciably by the introduction of doppler data.

To summarize, one might ask the following question: What is the advantage of adding DSIF range data to the tracking of a planetary probe such as *Mariner Venus 67*

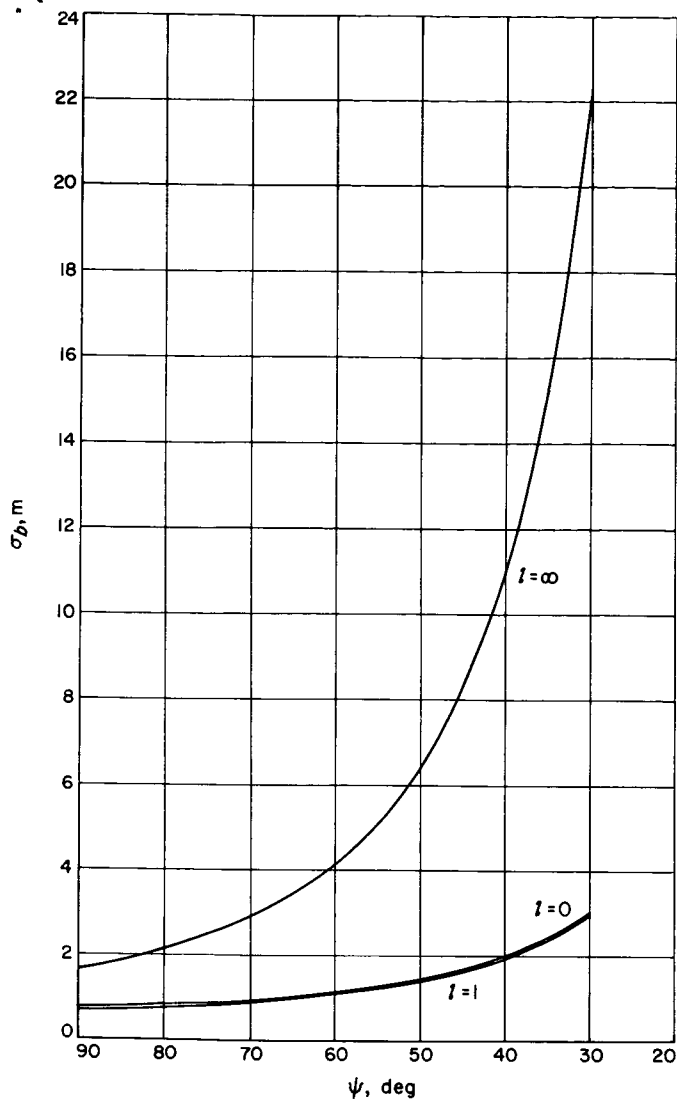


Fig. 13. Uncertainty in b as a function of ψ

or *Mariner Mars 1969*? At this stage, we can answer only in terms of the information content of a single pass of DSIF data. The implications for the determination of orbital elements and astronomical constants indicate the need for further study. For the present, it is clear that the range data provide one additional piece of information, the geocentric range, which is completely unknown for the case of doppler-only tracking; and, as a result, the dimension of the set of compression parameters for a single pass is increased from three to four. Of course, the combination of a series of parameter sets a, b, c from the doppler data can yield an indirect determination of d ; but the advantage of measuring d directly, and thus freeing a, b , and c for the determination of other parameters, is obvious.

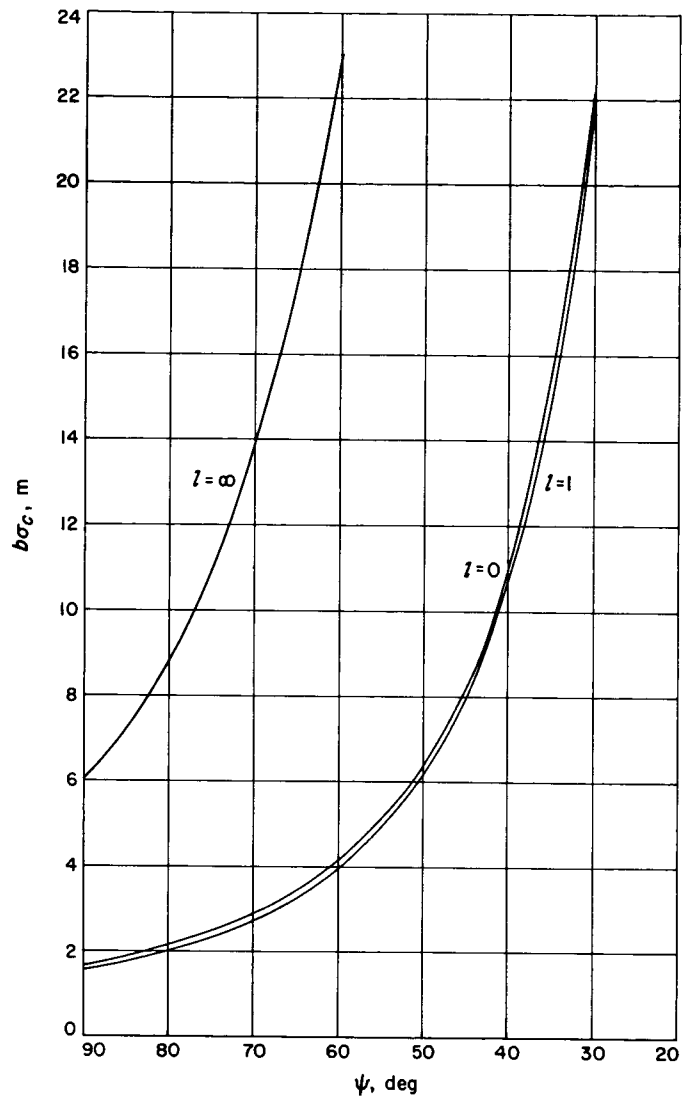


Fig. 14. Uncertainty in c as a function of ψ

Although the possibilities of using both range and doppler data to reduce the effects of systematic errors, such as those which arise from the presence of charged particles in the ray path, are not explored in this analysis, they can be very important in the evaluation of the accuracy of orbital parameters and astronomical constants as determined from range and doppler data.

Finally, we emphasize the fact that the analysis performed here is not valid for orbiters or for a spacecraft undergoing a close encounter with the Moon or a target planet during the pass. The necessary modifications required to handle these cases are important subjects for future study.

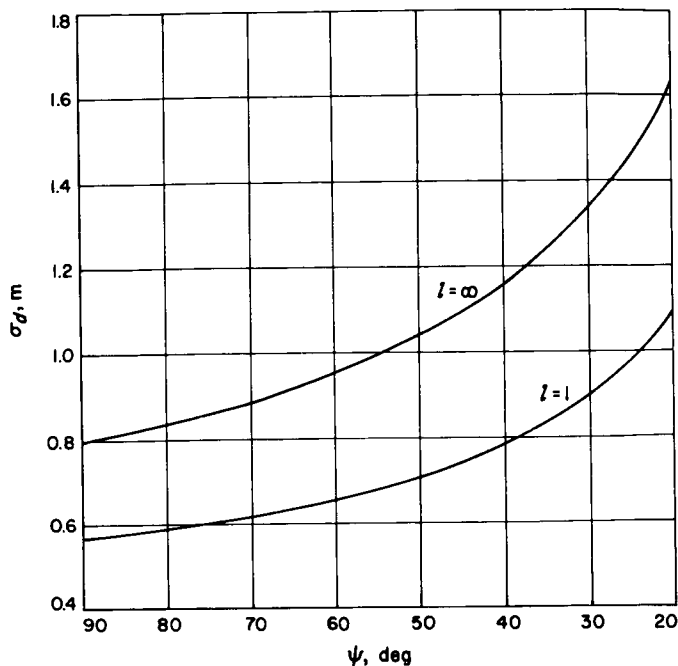


Fig. 15. Uncertainty in d as a function of ψ

D. Lunar Orbiter Ranging Data: Initial Results, W. L. Sjogren and J. D. Mulholland

1. Introduction

Analysis of the *Lunar Orbiter's* ranging data has verified that the system is working properly and that the accuracy of the data is sufficient to corroborate recent corrections applied to the lunar ephemeris. Also, other significant features of the data have helped in the real-time data reduction. Preliminary results indicate that the range data will be valuable for determining such parameters as tracking station location, a better Earth-Moon mass ratio, further refinements to the lunar ephemeris, and additional support for the solution of spherical harmonic coefficients for the lunar potential model.

2. Effect on Lunar Ephemeris

a. Discussion. The most striking and directly comparable result is the verification of the lunar ephemeris corrections in sine parallax (the radial component along the Earth-Moon line) recently published by W. J. Eckert, et al. (Ref. 12), who perform the transformations from the original rectangular coordinates of the Brown lunar theory to the polar coordinate system, preserving the full accuracy of the theory. The magnitude of these corrections varies from +1.4 to -1.3 km during the ranging period. Actual ranging data accurate to approximately

10 m are compared with theoretical calculations of range, derived independent of the ranging data and show good agreement to better than 100 m in more than half the cases when Eckert's corrections and the latest International Astronomical Union (IAU) physical constants are used.

Before the comparisons are examined, a brief explanation will be given of how ranging data from a spacecraft in orbit around the Moon can provide an independent test of the lunar ephemeris, and the causes from which the ephemeris corrections arise will be discussed briefly.

In the orbit determination program used for the *Lunar Orbiter* calculations, the selenocentric (i.e., Moon-centered) orbit of the spacecraft is established solely from doppler observations. These frequency-shift or range-rate data are independent of the range data. A lower limit on the accuracy of the orbit is due primarily to our limited knowledge of the Moon's gravitational potential field. An estimate of the standard deviation or uncertainty in the selenocentric position of the spacecraft due to this cause is about $\sigma = \pm 100$ m. On the other hand, the application of the doppler data to orbit determination is quite insensitive to errors in the position of the Moon; studies show that a constant bias of as much as 9 km in the lunar ephemeris has no discernible effect on the selenocentric orbit elements of the spacecraft. Also, time-varying biases in range on the order of Eckert's corrections that would directly affect the doppler data and the orbit solution are minor compared with the systematic error of the potential field. Other errors independent of the ephemeris are those in the locations of observing stations ($\sigma = \pm 30$ m) and those inherent in the single-precision range computation ($\sigma = \pm 4$ m). If these standard deviations are meaningful, then residuals of several hundreds of meters in the topocentric range (i.e., range from a point of the Earth's surface) must primarily reflect ephemeris error.

The initial analysis was performed with the standard JPL ephemeris tape (Ref. 13) which uses the improved Brown lunar theory of Eckert, Jones, and Clark (Ref. 14) as a basis for the lunar ephemeris.¹⁴ Such an ephemeris is known to be subject to several corrections. In an effort to improve its accuracy, these corrections have been applied to the JPL ephemeris (SPS 37-42, Vol. IV, pp. 2-5). The two corrections that are of interest here arise from two quite divergent causes: (1) an improved value of

¹⁴An ephemeris is a tabulation of predicted positions of a celestial object.

the Earth-Moon mass ratio, and (2) augmented accuracy in a coordinate transformation in the lunar theory. The new value of the mass ratio, $\mu = 81.30$, which is based on data from the *Mariner II* flight, was adopted by the IAU in 1964 (Ref. 15). Since this quantity appears in the gravitational potential of the lunar theory, it is necessary to make corresponding modifications to the affected terms in the expressions for the lunar coordinates. On the other hand, Eckert, Walker, and Eckert (Ref. 12) have noted that the published tables for the lunar theory are less accurate than the basic theory itself, because of a coordinate transformation that was permitted to be of a lower precision than the rest of the analysis. They have derived the necessary corrections for rendering the tables as accurate as the theory, including terms which correspond to linear distances as small as 20 cm, although the accuracy of the resulting ephemeris is not that high. The combined effects of these two corrections can amount to radial displacements of up to 2 km.

We should note that the 1964 adoption of a new value for the astronomical unit in meters (the scaling factor for the solar system) gives rise to by far the largest correction (about 10 km) to the lunar ephemeris. However, this does not directly affect the work presented here, because the JPL system has already taken the AU error into account.

The geometry of the problem is shown in Fig. 16. The selenocentric position vector r of the spacecraft is known to ± 100 m, independent of the range data. The geocentric position vector R of the tracking station is known to ± 30 m. The geocentric lunar position vector A_c is obtained from the ephemeris. The calculation of the range estimate

$$\rho_c = |\rho_c| = |A_c + r - R|$$

introduces another ± 4 -m uncertainty. The quantity ρ_c can be compared directly with the high-precision range data. For the initial analysis, it is assumed that the cor-

rections to sine parallax¹⁵ (the inverse geocentric distance of the Moon) could be treated as acting along the topocentric vector ρ rather than along the geocentric vector A_c ; this assumption causes an error of about 0.1 m, which is negligible for the present purpose. It is also assumed that the corrections to the other coordinates have a negligible effect on these calculations in the first approximation.

b. Results. Fig. 17 shows the residuals $\Delta\rho$ (observed-computed) for *Lunar Orbiter I* during the period September 14–October 20, 1966, and for *Lunar Orbiter II* over the interval November 11–December 19, 1966.¹⁶ The two sets of points correspond to the cases of (1) analysis with the uncorrected ephemeris, and (2) these same data with both corrections applied to the residuals. Since it is evident that at most time points in this period the Eckert corrections dominate over the mass ratio corrections, we have, accordingly, also plotted the transformation corrections to show the general trends that may be expected of the range data in the sparsely populated regions of the graph.

Some of the raw data have been analyzed using a preliminary ephemeris tape incorporating the fully corrected lunar ephemeris, as opposed to the more approximate calculations discussed above. Fig. 18 shows the range residuals from a doppler-only estimate for densely populated data over a one-day (seven orbits) interval, during which time the spacecraft was tracked continuously, except for occultation periods. Three widely separated tracking stations (DSS 12, DSS 41, and DSS 61)¹⁷ of the DSN participated. With the major portion of the model error eliminated, three significant features are evident in these data: (1) high frequency noise is discernible; (2) each station is slightly biased with respect to the others, probably evidence of station location error; and (3) the entire data set has a slight positive bias. This latter bias may be due to still further refinements required by the ephemeris; i.e., a slight change may yet be necessary in the scale factor required to convert the lunar

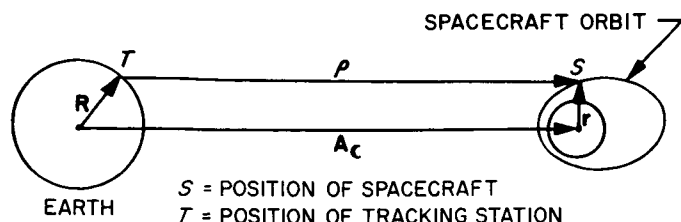


Fig. 16. Geometry of the Lunar Orbiter problem

¹⁵The authors thank Dr. W. J. Eckert, IBM Watson Laboratory, for the prepublication release of the tabular data in Ref. 12, and D. Dannenfeldt, IBM Federal Systems Division, who calculated the ephemeris corrections.

¹⁶The authors express appreciation to M. Grogan, director of The Boeing Company orbit determination efforts at JPL during the in-flight operations, for processing the ranging data in their doppler orbit estimates.

¹⁷Echo DSS, Goldstone, California (DSS 12); Woomera DSS, Island Lagoon, Australia (DSS 41); Robledo DSS, Madrid, Spain (DSS 61).

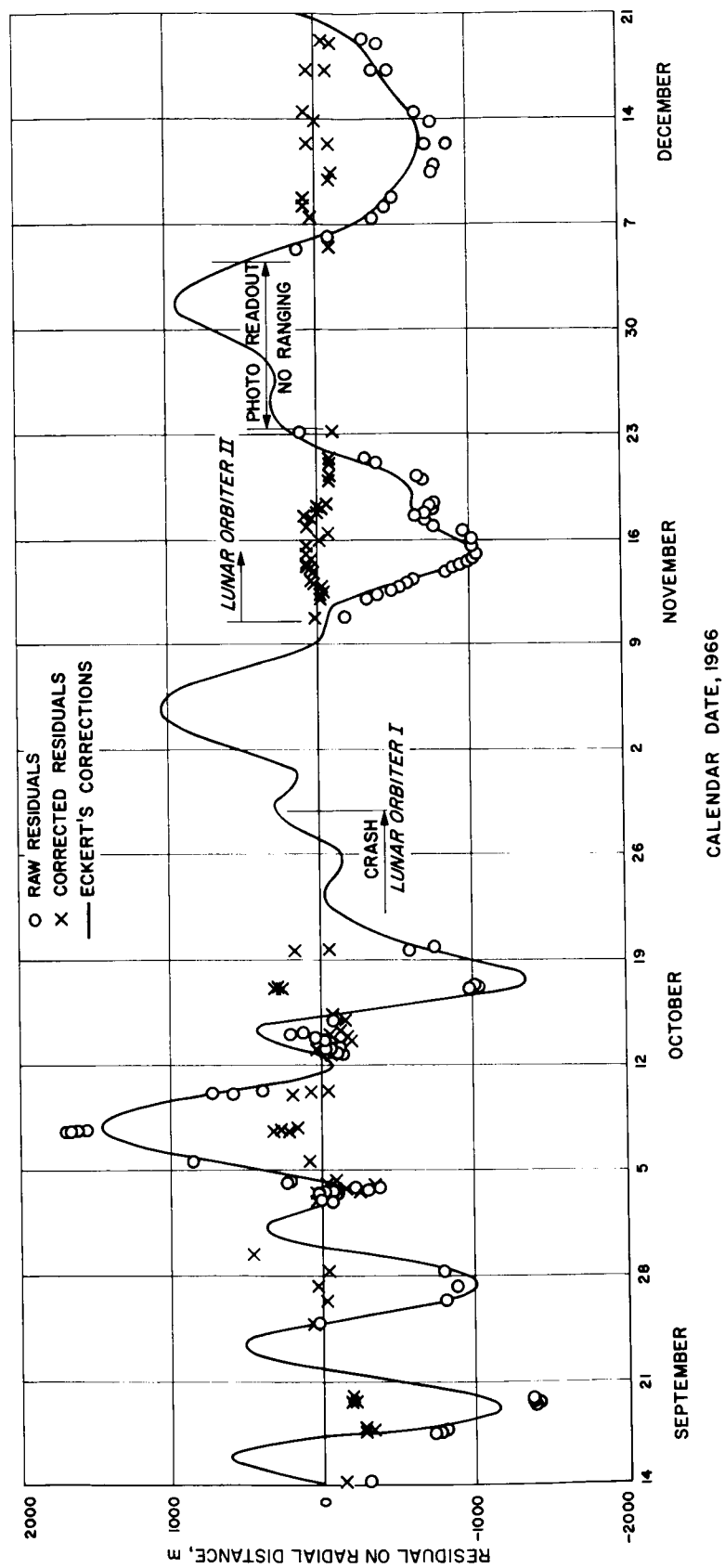


Fig. 17. Ranging residuals and Eckert's transformation corrections to the lunar radial distance

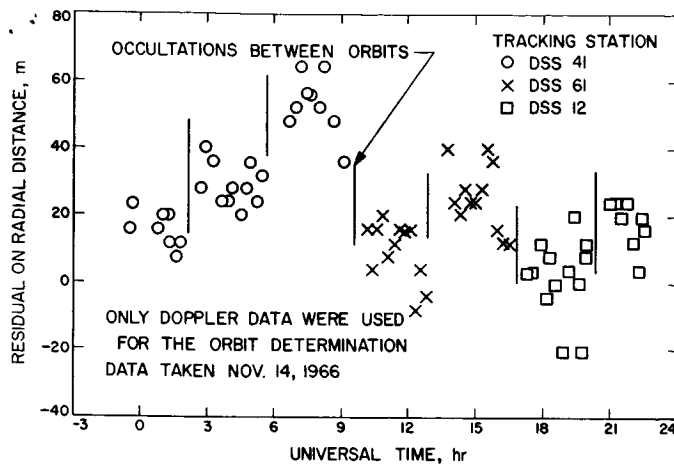


Fig. 18. Lunar Orbiter II ranging residuals using corrected ephemeris

ephemeris from Earth radii to meters. In the JPL system, this factor depends on our value of 299,792.5 km/sec for the speed of light.

We wish to stress that the corrected ephemeris tapes used in this work are still being tested and are not yet available for general distribution; indeed, they are not yet complete. When the new ephemeris is complete and has been thoroughly tested, it will supersede that detailed in Ref. 13.

3. Other Significant Features

In addition to the gratifying results obtained on the lunar ephemeris corrections, there are many other benefits realized from the use of ranging data. They are:

- (1) A check on computer program input for station transmitter frequency
- (2) Time synchronization
- (3) A barometer on accuracy of the doppler fit
- (4) Confirmation of unusual doppler residuals near pericenter
- (5) A reduction in the uncertainty of GM_{\oplus} from 1 to $0.24 \text{ km}^3/\text{sec}^2$.

a. Transmitter frequency. Transmitter-frequency errors became evident early in the real-time mission of *Lunar Orbiter II*, where extensive ranging data were being accumulated. Many times when a station transmitter frequency changed, either it was not incorporated into the computer program or it was not reported by the stations, and the ranging residuals consistently pinpointed the

error. Although these errors were not too significant for the actual mission, they are very important for future data reduction on selenodesy. The erroneous frequency causes a bias in both the ranging data and the doppler data. In practice, the stations change their transmitter reference frequency (22 MHz) in multiples of 10 Hz. A 10-Hz change causes a doppler bias of 0.01 Hz and a range bias of 170 m. The range bias is easily recognized. However, with the present data-reduction capabilities, the doppler biases are hard to discern because they are less than the present systematic errors caused by the incomplete potential model and only slightly larger than the high frequency noise.

b. Time synchronization. In reducing the time-synchronization ranging data taken during station overlapping views,¹⁸ the relative time between the three deep space tracking stations has been checked to better than 5 μsec . This is important for a *Lunar Orbiter* where accelerations are large and a 5-msec timing error can cause a 0.1-Hz bias in the doppler data.

c. Barometer. Shortly after maneuvers (i.e., deboost into initial ellipse, transfer to lower orbit, and transfer to a higher inclination), when data on the new orbit are scant, ranging residuals were a good barometer to indicate the accuracy of the orbit estimate. Although the doppler data were fitted as well as possible, the range residuals might show a skewness on the order of 10 km over a 3-hr data arc, indicating that the estimate was weak and unreliable. Eventually, after several orbits of data were accumulated, the range residuals straightened out and had less than a 100-m bias, indicating a good solution.

d. Confirmation of residuals. The variations in the ranging residuals confirm the unusual doppler residuals that were obtained near pericenter passage during the *Lunar Orbiter I* and *Lunar Orbiter II* missions (Fig. 19). These occasioned much speculation as to the validity of the *Lunar Orbiter I* doppler data, with such items as multipath effects, temperature variations, and antenna motion suggested as possible explanations. Comparison of the integrated doppler residuals with the range residuals obtained with the new ephemeris shows agreement to within the 4-m accuracy of the range computation. Thus, it appears that the peculiar doppler residuals are real and that the spacecraft has an anomalous pericenter motion on the order of 60 m. The doppler data should prove

¹⁸These data have been reduced by F. Borncamp, JPL Section 337, and W. Martin, JPL Section 331.

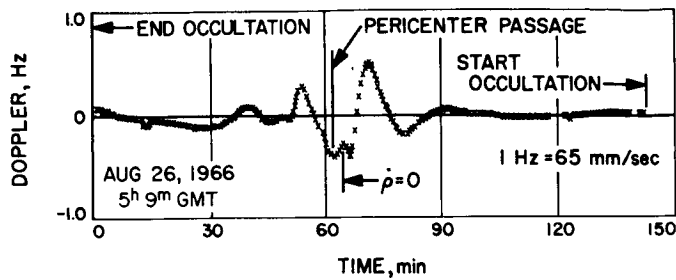


Fig. 19. DSS 12 doppler residuals from Lunar Orbiter I

very powerful for the determination of the lunar oblateness, which we regard as the most probable cause of these inequalities.

e. Reduction of GM_{\oplus} uncertainty. Another by-product of the good ranging residuals is the confirmation of the GM_{\oplus} and GM_{ζ} values that have been used in the data processing. Since most of the ranging residuals spanning the three-month period are less than 100 m, the Earth-Moon distance should be within 100 m of its correct value. Assuming then that the Earth-Moon distance is known to ± 70 m (1σ), the present uncertainty in GM_{\oplus} can be reduced from 1 to $0.24 \text{ km}^3/\text{sec}^2$ by applying the relationship

$$A_{\zeta} = K(GM_{\oplus} + GM_{\zeta})^{1/2}$$

This relationship is derived from the precise knowledge of the Moon's periodic motion, and variations on the relationship show how the uncertainty in A_{ζ} affects GM_{\oplus} uncertainty; i.e.,

$$\delta A_{\zeta} = \frac{A_{\zeta}}{3(GM_{\oplus} + GM_{\zeta})} (\delta GM_{\oplus} + \delta GM_{\zeta})$$

$$3\delta A_{\zeta} \approx \delta GM_{\oplus} + \delta GM_{\zeta}$$

Let $\sigma_{A_{\zeta}} = 0.07 \text{ km}$, and assume $\sigma_{GM_{\zeta}} = 0.1 \text{ km}^3/\text{sec}^2$ from *Mariner II* reduction, which are independent estimates. Then

$$\sigma_{GM_{\oplus}} = \{[3(0.07)]^2 + 0.1^2\}^{1/2} = 0.24 \text{ km}^3/\text{sec}^2$$

4. Conclusions

In conclusion, the ranging data obtained on *Lunar Orbiters I* and *II* have been very effective in giving us a lunar ephemeris correction check, a check on erroneous transmitter frequency, time synchronization, a barometer on doppler orbits, a confirmation of unusual doppler residuals near pericenter, and a firmer control on GM_{\oplus} . Further data reduction should show improvements

in tracking station location, the Earth-Moon mass ratio, greater refinement to the ephemeris scale factor, and additional support for the solution of harmonic coefficients for the lunar potential model.

E. Theoretical Basis for the Double Precision Orbit Determination Program: VI. Angular Observables, T. D. Moyer

1. Introduction

This sixth article in the series presenting the theoretical basis for the double precision orbit determination program (DPODP) gives the formulation for computing angular observables, which are of two types: (1) directly observed angles of the incoming radiation relative to the tracking station's Earth-fixed reference coordinate system, and (2) optical angles—topocentric right ascension α and declination δ —obtained from reduction of photographic plates. As opposed to directly observed angles, optical angles do not contain effects due to stellar aberration and atmospheric refraction (to first order).

The directly observed angle pairs are: (1) hour angle HA and declination δ —most DSN stations; (2) azimuth σ and elevation γ —most Air Force Eastern Test Range (AFETR) stations and some DSN stations; (3) X , Y angles—Manned Space Flight Network (MSFN stations); and (4) X' , Y' angles—MSFN stations.

The topocentric coordinate systems and unit vectors associated with each angle pair are described in Section 2. The formulation for computing the direction of the incoming radiation and each pair of angular observables is given in Section 3. Corrections to the directly observed angles due to small solve-for rotations of the Earth-fixed reference coordinate system are given in Section 4. Partial derivatives of the angular observables with respect to the heliocentric positions of the probe at the transmission time t_2 and the tracking station at the reception time t_3 are given in Section 5. These will be used in a future article of this series to form the partial derivatives of the angular observables with respect to the solve-for parameters.

2. Coordinate Systems and Unit Vectors

a. Right ascension, hour angle, and declination. Fig. 20 shows a rectangular coordinate system centered at the receiving station on Earth. The x - and y -axes are parallel to the Earth's true equator; the x -axis is toward the vernal

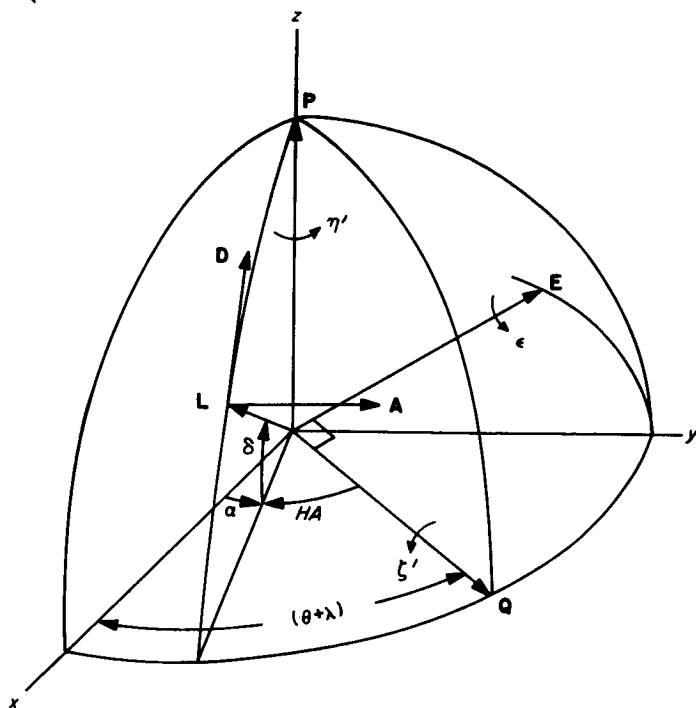


Fig. 20. Right ascension, hour angle, and declination

equinox, and the z-axis is parallel to the true axis of rotation of the Earth.

The unit vector L is directed from the receiving station at the reception time t_3 to the probe (a free probe or a station on some celestial body other than Earth) at its transmission time t_2 . The angles α and δ are the right ascension and declination of the probe. The observer's meridian contains the unit vectors P and Q and makes an angle $(\theta + \lambda)$ with the vernal equinox, where

θ = true sidereal time = Greenwich hour angle of true equinox at reception time t_3 (SPS 37-41, Vol. III, p. 37, Eq. 64)

λ = east longitude of receiving station, relative to true pole

The unit vector E is normal to P and Q . The angle HA is the hour angle of the probe. The reference coordinate system QEP may be rotated through the small angles ζ' about Q , ϵ about E , and η' about P . Corrections to the computed HA and δ are given in Section 4 as a function of the solve-for rotations ζ' , ϵ , and η' .

The unit vectors D and A in the directions of increasing declination and right ascension are used in computing the

partial derivatives. The vector A is normal to L and D . The rectangular components of D and A are

$$D = \begin{pmatrix} D_x \\ D_y \\ D_z \end{pmatrix} = \begin{pmatrix} -\sin \delta \cos \alpha \\ -\sin \delta \sin \alpha \\ \cos \delta \end{pmatrix} \quad (1)$$

$$A = \begin{pmatrix} A_x \\ A_y \\ A_z \end{pmatrix} = \begin{pmatrix} -\sin \alpha \\ \cos \alpha \\ 0 \end{pmatrix} \quad (2)$$

b. The north-east-zenith coordinate system. The angles azimuth and elevation, and the angles X , Y and X' , Y' for MSFN stations are all referred to the north-east-zenith coordinate system. Fig. 21 shows an Earth equatorial rectangular coordinate system with the x-axis directed toward the true vernal equinox and the z-axis along the instantaneous axis of rotation. The NEZ coordinate system is centered at the tracking station S , whose meridian makes an angle $(\theta + \lambda)$ with the x-axis. The unit vector Z is contained in the meridian plane and makes an angle ϕ_g with the true equatorial plane, where ϕ_g is the computed geodetic latitude. The unit vectors N and E are normal to Z and directed to the north and to the east, respectively. The rectangular components of these unit vectors are

$$N = \begin{pmatrix} N_x \\ N_y \\ N_z \end{pmatrix} = \begin{pmatrix} -\sin \phi_g \cos (\theta + \lambda) \\ -\sin \phi_g \sin (\theta + \lambda) \\ \cos \phi_g \end{pmatrix} \quad (3)$$

$$E = \begin{pmatrix} E_x \\ E_y \\ E_z \end{pmatrix} = \begin{pmatrix} -\sin (\theta + \lambda) \\ \cos (\theta + \lambda) \\ 0 \end{pmatrix} \quad (4)$$

$$Z = \begin{pmatrix} Z_x \\ Z_y \\ Z_z \end{pmatrix} = \begin{pmatrix} \cos \phi_g \cos (\theta + \lambda) \\ \cos \phi_g \sin (\theta + \lambda) \\ \sin \phi_g \end{pmatrix} \quad (5)$$

The geodetic latitude of the receiving station ϕ_g referred to the true pole and equator is computed from

$$\phi_g = \phi + (\phi_g - \phi) \quad (6)$$

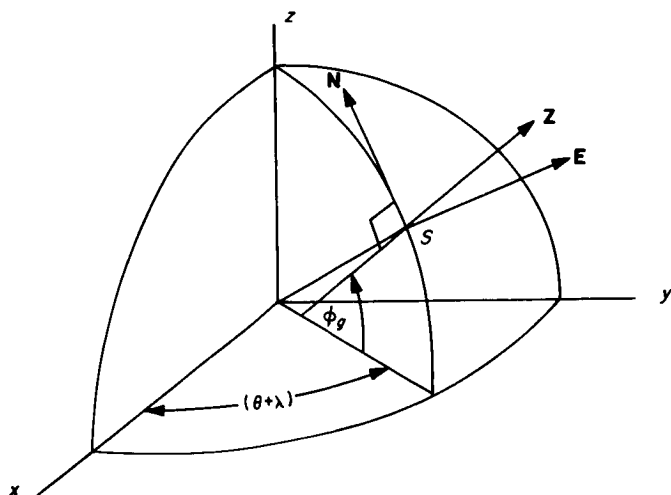


Fig. 21. The north-east-zenith coordinate system

where

ϕ = solve-for geocentric latitude of receiving station, referred to true pole and equator

and $(\phi_g - \phi)$ is computed from

$$(\phi_g - \phi) \approx \frac{e^2 a_e}{r} \sin \phi \cos \phi \times \left[1 + \frac{e^2 a_e}{r} - e^2 \left(\frac{2a_e}{r} - \frac{1}{2} \right) \sin^2 \phi \right] \quad (7)$$

where

e = eccentricity of reference spheroid

r = solve-for geocentric radius of receiving station

a_e = mean equatorial radius of Earth

The eccentricity e can be computed from the flattening f , using a nominal value of 298.3, as

$$e^2 = 2f - f^2 \quad (8)$$

c. Azimuth and elevation. Fig. 22 shows the unit vector L in the NEZ coordinate system centered at the receiving station S . The angles σ and γ are the azimuth and elevation, respectively. The reference coordinate system may be rotated through the small angles η about N , ϵ about E , and ζ about Z . Section 4 gives corrections to the computed values of azimuth σ and elevation γ as a function of the solve-for rotations η , ϵ , and ζ .

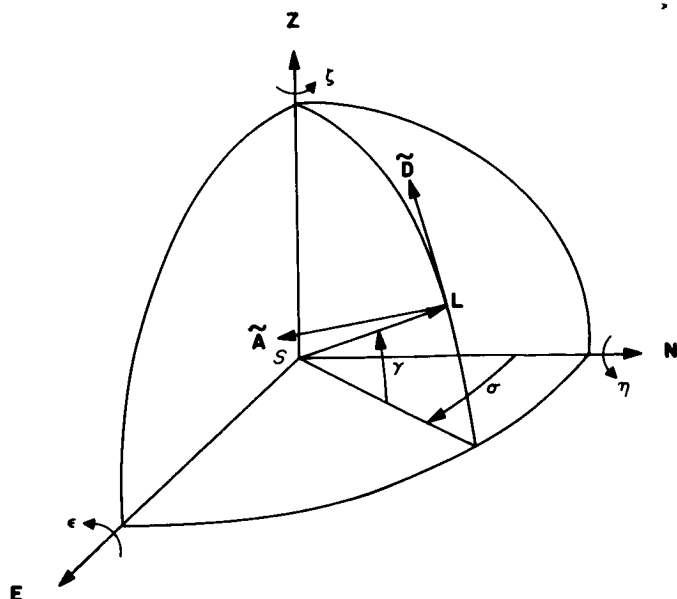


Fig. 22. Azimuth and elevation

The unit vectors \tilde{D} and \tilde{A} (normal to L) in the directions of increasing γ and σ , respectively, are used in computing the partial derivatives. The components of \tilde{D} and \tilde{A} along N , E , and Z are

$$\tilde{D} = \begin{pmatrix} \tilde{D}_N \\ \tilde{D}_E \\ \tilde{D}_Z \end{pmatrix} = \begin{pmatrix} -\sin \gamma \cos \sigma \\ -\sin \gamma \sin \sigma \\ \cos \gamma \end{pmatrix} \quad (9)$$

$$\tilde{A} = \begin{pmatrix} \tilde{A}_N \\ \tilde{A}_E \\ \tilde{A}_Z \end{pmatrix} = \begin{pmatrix} -\sin \sigma \\ \cos \sigma \\ 0 \end{pmatrix} \quad (10)$$

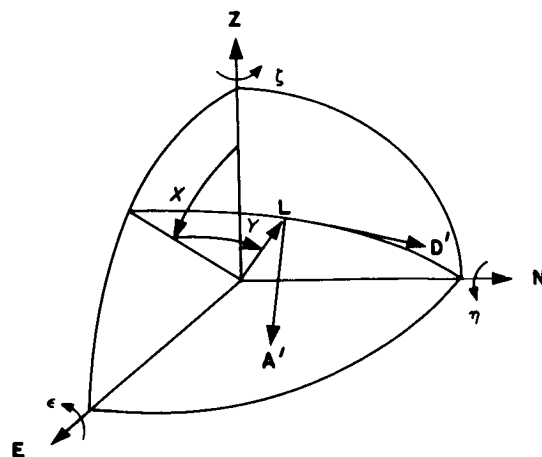


Fig. 23. X and Y angles

Using Eqs. (3), (4), and (5), the rectangular components of $\tilde{\mathbf{D}}$ and $\tilde{\mathbf{A}}$ referred to the true Earth equator and equinox are

$$\tilde{\mathbf{D}} = \begin{pmatrix} \tilde{D}_x \\ \tilde{D}_y \\ \tilde{D}_z \end{pmatrix} = \begin{pmatrix} \sin \gamma [\cos \sigma \sin \phi_g \cos (\theta + \lambda) + \sin \sigma \sin (\theta + \lambda)] + \cos \gamma \cos \phi_g \cos (\theta + \lambda) \\ \sin \gamma [\cos \sigma \sin \phi_g \sin (\theta + \lambda) - \sin \sigma \cos (\theta + \lambda)] + \cos \gamma \cos \phi_g \sin (\theta + \lambda) \\ - \sin \gamma \cos \sigma \cos \phi_g + \cos \gamma \sin \phi_g \end{pmatrix} \quad (11)$$

$$\tilde{\mathbf{A}} = \begin{pmatrix} \tilde{A}_x \\ \tilde{A}_y \\ \tilde{A}_z \end{pmatrix} = \begin{pmatrix} \sin \sigma \sin \phi_g \cos (\theta + \lambda) - \cos \sigma \sin (\theta + \lambda) \\ \sin \sigma \sin \phi_g \sin (\theta + \lambda) + \cos \sigma \cos (\theta + \lambda) \\ - \sin \sigma \cos \phi_g \end{pmatrix} \quad (12)$$

d. X and Y angles for MSFN stations with 20-ft antenna. Fig. 23 shows the angles X and Y referred to the NEZ reference coordinate system at the receiving station.

The unit vectors \mathbf{D}' and \mathbf{A}' (normal to \mathbf{L}) are in the directions of increasing Y and X , respectively. The components of \mathbf{D}' and \mathbf{A}' along the N, E, and Z axes are

$$\mathbf{D}' = \begin{pmatrix} D'_N \\ D'_E \\ D'_Z \end{pmatrix} = \begin{pmatrix} \cos Y \\ - \sin Y \sin X \\ - \sin Y \cos X \end{pmatrix} \quad (13)$$

$$\mathbf{A}' = \begin{pmatrix} A'_N \\ A'_E \\ A'_Z \end{pmatrix} = \begin{pmatrix} 0 \\ \cos X \\ - \sin X \end{pmatrix} \quad (14)$$

Using Eqs. (3)–(5), the rectangular components of \mathbf{D}' and \mathbf{A}' referred to the true Earth equator and equinox are

$$\mathbf{D}' = \begin{pmatrix} D'_x \\ D'_y \\ D'_z \end{pmatrix} = \begin{pmatrix} \sin Y [\sin X \sin (\theta + \lambda) - \cos X \cos \phi_g \cos (\theta + \lambda)] - \cos Y \sin \phi_g \cos (\theta + \lambda) \\ - \sin Y [\sin X \cos (\theta + \lambda) + \cos X \cos \phi_g \sin (\theta + \lambda)] - \cos Y \sin \phi_g \sin (\theta + \lambda) \\ \cos Y \cos \phi_g - \sin Y \cos X \sin \phi_g \end{pmatrix} \quad (15)$$

$$\mathbf{A}' = \begin{pmatrix} A'_x \\ A'_y \\ A'_z \end{pmatrix} = \begin{pmatrix} - \sin X \cos \phi_g \cos (\theta + \lambda) - \cos X \sin (\theta + \lambda) \\ - \sin X \cos \phi_g \sin (\theta + \lambda) + \cos X \cos (\theta + \lambda) \\ - \sin X \sin \phi_g \end{pmatrix} \quad (16)$$

e. X' and Y' angles for MSFN stations with 85-ft antenna. Fig. 24 shows the angles X' and Y' referenced to the NEZ reference coordinate system at the receiving station.

The unit vectors \mathbf{D}'' and \mathbf{A}'' (normal to \mathbf{L}) are in the directions of increasing Y' and X' , respectively. The components of \mathbf{D}'' and \mathbf{A}'' along the N, E, and Z axes are

$$\mathbf{D}'' = \begin{pmatrix} D''_N \\ D''_E \\ D''_Z \end{pmatrix} = \begin{pmatrix} \sin Y' \sin X' \\ \cos Y' \\ - \sin Y' \cos X' \end{pmatrix} \quad (17)$$

$$\mathbf{A}'' = \begin{Bmatrix} A''_x \\ A''_y \\ A''_z \end{Bmatrix} = \begin{Bmatrix} -\cos X' \\ 0 \\ -\sin X' \end{Bmatrix} \quad (18)$$

Using Eqs. (3)–(5), the rectangular components of \mathbf{D}'' and \mathbf{A}'' referred to the true Earth equator and equinox are

$$\mathbf{D}'' = \begin{Bmatrix} D''_x \\ D''_y \\ D''_z \end{Bmatrix} = \begin{Bmatrix} -\sin Y' [\sin X' \sin \phi_g \cos(\theta + \lambda) + \cos X' \cos \phi_g \cos(\theta + \lambda)] - \cos Y' \sin(\theta + \lambda) \\ -\sin Y' [\sin X' \sin \phi_g \sin(\theta + \lambda) + \cos X' \cos \phi_g \sin(\theta + \lambda)] + \cos Y' \cos(\theta + \lambda) \\ \sin Y' (\sin X' \cos \phi_g - \cos X' \sin \phi_g) \end{Bmatrix} \quad (19)$$

$$\mathbf{A}'' = \begin{Bmatrix} A''_x \\ A''_y \\ A''_z \end{Bmatrix} = \begin{Bmatrix} \cos X' \sin \phi_g \cos(\theta + \lambda) - \sin X' \cos \phi_g \cos(\theta + \lambda) \\ \cos X' \sin \phi_g \sin(\theta + \lambda) - \sin X' \cos \phi_g \sin(\theta + \lambda) \\ -\cos X' \cos \phi_g - \sin X' \sin \phi_g \end{Bmatrix} \quad (20)$$

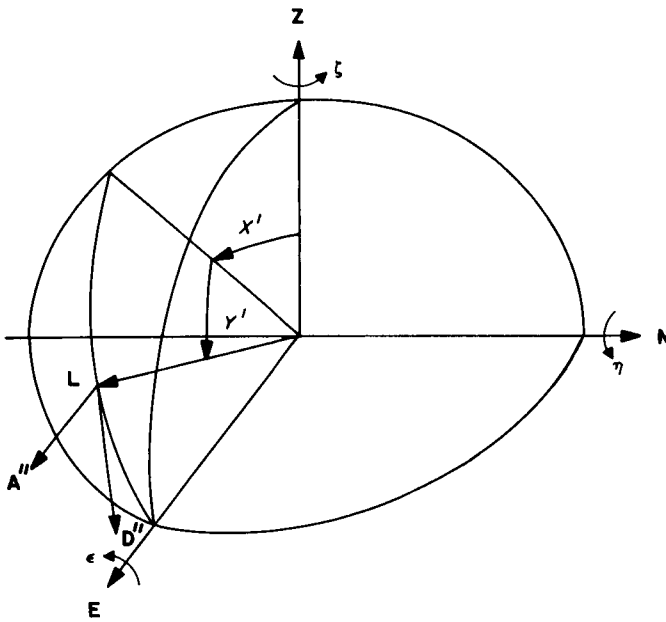


Fig. 24. X' and Y' angles

3. Computation of Angular Observables

a. Computation of unit vector \mathbf{L} . The unit vector \mathbf{L} will be computed by one procedure for the directly observed angles (hour angle–declination, azimuth–elevation, X – Y , and X' – Y') and will be computed by a second procedure for optical right ascension–declination obtained from the reduction of photographic plates.

Directly observed angles. The unit vector \mathbf{L} is directed from the heliocentric position of the receiving station at the reception time t_3 to the heliocentric position of the

probe (a free probe or a station on some celestial body other than the Earth) at its transmission time t_2 . The unit vector \mathbf{L}_{50} with rectangular components referred to the mean equator and equinox of 1950.0 is

$$\mathbf{L}_{50} = -\frac{\mathbf{r}_{23}}{r_{23}} \quad (21)$$

where

$$\mathbf{r}_{23} = \mathbf{r}_3 - \mathbf{r}_2 \quad (22)$$

$$r_{23} = \|\mathbf{r}_{23}\| \quad (23)$$

and

\mathbf{r}_3 = heliocentric position of receiving station at reception time t_3 , with rectangular components referred to mean Earth equator and equinox of 1950.0

\mathbf{r}_2 = heliocentric position of probe at transmission time t_2 , with rectangular components referred to mean Earth equator and equinox of 1950.0

The vector \mathbf{r}_{23} is obtained from the solution of the light time problem (SPS 37-41, Vol. III, pp. 31–38).

The unit vector \mathbf{L}_{50} is directed from the station to the probe in the heliocentric space–time frame of reference in which the DPODP operates. In the observer's topocentric space–time frame of reference, the direction to the probe is $\mathbf{L}_{50} + \Delta\mathbf{L}_{50}$, where $\Delta\mathbf{L}_{50}$ can be derived from the Lorentz transformation of special relativity. The following first-order expression for $\Delta\mathbf{L}_{50}$ is the same as that due to the stellar aberration of light, the change in

the direction of incoming light due to the heliocentric motion of the receiving station:

$$\Delta \mathbf{L}_{50} = \frac{1}{c} [\dot{\mathbf{r}}_3 - (\mathbf{L}_{50} \cdot \dot{\mathbf{r}}_3) \mathbf{L}_{50}] \quad (24)$$

where

c = speed of light

$\dot{\mathbf{r}}_3$ = heliocentric velocity of receiving station at reception time t_3 , with rectangular components referred to mean Earth equator and equinox of 1950.0

The unit vector \mathbf{L}_{true} with rectangular components referred to the true equator and equinox of the date of observation t_3 is given by

$$\mathbf{L}_{true} = N(t_3) A(t_3) (\mathbf{L}_{50} + \Delta \mathbf{L}_{50}) \quad (25)$$

where

$A(t_3)$ = precession matrix, transforming rectangular components of a vector referred to the mean Earth equator and equinox of 1950.0 to components referred to the mean Earth equator and equinox of the date of observation t_3 .

$N(t_3)$ = nutation matrix, transforming rectangular components of a vector referred to the mean Earth equator and equinox of the date t_3 to components referred to the true Earth equator and equinox of the date t_3 .

The direction \mathbf{L}_{true} from Eq. (25) does not account for the bending of the incoming ray due to atmospheric refraction, which increases the elevation angle γ of the incoming ray by $\Delta_r \gamma$. Referring to Fig. 22, the change in \mathbf{L} due to atmospheric refraction is $\Delta_r \gamma \tilde{\mathbf{D}}$. Thus, the unit vector from the observer outward along the incoming ray is given by

$$\mathbf{L}_{true} = \frac{N(t_3) A(t_3) (\mathbf{L}_{50} + \Delta \mathbf{L}_{50}) + \Delta_r \gamma \tilde{\mathbf{D}}}{\|N(t_3) A(t_3) (\mathbf{L}_{50} + \Delta \mathbf{L}_{50}) + \Delta_r \gamma \tilde{\mathbf{D}}\|} \quad (26)$$

This vector has been normalized since the value of the vector in the numerator is slightly greater than unity. In order to compute $\tilde{\mathbf{D}}$ and $\Delta_r \gamma$, the azimuth σ and elevation γ are required. They are obtained from Eqs. (35)–(37), using \mathbf{L}_{true} from Eq. (25). Given σ and γ , the rectangular

components of $\tilde{\mathbf{D}}$ referred to the true Earth equator and equinox of the date of observation t_3 are computed from Eq. (11). The refraction correction is computed as a function of the elevation angle γ from one of the two formulas given in Ref. 16, on p. 21.

Optical right ascension–declination. For optical right ascension–declination obtained from the reduction of photographic plates, the unit vector \mathbf{L} referred to the mean or true equator and equinox of the date t_R to which the observations are referred (generally not the date of observation) is computed from

$$\mathbf{L}_{opt (true)} = \frac{N(t_R) A(t_R) [\mathbf{L}_{50} + A(t_3)^T N(t_3)^T \Delta_r \gamma \tilde{\mathbf{D}}]}{\|N(t_R) A(t_R) [\mathbf{L}_{50} + A(t_3)^T N(t_3)^T \Delta_r \gamma \tilde{\mathbf{D}}]\|} \quad (27)$$

or

$$\mathbf{L}_{opt (mean)} = \frac{A(t_R) [\mathbf{L}_{50} + A(t_3)^T N(t_3)^T \Delta_r \gamma \tilde{\mathbf{D}}]}{\|A(t_R) [\mathbf{L}_{50} + A(t_3)^T N(t_3)^T \Delta_r \gamma \tilde{\mathbf{D}}]\|} \quad (28)$$

where $A(t_R)$ and $N(t_R)$ are the precession and nutation matrices evaluated at the reference time t_R , and $A(t_3)$ and $N(t_3)$ are these matrices evaluated at the data reception time t_3 . The vector \mathbf{L}_{50} is computed from Eq. (21). The vector $\tilde{\mathbf{D}}$ is computed from Eq. (11) with θ evaluated at t_3 and using σ and γ computed from Eqs. (35)–(37) with \mathbf{L}_{true} equal to

$$\mathbf{L}_{true} = N(t_3) A(t_3) \mathbf{L}_{50} \quad (29)$$

The right ascension and declination of a *star* obtained from the reduction of photographic plates is free from the effects of stellar aberration and refraction at least to first order. If a second-order plate reduction method is used, the effects of refraction can be removed completely. However, the right ascension and declination of a *probe* obtained from the reduction of photographic plates is affected to a small extent by refraction because the probe is much nearer than the background stars. The expression for the correction to the computed elevation angle $\Delta_r \gamma$ has been derived by D. Cain (Ref. 16, p. 22). However, the sign of the correction is wrong and should be *negative*. The right ascension and declination of a probe or star obtained from the reduction of photographic plates is not affected by stellar aberration; hence, $\Delta \mathbf{L}_{50}$ does not appear in Eqs. (27) or (28).

b. Computation of observed angles. Optical right ascension and declination are computed from \mathbf{L} of Eqs. (27) or (28). The directly observed angles are computed from

\mathbf{L} of Eq. (26). In either case, the rectangular Earth equatorial components of \mathbf{L} are denoted by

$$\mathbf{L} = \begin{pmatrix} L_x \\ L_y \\ L_z \end{pmatrix} \quad (30)$$

Right ascension and declination. Referring to Fig. 20, compute declination δ from

$$\sin \delta = L_z, \quad -90 \text{ deg} \leq \delta \leq 90 \text{ deg} \quad (31)$$

and compute the right ascension from

$$\sin \alpha = \frac{L_y}{\cos \delta}, \quad 0 \text{ deg} \leq \alpha \leq 360 \text{ deg} \quad (32)$$

$$\cos \alpha = \frac{L_x}{\cos \delta} \quad (33)$$

Hour angle and declination. Compute α and δ from Eqs. (31)–(33). Compute HA from (see Fig. 20)

$$HA = (\theta + \lambda) - \alpha, \quad 0 \text{ deg} \leq HA \leq 360 \text{ deg} \quad (34)$$

where

θ = true sidereal time at reception time t_r (SPS 37-41, Vol. III, p. 37, Eq. 64)

λ = east longitude of receiving station, referred to true pole

Azimuth and elevation. Given the unit vectors \mathbf{N} , \mathbf{E} , and \mathbf{Z} computed from Eqs. (3)–(5) at the data reception time t_r , compute the elevation angle γ from (see Fig. 22)

$$\sin \gamma = \mathbf{L} \cdot \mathbf{Z}, \quad 0 \text{ deg} \leq \gamma \leq 90 \text{ deg} \quad (35)$$

and compute the azimuth σ from

$$\sin \sigma = \frac{\mathbf{L} \cdot \mathbf{E}}{\cos \gamma}, \quad 0 \text{ deg} \leq \sigma \leq 360 \text{ deg} \quad (36)$$

$$\cos \sigma = \frac{\mathbf{L} \cdot \mathbf{N}}{\cos \gamma} \quad (37)$$

Note that σ is indeterminate for $\gamma = 90 \text{ deg}$.

X and Y angles for MSFN stations with a 30-ft antenna. Referring to Fig. 23, compute the angle Y from

$$\sin Y = \mathbf{L} \cdot \mathbf{N}, \quad -90 \text{ deg} \leq Y \leq 90 \text{ deg} \quad (38)$$

and compute the angle X from

$$\sin X = \frac{\mathbf{L} \cdot \mathbf{E}}{\cos Y}, \quad -90 \text{ deg} \leq X \leq 90 \text{ deg} \quad (39)$$

Note that X is indeterminate for $Y = \pm 90 \text{ deg}$, which can occur only when the probe is on the horizon.

X' and Y' angles for MSFN stations with an 85-ft antenna. Referring to Fig. 24, compute the angle Y' from

$$\sin Y' = \mathbf{L} \cdot \mathbf{E}, \quad -90 \text{ deg} \leq Y' \leq 90 \text{ deg} \quad (40)$$

and compute the angle X' from

$$\sin X' = -\frac{\mathbf{L} \cdot \mathbf{N}}{\cos Y'}, \quad -90 \text{ deg} \leq X' \leq 90 \text{ deg} \quad (41)$$

Note that X' is indeterminate for $Y' = \pm 90 \text{ deg}$, which can occur only when the probe is on the horizon.

4. Corrections Due to Small Rotations of Reference Coordinate System at Observing Station

The computed angles may not agree with the observed angles because the mathematical model for the orientation of the reference coordinate system at the receiving station differs from the actual orientation of the coordinate system (instrument axes). The difference in orientation is due to two errors: (1) errors in the mathematical model (primarily the difference between the actual plumb bob direction and the geodetic plumb bob direction computed from a reference ellipsoid of revolution), and (2) errors in orientation of the instrument axes (e.g., alignment of the vertical axis with the plumb bob direction for the azimuth-elevation system).

Formulas are developed for corrections to the computed angles as linear functions of the small rotations of the computed reference coordinate system about each of its three mutually perpendicular axes.

This type of correction does not apply for right ascension and declination obtained from the reduction of photographic plates.

a. Hour angle–declination. Referring to Fig. 20, the reference coordinate system is **QEP** and the rotations are ζ' about the **Q** axis, ϵ about the **E** axis, and η' about the **P** axis. All rotations are in the positive direction, using the right-hand rule.

The dot products of **L** with **Q**, **E**, and **P** are

$$\mathbf{L} \cdot \mathbf{Q} = \cos \delta \cos HA \quad (42)$$

$$\mathbf{L} \cdot \mathbf{E} = -\cos \delta \sin HA \quad (43)$$

$$\mathbf{L} \cdot \mathbf{P} = \sin \delta \quad (44)$$

In terms of the rotations, the variations in the unit vectors are

$$\Delta \mathbf{Q} = \eta' \mathbf{E} - \epsilon \mathbf{P} \quad (45)$$

$$\Delta \mathbf{E} = \zeta' \mathbf{P} - \eta' \mathbf{Q} \quad (46)$$

$$\Delta \mathbf{P} = \epsilon \mathbf{Q} - \zeta' \mathbf{E} \quad (47)$$

The variation in δ due to the variation in **P** is obtained from Eq. (44) as

$$(\cos \delta) \Delta \delta = \mathbf{L} \cdot \Delta \mathbf{P} \quad (48)$$

Substituting Eqs. (47), (42), and (43) gives

$$\Delta \delta = \zeta' \sin HA + \epsilon \cos HA \quad (49)$$

From Eq. (42), the variation in HA is given by

$$(\cos \delta \sin HA) \Delta HA = -\mathbf{L} \cdot \Delta \mathbf{Q} - (\sin \delta \cos HA) \Delta \delta \quad (50)$$

Substituting Eqs. (43), (44), (45), and (49) and simplifying gives

$$\Delta HA = \eta' + \tan \delta (\epsilon \sin HA - \zeta' \cos HA) \quad (51)$$

This same equation may be obtained by differentiating Eq. (43).

The meridian plane is determined by the vector **P** to the pole and by the plumb bob line. If the plumb bob is displaced to the west through the angle θ_w , the meridian plane is displaced to the east through the angle

$$\eta' = \frac{\theta_w}{\cos \phi_g} \quad (52)$$

If θ_w is known, Eq. (52) provides an *a priori* estimate of η' .

b. Azimuth–elevation. Referring to Fig. 22, the reference coordinate system is **NEZ** and the rotations are η about **N**, ϵ about **E**, and ζ about **Z**.

The variations in the unit vectors due to the rotations are

$$\Delta \mathbf{N} = \epsilon \mathbf{Z} - \zeta \mathbf{E} \quad (53)$$

$$\Delta \mathbf{E} = \zeta \mathbf{N} - \eta \mathbf{Z} \quad (54)$$

$$\Delta \mathbf{Z} = \eta \mathbf{E} - \epsilon \mathbf{N} \quad (55)$$

The variations in elevation γ and azimuth σ due to the variations in the unit vectors are obtained from Eqs. (35) and (36) or (37). Substituting Eqs. (53)–(55) gives

$$\Delta \gamma = \eta \sin \sigma - \epsilon \cos \sigma \quad (56)$$

$$\Delta \sigma = \zeta - \tan \gamma (\eta \cos \sigma + \epsilon \sin \sigma) \quad (57)$$

c. Angles X , Y . Referring to Fig. 23, the reference coordinate system and rotations are the same as for the azimuth–elevation system. Using Eqs. (38), (39), (53), and (54),

$$\Delta Y = -\zeta \sin X + \epsilon \cos X \quad (58)$$

$$\Delta X = -\eta + \tan Y (\epsilon \sin X + \zeta \cos X) \quad (59)$$

d. Angles X' , Y' . The azimuth–elevation reference coordinate system and rotations are also used for the $X'Y'$ system. Using Eqs. (40), (41), (53), and (54),

$$\Delta Y' = -\zeta \sin X' - \eta \cos X' \quad (60)$$

$$\Delta X' = -\epsilon + \tan Y' (\zeta \cos X' - \eta \sin X') \quad (61)$$

5. Partial Derivatives of Angular Observables With Respect to Heliocentric 1950.0 Position Vector of Probe and Receiving Station

This section gives partial derivatives of each angular observable with respect to rectangular components of the heliocentric position vector of the probe and receiving station, referred to the mean equator and equinox of 1950.0. These subpartial derivatives will be used in a future article of this series to form the partial derivative of each angular observable with respect to the total parameter vector q .

The partial derivatives of the observed angles with respect to r_2 , obtained from an examination of Figs. 20 and 22-24, are given below. In these expressions, a subscript 50 after a unit vector indicates that the rectangular components of the vector are referred to the mean Earth equator and equinox of 1950.0.

$$\begin{aligned} \frac{\partial \alpha}{\partial r_2} &= \left(\frac{\partial \alpha}{\partial x_2}, \frac{\partial \alpha}{\partial y_2}, \frac{\partial \alpha}{\partial z_2} \right) = \frac{\mathbf{A}_{50}^T}{r_{23} \cos \delta} \\ &= \left(\frac{A_{x50}}{r_{23} \cos \delta}, \frac{A_{y50}}{r_{23} \cos \delta}, \frac{A_{z50}}{r_{23} \cos \delta} \right) \end{aligned} \quad (62)$$

$$\frac{\partial \delta}{\partial r_2} = \frac{\mathbf{D}_{50}^T}{r_{23}} \quad (63)$$

$$\frac{\partial HA}{\partial r_2} = - \frac{\partial \alpha}{\partial r_2} \quad (64)$$

$$\frac{\partial \sigma}{\partial r_2} = \frac{\tilde{\mathbf{A}}_{50}^T}{r_{23} \cos \gamma} \quad (65)$$

$$\frac{\partial \gamma}{\partial r_2} = \frac{\tilde{\mathbf{D}}_{50}^T}{r_{23}} \quad (66)$$

$$\frac{\partial X}{\partial r_2} = \frac{\mathbf{A}_{50}^T}{r_{23} \cos Y} \quad (67)$$

$$\frac{\partial Y}{\partial r_2} = \frac{\mathbf{D}_{50}^T}{r_{23}} \quad (68)$$

$$\frac{\partial X'}{\partial r_2} = \frac{\mathbf{A}_{50}^{\prime T}}{r_{23} \cos Y'} \quad (69)$$

$$\frac{\partial Y'}{\partial r_2} = \frac{\mathbf{D}_{50}^{\prime T}}{r_{23}} \quad (70)$$

For any of these angles,

$$\frac{\partial \text{angle}}{\partial r_3} = - \frac{\partial \text{angle}}{\partial r_2} \quad (71)$$

For the directly observed angles, compute \mathbf{D}, \mathbf{A} from Eqs. (1) and (2); $\tilde{\mathbf{D}}, \tilde{\mathbf{A}}$ from Eqs. (11) and (12); \mathbf{D}', \mathbf{A}' from Eqs. (15) and (16); and $\mathbf{D}'', \mathbf{A}''$ from Eqs. (19) and (20). These unit vectors all have rectangular components referred to the true equator and equinox of the date of observation t_3 . Transform the rectangular components of each of these vectors to the mean equator and equinox of 1950.0 as

$$\mathbf{D}_{50} = \mathbf{A}^T(t_3) \mathbf{N}^T(t_3) \mathbf{D} \quad \mathbf{D} \rightarrow \mathbf{A}, \tilde{\mathbf{D}}, \tilde{\mathbf{A}}, \mathbf{D}', \mathbf{A}', \mathbf{D}'', \mathbf{A}'' \quad (72)$$

For optical right ascension and declination, compute \mathbf{D}, \mathbf{A} from Eqs. (1) and (2), and transform to 1950.0 rectangular components using

$$\mathbf{D}_{50} = \mathbf{A}^T(t_R) \mathbf{N}^T(t_R) \mathbf{D} \quad \mathbf{D} \rightarrow \mathbf{A} \quad (73)$$

for angles referred to the true equator and equinox of the date t_R . For angles referred to the mean equator and equinox of the date t_R ,

$$\mathbf{D}_{50} = \mathbf{A}^T(t_R) \mathbf{D} \quad \mathbf{D} \rightarrow \mathbf{A} \quad (74)$$

Note that the partial derivatives are computed using angles affected by refraction. Strictly, these angles should not include refraction and the refraction correction should also be differentiated with respect to the position of the probe. Because of the approximations made, the partial derivatives of the angular observables with respect to position of the probe and receiving station are accurate to roughly five significant figures for \mathbf{L} directed near the zenith and three significant figures for \mathbf{L} directed toward the horizon. These figures apply for directly observed angles. For optical angles obtained from the reduction of photographic plates, the secondary refraction correction and the error in the partial derivatives approach zero with increasing range.

1. Introduction, D. W. Curkendall

The *Pioneer* program consists of a series of spacecraft whose purpose is to gather scientific information concerning the deep-space environment in the region near the ecliptic plane and at a distance from the Sun varying from 0.8 to 1.2 AU. The DSN is committed to track the *Pioneer* spacecraft, obtain engineering and scientific telemetry, determine the orbit of each probe, and provide facilities to the Project within the SFOF and the DSIF for the conduct of the mission and reduction of data. Specific items under this task will be selected during each report period for further discussion.

In this issue, the second of two articles analyzing the high-frequency noise characteristics of *Pioneer VI* doppler tracking data is presented. The properties of the noise autocorrelation function that allow the identification and separation of receiver noise and reference oscillator instability are reviewed. Estimates of these two noise sources are made from inspection of the correlation function.

2. Pioneer VI High Frequency Data Noise Analysis,

Part II, R. Motsch and D. W. Curkendall

a. Introduction. In a previous article (SPS 37-41, Vol. III, pp. 57-59), the removal of a dominating periodicity from *Pioneer VI* tracking data was described. This periodicity was attributed to the existence of a spacecraft rotation rate and an apparent spacecraft antenna offset. Measures of both the rotation rate and antenna offset were made from the data. The removal of this periodicity was necessary in order to analyze the nature of the random phase jitter in the doppler signal and the short-term drift characteristics of the rubidium oscillators. Such an analysis has been performed and is documented here.

b. Phase jitter and oscillator noise. Our basic data type is two-way doppler, which is integrated to obtain phase measurements at a series of equally spaced times. Each adjacent pair of measurements is differenced and divided

by the time interval to provide differenced continuously counted doppler, which may be expressed mathematically as

$$y_i = \frac{\Phi_i - \Phi_{i-1}}{\Delta t}, \quad i = 2, \dots, N$$

where

Φ_i = observation of phase at $t = t_i$

Δt = sampling interval

The observations Φ_i are corrupted with noise arising from a variety of physical sources. A significant portion of this error is high-frequency phase jitter, often referred to as receiver noise. In addition, there is usually a significant amount of quantization error due to roundoff in the electronic doppler counter that is difficult to separate from the receiver noise. However, the data used for this analysis were taken with a high-resolution counting device that reduces this error to an insignificant level. It is easily shown that if the receiver noise is taken to be white, the variance and autocorrelation of the error induced in the y_i are given respectively by

$$E[\epsilon_{p_i}^2] = 2\sigma_p^2/\Delta t^2 \quad (1)$$

$$E[\epsilon_{p_i} \epsilon_{p_{i+j}}] = -\sigma_p^2/\Delta t^2, \quad j = \pm 1 \\ = 0, \quad \text{otherwise} \quad (2)$$

In the above equations, $E[\]$ is the expected value operator, ϵ_{p_i} is the error in y_i due to phase jitter, and σ_p^2 is the variance of the phase jitter expressed in meters² or cycles².

In addition to the noise due to phase jitter, doppler data will be corrupted through the reference oscillator frequency instability. By assuming that the oscillator has impressed on it white frequency noise, it has been shown (SPS 37-41, Vol. III, pp. 42-47) that the variance and autocorrelation of the error induced in the y_i , assuming the round-trip light time is greater than the sampling time, are given respectively by

$$E[\epsilon_{0_i}^2] = 2\sigma_0^2/\Delta t \quad (3)$$

and

$$E[\epsilon_{0_i} \epsilon_{0_{i+j}}] = -\frac{\sigma_0^2}{\Delta t^2}(\Delta t - |\tau - j\Delta t|), \quad \tau - \Delta t < j\Delta t < \tau + \Delta t \\ = 0, \quad \text{otherwise} \quad (4)$$

In these equations, ϵ_{0i} is the error in y_i due to oscillator instability, τ is the round-trip light time, and σ_0^2 is the variance of the oscillator noise expressed in cycles²/sec. It is emphasized that the above relations for the correlation function are a direct consequence of the phase coherence of the two-way tracking mode and are not valid for noncoherent or three-way systems.

c. Expected effects on sample autocorrelation function. Examination of Eqs. (2) and (4) will show that, if the assumptions in the derivations are reasonable, there should appear in the sample autocorrelation of the tracking data three negative spikes: one at the one-lag point, representing the contribution from phase jitter, and two embracing the round-trip light time, representing the contribution from oscillator noise. The sum of these last

two is $-\sigma_0^2/\Delta t$; i.e., if the k th log point is the one immediately preceding the round-trip light time, we see that

$$\begin{aligned} R_\tau &= E[\epsilon_{0i} \epsilon_{0i+k}] + E[\epsilon_{0i} \epsilon_{0i+k+1}] \\ &= -\frac{\sigma_0^2}{\Delta t^2}(\Delta t - |\tau - k\Delta t|) - \frac{\sigma_0^2}{\Delta t^2}(\Delta t - |\tau - (k+1)\Delta t|) \\ &= -\frac{\sigma_0^2}{\Delta t} \end{aligned}$$

where R_τ is the sum in question.

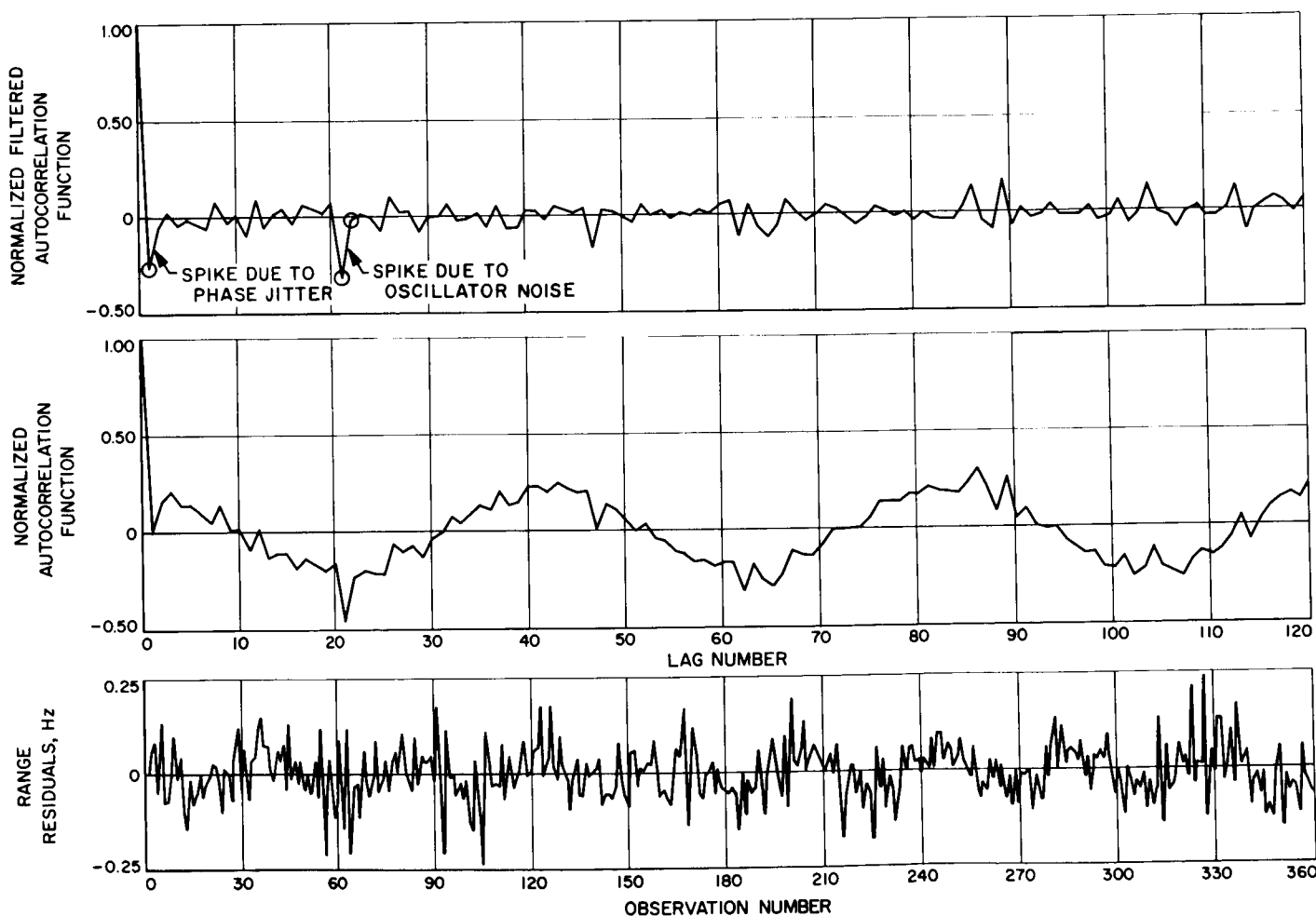


Fig. 25. Range residuals, normalized autocorrelation function, and normalized filtered autocorrelation function for Pioneer VI on January 5, 1966, using Echo DSS 12 data

When the autocorrelation function is normalized by dividing all points by the zero-lag point, we see that the sum of the spikes should be $-\frac{1}{2}$, for

$$\frac{R_1 + R_7}{R_0} = \frac{-(\sigma_p^2/\Delta t) - (\sigma_o^2/\Delta t)}{(2\sigma_p^2/\Delta t^2) + (2\sigma_o^2/\Delta t)} \\ = -\frac{1}{2}$$

Here it has been assumed, reasonably enough, that the phase jitter and the oscillator noise are independent.

d. Results from Pioneer VI data analysis. Sample autocorrelations have been formed from *Pioneer VI* tracking data. Once the dominating periodicity due to spacecraft rotation has been removed, the spikes are readily observed. As predicated in the theory, they sum to $-\frac{1}{2}$, to within the noise on the sample autocorrelation. Fig. 25 shows the results obtained by processing one pass of data. A detailed explanation of the formation of the plots can be found in SPS 37-41, Vol. III, pp. 57-59; in the uppermost plot, the one lag and the round-trip light-time ($\cong 21.3$ sec for day shown) lag points have been circled. Measures of the phase noise and short-term oscillator drift have been made from several passes, using Eqs. (2) and (4), and are given in Table 10.

Table 10. Pioneer VI phase jitter and oscillator drift measurements

Date	$\sigma_t = R_0^{1/2}$, cps	$\sigma_p/\Delta t$, cps	σ_p , deg	$\sigma_o/(\Delta t)^{1/2}$, cps	$\Delta f/t$, over 1 sec
Jan. 5	0.061	0.032	12	0.034	1.4×10^{-11}
Jan. 5	0.058	0.026	9	0.034	1.4×10^{-11}
Jan. 30	0.085	0.044	16	0.043	1.9×10^{-11}
Feb. 8	0.087	0.050	18	0.040	1.5×10^{-11}
The above measurements were derived from 1-sec tracking data.					

In Table 10, we have used $\sigma_o/(\Delta t)^{1/2}$ as our measure of Δf . The results obtained compare favorably with an independent analysis of oscillator drift (SPS 37-38, Vol. III, pp. 8-13) using *Mariner IV* data, $2^{1/2}\sigma_o/\Delta t^{1/2}$ being the estimator used for Δf .

G. Definition and Analysis of the Tracking Data System, L. W. Miller

1. Introduction

This article is a resume of a study initiated to investigate the Tracking Data System as a system concept and

to define and analyze it for support of the *Mariner Venus 67* mission. The study, however, is not limited to *Mariner Venus 67* usage, but may also be used to formulate support for other projects.

2. Definition of the System

The system has the responsibility of providing navigational information for the projects. This is used for the orbit determination (OD) function, which provides the time history of the spacecraft position and velocity. The system must also provide the prediction information necessary for acquiring the spacecraft and locking to its frequency. Providing scientific information on the mass of the planets and station location may also be part of the system's responsibility.

The Tracking Data System is defined as that system which performs the following six functions:

- (1) Acquisition—the process of acquiring, locking up, and tracking the spacecraft.
- (2) Data handling—the techniques and equipment necessary to process the data once the spacecraft is acquired.
- (3) Data transmission—the transmission of the data from the station through the SFOF (Space Flight Operations Facility) data stream.
- (4) Data editing—the process of analyzing and editing the data.
- (5) OD—the transformation of the raw angle, doppler, and ranging data observations into coordinates of the spacecraft position and velocity.
- (6) Prediction—the transformation of spacecraft position and velocity information into data prediction values for use by the stations in acquiring the spacecraft.

Fig. 26 shows how these functions tie together.

Essentially the system has three phases: preflight, in-flight, and postflight. In the preflight phase the planning and activities that are necessary to support the in-flight phase must be accomplished. During the in-flight phase the operations must be supported. The postflight phase consists of postflight data processing, reports, and system improvements.

The following paragraphs explain how the six functions are implemented in each phase.

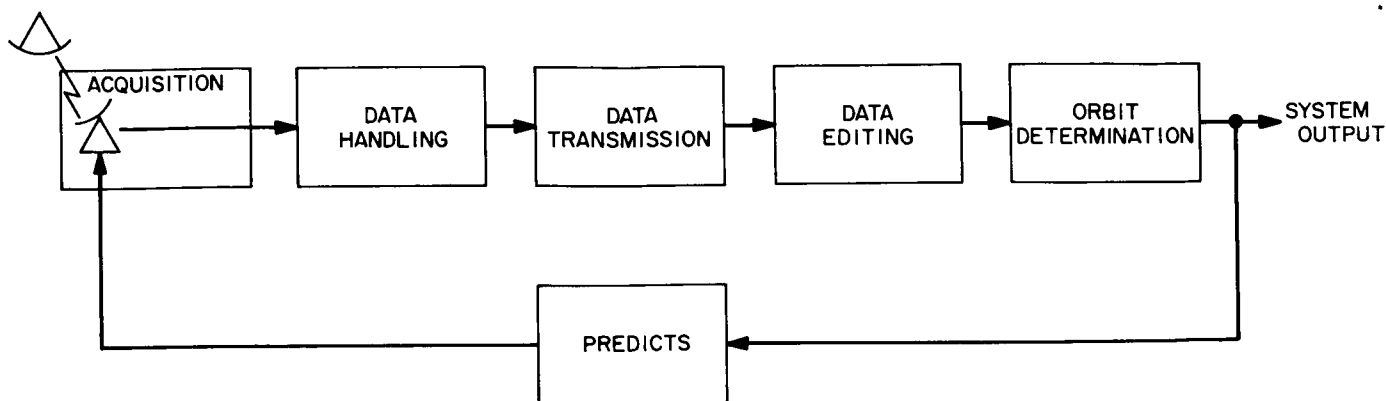


Fig. 26. Intrarelationship of trading data navigation system functional elements

a. Preflight phase. During the preflight phase the necessary analysis, planning, scheduling, activities, and implementation take place to insure the successful completion of the inflight activities. It is important to realize that the planning must be accomplished early because of long lead time involved in implementing changes. The table below approximates the time involved.

Changes	Lead time before launch
Spacecraft hardware	1½–2½ yr
Launch vehicle	1½–2½ yr
DSIF hardware and station commitments	1 day–2½ yr
AFETR	½ mo–2 yr
Computer changes	½ mo–2½ yr
Trajectory	½ mo–2½ yr

This subsection outlines the work that must be done, and indicates the responsible groups. It is restricted to a discussion of the information that is necessary among the groups.

During the preflight phase the tasks necessary to the support of the inflight function described in the six system functions listed above must be defined and accomplished. These must be interfaced with the following:

- (1) Mission objectives
- (2) Trajectory and maneuver design
- (3) Spacecraft design and hardware
- (4) Launch vehicle (L/V) characteristics and accuracy
- (5) AFETR (Air Force Eastern Test Range)

Fig. 27 shows the elements that compose the pre-launch phase and the major interdependencies between them. Only the major interfaces are indicated here. For an example of how the chart works, consider the trajectory design block. The mission objectives, spacecraft design and hardware, launch vehicle accuracies and characteristics, all directly affect the trajectory design. The OD can affect trajectory design directly by virtue of the fact that OD capabilities may be dramatically better on one trajectory than another, or OD objectives may affect trajectory design indirectly by causing a change in mission objectives. In general, it will be considered that there are two ways by which one element can influence another: directly, when the elements are connected together, or indirectly, if the influence is due to another element in the chain. The effects and interaction are also dependent on the mission. For example, the trajectory design on *Mariner Venus '67* (vs *Mariner Mars '64*) affects the spacecraft design and hardware because the orientation of the solar panels must be reversed. On *Pioneer*, however, the spacecraft is designed so that the direction of the trajectory (inward or outward) does not change the spacecraft hardware.

Fig. 28 is a slight revision of Fig. 27. In Fig. 28, the areas of acquisition, predicts, OD, etc are expanded to show how these activities are carried on by the various groups and their interfaces.

Fig. 29 is another expansion of the previous charts and shows specifically what information each group needs and where it is obtained; for this representation, it is shown as a partial control theory representation. Thus, it is a summing junction and black-box transfer function. However, instead of the usual mathematical representation, only the required outputs are listed. Convention-

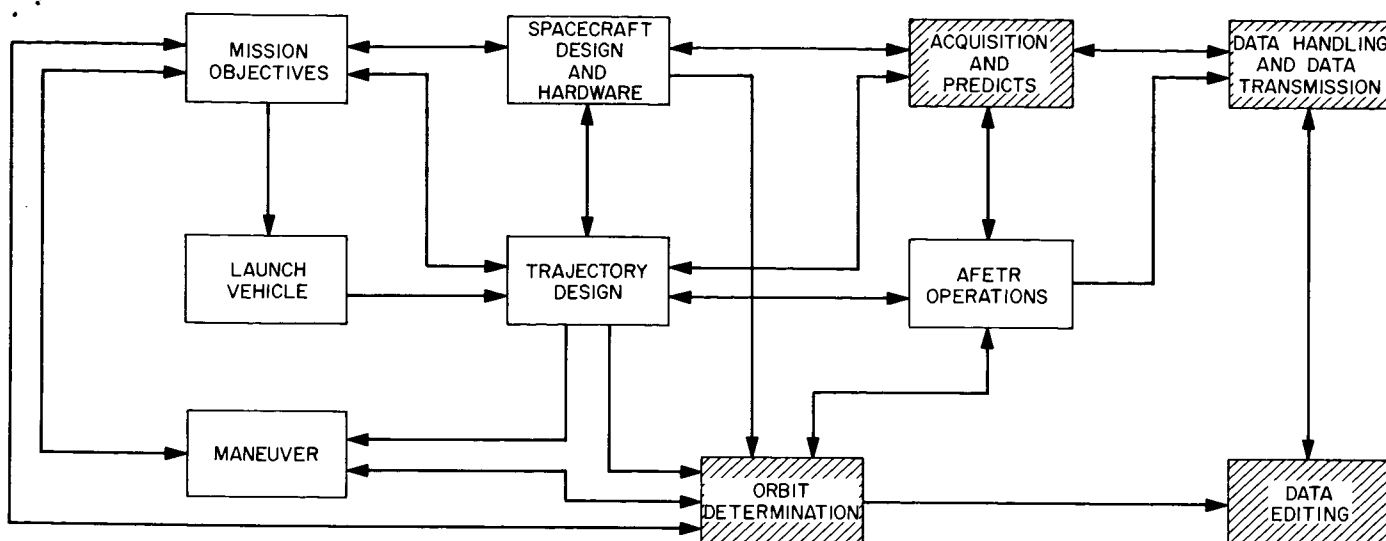


Fig. 27. TDS preflight phase information flow between the elements

ally, outputs are listed outside the box; but for this representation, it is easier to place them inside. Also, the outputs have been separated into those that are necessary for analytic planning and studies and those that are necessary for operational support. The chart below shows how the box is divided.

Group name	
Function	Output
Analysis and planning	Analysis and planning
Operations planning	Operations requirements

Each output function is given a unique number. These are then fed to the summing function of the appropriate group. The labeling at each summing junction gives the abbreviation of the group's name and the functions that are fed into the summing junction. In some cases, in order to minimize interconnecting of lines, the input to the summing junction will not come from the corresponding box, but will merely be a short line connecting the summing junction with the corresponding group's name and appropriate functions. Also, to help simplify the figure, the AFETR activities are not shown.

Although the chart is not complete, because only the major interfaces are shown, it contains several items of interest. Note that there is a large amount of interaction between the elements. Also, note that a change in one piece of information can change or affect many other areas. It is important to insure that this information is

passed on and acted upon in a timely manner. Two considerations accompany this requirement. One is that the speed of action and response is dependent upon the source from which the information is obtained. If the transfer is by formal documentation, it may be months before the documentation process is completed; thus, informal methods of transfer are also needed. The second consideration is that change control procedures must be well defined so that a group can effectively control the capabilities it needs to meet the requirements imposed upon it.

This chart roughly spans a period from about 2½ yr to a few weeks before launch. Thus, the entire spectrum of activities is not in motion at one time; but rather, there are subnetworks wherein many of the groups are in active interface while other parts of the network are inactive.

Information is not in continuous flow through the system. The network responds to discrete bits of information. One group must wait to receive information from another group then act upon it and, when necessary, pass it on. Occasionally, when many groups are active at once the network becomes busy and may become saturated.

These groups are usually staffed by one or, at most, two people. Management and the groups have a responsibility to ascertain that the staffing is always adequate.

b. Inflight phase. During the inflight phase the TDS provides inflight navigational information to the projects,

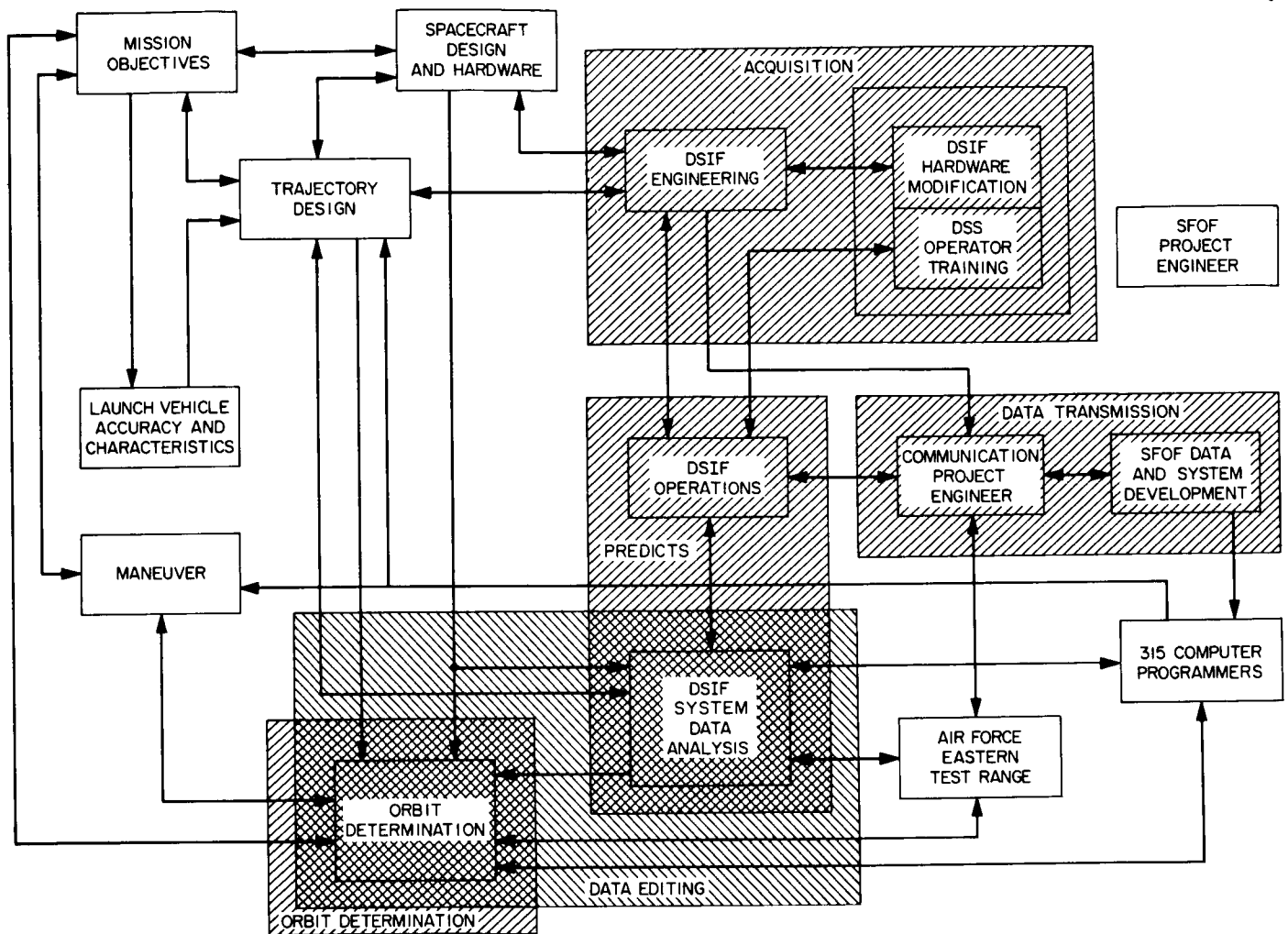


Fig. 28. TDS preflight phase expanded to show which groups compose the system

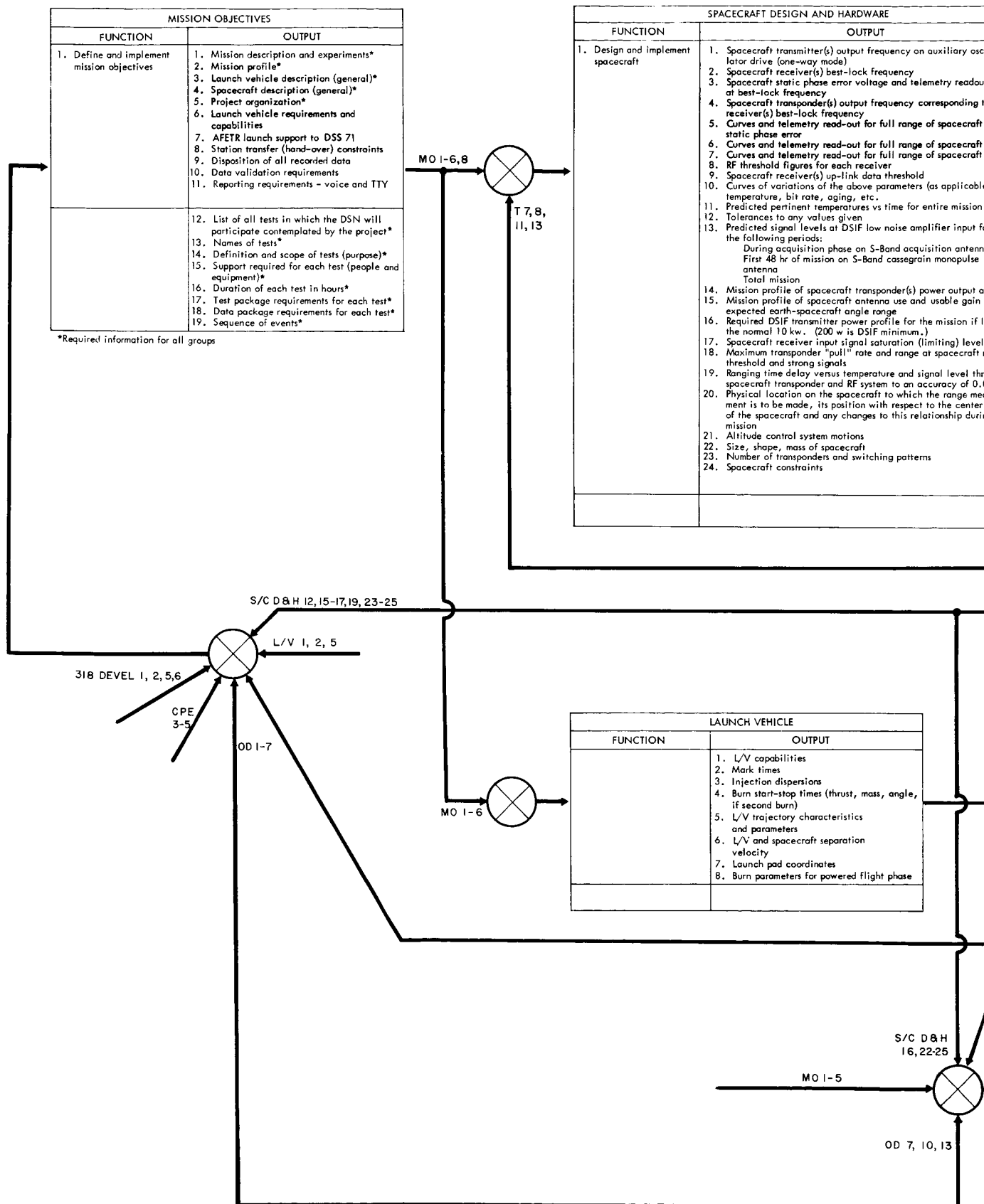
performing the six functions previously described. Fig. 26 shows how these functions tie together. Fig. 30 shows how these functions are implemented during the inflight phase. The discussion of Fig. 31 below will provide some background.¹⁸

Fig. 31 is a simplified diagram showing how the tracking data system ties into the project. The six functions (acquisition, data handling, etc.) are performed in the block labeled tracking data navigation system. Groups that perform the duties and interface with the other parts of the project are emphasized. This chart shows

¹⁸For more details on the definition of the system read Interoffice Memorandum (IOM) 319-872 by R. E. Holzman, April 4, 1966, titled *DSN Tracking Data System* and IOM 319-922 by L. W. Miller, April 28, 1966, titled *Man-Machine Charts for Tracking Data System*.

the inflight phase configuration, and it is valid for lunar flights of a few days or planetary flights of several months. However, the activity levels for each group or function shown in the figure vary greatly during various phases of the flight. Before and during the maneuver, the maneuver preempts almost all other considerations. However, after it is completed, the emphasis may shift to data analysis and monitoring in the TDS block.

This diagram was prepared to show the relationships of the present system, but with the inclusion of the block labeled "monitor system" it applies to future configurations also. Other elements that make up future configurations such as the communications processor and the redesigned 7044 computer, will not change the functional relationships shown in the figure; they will only change hardware capabilities.



AGC
AFC

) vs

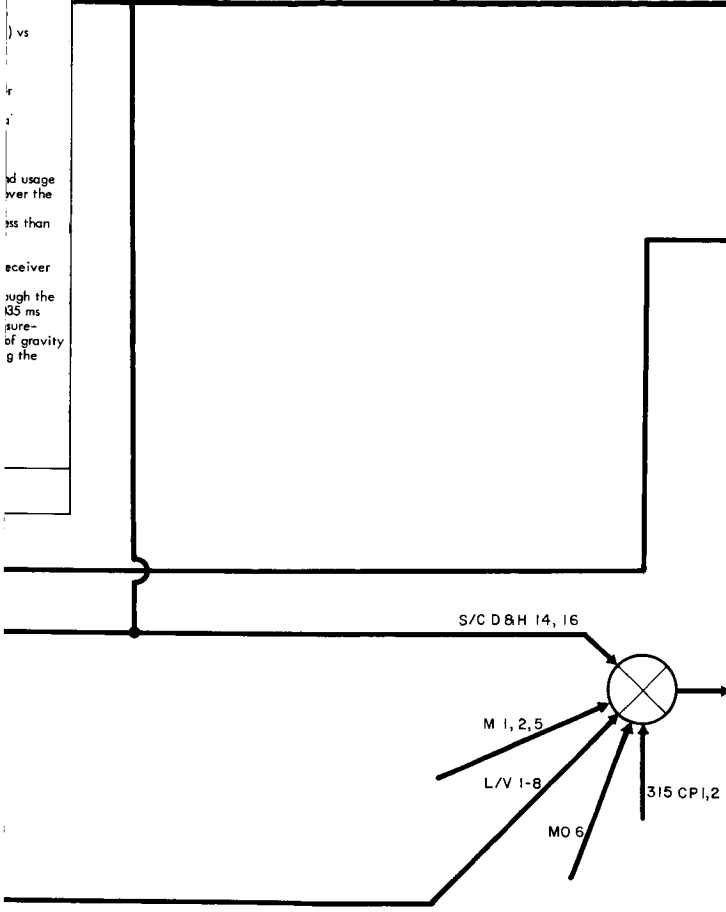
d usage
ver the
ss than

ceiver

ugh the
35 ms
sure-
of gravity
g the

CPE Communications Project Engineer
DSIF EI DSIF Engineering Interface Project Engineer
DSS HM DSS Hardware Modification
DSS OT DSS Operation Training
L/V Launch Vehicle

M Maneuver
MO Mission Objectives
OD Orbit Determination
OPS DSIF Operations Project Engineer
S/C D&H Spacecraft Design and Hardware



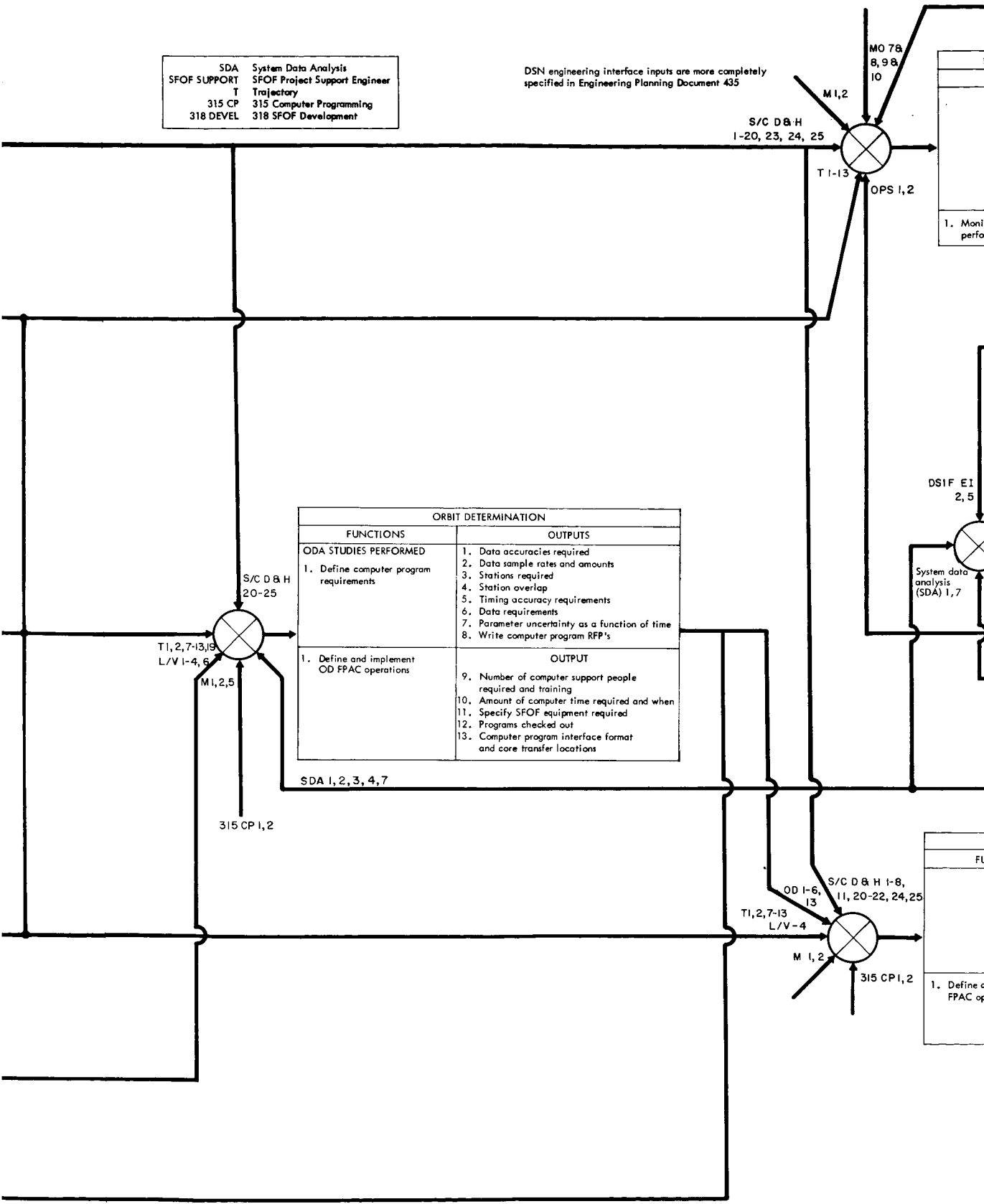
TRAJECTORY	
FUNCTION	OUTPUT
1. Design trajectories for mission	<p>GENERAL TRAJECTORY INFORMATION</p> <ol style="list-style-type: none">1. Parking orbit elements2. Transfer orbit elements3. Injection altitude4. Maximum and minimum injection values5. Mercator injection - locus map showing day-to-day motion6. Typical plot of geocentric range vs time from injection to arrival <p>FLIGHT-PHASE DEPENDENT INFORMATION</p> <ol style="list-style-type: none">7. Launch phase, L to L + 4 hr<ul style="list-style-type: none">o Stereographic plots of HA, DEC (AZ, EL) for three launch azimuths per day (94, 102, 110 deg) covering committed stations in viewo Plots vs time of:<ul style="list-style-type: none">o Range (km)o Range rate (km/sec)o Range acceleration (km/sec²)o HA-rate (AZ-rate) (deg/sec)o DEC-rate (EL-rate) (deg/sec) for three launch azimuths per launch day (94, 102, 110 deg) covering committed stations in view <p>POST-ARRIVAL PHASE</p> <ol style="list-style-type: none">8. Range-rate and range-acceleration vs time plots depicting the full scope of typical encounter or targets orbiting characteristics9. Typical range (km) vs time from launch (hours) for the entire mission10. Station tracking and view periods for entire mission11. Doppler frequencies and rates vs time for entire mission12. Local HA and DEC angles and rates vs time13. Range and range rate vs time for entire mission14. Write computer program request for programming (RFP)
1. Define and implement trajectory Flight Path analysis and command (FPAC) operations	<ol style="list-style-type: none">15. Specify SFOF equipment needed16. Number of computer support people required and training17. Amount of computer time required and when18. Programs checked out19. Computer program interface formats and core transfer locations

T 2, 8, 9, 10, 13

MANEUVER	
FUNCTION	OUTPUT
1. Design maneuvers for mission as per mission objectives and subject to spacecraft, trajectory, and orbit determination constraints	<p>WHAT PARAMETERS AND UNCERTAINTIES ARE NEEDED AND TIMES THAT ACCURACIES ARE NEEDED</p> <ol style="list-style-type: none">1. Nominal thrust-acceleration during mid-course maneuvers (m/sec²)2. Typical terminal propulsion range-rate and range acceleration versus time plots
2. Define computer program requirements	
3. Define and implement maneuver FPAC/operations	<ol style="list-style-type: none">3. Specify SFOF equipment needed4. Amount of computer time needed and when needed5. Computer program interface format and transfer locations

SDA	System Data Analysis
SFOF SUPPORT	SFOF Project Support Engineer
T	Trajectory
315 CP	315 Computer Programming
318 DEVEL	318 SFOF Development

DSN engineering interface inputs are more completely specified in Engineering Planning Document 435



ORBIT DETERMINATION	
FUNCTIONS	OUTPUTS
ODA STUDIES PERFORMED 1. Define computer program requirements	1. Data accuracies required 2. Data sample rates and amounts 3. Stations required 4. Station overlap 5. Timing accuracy requirements 6. Data requirements 7. Parameter uncertainty as a function of time 8. Write computer program RFP's
1. Define and implement OD FPAC operations	OUTPUT 9. Number of computer support people required and training 10. Amount of computer time required and when 11. Specify SFOF equipment required 12. Programs checked out 13. Computer program interface format and core transfer locations

SDA 1, 2, 3, 4, 7

DSIF ENGINEERING INTERFACE PROJECT ENGINEER	
FUNCTION	OUTPUT
	VOL 1
	1. Recording requirements Initial acquisition
	2. Provides inputs for Volume 1 of TM
	3. Specifies and coordinates station hardware changes
	4. Station hand-over and initial acquisition
and analyze station performance during flight	5. Specify SFOF equipment needs

DSS HARDWARE MODIFICATION	
FUNCTION	
1. Implement changes to insure station capability	1. Status reports
DSS OPERATOR TRAINING	
FUNCTION	
	PREMISSION TEST
	1. Status reports
	2. Critiques of training

DSIF OPERATIONS PROJECT ENGINEER	
FUNCTION	OUTPUT
	1. Station operator training procedures
	2. Issues TIM's
1. Define and implement TDS OPS Project Operation	3. Specify SFOF equipment needed
	4. Specify DSIF net simulations
	5. Communication needs

COMMUNICATIONS PROJECT ENGINEER	
FUNCTION	
1. Define and implement communications project operations	1. Communication
	2. SFOF equipment
	3. Communication
	4. Expected outages
	5. Schedule conflicts

SYSTEM DATA ANALYSIS	
FUNCTION	OUTPUT
	1. Data format and modes
	2. Data accuracy
	3. Timing capability
	4. Predict accuracy required
	5. Predict documents
	6. Predict format
	7. Angle coefficients for TIM Vol. 3
	8. Computer program RFP's
and implement TDA requirements	9. Programs checked out
	10. SDA communications requirements
	11. Number of computer support people required and trained
	12. SFOF equipment needs

315 COMPUTER PROGRAMMING	
FUNCTION	
1. Develop computer programs	1. Provide check groups
2. Implement requested RFP's	2. Train computer operator personnel

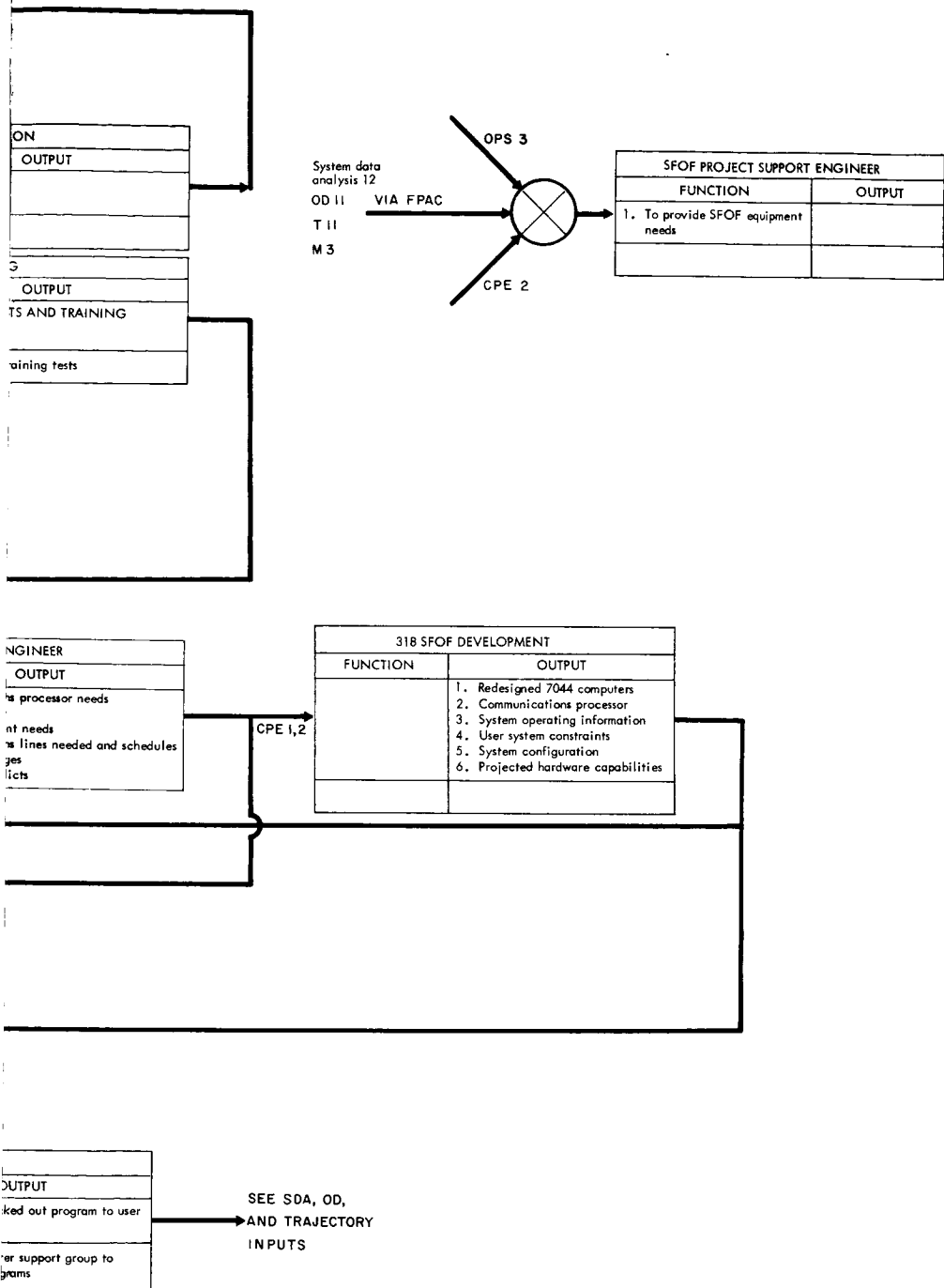


Fig. 29. Expanded view of information requirements in the preflight phase of the TDS

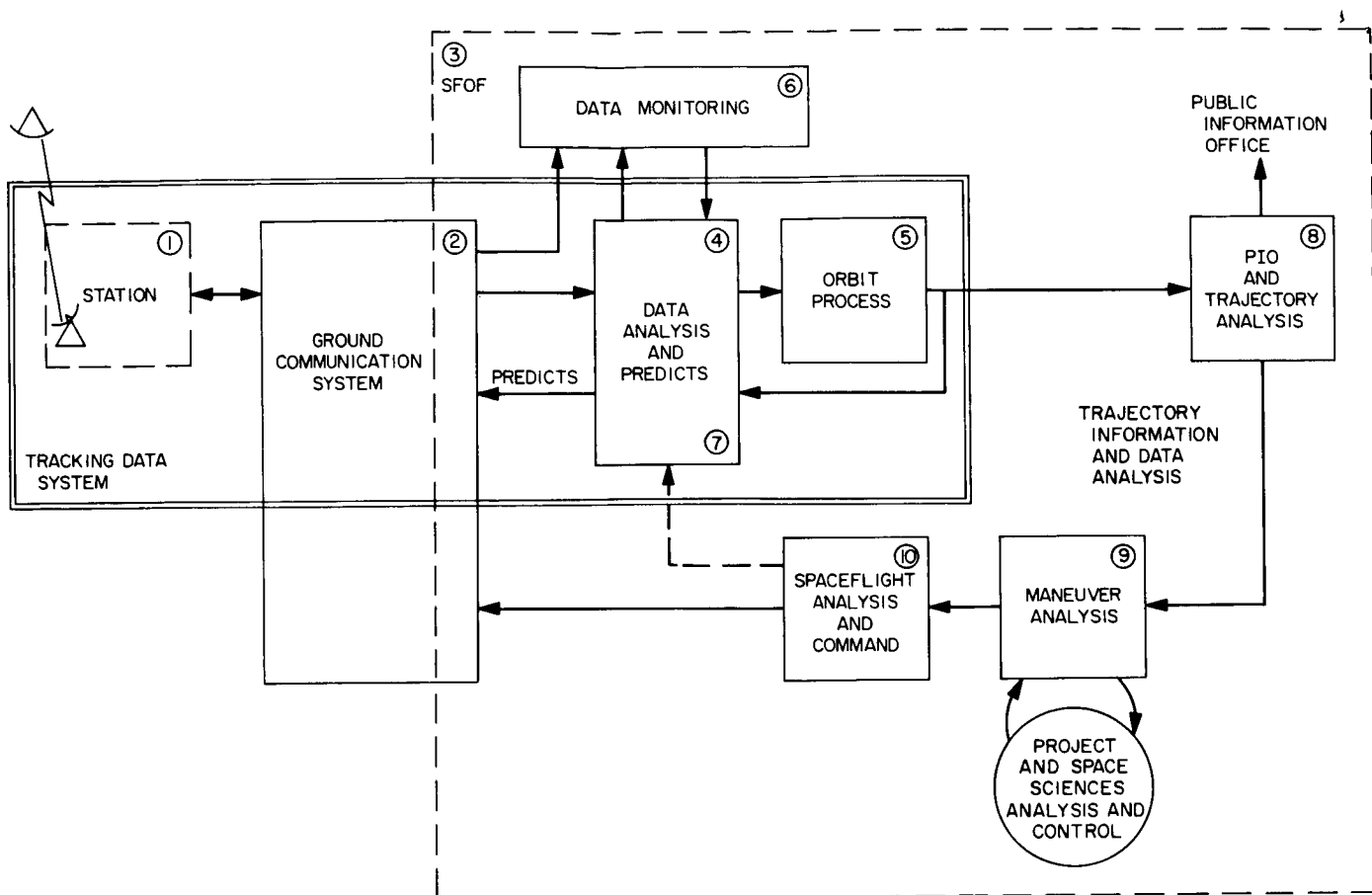


Fig. 31. Relationship of the TDS to the project

The essential functional relationships appearing in Fig. 31 are itemized as follows:

- ① The deep space stations take precision measurements along the spacecraft trajectory by transmitting a signal to the spacecraft which is returned by means of a turn-around transponder. The received signal is compared to the transmitted signal to derive the doppler shift. Pointing information (angles) and range data may also be derived.
- ② Measurements from the deep space stations are transmitted via the DSN ground communications system (DSN/GCS) to JPL.
- ③, ④, ⑤ The receiving point at JPL is the Space Flight Operations Facility (SFOF). The measurements are fed into the SFOF data processing system (DPS) where they are analyzed, edited, and then processed by the JPL OD Program to improve previous trajectory estimates.
- ⑥ The monitor area provides alarms and recording equipment to monitor the status of the stations, SFOF, and data stream. This information is used to improve the data editing process.
- ⑦ Predicted data values are generated and transmitted via the DSN/GCS to the deep space stations. These values are then used for succeeding acquisitions of the spacecraft transponder.
- ⑧ The improved orbit estimates are given to the trajectory group. This group then runs the trajectory program and analyzes the trajectory for the project and public information purposes.
- ⑨ During the flight maneuver and orientation analyses are performed to determine how best to achieve mission objectives.

- ⑩ The inputs from maneuvers are sent to SPAC (spacecraft performance and command), where the commands are then formulated and transmitted to the spacecraft. Inputs from SPAC on spacecraft maneuvers and spacecraft perturbations are also fed into the data analysis and orbit process to account for apparent trajectory anomalies and predict corrections.

c. Postflight phase activities. When the flight is ended, many tasks must be performed. Inflight performance is re-evaluated, data validated scientific values are determined, and recommendations for improvement of system operations are made.

Postflight activities may be described as:

- (1) Data transmission, data editing and orbit determination
- (2) Reporting
- (3) Improvements

The activities and the groups that participate in the activities are also given. The activities are numbered to

correspond with those given in Fig. 32, which shows the sequence in which the activities are performed.

- ① *Inflight evaluation reports written.* Shortly after the flight, or during the flight, if a long interplanetary one, the inflight evaluation reports are written. These include station and spacecraft performance reports, and SFOF operation evaluations. The purpose is to describe what happened, and to indicate where improvements are needed.

- ② *Inputs from spaceflight analysis and command (SPAC).* During the flight and afterwards, when more sufficient analysis has been performed, there is a need to feed information to the OD group in order to investigate the effect of spacecraft motions and gas jets upon the trajectory. This helps to explain trajectory anomalies.

- ③, ④, ⑤ *Data sent to SDA group, communications transmission, data records control.* Although most of tracking data taken is usually analyzed in flight, there are certain special data types that are usually transmitted to

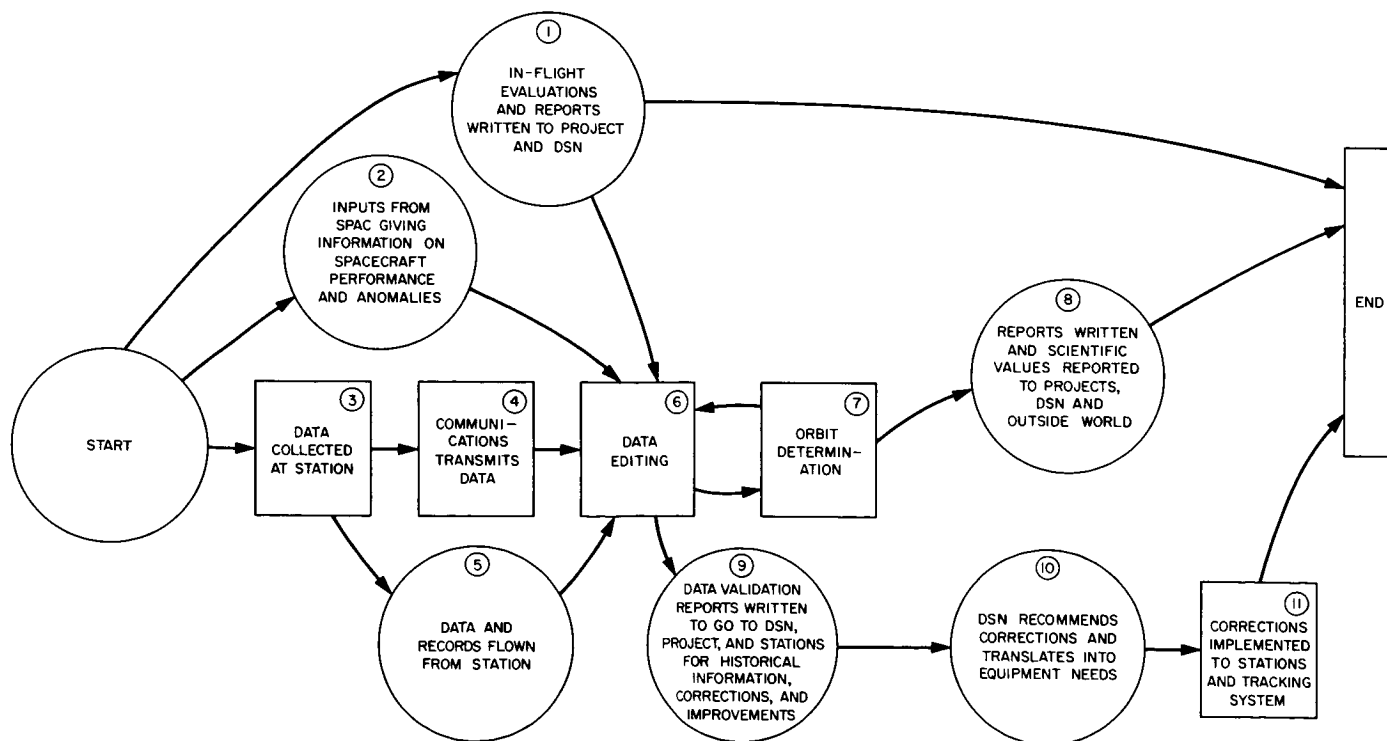


Fig. 32. Flow chart showing activities in the postflight phase of the tracking data navigational system

the SFOF only after the flight is over. Doppler data taken at the rate of one sample per second is an excellent example. A sample is recorded every second, but it takes up an inordinate amount of communication transmission time during the flight. Thus, the data may be flown back along with the data records to document control and then to the system data analysis group. These data are taken because they have both project and DSN inherent accuracy applications.

- ⑥, ⑦ *Data editing and orbit determination.* Data is edited by inspecting station records, space performance and command group reports, the interim monitor program, and operations records, in addition to the orbit program plots and residuals. The accuracy of the orbit program often makes it the final arbitrator as to whether data are good or bad. Thus, the data editing and the OD process are tied together in an iterative process and are actually done together. This effort, extending anywhere from 1 mo to 1½ yr after the flight, is to:

- (1) Provide the project with a "best estimate" of the trajectory for comparison with TV pictures, etc.
- (2) Provide better estimates of physical constants and station locations.
- (3) Provide data analysis for inherent accuracy, etc.

These are the primary reasons for the data editing and orbit phases of the postflight operations. An additional advantage of this period may be taken as an opportunity for personnel training and program checkout.

- ⑧ *Reports written and scientific values reported to projects, DSN and outside world.* These reports include the "flight path and its determination from tracking data" report and project experiments, such as occultation. Also, we have the reports such as station location determination, analyses, etc. In either case, although considerable work can be done before the data editing and OD phase is complete, the final portion of this work depends on the completion of the orbit phase.

- ⑨ *Data validation reports.* These reports give the results of the data analysis validation. The system data analysis group, for example, puts out reports of this type. Also, it is dependent on the orbit process, but usually partial completion of the orbit process is satisfactory.

- ⑩, ⑪ *Recommendations translated into engineering terms and improvement initiated.* After the data reports are prepared and reviewed, improvements are recommended which are then translated into schedules and hardware.

3. Conclusion

In this article the six functions and three phases that comprise the tracking data system have been presented. The functions and phases have been analyzed singularly and in combination.

There was a time when a work of this nature was not necessary, as the information presented here was known by everyone in the system. However, as the operations become more complex, and as more and more new people are brought into operations, it becomes necessary to clearly define the system and to insure that each person involved has the necessary background and knowledge.

References

1. Veis, G., *A Comparison of Station Position Obtained From Photographic and Radio-Tracking Data*, SAO Report 610-29, Smithsonian Institution Astrophysical Observatory, Cambridge, Mass., October 1966.
2. Köhnlein, W., *Corrections to Station Coordinates and Nonzonal Harmonics From Baker-Nunn Observations*, Paper presented at the VIIth International COSPAR Meeting, Vienna, May 1966 (to be published in *COSPAR Proceedings*).
3. Sjogren, W. L., Trask, D. W., Vegos, C. J., and Wollenhaupt, W. R., *Physical Constants as Determined From Radio Tracking of the Ranger Lunar Probes*, Technical Report 32-1057, Jet Propulsion Laboratory, Pasadena, California, December 30, 1966.
4. Sjogren, W. L., Curkendall, D. W., Hamilton, T. W., Kirhofer, W. E., Liu, A. S., Trask, D. W., Winneberger, R. A., and Wollenhaupt, W. R., *The Ranger VI Flight Path and Its Determination From Tracking Data*, Technical Report 32-605, Jet Propulsion Laboratory, Pasadena, California, December 15, 1964.
5. Wollenhaupt, W. R., Trask, D. W., Sjogren, W. L., Piaggi, E. G., Curkendall, D. W., Winneberger, R. A., Liu, A. S., and Berman, A. L., *The Ranger VII Flight Path and Its Determination From Tracking Data*, Technical Report 32-694, Jet Propulsion Laboratory, Pasadena, California, December 15, 1964.
6. Wollenhaupt, W. R., et al., *The Ranger VIII Flight Path and Its Determination From Tracking Data*, Technical Report 32-766, Jet Propulsion Laboratory, Pasadena, California (to be published).
7. Vegos, C. J., et al., *The Ranger IX Flight Path and Its Determination From Tracking Data*, Technical Report 32-767, Jet Propulsion Laboratory, Pasadena, California (to be published).
8. Yumi, S., *Annual Report of the International Polar Motion Service for the Year 1964*, UNESCO Subvention—1966—AVS/414/22, Central Bureau of the International Polar Motion Service, Mizusawa, Japan, 1966 (for *Rangers VI and VII*); and *Monthly Notes of the International Polar Motion Service*, No. 4, April 1965, No. 5, May 1965 (for *Ranger VIII*); No. 5, May 1965, No. 6, June 1965 (for *Ranger IX*).
9. Warner, M. R., Nead, M. W., and Hudson, R. H., *The Orbit Determination Program of the Jet Propulsion Laboratory*, Technical Memorandum 33-168, Jet Propulsion Laboratory, Pasadena, California, March 18, 1964.
10. Warner, M. R., and Nead, M. W., *SPODP—Single Precision Orbit Determination Program*, Technical Memorandum 33-204, Jet Propulsion Laboratory, Pasadena, California, February 15, 1965.
11. *Goddard Directory of Tracking Station Locations*, X-554-64-176, July 1, 1964 (DSS 12 is based on Geodetic Data Sheet (GDS) D-3-2, June 1964; DSS 41 on GDS D-1, April 1964; and DSS 51 on GDS D-3-4, June 1964).
12. Eckert, W. J., Walker, M. J., and Eckert, D., *Astronomical Journal*, Vol. 71, pp. 314–332, 1966.

References (contd)

13. Peabody, P. R., Scott, J. F., and Orozco, E. G., *JPL Ephemeris Tapes E9510, E9511, E9512*, Technical Memorandum 33-167, Jet Propulsion Laboratory, Pasadena, California, March 2, 1964.
14. Eckert, W. J., Jones, R., and Clark, H. K., *Improved Lunar Ephemeris 1952-1959*, Nautical Almanac Office, U. S. Naval Observatory, U. S. Government Printing Office, Washington, D.C., 1954.
15. Clemence, G. M., "Masses of the Principal Planets," in *Transactions of the International Astronomical Union, 1964*, Vol. 12B, pp. 609-614, J. C. Pecker, Ed., Academic Press, New York, 1966; see also Clemence, G. M., *Annual Review of Astronomy and Astrophysics*, Vol. 3, pp. 93-112, 1965.
16. Warner, M. R., Nead, M. W., and Hudson, R. H., *The Orbit Determination Program of the Jet Propulsion Laboratory*, Technical Memorandum 33-168, Jet Propulsion Laboratory, Pasadena, California, March 18, 1964.

III. Communications Research and Development

A. Low Noise Receivers: Microwave Maser Development, R. C. Clauss

Traveling wave masers (TWM) in JPL installations have used permanent magnets to provide the magnetic field necessary for maser operation. The permanent magnet is a very simple and reliable device, however, a maser frequency stability problem has occurred because the magnet is temperature sensitive. Laboratory tests of a temperature compensator shunt assembly for the magnet have shown that the magnetic field change caused by temperature changes from 80° to 125°F can be reduced to the point where maser instability caused by temperature changes will not be noticeable.

A magnetic field of 2457 gauss is required for maser operation at 2295 MHz. A change in the magnetic field causes a change in the operating frequency of the maser at the rate of approximately 2 MHz/gauss.

A magnet assembly used for a DSIF TWM is shown in Fig. 1. The alnico V castings are charged to provide a magnetic field of approximately 2500 gauss. A current

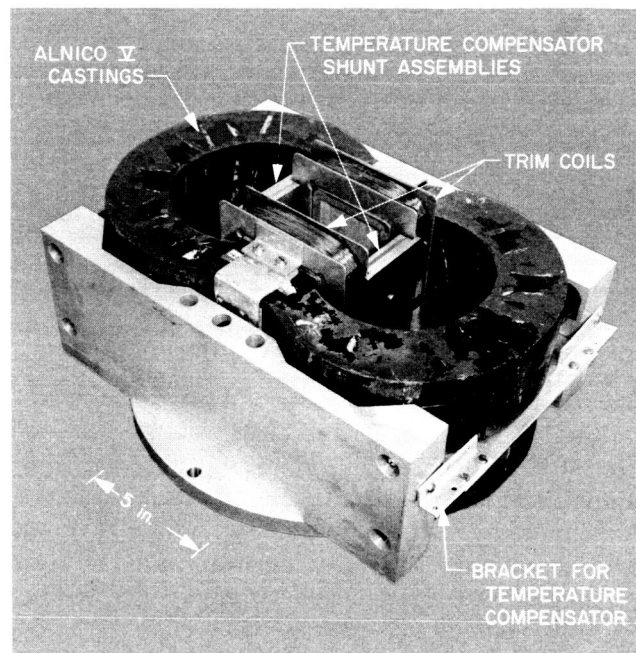


Fig. 1. DSIF TWM magnet assembly with temperature compensator shunts

regulated power supply is used to energize the trim coils and adjust the magnetic field for maser operation at the desired frequency.

Laboratory tests of a DSIF TWM magnet have been made to determine the change in magnetic field caused by changes in temperature. The temperature range of interest is from 80° to 125°F because the temperature controllers in existing TWM installations work well in this range. The measured magnetic field change of a magnet without compensation causes the TWM center frequency to change at the rate of 0.57 MHz/°F.

A temperature compensator shunt assembly (Fig. 1) has been used to eliminate the temperature sensitivity of the magnet. A commercially available Carpenter Steel alloy was chosen because it has the required permeability characteristics. The shunts are shims of Carpenter temperature compensation "30" type 2 and are shown in Fig. 2 with the brackets required for installation. The shunt assembly may be installed without removing the magnet from the TWM package.

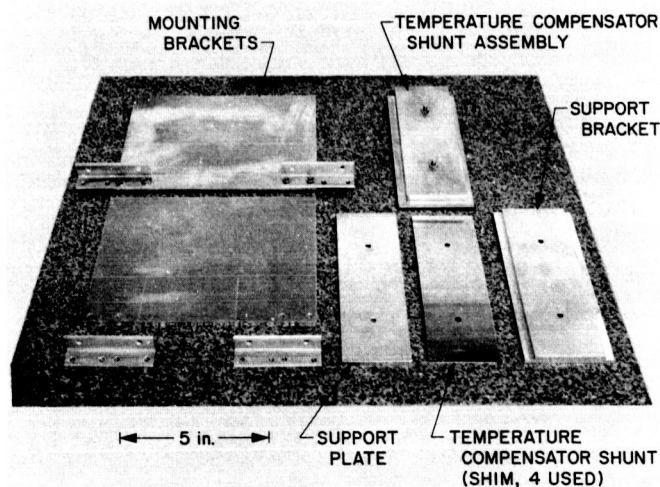


Fig. 2. Temperature compensator shunt with brackets

Installation of the shunt reduces the magnetic field by approximately 25 gauss (at 100°F). This field change can be corrected by a change in trim coil current of 0.1 amp. Test data obtained from measurements with the magnet in a temperature controlled oven are shown in Fig. 3. Fig. 4 shows predicted and measured values for an operating maser in a magnet without compensation and measured values for a magnet with optimum compensation.

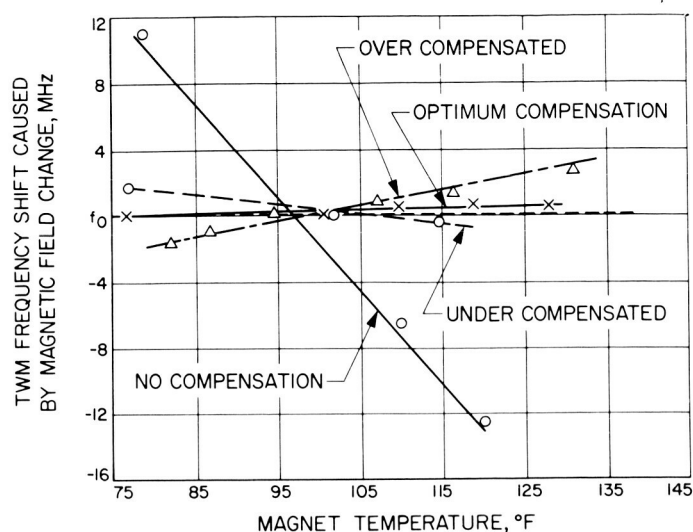


Fig. 3. Oven measured data of magnetic field vs temperature with and without compensation

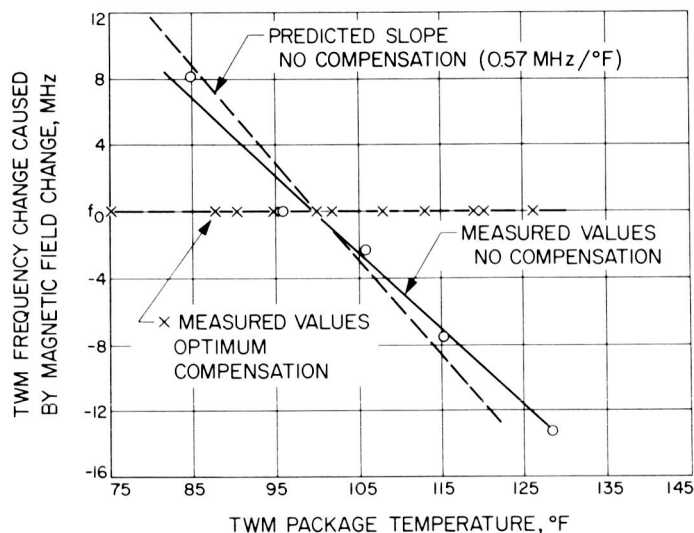


Fig. 4. DSIF maser frequency stability vs package temperature with and without magnet compensation

The combination of temperature compensation and temperature control can eliminate maser instability caused by the temperature sensitivity of the permanent magnet.

B. Frequency Generation and Control: Atomic Hydrogen Frequency Standard, W. H. Higa

Two Varian Associates Model H-10 atomic hydrogen masers have been in operation approximately one year.

One unit has operated very satisfactorily while the other has required major repairs.

The latter unit was recently returned to Varian, Beverly, Massachusetts, for a complete diagnosis and correction. It was found to have a loaded cavity Q , which was lower (31,000) than normal (36,000), and a defective dissociator.

The dissociator, which produces atomic hydrogen from molecular hydrogen, is probably the crucial component in the hydrogen maser, from an operational aspect. The reason is that the physical mechanism producing the dissociation is complex and somewhat anomalous. A glass bulb with hydrogen gas at around 1 mm Hg pressure is subjected to a strong RF field (nominally 10 w at 200 MHz.). This produces a glow discharge, and the beam effusing from an opening in the bulb is rich in atomic hydrogen. The proper discharge occurs with a red glow, due to one of the electronic transitions in atomic hydrogen; however, occasionally a white glow occurs, due to transitions in molecular hydrogen. This white glow is detrimental to maser operation; the hydrogen beam is rich in molecular hydrogen. The effect is anomalous, in that it is difficult to predict when it will occur.

A complex surface "conditioning" inside the glass bulb usually occurs in the first few weeks of operation; subsequently, the glow remains red and satisfactory maser action is obtained. Occasionally a bulb will be erratic and enhance the white molecular discharge. This condition may last for several hours.

The Quantum Electronics Division of Varian has been doing spectral analysis of the glow discharge under different conditions in order to solve this enigma. Some research on a thermal dissociator is also in progress.

Measurements on the short term stability of hydrogen masers (SPS 37-42, Vol. III, p. 24) will be resumed when the repaired maser is returned to JPL.

C. Efficient Antenna Systems: Refrigerated Transmission Line Study, P. D. Potter

In DSIF-type low-noise receiving systems, one of the major contributions to the system noise temperature is the noise generated by dissipative losses in the waveguide circuitry. Since this contribution is proportional to both the waveguide power transmission coefficient and the physical temperature, it is interesting to consider the

possibility of refrigerating the waveguide circuitry to cryogenic temperatures. Because the waveguide surface resistivity decreases with decreasing physical temperature, a large improvement may be obtained.

Based upon a competitive solicitation, an eight-month study contract was awarded to Rantec Corporation, Calabasas, California, to investigate the practicality of introducing waveguide refrigeration into DSIF-type installations. Rantec Corporation is assisted in this effort by a refrigeration analysis subcontract to Arthur D. Little, Inc. (ADL). The output of the study is a report with graphs, equations and component conceptual designs. A Phase II effort will utilize this information to introduce refrigeration into, presently unselected, JPL receiving equipment.

The study has three basic parts: (1) microwave considerations; (2) refrigeration; and (3) system considerations. Item (1) (Rantec) consists of an experimental and analytical study of WR 430 (S-band) waveguide loss as a function of physical temperature and surface finish or material. Item (2) (ADL) consists of a study of cooling mechanization, component heat loads and refrigerator considerations. Item (3) consists of conceptual designs for refrigerated versions of all normally-utilized waveguide components together with simple system performance estimates; this item is performed jointly by Rantec and ADL.

In order to produce a study output, which will be of direct use to the DSIF, the study is highly constrained. Some of the major constraints are:

- (1) All experimental data must be directly usable (no questionable analytic conversion formulas).
- (2) Refrigerant to be liquid nitrogen.
- (3) Detailed consideration of readily-detachable, thermally-insulating waveguide joints for easy maintenance.
- (4) Refrigerator to be air liquefaction or separator type, and of standard commercial or military design.
- (5) No hazardous features in refrigeration system.
- (6) Desired cool-down time 3 hr, with maximum of 24 hr.
- (7) Failure of refrigeration system does not degrade performance more than that expected due to the increased physical temperature. (Possibly refrigeration use would be only for critical missions.)

At this time, Rantec has performed preliminary insertion loss tests at both ambient and liquid nitrogen temperatures; these measurements compare favorably with JPL-performed ambient-temperature tests, as described (Subsection D, C. T. Stelzried). Preliminary results are encouraging; a ratio of approximately 1.75 was obtained between the decibel waveguide losses at ambient and liquid nitrogen temperatures. This result indicates a possible reduction factor of approximately 6 for noise generated by the waveguide circuitry.

D. Improved RF Calibration Techniques: Precision Insertion Loss Measurement of WR 430 Aluminum Waveguide Test Section

C. T. Stelzried and T. Y. Otoshi

JPL has initiated Rantec contract 951638 for a study of cooled transmission line components (see subsection C). The preliminary work at Rantec involves insertion loss measurements¹ of WR 430 waveguide sections both at ambient temperatures and at cooled-to-liquid-nitrogen temperatures with a cavity Q-measurement technique (Ref. 2). JPL has made a verification insertion loss measurement of an aluminum WR 430 waveguide section using a standard insertion loss power measurement technique between matched loads.

1. Measurement Techniques

The insertion loss of a 6061 aluminum WR 430 waveguide section SN 1754 obtained from Rantec has been measured. The overall length of this section, shown in Fig. 5, is 12.834 in.

Prior to the measurement, stainless steel bushing inserts were installed (RFT Dwg 10023) and dowel holes were jig bored according to JPL print C4134616. The critical dimensions of the dowel pin locations and waveguide opening are shown in Figs. 6 and 7.

The DC insertion loss test set model MTT 100A SN 004 was used for the 2295 MHz insertion loss measurements. Critical dimensions of the WR 430 waveguide tuner flanges, used with the insertion loss set up, are shown in Figs. 8 and 9.

Four complete sets of insertion loss measurements were made. Each set consisted of 11 separate readings (6 references and 5 test piece readings). All flanges were

¹Plan for attenuation constant measurements per requirements of JPL, Rantec No. 66327-2 Rev. A., October 5, 1966.

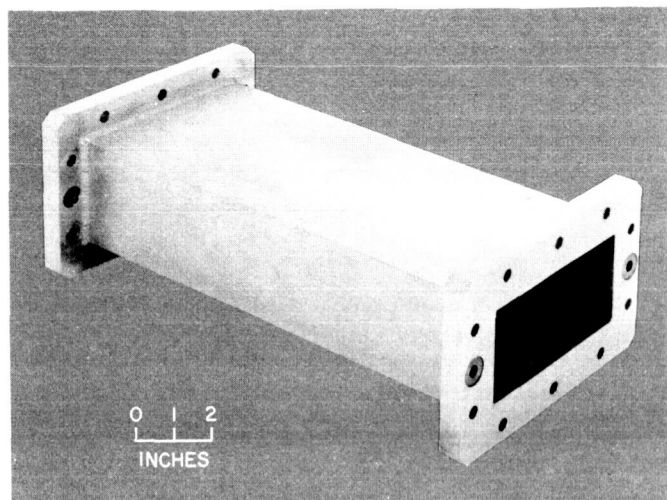
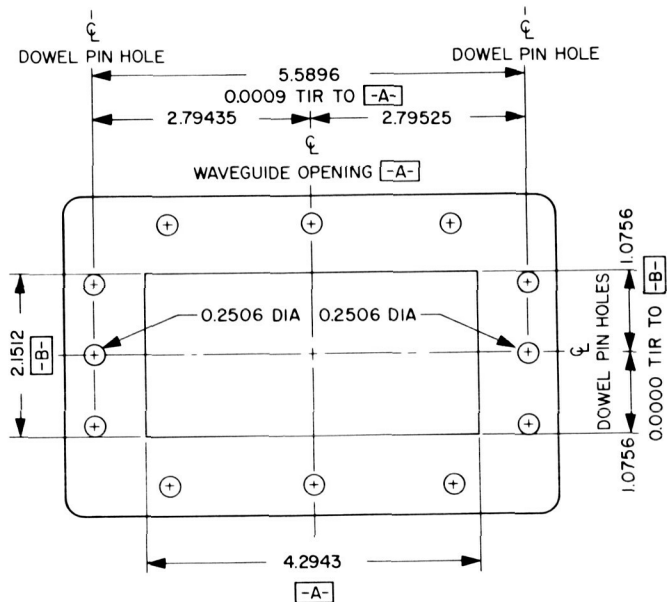


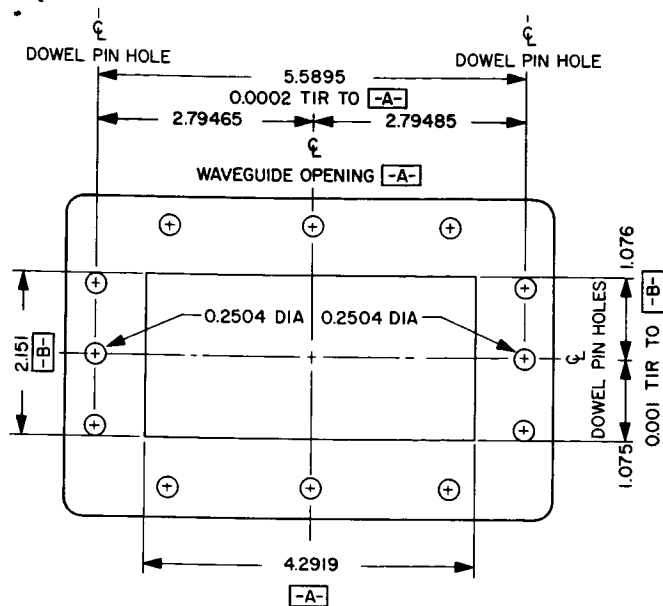
Fig. 5. Photograph of Rantec aluminum WR 430 waveguide test section (SN 1754)



NOTES:
TOTAL INDICATED READING (TIR)
ALL DIMENSIONS ARE IN in.

Fig. 6. Rantec WR 430 waveguide section flange 1

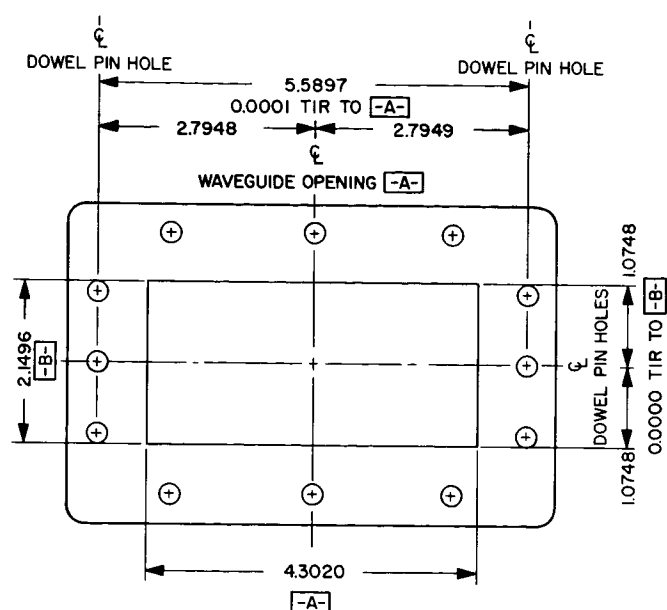
relapped after each set. The insertion loss heads were rematched after lapping and rechecked after each set. The dynamic range of the reflectometer was greater than 70 db. The match of the heads was better than 60 db after each set, as indicated by the reflectometer. The reflectometer was matched out with a high-precision WR 430 waveguide sliding load (FXR model 502-A01 SN 110) before and after each reflectometer reading.



2. Measurement Results

The insertion measurement data are summarized in Table 1, and the probable error of the measurement set is included. The insertion loss individual set averages are plotted in Fig. 10 with their measurement probable errors. Bias errors are not included here. The overall average of the sets (0.00414 db) is also shown. This is a straight average and was not obtained by weighting the individual set averages. The 0.00006-db probable error shown on the graph associated with the overall average is obtained by treating the individual sets as independent measurements. This is the best estimate of the overall measurement resolution error because it averages mismatch errors, etc. The Rantec measurement of 0.00427 db, with an overall probable error less than ± 0.00005 db

Run	Temp, °F	IL, db	(PE _{IL}) _M , db	Peak mismatch error, db
1	70.5	0.00414	0.00026	8.529 x 10 ⁻⁵
2	71.0	0.00412	0.00011	8.031 x 10 ⁻⁵
3	70.7	0.00407	0.00006	8.614 x 10 ⁻⁵
4	68.8	0.00421	0.0002	8.363 x 10 ⁻⁵
Average		0.00414	0.00006	



(assuming the reported overall accuracy of 0.0002 db to be a 3- σ error), is also shown for completeness. Measurement linearity errors ($\approx 0.1\%$) are negligible, so that the

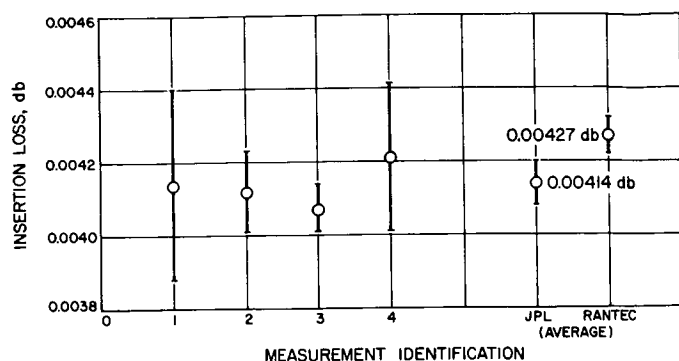


Fig. 10. Plot of insertion loss vs measurement set No.

overall error is due almost solely to measurement resolution and mismatch errors.

The reflection coefficient of the test section, when terminated in a matched load, was found to be 0.00182 ± 0.00031 at 2295 MHz. The residual errors of the reflectometer system were accounted for in all measured reflection coefficient values. Using the equation given by Beatty in Ref. 3, the maximum error of the insertion loss measurement for each run was calculated and is shown in Table 1. The maximum mismatch error was found to be less than ± 0.00009 db peak for all runs. Treating this as a $3\text{-}\sigma$ error (a rough estimate) in order to combine it with the measurement error results in an overall measurement error of ± 0.00007 db (probable error).

The JPL insertion loss measurements were made at an average temperature of 2°C lower than those at Rantec. Handbook temperature resistivity coefficients indicate a difference of less than 0.00002 db error due to this temperature difference.

E. Efficient Antenna Systems: X-Band Cone Receiving System Description and Calibration, T. Y. Otoshi and C. T. Stelzried

1. Introduction

The X-band cone RF instrumentation and preliminary calibration of the receiving system were initially described in SPS 37-42, Vol. III, p. 46. The experimental cone will provide information about antenna performance at 8448 MHz. It can be used with either the 85-ft Venus DSS or 210-ft Mars DSS antennas.

Insertion losses and reflection coefficients of the cone receiving system transmission lines were measured in a laboratory setup. A photograph of the setup may be seen

in the referenced SPS article. After final installation of these waveguide transmission lines and receiving system components in the cone, additional reflection coefficient measurements were made. This article describes the completed RF calibration system and summarizes the transmission line loss calibrations made at 8448 MHz.

Considerable 8448 MHz noise temperature data have been obtained for the receiving system:

- (1) Outside of the cone on the roof of JPL Building 238
- (2) Inside the cone on the roof of JPL Building 238
- (3) Inside the cone on the 85-ft paraboloid at the Venus Station.

These data are currently being reduced and analyzed. The noise temperature calibration data will be reported in a subsequent SPS.

2. Description

An operational block diagram of the cone waveguide system and RF instrumentation was given in the referenced SPS article. Figs. 11 and 12 of the cone interior show the turnstile junction, waveguide transmission line, maser receiver system, and calibration terminations installed in the upper level. Fig. 13 shows the auxiliary RF instrumentation control rack X3 mounted in the lower level.

The primary cryogenic load used for noise temperature calibrations of this receiving system is the Lab Standard liquid helium waveguide load with a UG 52A/U to CPR 112 flange transition section (Part No. 229). Previous calibrations of the Lab Standard helium load were described in SPS 37-23, Vol. IV, pp. 206-208 and SPS 37-30, Vol. III, p. 59.

3. Transmission Line Loss Calibrations

For absolute antenna temperature calibrations by the Y-factor method, the total noise power received from the antenna is compared to the total noise power received from two thermal noise standards. To accurately translate these noise powers (or effective noise temperatures) from one reference point in the measurement system to another, it is necessary that the transmission line loss between reference points be known. In addition, reflection coefficients of the transmission lines, noise sources, and receiver must be known in order to account for effects due to mismatch.

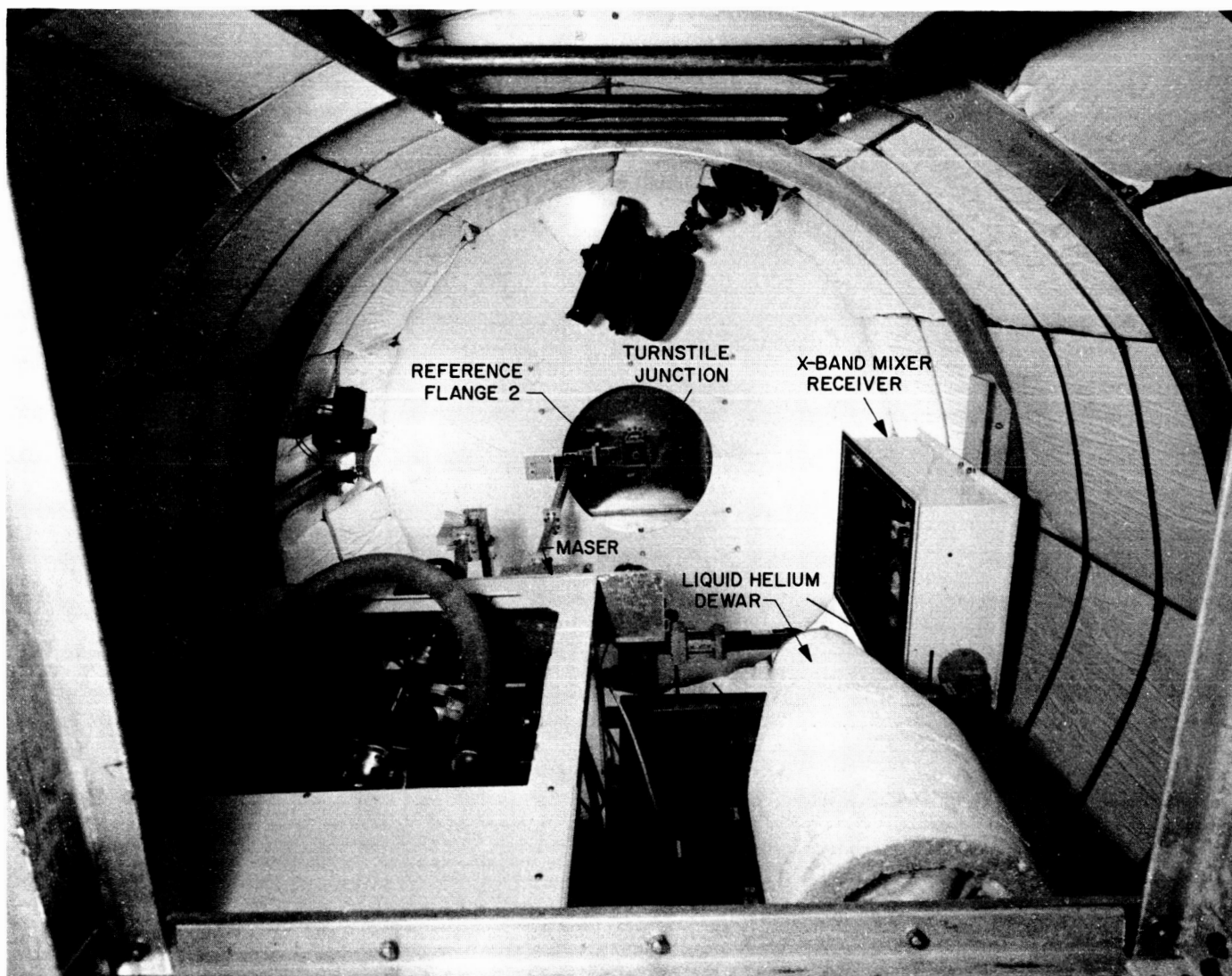


Fig. 11. X-band receiving system in the upper level of the cone interior

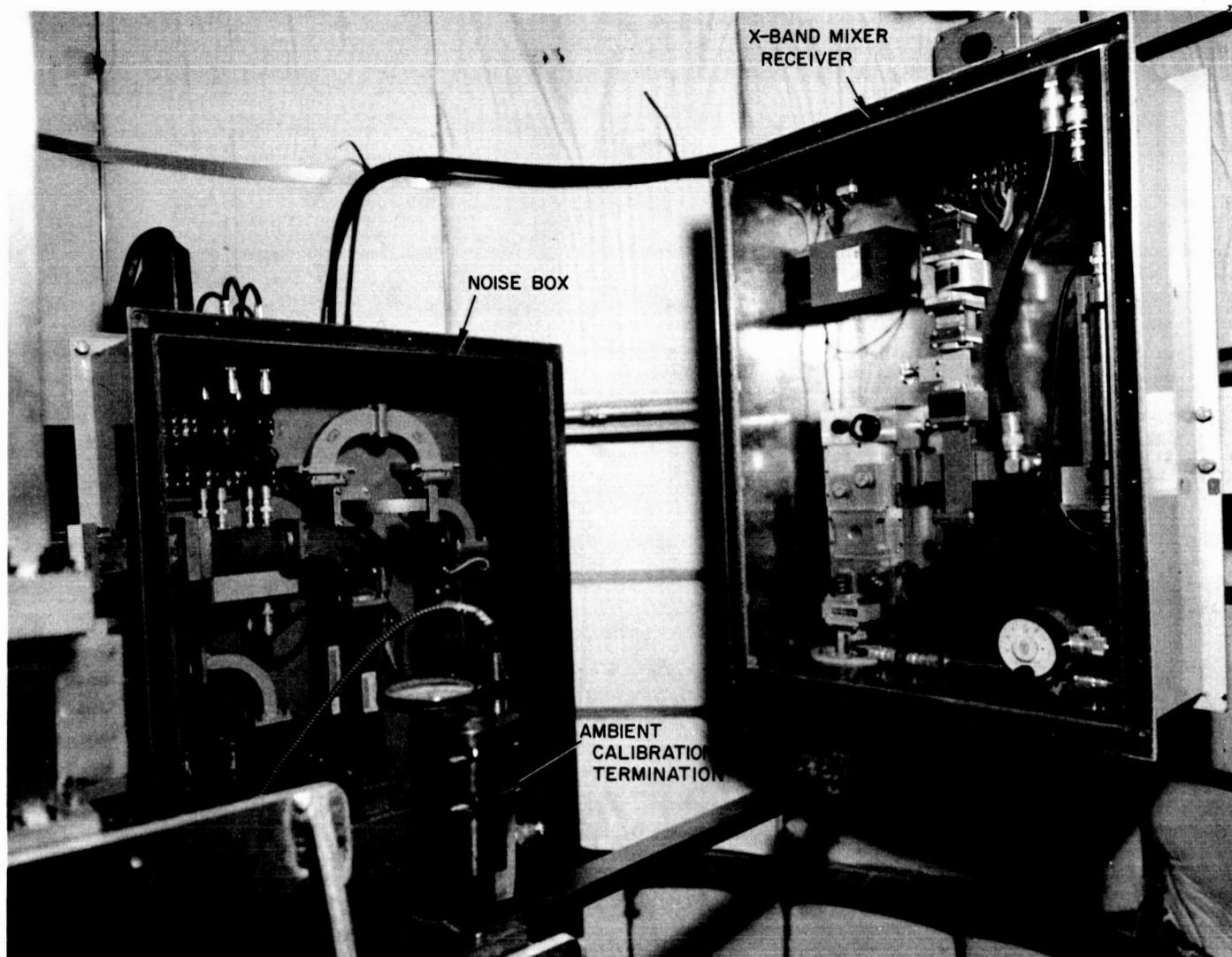


Fig. 12. X-band RF calibration equipment in the upper level of the cone interior

Fig. 14 is a block diagram of the cone RF waveguide calibration system depicting the critical transmission lines which connect the horn and waveguide termination noise sources to the receiver.

The receiver input reference flange (No. 1) is the CPR 112 input flange of the waveguide low-pass filter of the maser assembly. The antenna output reference flange (No. 2) is the CPR 112 output flange of the 4.00-in. long waveguide section, which follows the turnstile junction assembly. The cryogenic load reference flange (No. 3) is defined as the CPR 112 input flange of the 90-deg E-plane bend, which is connected to waveguide switch No. 2. The ambient load reference flange (No. 4) is defined as the CPR 112 flange of waveguide switch No. 2 as indicated in Fig. 14.

For reference purposes, the reflection coefficient symbols used in this article are defined in the following for a general noise source, a two-port transmission line, and a receiver. Some of these are indicated in Fig. 4.

Γ_s = voltage reflection coefficient of the noise source

Γ_R = voltage reflection coefficient of the receiver

Γ_{2s} = input voltage reflection coefficient, as seen at the receiver reference flange looking into the transmission line with the opposite port terminated in a Γ_s load

S_{11} = voltage reflection coefficient, as seen at the noise source reference flange looking into the transmission line with the opposite port terminated in a matched load

S_{22} = voltage reflection coefficient, as seen at the receiver reference flange looking into the transmission line with the opposite port terminated in a matched load

For the antenna, cryogenic load, and ambient load noise source cases, the symbol S is replaced by A , C , and H , respectively.

The critical reflection coefficients associated with the antenna, waveguide termination noise sources, and receiver have been measured at 8448 MHz and are listed in Table 2. The limits shown in the table represent the

Table 2. Summary of reflection coefficient measurements for X-band cone receiving system at 8448 MHz

Antenna-related parameters				
Voltage reflection coefficient symbol	Flanges (Fig. 14)		Measured voltage reflection coefficient amplitude	Comments
	Input	Load		
A_{11}	2	1	0.00017 ± 0.00015	Horn is in the right-hand circular polarization mode. Cone is on the ground.
A_{22}	1	2	0.00700 ± 0.00093	
Γ_{2A}	1	2	0.00447 ± 0.00073	
Γ_A	2		0.00462 ± 0.00068	
Cryogenic load-related parameters				
C_{11}	3	1	0.02116 ± 0.00263	
C_{22}	1	3	0.00043 ± 0.00031	
Γ_{2C}	1	3	0.01035 ± 0.00139	Cryogenic load is Lab Standard liquid helium load plus transition section (No. 229).
Γ_C	3		0.01288 ± 0.00173	
Γ_{2C}	1	3	0.00989 ± 0.00134	Cryogenic load is portable liquid nitrogen load MMC Model 8023 SN013.
Γ_C	3		0.01216 ± 0.00159	
Ambient load-related parameters				
Γ_{2H}	1	4	0.00282 ± 0.00055	
Maser assembly				
Γ_R	1		0.0197 ± 0.0105	

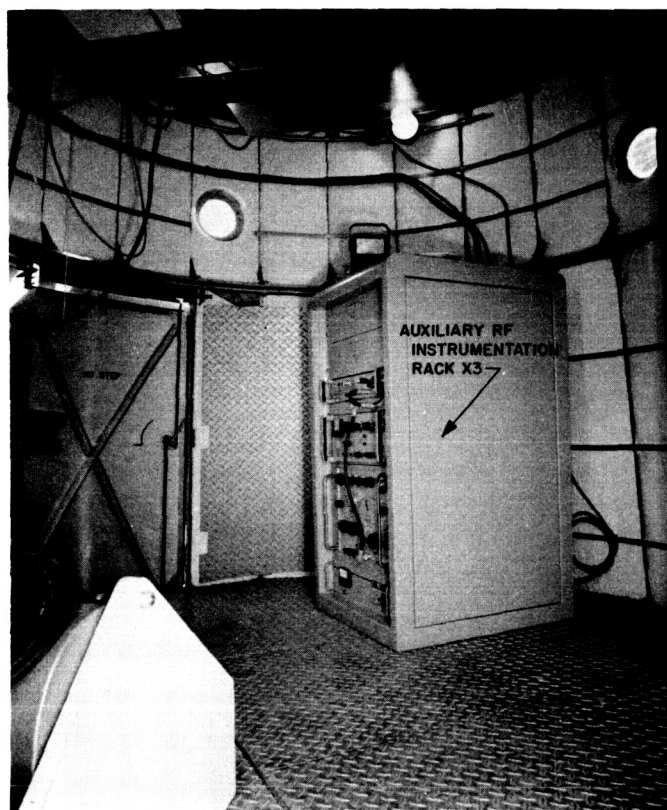


Fig. 13. X-band RF instrumentation rack X3 in the lower level of the cone interior

peak uncertainties in the reflection coefficient measurements. Transmission line insertion loss measurement results are shown in Table 3. A noise temperature measurement mismatch error analysis involving the application of these reflection coefficient and line losses may be found in SPS 37-40, Vol. IV, pp. 190-197.

Table 3. Summary of transmission line losses for the X-band cone receiving system at 8448 MHz

Transmission line	Flanges (Fig. 14)		Transmission line voltage reflection coefficient	Attenuation, db	Dissipative attenuation, db
	In-put	Out-put			
Antenna	2	1	0.00017 ± 0.00015	0.1499 ± 0.0004 (p.e.) ^a	0.1499 ± 0.0004 (p.e.)
Cryogenic load	3	1	0.02116 ± 0.00263	0.1721 ± 0.0004 (p.e.)	0.1702 ± 0.0005 (p.e.)

^a(p.e.) = probable error

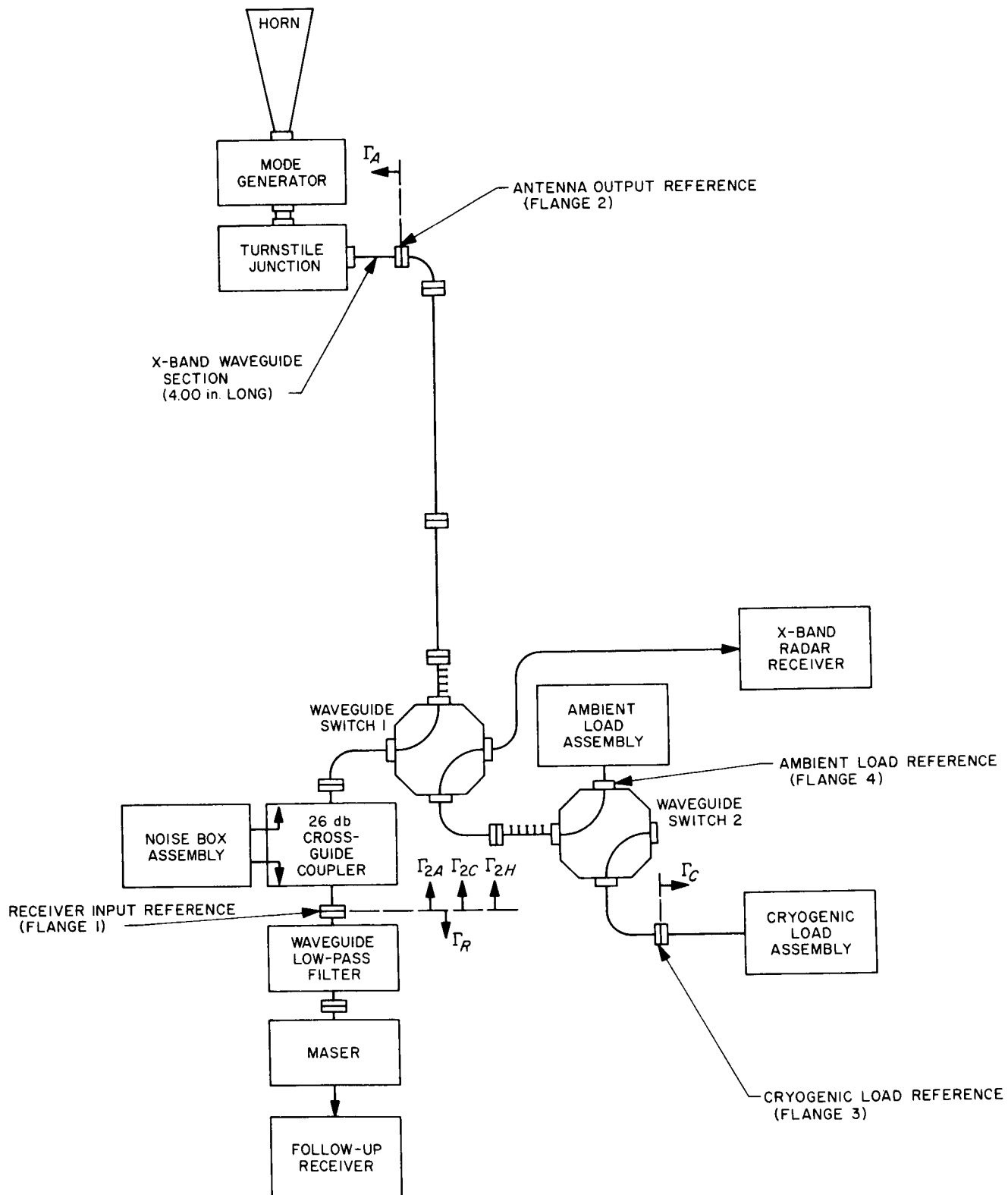


Fig. 14. Block diagram of the X-band cone RF waveguide calibration system

F. Efficient Antenna Systems: X-band Gain Measurements, D. A. Bathker

1. Introduction

An experimental program has been undertaken to investigate the behavior of the DSIF antennas as they approach gain limit (SPS 37-42, Vol. III, p. 40). Gain measurements have been made in the past at S-band. The next step is to make measurements at X-band; and, in the future, repeat these measurements at C- and K-bands.

Initially the 85-ft AZ-EL reflector at DSS 13, Venus station, will be evaluated by using the Tiefert mountain collimation station and by using radio star flux density measurements. An X-band Cassegrain feedcone, compatible with 85- and 210-ft reflectors, has been completed within a standard DSIF support cone and includes traveling wave maser (TWM) and crystal mixer front ends. The TWM will be used in a standard radiometer configuration; the crystal mixer front end will drive standard station equipments to derive AGC levels and antenna radiation patterns. The Venus station SDS 930 computer has been programmed to process received data and plot antenna patterns as received from the collimation station.

2. Test Description

The method of gain measurement to be employed requires the accurate determination of the difference between two RF power levels; approximately +30 dbm at the collimation station and approximately -20 dbm at the Venus station. By use of an RF attenuator having precision resettability, but not accuracy, the +30 dbm signal may be calibrated using a standard 10 mw maximum power meter provided the power meter linearity can be established over a 20-db range. In order to avoid possible bias errors in the gain test, the same power meter will be employed at the receiver site, provided the power meter linearity can be established over a 30-db range (10 mw to -20 dbm). The use of a single instrument in this manner precludes any necessity to obtain absolute RF power determinations, a difficult task but does require the accurate determination of linearity over a 30-db range.

A series of tests has been completed on a Hewlett Packard Company model 431C power meter (serial 618-00553) when connected to a Hewlett Packard model H486A (serial 1609) thermistor mount. These tests were designed and conducted with two major goals: the care-

ful determination of linearity of the power meter and thermistor mount and a determination of drift rates. The method of DC substitution was used, facilitated by use of a Hewlett Packard model 8402A (serial 243-00124) power meter calibrator. The calibrator simply provided a constant current source with 100 and 1000 $\pm 0.05\%$ Ω sampling resistors in the DC substitute mode; therefore, the primary concern was the ratio of the 10:1 divider. A Hewlett Packard integrating digital voltmeter model 2401B (serial 350-01159) was used as the DC voltage standard. Note that, for a linearity check, thermistor operating resistance need not be determined since operating resistance remains constant (within the ability of the instrument servo loops to reduce the initial disturbance).

The power meter was tested "as received." The thermistor mount was modified for improved thermal time constant and isolation.²

A first series of four test runs was made using an auxiliary digital voltmeter Hewlett-Packard Model 5265A/5245L to provide increased resolution over that provided by the meter scale. Table 4 shows a typical run revealing the magnitude of the thermoelectric effect.

A single second test was performed using the 2401B DVM to provide both the increased meter scale resolution and the voltage standard functions. A single test provides data more typical of those experienced under field conditions. Table 5 shows the averaged first series compared with the single second test. It is interesting to note that the error of the single test is generally less than 0.1% compared to the smoothed data, with the exception of the 3-mw scale. (More about this later.)

The smoothed and single run data were each normalized to the full scale value and converted to db. Table 6 shows the deviations for each scale, in db, from 100% to 50% scale (0.000 to -3.010, -5.000 to -8.010 etc., db). Apparent factory alignment errors of 1% and 5% in the 3 and 0.1 mw scale data were adjusted in Table 6 to gain a better view of the attainable linearity. The linearity (100% to 50% of scale) is 0.013 ± 0.002 db standard deviation. The linearity from 100% to 100% of next scale (0.000 to -5.000, -5.000 to -10.000 etc., db) is approximately 0.0035 ± 0.0035 db standard deviation.

²Suggested by C. T. Stelzried; now commercially available from the Maury Microwave Corporation in the coaxial version. More recently available in WR-90 waveguide from the Hewlett Packard Company.

Table 4. Typical run using auxiliary digital voltmeter

Power meter, mw	% scale ^a	Substituted power, mw ^b		Thermoelectric effect, % ^c
		$P_{DC} +$	$P_{DC} -$	
10	100	9.783	9.773	0.10
10	50	4.880	4.873	0.14
3	100	3.075	3.064	0.37
3	50	1.533	1.529	0.27
1	100	0.9810	0.9775	0.36
1	50	0.4893	0.4869	0.49
0.3	100	0.3108	0.3089	0.61
0.3	50	0.1550	0.1539	0.71
0.1	100	0.1034	0.1024	1.00
0.1	50	0.5170	0.05098	1.38
0.03	100	0.03114	0.03064	1.62
0.03	50	0.01560	0.01525	1.62
0.01	100	0.009923	0.009610	3.2
0.01	50	0.004973	0.004774	4.0

^a 100% and 50% scale is defined as being produced on the auxiliary digital voltmeter, following zero set, with no correction for input impedance of 10 MΩ.

^b Substituted power = $[V_c / (2 \times 10^3)]^2 R_T$ for the 10 and 3 mw scales (100-Ω sample). Substituted power = $[V_c / (2 \times 10^3)]^2 R_T$ for all other scales (1000-Ω sample), where V_c is the impedance corrected DC voltage across the sampling resistor. R_T is the nominal thermistor operating resistance, set equal to 100 Ω, all data.

^c Thermoelectric effect is defined as $(P_{DC+} - P_{DC-}) / P_{DC+}$

The 50% scale data show a definite error on each scale of -0.3%, attributable to the squaring circuit.³ The 100% to 100% scale data show about four times better performance, on the verge of being resolution limited, with the exception of the two scales requiring alignment. It will be noted that in both the thermoelectric effect data and the Table 5 data that the 3-mw scale is consistently noisy.

Data related to the drift problem were taken by observing the ability to establish and hold the zero, 50% and 100% scale deflections using the adjustable calibrator source. Table 7 summarizes the drifts experienced during a single substitution (≈ 1 min). Table 7 data represent four attempts at each level on each scale.

³ Discussions with Mr. Jim Macrie and Fred Praman of Hewlett-Packard, Palo Alto, showed that the squaring circuit was originally designed for $\pm 0.25\%$ linearity. The error due to finite loop gain not allowing a complete rebalancing of thermistor operating resistance, is estimated to be $1/10$, or less, of the squaring circuit error.

Table 5. Averaged four runs compared with a single second test run

Power meter, mw	% scale ^a	Substituted power, mw ^b (mean of 4 runs in first series)	Substituted power, mw ^b (single second test)	Error of the single test, ^c %
10	100	9.784	9.782	-0.02
10	50	4.878	4.880	+0.04
3	100	3.068	3.060	-0.27
3	50	1.529	1.525	-0.26
1	100	0.9799	0.9800	+0.10
1	50	0.4882	0.4883	+0.02
0.3	100	0.3099	0.3101	+0.07
0.3	50	0.1544	0.1545	+0.07
0.1	100	0.1030	0.1029	-0.10
0.1	50	0.05135	0.05132	-0.06
0.03	100	0.03094	0.03094	0.00
0.03	50	0.01544	0.01543	-0.07
0.01	100	0.009786	0.009785	-0.01
0.01	50	0.004879	0.004876	-0.06

^a As before, 100% and 50% scale is defined as being produced on the auxiliary digital voltmeter, following zero set, with no correction for input impedance. Input impedance is 10 MΩ for 4 runs, 1 MΩ for second test.

^b Corrected for thermoelectric effect.

^c Error is defined as (single test - mean of 4 runs) mean.

All tests utilized the 2401B voltmeter at 1-sec integration; the power meter calibration factor was constant at 98%. As the results show, full scale deflection occurs with DC substituted power within 0.17% of the theoretical value on the highest range.

The instrument, when carefully used with a thermally improved thermistor head, is seen to be limited by the squaring circuit to 0.3%. With reasonable instrumentation, DC substitution can be very conveniently applied for an accuracy of 0.1% or better over a 30-db range. The worst case short term drift (≈ 1 min) experienced during the tests represents a thermal change of 10^{-4} deg C, due to thermistor and bridge constants producing a sensitivity of about $100 \mu\text{W}/^\circ\text{C}$.

Further comments by Messrs Macrie and Praman of Hewlett-Packard Company indicate the thermoelectric effect exhibited by serial 1609 thermistor is about twice average. Also, their comments are of interest concerning effective efficiency, i.e., the DC-RF conversion factor. For the single detection element (waveguide) type mounts

Table 6. Measured deviations from linearity

Power meter, mw	% scale	Deviation, db ^a (first series)	Deviation, db ^a (single second test)	Single scale 3-db linearity, db (first series)	Single scale 3-db linearity db (single second test)
10	100	0.000 ^b	0.000 ^b		
10	50	-0.013	-0.011	-0.013	-0.011
3 ^c	100	+0.013	0.000		
3 ^c	50	-0.001	-0.011	-0.014	-0.011
1	100	+0.006	+0.008		
1	50	-0.009	-0.007	-0.015	-0.015
0.3	100	+0.007	+0.011		
0.3	50	-0.009	-0.005	-0.016	-0.016
0.1 ^d	100	+0.003	+0.002		
0.1 ^d	50	-0.009	-0.012	-0.012	-0.014
0.03	100	0.000	+0.001		
0.03	50	-0.009	-0.011	-0.009	-0.012
0.01	100	+0.001	+0.001		
0.01	50	-0.011	-0.014	-0.012	-0.015

^a Deviation is here defined as measured-indicated.

^b Approximately 0.02% error in data adjustment of each full scale to 0.000 db. See Table 5.

^c Adjusted data +0.050 db (1%); apparent factory error. (The instrument requires alignment of potentiometer A2R6, full scale accuracy adjustment in the DC feedback current generator.)

^d Adjusted data -0.220 db (5%); apparent factory error. (The instrument also requires alignment of potentiometer A2R3, same circuit.)

there is no known reason for suspecting efficiency to change with applied power levels. To date, this has been experimentally verified by the National Bureau of Standards to 0.1% over 1 to 10 mw. In the case of the dual detection element (coaxial) mounts, either balanced or unbalanced, there is a known dual element error, apparent when operating on the upper ranges of the instrument when the applied RF power causes a decrease in bias power of nearly equal magnitude. This error is controlled, at manufacture, to something better than 0.1%.

3. Conclusion

For the above reason waveguide mounts should be favored over coaxial mounts whenever possible. In conclusion it appears that the laboratory calibration indicates on-site DC calibrations will be necessary to achieve an accuracy in the order of 0.1% and avoid possible further misalignments due to rough handling.

Table 7. Ability to hold levels during a single DC substitution

Power meter, mw	Power meter output, mv DC			Full scale uncertainty, %
	0 set	50 % scale	100 % scale	
10	±0.03	±0.10	±0.10	0.01
3	0.03	0.10	0.10	0.01
1	0.05	0.10	0.10	0.01
0.3	0.10	0.10	0.10	0.01
0.1	0.20	0.20	0.20	0.02
0.03	0.50	0.50	0.50	0.05
0.01	1.0	1.0	1.0	0.10

The assistance of R. Haag of the Goldstone Microwave Test Facility in making these tests is gratefully acknowledged.

G. Efficient Antenna Systems: System Noise Temperature as a Function of Meteorological Conditions, P. D. Potter

1. Summary

Microwave antenna noise temperature and, hence, system noise temperature are affected by antenna elevation angle and various meteorological conditions, notably temperature, relative humidity, and rain. These effects have been analyzed extensively in the literature, and some limited experimental data have been reported.

In order to provide a convenient tool for system noise temperature performance prediction and analysis, a simple program has been written in Fortran II for use on the IBM 1620. Based on a brief review of the literature, the program uses simple functional dependences together with various experimentally determined constants; the formulation is such as to allow convenient upgrading as better functional dependences and experimental data become available. Machine execution time is 5 min/case.

2. Program Formulation⁴

In the 1-10 GHz microwave band, absence of molecular resonance lines provides a smooth and generally monotonic variation of noise temperature dependences

⁴ This discussion includes various modifications made by C. T. Stelzried to provide compatibility with millimeter-band calculations; use of the program for such calculations will be separately described in a future SPS Vol. IV.

upon frequency, elevation angle, and meteorological environment. Furthermore, to a first approximation, these dependences may be expressed as separable functions of each parameter. The system noise temperature T_{sys} is given by:

$$T_{sys} = T_{fixed} + T_{phys} (1 - F_{loss}) + T_{gal} \cdot F_{loss}, ^\circ K \quad (1)$$

where

T_{phys} = equivalent physical temperature of the Earth's atmosphere, $^\circ K$

F_{loss} = fractional power transmission through the Earth's atmosphere

T_{gal} = extra-atmospheric universal noise component

$T_{fixed} = T_{spil} + T_{scat} + T_{loss} + T_{rec}$

T_{spil} = noise temperature component due to feed system spillover

T_{scat} = noise temperature component due to antenna quadripod scattering

$T_{loss} + T_{rec}$ = transmission line and receiver noise temperature components, defined at the antenna output terminals

For each particular case, all factors in Eq. (1) other than F_{loss} are taken to be constants. In computing F_{loss} , the Earth's atmospheric and physical rain distributions are approximated by horizontal slabs, an assumption which is good for elevation angles θ greater than approximately 10 deg; for elevation angles less than this, Earth curvature is significant and difficulties with horizontal rain distribution become very serious. If F_{loss} is expressed in decibels as Db_{tot} ,

$$Db_{tot} = \text{Cosec } \theta [Db_{oz}(f) + Db_{wz}(f) \cdot F_1(T_{phys}, h) + Db_{rz}(f) \cdot F_2(R)] \quad (2)$$

where

R = ground rain rate, in./hr

h = relative humidity, %

f = frequency, GHz

$Db_{oz}(f)$ = zenith oxygen attenuation, decibels

$Db_{wz}(f)$ = a zenith water vapor attenuation constant

$Db_{rz}(f)$ = a zenith rain attenuation constant

The function $F_1(T_{phys}, h)$ converts information on temperature and humidity to atmospheric water content and also establishes the functional dependence of attenuation upon water content. Fig. 15 shows two simple models for atmospheric water content profiles. In (a), the slab height is taken to be independent of ground-level water content, and in (b) the rate of change of water content with height is taken to be independent of ground-level water content. It is easily shown that the former model leads to a total attenuation which is linearly proportional to ground-level water content, and the latter model leads to a proportionality given by the square of the ground-level water content. The latter type of model was used by Hogg (Ref. 4); however, the former model has considerable physical merit. Since few experimental data presently exist to resolve this choice of models, the program formulation allows a choice of an arbitrary exponent.

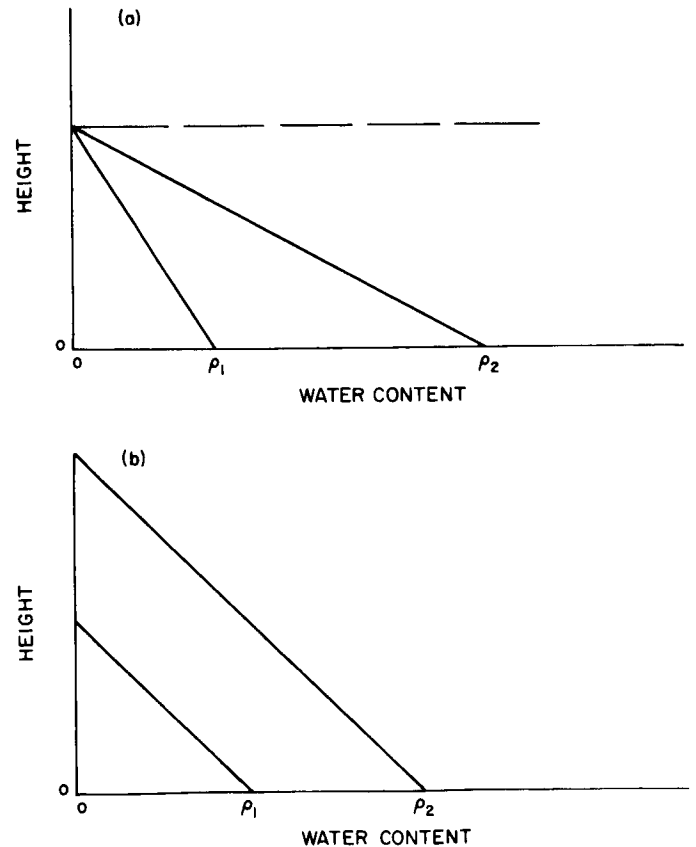


Fig. 15. Atmospheric water content profiles:
(a) constant height slab; (b) constant slope, variable height slab

The relationship between temperature and atmospheric saturated water content is readily available in tabular form (Ref. 5). Fig. 16 is a comparison between these exact data and a simple empirical relationship given by

$$\rho_{sat} = 5.71 + 0.0079424 (T - 30.0)^2 \quad (3)$$

where

ρ_{sat} = saturated water content in g/m^3

$T = T_{phys}$, converted to $^{\circ}\text{F}$

Finally, the function $F_1(T_{phys}, h)$ is taken to be

$$F_1(T_{phys}, h) = [\rho_{sat}(T_{phys})]^{B_1}, \text{ during rain} \quad (4a)$$

$$= \left[\frac{h \cdot \rho_{sat}(T_{phys})}{100} \right]^{B_1}, \text{ without rain} \quad (4b)$$

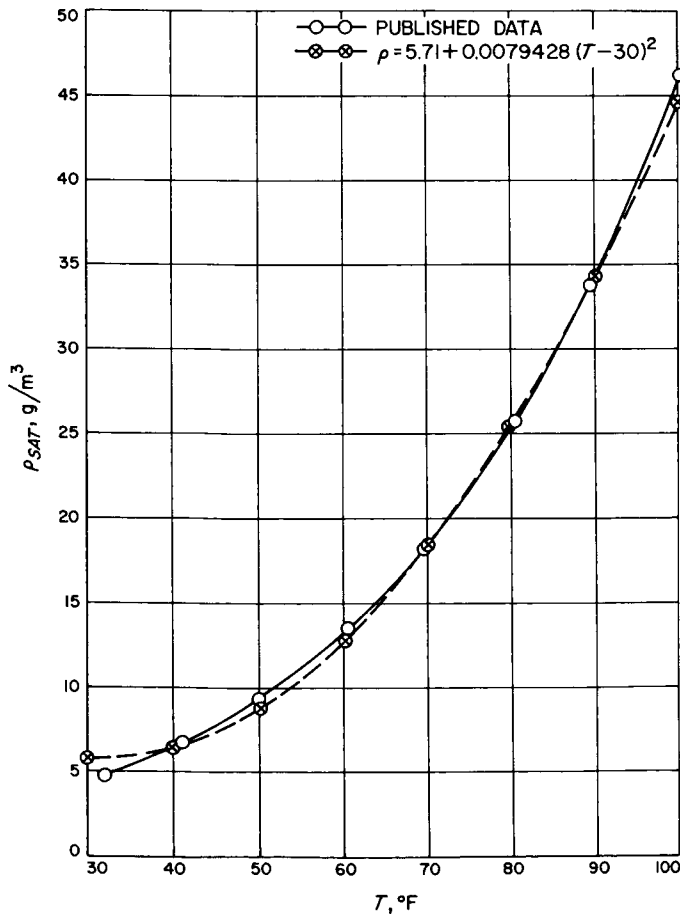


Fig. 16. Saturated water content vs temperature

The dependence of rain attenuation upon rain rate and frequency has been discussed by Feldman (Ref. 6). To good approximation the attenuation (in decibels) is linearly related to rate and related to frequency by frequency to a power between 3 and 4. Therefore, the following dependences are selected:

$$F_2(R) = R, \text{ in./hr} \quad (5a)$$

$$Db_{rz}(f) = -Af^B \quad (5b)$$

By fitting to published data (Ref. 4), the remaining frequency dependences are empirically established as follows:

$$Db_{oz} = - (0.0219 + 0.001067 f) \quad (6)$$

$$Db_{wz} = - \frac{0.0000219 f^2}{10^{(B_1-1)}} \quad (7)$$

Where the denominator of Eq. (7) is introduced to force exact agreement with Hogg's data for the typical condition of 10 g/m^3 water content. The values presently being used for the various other constants are given in Table 8.

Table 8. Program constants — December 15, 1966

Constant	Value
T_{gal}	3.0°K
T_{spil}	1.0°K
T_{scat}	3.0°K
A	0.00347
B	3.0
B_1	1.5

3. Rain Statistics

The rain conditions at any site may be described in terms of a few simple parameters:

- (1) Total annual rate.
- (2) Hours of rain per year.
- (3) Rain rate probability distribution.

Note that these factors are not independent, since summation over a year of rain rate times time must equal annual rainfall.

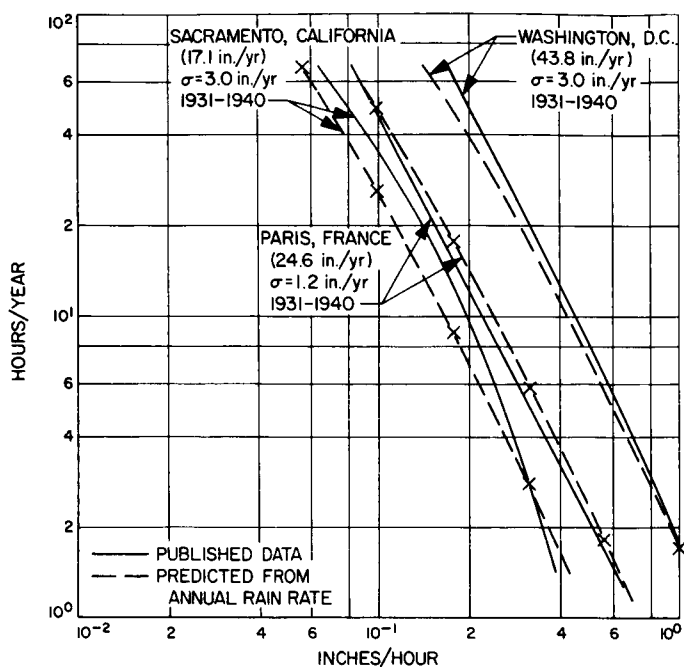


Fig. 17. Rain rate statistics

Fig. 17 shows typical rain rate statistics (Ref. 7) for three temperate sites, together with simple predictions (described below) from annual rainfall data. Fig. 7 shows a more detailed comparison of measured and predicted rain statistics for Washington, D. C., for which detailed data are available (Ref. 8). Curiously, the total hours of rain per year are roughly constant (400-600 hr/yr, or about 5% of the time) for most temperate sites. The factors which appear to vary most with site location (e.g., New England vs Southern California) are mean rain rate during rain and probability of rain vs time of year.

Fig. 19 shows a simplified empirical rain rate model (solid curve) together with the model assumed in the computer program (dashed curve). The former model is characterized by a probability β of having rain at any rate; a minimum rate R_0 and a maximum rate R_M and an inverse-square dependence for intermediate rates. The inverse square dependence is empirically chosen, based on data shown in Fig. 17. The cumulative probability

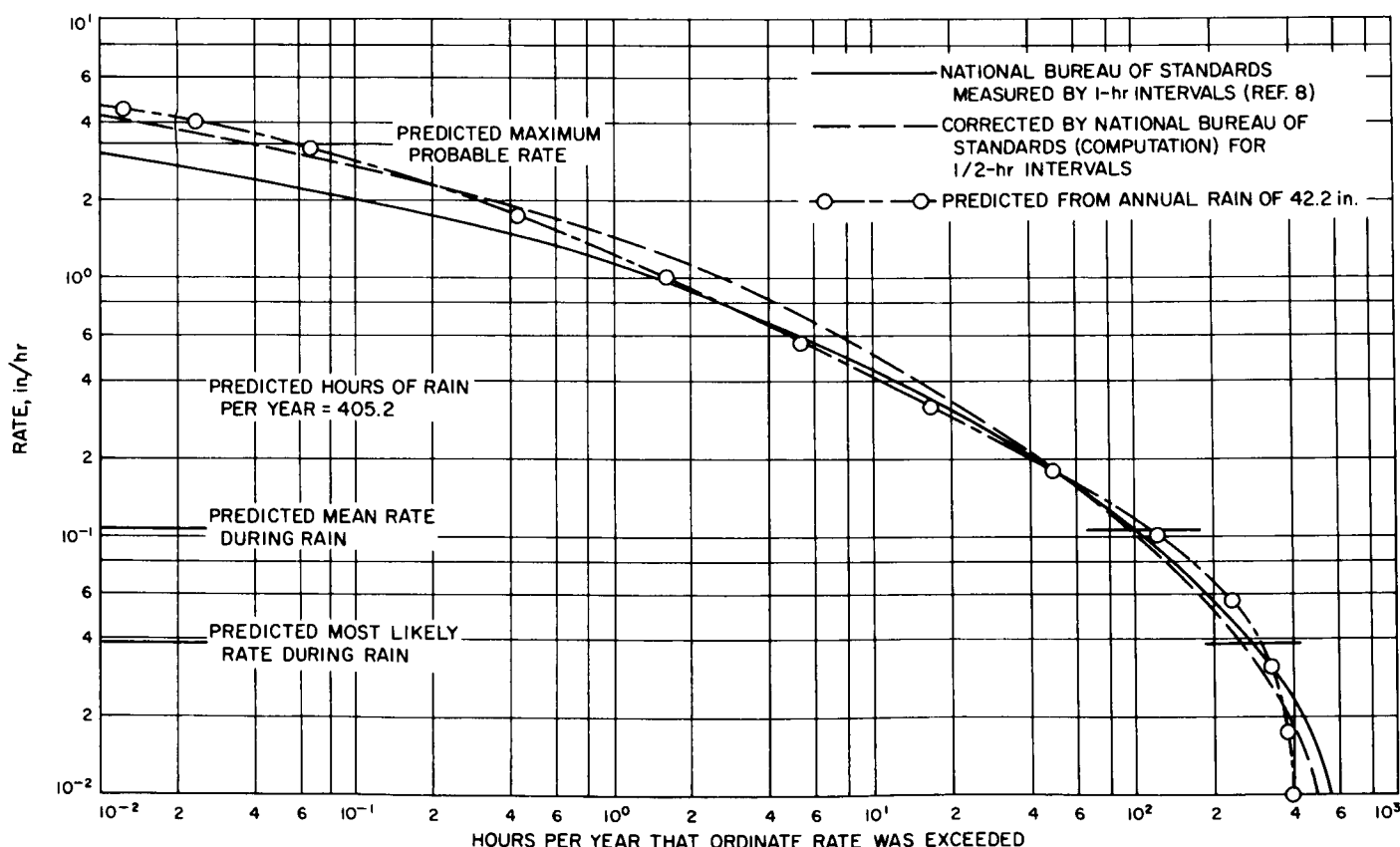


Fig. 18. Comparison of measured rain data with simple prediction from annual rate

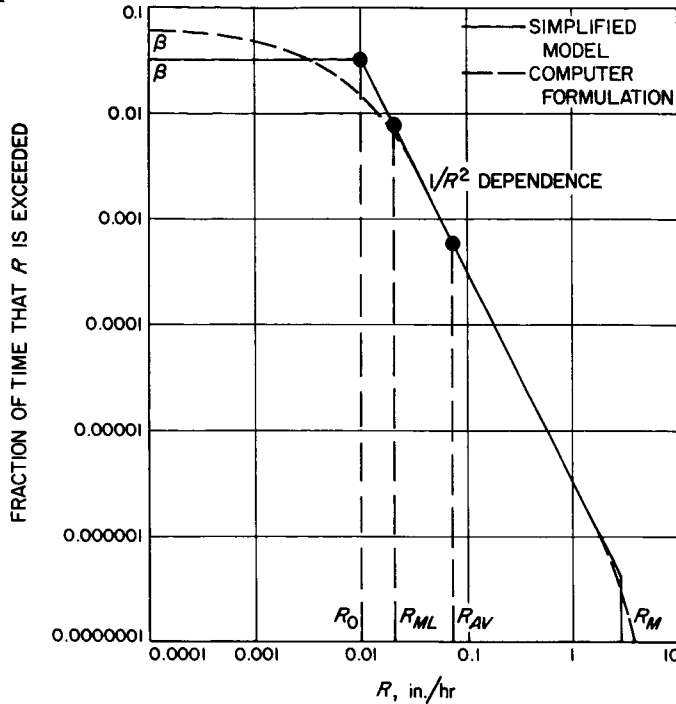


Fig. 19. Models for rain rate statistics

distribution $P(R)$ chosen for the computer program is given by

$$P(R) = 1 - \frac{\beta R_0^2}{R_0^2 + R^2} \quad (8)$$

leading to a probability density function $p(R)$ given by

$$p(R) = \frac{2\beta R_0^2 R}{(R_0^2 + R^2)^2} \quad (9)$$

and by differentiating Eq. (9) the most likely rate R_{ML} is found to be given by

$$R_{ML} = R_0/\sqrt{3} \quad (10)$$

The mean rate R_{AV} during rain is given by

$$R_{AV} = \frac{\int_0^\infty R \cdot p(R) dR}{\int_0^\infty p(R) dR} = (\pi/2) R_0 \quad (11)$$

The total rain in one year Y_{rain} is given by

$$Y_{rain} = \beta H R_{AV}, \text{ in./yr} \quad (12)$$

where $H = 8760$ = number of hours in one year.

From Eqs. (11) and (12), R_0 and, hence, all other parameters are established as a function of Y_{rain} . The cumulative probability distribution is thus found to be:

$$P(R) = \frac{\beta}{1 + \frac{\pi^2 H^2 \beta^2}{4 (Y_{rain})^2} R^2} \quad (13)$$

To Eq. (13) a multiplicative correction factor $\exp -(4 R^2) Y_{rain}$, is applied to produce a rapid cutoff of rain probability above a certain rate. The preceding analysis is not significantly affected by this cutoff because in Eq. (11) the integrand decays as inverse rain-rate squared. A maximum probable rain rate R_M is defined as the point at which the correction factor has a value of $1/e$.

4. Sample Case

The primary purpose of the program described in this article is to provide a convenient tool for system performance predictions. For this reason and to minimize human error, a minimal four-card input is used. Fig. 20(a) shows the first page of a sample case output, listing the necessary input parameters. The reference temperature and humidity inputs determine a standard meteorological condition to which system temperature performance is compared. Fig. 20(b) shows the first page of elevation angle data; the final column gives the sum of decibel path loss and decibel ratio of standard condition zenith system noise temperature to the actual system temperature in column three. Tables of data, such as shown in Fig. 20(b) are printed up to a maximum rain rate of 10 in./hr; the rates are chosen such that four values are obtained per octave of rate.

Fig. 20(c) shows the final page of output. In this part of the output, elevation angle dependence has been eliminated by averaging loss, temperature, and total degradation over all elevation angles, weighted by the solid angle surrounding the antenna. The hours of rain per year result from a choice of 0.0462 for β , a value determined empirically from Figs. 18 and 19.

(a)	
SYSTEM TEMPERATURE PROGRAM	
PROGRAM NUMBER PDP7CTS-2	
SAMPLE CASE FOR SPACE PROGRAMS SUMMARY	
CASE NUMBER 25	
DATE 12/15/66	
INPUT PARAMETERS FOLLOW	
FREQUENCY=	2.29500 GIGACYCLES
RECEIVER TEMPERATURE=	6.0 DEGREES KELVIN
TRANSMISSION LINE NOISE=	2.0 DEGREES KELVIN
MINIMUM ELEVATION ANGLE=	10.0 DEGREES
ELEVATION INCREMENT=	10.0 DEGREES
YEARLY RAIN=	10.0 INCHES
TEMPERATURE=	70.0 DEGREES F
REL HUMIDITY=	60.0 PER CENT
REF TEMPERATURE=	50.0 DEGREES F
REF REL HUMIDITY=	40.0 PER CENT

(b)

CASE NUMBER 25

OUTPUT FOLLOWS

RAIN RATE= 0.00000 INCHES/HOUR

ELEVATION	DB PATH LOSS	SYSTEM TEMP	TOTAL DB DEGRADATION
10.0	-.18991	27.46	-2.26030
20.0	-.09642	21.39	-1.08262
30.0	-.06595	19.39	-.62472
40.0	-.05130	18.42	-.38731
50.0	-.04305	17.87	-.24797
60.0	-.03808	17.54	-.16202
70.0	-.03509	17.34	-.10960
80.0	-.03348	17.23	-.08112
90.0	-.03297	17.20	-.07207

RAIN RATE= .00100 INCHES/HOUR

ELEVATION	DB PATH LOSS	SYSTEM TEMP	TOTAL DB DEGRADATION
10.0	-.19904	28.04	-2.36103
20.0	-.10105	21.69	-1.14849
30.0	-.06912	19.59	-.67453
40.0	-.05377	18.58	-.42813
50.0	-.04511	18.01	-.28330
60.0	-.03991	17.66	-.19386
70.0	-.03678	17.45	-.13929
80.0	-.03509	17.34	-.10963
90.0	-.03456	17.30	-.10021

RAIN RATE= .00177 INCHES/HOUR

ELEVATION	DB PATH LOSS	SYSTEM TEMP	TOTAL DB DEGRADATION
10.0	-.19923	28.06	-2.36309
20.0	-.10115	21.70	-1.14984
30.0	-.06919	19.60	-.67555
40.0	-.05382	18.58	-.42897
50.0	-.04516	18.01	-.28403
60.0	-.03994	17.66	-.19452
70.0	-.03681	17.45	-.13990
80.0	-.03513	17.34	-.11021
90.0	-.03459	17.31	-.10078

(c)

CASE NUMBER 25

YEARLY RAIN= 10.0 INCHES

MEAN RAIN RATE= .024 INCHES/HOUR

MOST LIKELY RAIN RATE= .009 INCHES/HOUR

MAXIMUM PROBABLE RAIN RATE= 1.581 INCHES/HOUR

HOURS OF RAIN PER YEAR= 405.2

RAIN RATE	HOURS/YEAR	PER CENT TIME	AV DB PATH LOSS	AV SYSTEM TEMP	AV TOTAL DB DEGRADATION
0.00000	8760.000	100.00	-.08	20.56	-.77
.00100	403.651	4.60	-.08	20.82	-.82
.00177	400.158	4.56	-.08	20.83	-.82
.00316	389.499	4.44	-.08	20.84	-.83
.00562	359.240	4.10	-.08	20.85	-.83
.01000	288.389	3.29	-.08	20.88	-.84
.01778	177.607	2.02	-.08	20.94	-.85
.03162	80.176	.91	-.09	21.04	-.86
.05623	29.296	.33	-.09	21.21	-.90
.10000	9.720	.11	-.09	21.51	-.95
.17782	3.098	.03	-.10	22.05	-1.05
.31622	.958	.01	-.12	23.01	-1.23
.56234	.278	0.00	-.14	24.70	-1.51
1.00000	.067	0.00	-.19	27.67	-1.97
1.77827	.008	0.00	-.27	32.85	-2.67
3.16227	0.000	0.00	-.41	41.71	-3.70
5.62341	0.000	0.00	-.66	56.50	-5.09
10.00000	0.000	0.00	-1.09	80.02	-6.89

END OF CASE NUMBER 25

Fig. 20. Sample computed output: (a) input parameters; (b) elevation angle data; (c) averaged data

H. Efficient Antenna Systems: Effect of Wind and Elevation Angle Upon Antenna Gain,

P. D. Potter

1. Introduction

Microwave antenna gain is a function of size, frequency of operation, feed system design and surface tolerance; the associated functional dependences are well known and easily evaluated. The dependence of surface tolerance upon structural design approach, antenna size, antenna pointing direction, and prevailing wind conditions is, however, complex and can only be analyzed in detail by extensive machine computation or exhaustive field measurements. A need exists, therefore, for conveniently producing approximate surface tolerance data.

This article describes a simple computer program written in Fortran II for the IBM 1620; the program uses simple functional dependences and constants empirically derived from detailed engineering studies performed for the Advanced Antenna System (AAS). Antenna gain is computed as a function of frequency, antenna size, feed system efficiency, structural efficiency, wind and elevation angle. Machine execution time is 3 min/case.

2. Program Formulation⁵

Using the standard Ruze formulation for gain loss due to random reflector surface imperfections, the gain G of the antenna is given by

$$G = \eta_F \pi^2 \left(\frac{D}{\lambda} \right)^2 \exp -\bar{\delta}^2 \quad (1)$$

where

η_F = feed system aperture efficiency

D = antenna diameter, inches

λ = wavelength, inches

$\bar{\delta}^2$ = mean-squared path length phase error in radians due to surface imperfections

$$= (4\pi/\lambda)^2 \bar{\sigma}^2$$

$\bar{\sigma}^2$ = mean-squared one-half path length error, inches

⁵The surface tolerance functional dependencies and associated proportionality constants used in this formulation were supplied by M. S. Katow and C. Valencia of JPL Section 332. Mr. Katow also provided indispensable assistance in reviewing test case results.

The quantity $\bar{\sigma}^2$ is given by

$$\bar{\sigma}^2 = \sigma_1^2 + \sigma_s^2 + \sigma_c^2 (D) + \sigma_u^2 \quad (2)$$

where

σ_s^2 = mean-square panel-setting error

σ_c^2 = Cassegrain subreflector mean-square error

σ_u^2 = mean square panel-manufacturing error

and

$$\sigma_1^2 = [\sigma_w(D, w) + \sigma_T(D) + \sigma_G(D, \theta, \theta_0)]^2 \quad (3)$$

where

θ = elevation angle, degrees

w = average wind speed, miles/hour

σ_w = rms error due to wind

σ_T = rms error due to thermal distortions

θ_0 = panel setting elevation angle, degrees

σ_G = rms gravity distortion

the selected functional dependences are as follows:

$$\sigma_w(D, w) \propto w_{corr} \cdot w^2 \cdot D \quad (4a)$$

$$\sigma_T(D) \propto D \quad (4b)$$

$$\sigma_G(D, \theta, \theta_0) \propto G_{corr} \cdot D^2 \cdot |\theta - \theta_0| \quad (4c)$$

$$\sigma_G \propto D \quad (4d)$$

where proportionality constants are chosen to force agreement with known AAS surface tolerance data. The parameters w_{corr} and G_{corr} , whose values are unity for the AAS, are input design correction factors to allow for different structural design approaches. Eq. (4c) is based on STAIR program computations, which show this simple relationship to be surprisingly good.

3. Sample Case

The primary purpose of this program is to provide a convenient tool for system performance predictions and parametric studies. For this reason, and to minimize human error, a minimal four-card input is used. Fig. 21(a) shows the first page of a sample case output, listing the necessary input parameters. Fig. 21(b) shows the second page, with typical tables of σ , surface tolerance loss, and gain vs elevation angle; tables are produced for steps of 5 mph in wind speed, up to a maximum of 45 mph. Fig.

(a) ANTENNA TOLERANCE/GAIN PROGRAM
PROGRAM NUMBER PDP-7

SAMPLE CASE FOR SPACE PROGRAMS SUMMARY
CASE NUMBER 8
DATE 12/15/66

INPUT PARAMETERS FOLLOW

FREQUENCY= 2.29500 GIGACYCLES
ANTENNA DIAMETER= 210.000 FEET
MINIMUM ELEVATION ANGLE= 10.0 DEGREES
ELEVATION INCREMENT= 5.0 DEGREES
PANEL SETTING ELEVATION ANGLE= 45.0 DEGREES
FEED SYSTEM EFFICIENCY= .650
PANEL SETTING ACCURACY= .019 INCHES
PANEL MFG ERROR= .035 INCHES
GRAVITY DESIGN FACTOR= 1.0
WIND DESIGN FACTOR= 1.0

(b) CASE NUMBER 8
OUTPUT FOLLOWS, POSSIBLE POINTING LOSS NOT INCLUDED

WIND= 0.00 MPH

ELEVATION	SIGMA	SURFACE LOSS, DB	GAIN, DB
10.0	.068	-.12	61.75
15.0	.065	-.11	61.76
20.0	.063	-.10	61.77
25.0	.060	-.09	61.78
30.0	.058	-.08	61.78
35.0	.056	-.08	61.79
40.0	.054	-.07	61.80
45.0	.052	-.07	61.79
50.0	.055	-.07	61.79
55.0	.058	-.09	61.78
60.0	.062	-.10	61.77
65.0	.067	-.11	61.75
70.0	.072	-.13	61.74
75.0	.077	-.15	61.72
80.0	.082	-.17	61.70
85.0	.087	-.19	61.67
90.0	.093	-.22	61.65

WIND= 5.00 MPH

ELEVATION	SIGMA	SURFACE LOSS, DB	GAIN, DB
10.0	.070	-.12	61.74
15.0	.067	-.11	61.75
20.0	.064	-.10	61.76
25.0	.062	-.10	61.77
30.0	.059	-.09	61.78
35.0	.057	-.08	61.79
40.0	.055	-.07	61.79
45.0	.053	-.07	61.80
50.0	.056	-.08	61.79
55.0	.060	-.09	61.78
60.0	.064	-.10	61.76
65.0	.069	-.12	61.75
70.0	.074	-.14	61.73
75.0	.079	-.16	61.71
80.0	.084	-.18	61.69
85.0	.090	-.21	61.66
90.0	.095	-.23	61.63

(c) CASE NUMBER 8

WIND, MPH	AV SIGMA	AV SURFACE LOSS, DB	AV GAIN, DB
0.0	.061	-.10	61.77
5.0	.063	-.10	61.77
10.0	.069	-.12	61.75
15.0	.079	-.16	61.71
20.0	.095	-.23	61.63
25.0	.117	-.35	61.51
30.0	.145	-.54	61.32
35.0	.179	-.83	61.04
40.0	.219	-1.24	60.62
45.0	.264	-1.82	60.05

END OF CASE NUMBER 8

Fig. 21. Sample computed output: (a) input parameters; (b) elevation angle data; (c) averaged data

21(c) shows the final page of the output. Elevation angle dependence is eliminated by averaging over all angles, weighted by the solid angle surrounding the antenna.

I. Digital Communication and Tracking: Design of Lock Detectors, R. Tausworthe

1. Introduction

The implemented version of a phase-tracking loop is almost always instrumented with a device to indicate when the loop is locked. In its usual connection, what is meant by the term "lock" tends to be rather subjective, and a comprehensive definition applicable to all circumstances is difficult to formulate. But, certainly, when the loop is operating in its linear region, almost everyone agrees that lock is in effect, and when the loop is slipping cycles, there is almost universal agreement that lock has been broken. The lock concept is thus some quantized measure of the phase error.

Ideally, the lock detector should switch on when the loop has reached lock during acquisition, stay on whenever the loop phase error lies between specified limits during the track, and switch off whenever satisfactory tracking has been interrupted.

The definition which we impose here for definiteness is that lock is a condition during which the phase error stably wanders about one of the lock-in points and has not yet wandered out of the lock-in region associated with that lock point. Sooner or later the phase error will exit to a new stable lock point, slipping a number of cycles in the process, during which time the loop is momentarily "out of lock." Such losses of lock occur at some mean rate determined by the loop damping factor, bandwidth, and SNR.

The only information available concerning lock is to be obtained from a synchronous amplitude detector in quadrature with the phase detector. In the ordinary receiver, for example, the AGC detector is often used. The mean output of the quadrature channel (Ref. 9, Chap. 7) depends on the incoming signal level and the loop phase jitter. In addition, however, there are fluctuations about this mean component due to the quadrature component of loop input noise (hence, altogether independent of the loop phase jitter), plus amplitude deviations due to the jittering detector reference. This latter quantity contains the phase error information we seek as to whether the loop is locked or not, but it can be obscured in the former.

For example, at high SNR's, one may discern the rare slippages with high reliability; but at low SNR's, when lost cycles are more common, the task is correspondingly more difficult because of the increased system noise.

A typical lock detector consists of a synchronous amplitude detector followed by a filter, and in turn by a level-comparison device. Ideally, as lock is lost, the amplitude detector response drops sharply, causing the filter output to fall below the threshold level, whereupon there is a loss-of-lock indication. The noise, of course, can cause erroneous indications which can be removed in part by filtering; but filtering also tends to smooth the amplitude fluctuations as well, making it difficult to tell when a single cycle or a consecutive small number of cycles has been lost. There is thus an optimum bandwidth for the filter and optimum threshold for the comparator which will best correlate out-of-lock indications with actual slipped cycles.

As cycles slip, the amplitude detector response is alternately positive and negative, so the filter output will consist of the smoothed version of this alternation, impressed on a decaying exponential, plus filtered noise. If the level comparator is set accordingly, the lock indicator may "clatter" for a while when cycles are skipped, or if the level is raised suitably, may not clatter at all. It is also possible to design the detector so that it will indicate only when a given number of cycles are slipped, whenever it has been decided that slippages less than this number are inconsequential. Both clatter and nonclatter types of detector are discussed in this article.

There are two kinds of errors that a lock detector can make in trying to perform its job: (1) it can indicate that cycles have been slipped when none have (a false alarm) and, (2) it can fail to indicate when cycles have been slipped (a miss). Naturally, the threshold level setting can control which of these two possibilities is most frequently observed. Both are incorrect detections, but one may be more serious than the other, according to the particular application of the loop. In what follows, we shall consider both occasions equally serious, but it will be obvious to the reader that this need not be a limitation of the theory. Concerning the theory, our calculations will be based on a simple mathematical model meant to point out what the important relationships are, rather than to produce precise and accurate design numbers.

2. The Lock Detector and Cycle Slip Model

The lock detector configuration we analyze is schematically shown in Fig. 22. It consists of a synchronous

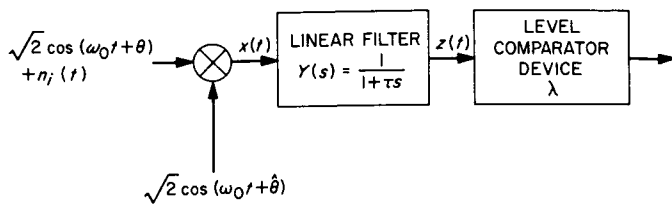


Fig. 22. Synchronous amplitude loop-lock detector.
As cycles are slipped $z(t)$ drops below the threshold λ , indicating lock has been interrupted

amplitude detector followed by a simple R-C filter whose response is

$$Y(s) = \frac{1}{1 + \tau s} \quad (1)$$

in turn followed by a level comparator. The amplitude detector reference is the loop quadrature signal which, of course, is perturbed by the loop phase jitter. Whenever the voltage presented to the comparator falls below a preassigned level λ , there is an unlock indication published by the device.

The input to $Y(s)$, under suitable normalization, takes the form

$$x(t) = \cos \phi + n(t) \quad (2)$$

where ϕ is the instantaneous loop phase error and $n(t)$ is a wideband noise with two-sided density equal to the loop input noise-density-to-signal-power ratio, N_0/A^2 .

During the time the loop is stably in lock, the mean value of $x(t)$ is

$$\begin{aligned} E[x(t) | -\pi < \phi < \pi] &= E[\cos \phi | -\pi < \phi < \pi] \\ &= \cos \phi_0 \end{aligned} \quad (3)$$

for suitably chosen ϕ_0 . Fluctuations away from this mean value are due to $n(t)$ and $[\cos \phi - \cos \phi_0]$, both zero-mean processes in themselves.

As the reference loop slips and relocks after M cycles, the waveform $x(t)$, omitting $n(t)$ for a moment, would appear much like that shown in Fig. 23(a) and the filter output $z(t)$ would resemble that displayed in Fig. 23(b). Mathematically, this output is given by

$$z(t) = \cos \phi_0 e^{-t/\tau} + \frac{1}{\tau} \int_0^t e^{-u/\tau} \cos \phi(t-u) du + N(t) \quad (4)$$

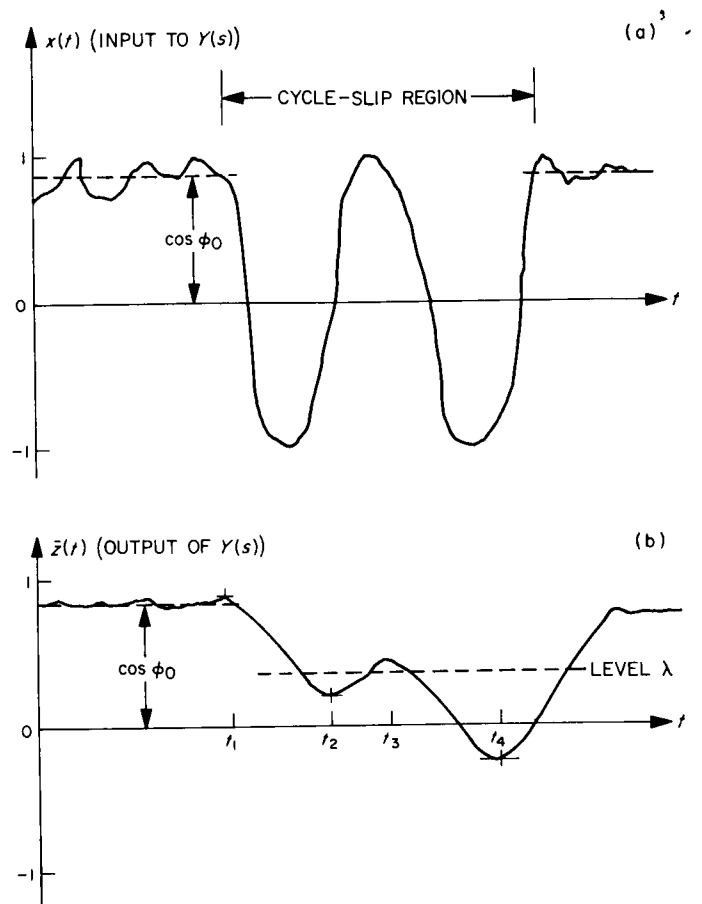


Fig. 23. Typical waveforms in the lock detector during cycle slip. Noises on $x(t)$ and $z(t)$ from the wideband noise component are omitted for clarity. Time constant of the filter and the level λ giving best detection are to be found.

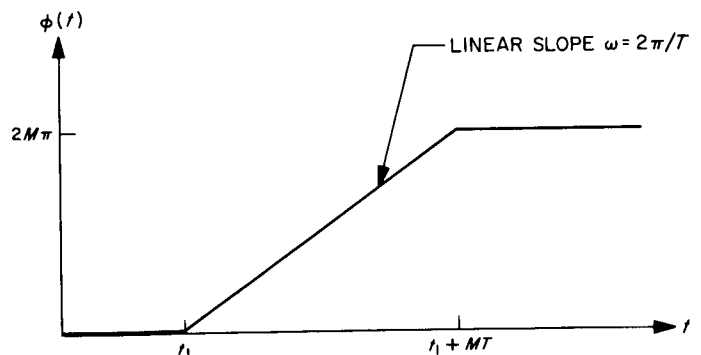


Fig. 24. Simple model for the phase transit from one lock point to another

in which $N(t)$ is a stationary zero-mean process with variance $\sigma_N^2 = N_0 \omega_Y / A^2 = N_0 / 2\tau A^2$.

To develop the behavior of $z(t)$, we need to know how $\phi(t)$ behaves over the slip interval, and to this end we make the assumption that during a slip of M cycles, $\phi(t)$ takes the simplified form shown in Fig. 24—a linear rise from 0 to $2M\pi$ in MT seconds. Some assumption of this sort seems to be necessary in that the actual $\phi(t)$ is the solution to a stochastic differential equation to which analytical evaluations are extremely difficult. Further, we can make T a function of M , of the loop bandwidth w_L , and of the loop detuning to account for the best first-order fit to $\phi(t)$.

Without loss in generality, we can assume the slip begins at $t = 0$, whereupon our model predicts

$$\phi(t) = \omega t, \quad \omega = 2\pi/T, \quad (0 \leq t \leq MT). \quad (5)$$

During the transient then,

$$\begin{aligned} z(t) &= N(t) + \left[\cos \phi_0 - \frac{1}{1 + (\omega\tau)^2} \right] e^{-t/\tau} \\ &\quad + \left[\frac{1}{1 + (\omega\tau)^2} \right] [\cos \omega t + \omega\tau \sin \omega t] \\ &= N(t) + [\cos \phi_0 - \cos^2 \psi] e^{-t/\tau} + \cos \psi \cos(\omega t - \psi) \end{aligned} \quad (6)$$

in which we have chosen $\psi = \tan^{-1} \omega\tau$. The mean behavior $\bar{z}(t)$ of $z(t)$, or the latter terms in Eq. (6) above, has minima and maxima at values $t = t_k$ satisfying the equation

$$(\cos \phi_0 - \cos^2 \psi) e^{-\omega t/\omega\tau} = -\sin \psi \sin(\omega t - \psi) \quad (7)$$

at which times $\bar{z}(t)$ is given by

$$\bar{z}(t_k) = \cos \omega t_k. \quad (8)$$

As one can readily verify from Fig. 23(b), the values $\bar{z}(t_{2k})$ and $\bar{z}(t_{2k+1})$ decrease monotonically in their t_k .

3. Lock-Detector Errors

As we indicated earlier, there are two kinds of errors a lock detector can make: it can fail to indicate a slip when there has been one (a miss), and it can indicate that a slip occurred when in fact none has (a false alarm). The probability that a false alarm occurs is

$$\begin{aligned} P_F &= \text{prob} \{z(t) < \lambda | \text{no slip}\} \\ &= \text{prob} \{\cos \phi + n(t) < \lambda | -\pi < \phi < \pi\}. \end{aligned} \quad (9)$$

We assume that the noise distribution is Gaussian; the model developed in Ref. 9, Chap. 9, shows that there the distribution of $\phi \pmod{2\pi}$ is well approximated by a folded Gaussian density with variance $\sigma^2 = E[\phi \pmod{2\pi}]^2$ for $\sigma^2 < 1$. These assumptions yield

$$P_F = \frac{\int_0^\pi \text{erfc}\left(\frac{\cos \phi - \lambda}{\sigma_N 2^{1/2}}\right) e^{-\phi^2/2\sigma^2} d\phi}{\sigma(2\pi)^{1/2} \text{erf}\left(\frac{\pi}{\sigma 2^{1/2}}\right)}. \quad (10)$$

The functions $\text{erf}(\)$ and $\text{erfc}(\)$ are the well-known Gaussian error functions (Ref. 10 pp. 298–302). The Taylor expansion of $\text{erfc}(x)$ about x_0 is

$$\begin{aligned} \text{erfc}(x) &= \text{erfc}(x_0) \\ &\quad - \frac{2}{(\pi)^{1/2}} \sum_{n=1}^{\infty} \frac{(-1)^n}{n!} H_n(x_0) e^{-x_0^2} (x - x_0)^n \end{aligned} \quad (11)$$

in terms of the Hermite polynomials $H_n(x)$. Inserting $x = (\cos \phi - \lambda)/\sigma_N(2)^{1/2}$, we can approximate P_F by keeping only the first term:

$$P_F \approx \frac{1}{2} \text{erfc}\left(\frac{\cos \phi_0 - \lambda}{\sigma_N(2)^{1/2}}\right).$$

The probability P_M that the detector fails to indicate a slip of M cycles is

$$\begin{aligned} P_M &= \text{prob} \{z(t) > \lambda | \text{slip occurred}\} \\ &\leq \text{prob} \{z(t_{2M}) > \lambda | \text{slip occurred}\}. \end{aligned} \quad (12)$$

The bound in Eq. (12) above is merely the statement that the probability with which the detector fails to recognize the slip altogether is certainly less than the probability it failed to detect it when $\bar{z}(t)$ was at its least numerical value, i.e., at the final minimum point $t = t_{2M}$ before relock. And since t_{2M} is the time the detector is most likely to be correct, the bound above is actually a fairly good approximation to P_M ,

$$\begin{aligned} P_M &\approx \text{prob} \{n(t) > \lambda - \cos \omega t_{2M}\} \\ &\approx \frac{1}{2} \text{erfc}\left(\frac{\lambda - \cos \omega t_{2M}}{\sigma_N(2)^{1/2}}\right). \end{aligned} \quad (13)$$

Both the error probabilities are approximated by the complementary error function.

Arbitrarily, the threshold λ and time constant τ can be set to give any desired apportionment to P_F and P_M , but here we shall set $P_F = P_M$ by requiring

$$\lambda = \frac{1}{2}(\cos \phi_0 + \cos \omega t_{2M}). \quad (14)$$

The corresponding error probability is then approximately equal to

$$P_e = P_F + P_M = \operatorname{erfc} \left(\frac{\cos \phi_0 - \cos \omega t_{2M}}{2\sigma_N(2)^{1/2}} \right). \quad (15)$$

Values of $\cos \phi_0$, σ^2 , and the loop SNR ρ are related by

$$\cos \phi_0 = e^{-\sigma^2/2}$$

$$\rho = \frac{A^2}{N_0 \omega_L} = \frac{1}{\sigma} \left(\frac{2}{1 - e^{-2\sigma^2}} \right)^{1/2}$$

$$\sigma_N^2 = \frac{N_0}{2\tau A^2} = \frac{1}{2\tau \omega_L \rho}. \quad (16)$$

The first relation in Eq. (16) is straightforward evaluation of Eq. (3) assuming a folded Gaussian distribution for $\phi \pmod{2\pi}$, and $\sigma^2 < 1$; the second is a linear spectral approximation (Chap. 9 of Ref. 9) to ρ based on a first-order loop (the result is very good for second-order loops as well). The error probability depends solely on the argument of Eq. (15),

$$\frac{\cos \phi_0 - \cos \omega t_{2M}}{2\sigma_N(2)^{1/2}} = \frac{1}{2}(\cos \phi_0 - \cos \omega t_{2M}) \left[\left(\frac{\omega_L}{\omega} \right) (\omega\tau\rho) \right]^{1/2}. \quad (17)$$

For a fixed value of σ^2 , we can find the value of $\omega\tau$ which minimizes P_e by computing the value which maximizes the value

$$V = (\cos \phi_0 - \cos \omega t_{2M}) (\omega\tau\rho)^{1/2}. \quad (18)$$

The error probability is then $P_e = \operatorname{erfc} [1/2 V_{\max} (\omega_L/\omega)^{1/2}]$. Fig. 15 shows how V varies as a function of $\omega\tau$ for various values of σ^2 and M , and verifies that, as a function of $\omega\tau$, V increases with decreasing σ^2 and with increasing M . Note for each pair σ^2, M , there is a rather broad maximum in V . Figs. 26(a) (b) (c) indicate how the optimum value of V , λ , and $\omega\tau$ vary as a function of the loop phase error variance σ^2 . Fig. 26(c) shows that $(\omega\tau)_{\text{opt}}$ is very insensitive to changes in loop jitter, which means that once the

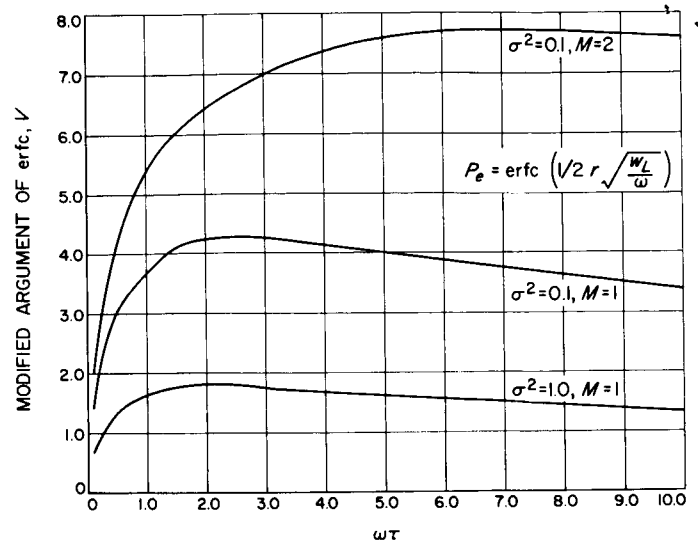


Fig. 25. Behavior of V related to the detector error probability as a function of filter-normalized time constant $\omega\tau$ for several loop jitters σ^2 and cycle-slip designs

loop bandwidth and number of cycles to be detected are given, the filter $Y(s)$ does not need to be further altered to accommodate the particular operating jitter level. The same cannot be said about the threshold, λ_{opt} , however, for as shown in Fig. 26(b), an increased jitter in the loop is best accommodated by a somewhat lower comparator threshold.

As one might expect, Fig. 26(a) indicates that the detector failure probability is much decreased at low loop errors, and decreases even more when the detector is designed to catch multiple slips only.

4. Detector Clatter

Considering a typical trajectory such as that shown in Fig. 23, the value $\bar{z}(t_{2k})$ may lie below the comparator level λ , but the next value $\bar{z}(t_{2k+1})$ may rise above λ ; such an event would cause the detector to switch back and forth between unlock and lock indications (i.e., the detector would clatter). The value of λ can be raised to avoid this phenomenon at a corresponding increase in the false alarm probability and decrease in miss probability.

For a detector designed optimally to catch slippages of M or more cycles, it is found through computation of the minima and maxima $\bar{z}(t_k)$, that there is never more than one switchback whenever $M \geq 2$, and for many M this switch is absent altogether. For other values of M , the

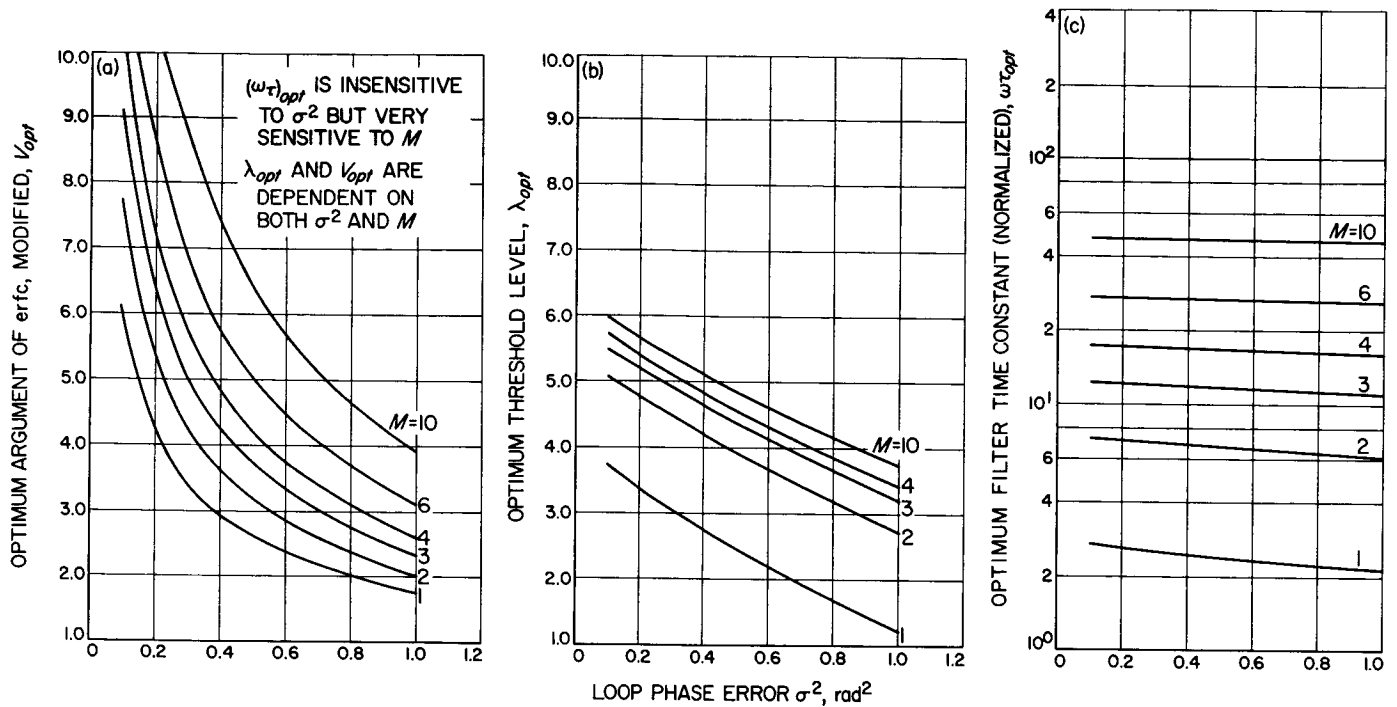


Fig. 26. Variation of the optimized error probability argument V_{opt} , the threshold level λ_{opt} , and filter-normalized time constant $(\omega\tau)_{opt}$ as a function of loop phase jitter σ^2 . Sharp rise of V_{opt} at small σ^2 indicates very reliable operation at these phase-error levels

switch disappears for smaller values of σ^2 . And for still other M , there is inevitably one switchback. For most cases where there is a switchback, the value of λ needs only to be raised slightly above λ_{opt} to dismiss the clatter.

The worst case that could occur corresponds to the instance in which $\bar{z}(t_{2k}) = \lambda_0 - \epsilon$, for some k and very small ϵ . By Eq. (6) the largest amount λ would have to change to remove clatter would then be

$$\Delta\lambda = \bar{z}(t_{2k+1}) - \bar{z}(t_{2k}) < 2 \cos \psi - e^{-t_{2k}/\tau} (\cos \phi_0 - \cos^2 \psi) (1 - e^{-\Delta t_{2k}/\tau}).$$

But for $M \geq 3$, Fig. 26(c) shows $\omega\tau_{opt} > 10$; as a result, $\cos \psi$ is small. We may also approximate $\omega\Delta t_{2k}$ by π , and the time that z crosses λ_{opt} by

$$\cos \phi_0 e^{-t/\tau} \approx \lambda_{opt}.$$

Thus we have as a somewhat rough bound on the largest $\Delta\lambda$, the expression

$$\Delta\lambda < (2 - \pi\lambda_{opt})/\omega\tau.$$

As an example, for $M = 3$, Fig. 26 gives $\omega\tau \approx 11$ and $\lambda_{opt} > 0.3$. Hence,

$$\Delta\lambda < 0.1.$$

The largest amount $\bar{z}(t_{2k+1})$ ever exceeds λ_{opt} , given $\bar{z}(t_{2k}) < \lambda_{opt}$, for $M = 3$ by actual evaluation is 0.07.

Since as M gets larger, the value of $(\omega\tau)_{opt}$ increases, the bound $\Delta\lambda$ becomes insignificantly small, and there is little change in P_e for these cases.

5. Conclusions

The optimal lock detector designed to signal bursts of M or more consecutive slipped cycles is nearly clatter-free for $M \geq 2$, having at most one switchback during the entire slip. In those cases where there is a switchback, λ can be raised slightly from λ_{opt} to stop the clatter, and at $M \geq 3$ the maximum change in λ is small enough that P_e is not seriously degraded. The optimum detector time-constant is relatively insensitive to loop phase jitter σ^2 , but does depend on M . The optimum threshold depends not only on M , but on σ^2 as well. Detection becomes very reliable at larger values of M and at small values of σ^2 .

J. Digital Communication and Tracking: Experimental Study of the First-Slip Statistics of the Second-Order Phase-Locked Loop,

D. Sanger and R. Tausworthe

1. Introduction

Cycle slipping in phased-locked loops is an observed phenomenon unaccounted for by linear analyses of the loop. For the first-order loop, Viterbi (Ref. 11) was able to derive an exact expression for the expected time between cycle slips by solving a Fokker-Planck equation for the phase-error distribution function. The extension of this method to higher-order loops has not been forthcoming. Tausworthe (Ref. 12) formulated and solved a differential equation for the mean first-slip of a loop of any order, subject to the evaluation of a conditional expectation, $E[\dot{\phi}|\phi]$. Based on some of the results (Sec. 4c) of this article, he was able to argue that the expectation could be approximated in a certain way, and thus evaluate the mean first-slip time.

This article reports on certain experimental studies performed by digital simulation of the second-order loop equation. From these were obtained: (1) mean time to first-slip, (2) standard deviation of the time to first slip; (3) probability density and distribution of these times; and (4) mean phase error rates at a given phase error value, $E[\dot{\phi}|\phi]$, all examined at several loop signal to noise ratios (SNR) and damping values. Approximate formulas are given for the results, and comparison with the experimental data is presented.

2. The Second-Order Phase-Locked Loop

Let $\phi(t)$ be the phase-error process of a phase-locked loop subjected to a constant frequency offset; it is described by the equation (Ref. 13):

$$\dot{\phi} = \Omega_0 - AKF(p) \left[\sin \phi + \frac{n(t)}{A} \right] \quad (1)$$

where, in the usual model, A is the RMS input signal voltage, K is the open-loop gain, $F(s)$ is the loop filter,⁵ Ω_0 is the VCO frequency offset, $p \equiv d/dt$ is the Heaviside operator, and $n(t)$ is stationary white noise with spectral density N_0 . In this article we treat only the case $\Omega_0 = 0$; a subsequent article will examine the effects of nonzero Ω_0 .

⁵Here $F(s)$ represents the Laplace transform of the filter's unit impulse response. The time-domain filter output then is denoted by the time-operator $F(p)$ operating on the filter input, as in the Heaviside operator calculus, to be evaluated as in Eq. (2).

We denote the loop filter impulse response by $f(t)$. Computationally, the operator notation we have used signifies

$$F(p)y(t) \equiv \int_0^\infty f(\tau)y(t-\tau)d\tau. \quad (2)$$

We shall assume that $f(t)$ is of the form

$$f(t) = F\delta(t) + c(t) \quad (3)$$

where $c(t)$ is continuous on $(0, \infty)$, and the constant F is merely $F(\infty)$.

The system of interest in this report is one whose loop filter is a "perfect integrator" of the mathematical form

$$F(s) = \frac{1 + \tau_2 s}{s} \quad (4)$$

with impulse response

$$f(\tau) = \tau_2 \delta(\tau) + 1, \quad \tau \geq 0. \quad (5)$$

As in Ref. 9 we define

$$r = AK\tau_2^2 \quad (6)$$

whereupon the loop fiducial bandwidth w_L and damping factor ζ are given by

$$w_L = \frac{r+1}{2\tau_2} \quad (7)$$

$$\zeta = \frac{1}{2} r^{1/2}.$$

In the above notation, the loop equation may be written as

$$\begin{aligned} \dot{\phi} &= -\left(\frac{2rw_L}{r+1}\right) \left(\sin \phi + \frac{n(t)}{A} \right) \\ &\quad - r \left(\frac{2w_L}{r+1} \right)^2 \int_0^t \left[\sin \phi(\tau) + \frac{n(\tau)}{A} \right] d\tau \\ &= -r \left(\frac{2}{r+1} \right)^2 \\ &\quad \times \left\{ \left(\frac{r+1}{2} \right) [\sin \phi + N(t)] \right. \\ &\quad \left. + \int_0^t [\sin \phi(\tau) + N(\tau)] d\tau \right\} \end{aligned} \quad (8)$$

in which we have used $N(t) = n(t)/A$ as white noise with two-sided spectral density N_0/A^2 .

It is convenient to express the results as a function of the loop signal to noise ratio ρ , defined as

$$\rho = \frac{A^2}{N_0 w_L}. \quad (9)$$

(The linear loop theory [Ref. 13] estimates $\sigma_\phi^2 = 1/\rho$.)

3. Computer Simulation

The phase-locked loop characterized by Eq. (8) can readily be adapted for simulation on a digital computer by quantizing time in Δ -sec intervals, provided $w_L \Delta \ll 1$. To generate white Gaussian noise, a random number technique [Refs. 13, 14] was used to provide unit-variance, zero-mean, uncorrelated numbers v_m with the proper distribution. Since these samples must represent the value of the noise over a Δ interval, the noise-sample process will have autocorrelation function $R_{vv}(\tau)$

$$R_{vv}(\tau) = \begin{cases} 1 - |\tau|/\Delta & |\tau| \leq \Delta \\ 0 & |\tau| > \Delta \end{cases} \quad (10)$$

and power spectral density $S_{vv}(j\omega)$

$$S_{vv}(j\omega) = \Delta \left(\frac{\sin \omega\Delta/2}{\omega\Delta/2} \right)^2. \quad (11)$$

However, since we want to approximate the density N_0/A^2 over the bandwidth of the loop, we must multiply v_m by $N_0/A^2\Delta$; i.e., compute $N(t)$ at $t = m\Delta$ as

$$N(m\Delta) = \left(\frac{N_0}{A^2\Delta} \right)^{1/2} v_m = v_m/(\rho w_L \Delta)^{1/2}. \quad (12)$$

Further, we may normalize the time axis by w_L , or equivalently, set $w_L = 1$, without loss in generality. Then Eq. (8) is approximated by

$$\begin{aligned} \dot{\phi}_n = & -b^2 r \left\{ b^{-1} [\sin \phi_n + v_n/(\rho\Delta)^{1/2}] \right. \\ & \left. + \Delta \sum_{k=0}^n [\sin \phi_k + v_k/(\rho\Delta)^{1/2}] \right\} \end{aligned} \quad (13)$$

with $b = 2/(r+1)$ for convenience. Notice in Eq. (13) that $\dot{\phi}_n$ depends not only on past ϕ_k , but also on the present

value ϕ_n . Knowing $\dot{\phi}_n$ and ϕ_n , we may then compute ϕ_{n+1} as

$$\phi_{n+1} = \phi_n + \dot{\phi}_n \Delta, \quad (14)$$

and iterate until $|\phi| \geq 2\pi$. From this the slip time and $\dot{\phi}$ versus ϕ information are available.

4. Experiments

The following experiments were performed for values of Δ from 0.01 to 0.1 (the latter being used for the high SNRs) for all combinations of the parameters ρ and r .

$$\rho = 0.5, 1, 2, 3$$

$$r = 2, 4, 10, 1000.$$

In each case, ϕ was allowed to wander until its magnitude equalled or exceeded 2π ; at this point the loop had slipped one cycle; ϕ was then reset to zero and the process repeated until a total of 1000 slips had been computed.

a. Mean-time to first slip

The mean first-slip time T , is plotted in Fig. 27 as a function of ρ for various values of r along with the approximate theoretical results given in Ref. 9. There appears to be the same type of discrepancy between theoretical and experimental values for each value of r although its magnitude varies with r : the difference between theoretical and experimental values of T increases as T increases. This is probably due to the prolonged effect of estimating ϕ_{n+1} from $\dot{\phi}_n$ and ϕ_n for extended periods of time. Since the number of computations made when T is large is greater than when T is small, the slight errors made in estimating ϕ_n tend to accumulate, causing greater discrepancy between actual and simulated loop cycle slippage. A loop with $r = 1000$, for all practical purposes, is the same as a first-order loop, so the slip time of the actual loop should coincide with the upper curve in Fig. 27. The fact that our simulation produced answers somewhat less is an indication of the magnitude of the iteration error. It is interesting to note that at $r = 4$ (corresponding to critical damping of the loop) there is practically no iteration error; but for $r > 4$, errors tend to be away from the lock-point (shorter slip time measured) whereas for $r < 4$ the errors tend to be toward it (longer slip times measured). This type of error is typical of attempts to solve differential equations using numerical techniques and digital methods (Ref. 15).

b. Probability density and distribution. The measured first slip time t , for each pair of parameters (ρ, r) was

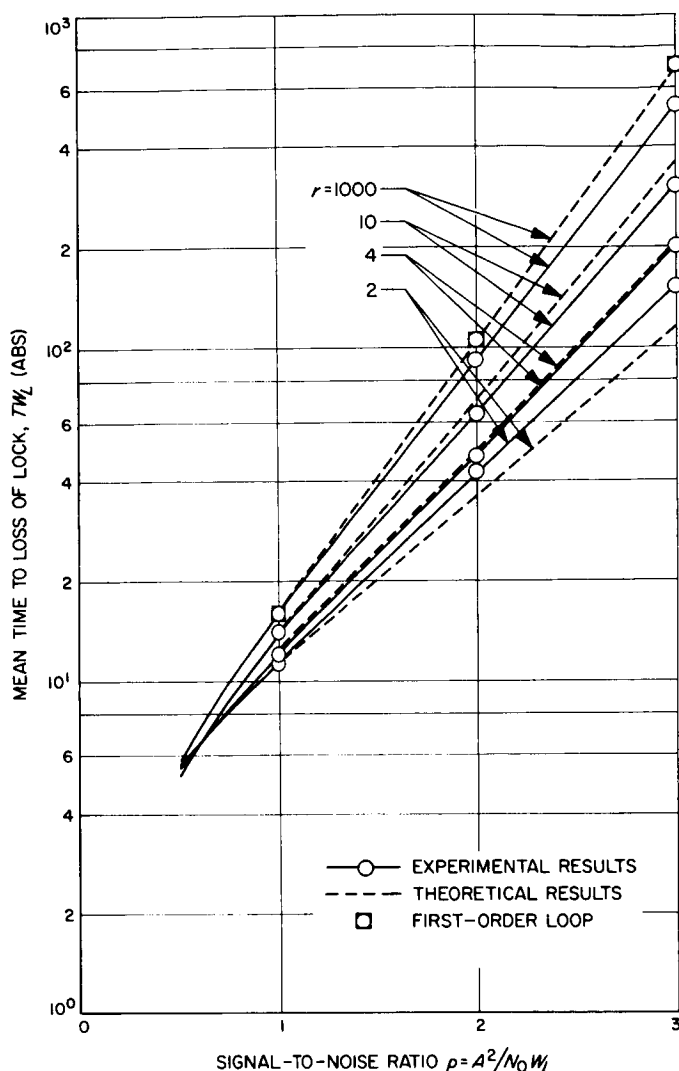


Fig. 27. Variation of mean first-slip time T_{wL} of second-order loop as a function of loop-signal-to-noise ratio ρ and the damping parameter $r = AK_{T_{\frac{1}{2}}}^2$.

normalized by its average measured value T , discussed in Part *a* above, and arranged into probability densities as shown in Fig. 28. Since the densities were relatively insensitive to variations in loop damping (i.e., to r) for a given SNR, the plots in Fig. 28 are composite densities of $r = 2, 4, 10, 1000$ at each SNR value. In addition to the experimental density, Fig. 28 also shows a fit to the gamma-density function (Ref. 17).

$$p(x) = \frac{a^a x^{a-1} e^{-ax}}{\Gamma(a^2)} \quad (15)$$

with $x = t/T$ and $a = T/\sigma_t$. The mean-to-standard-deviation ratio a , used in each of the plots, was derived

from the data. In computing the factor a , the measured T/σ_t ratio was averaged over $r = 2, 4, 10, 1000$ at a fixed SNR. There is a remarkable fit between the two plots on each graph, especially at the higher values of loop SNR. Fig. 29 illustrates the way the measured parameter $a = T/\sigma_t$ varies as a function of the damping parameter r . It is noteworthy that as the loop SNR increases, the T/σ_t ratio nears unity, which would lead to a Poisson fit by Eq. (15).

$$p(x) \rightarrow e^{-x}. \quad (16)$$

Integrating each curve in Fig. 28 yields the probability distribution function of the first-slip times. All four of these distributions were similar. Thus only a composite distribution was plotted and appears in Fig. 30.

c. Conditional expectation of $\dot{\phi}$. For each (ρ, r) pair, the quantity $E(\dot{\phi}|\phi)$ was measured as a function of ϕ . Each of the experiments showed independence of ρ but a marked dependence on the value of r . Curves of $E(\dot{\phi}|\phi)$ are shown in Fig. 31. As discussed in Ref. 9, the form of $\mu = E(\dot{\phi}|\phi)$ should be independent of ρ , and given by

$$\mu = E(\dot{\phi}|\phi) = -br \sin \phi + B(\phi) \quad (17)$$

where, as in Eq. (13), $b = 2/(r+1)$. Generally $B(\phi)$ is not known; however, the first term in its Taylor expansion was shown to be

$$b_1 \phi = \frac{2r}{(r+1)^2} \phi. \quad (18)$$

Having measured μ , the function $B(\phi)$ of Eq. (17) was experimentally determined as a function of r ; these plots appear in Fig. 32. The linearity of these curves suggests that the approximation

$$B(\phi) \approx b_1 \phi$$

is a surprisingly good one, and further verifies the theoretic results in Ref. 9 which were based on this approximation.

5. Conclusions

The experiments we have performed and reported here indicate the following: (1) The theoretical approximation in Ref. 9 to the mean first slip-time of the second-order loop is a very good one; (2) the probability density on first-slip times very nearly follows the gamma-density, and tends to the Poisson at large loop SNRs, and (3) the expectation $E(\dot{\phi}|\phi)$ is well represented by the sum of a sinusoid plus a linear term in ϕ , as hypothesized in Ref. 9.

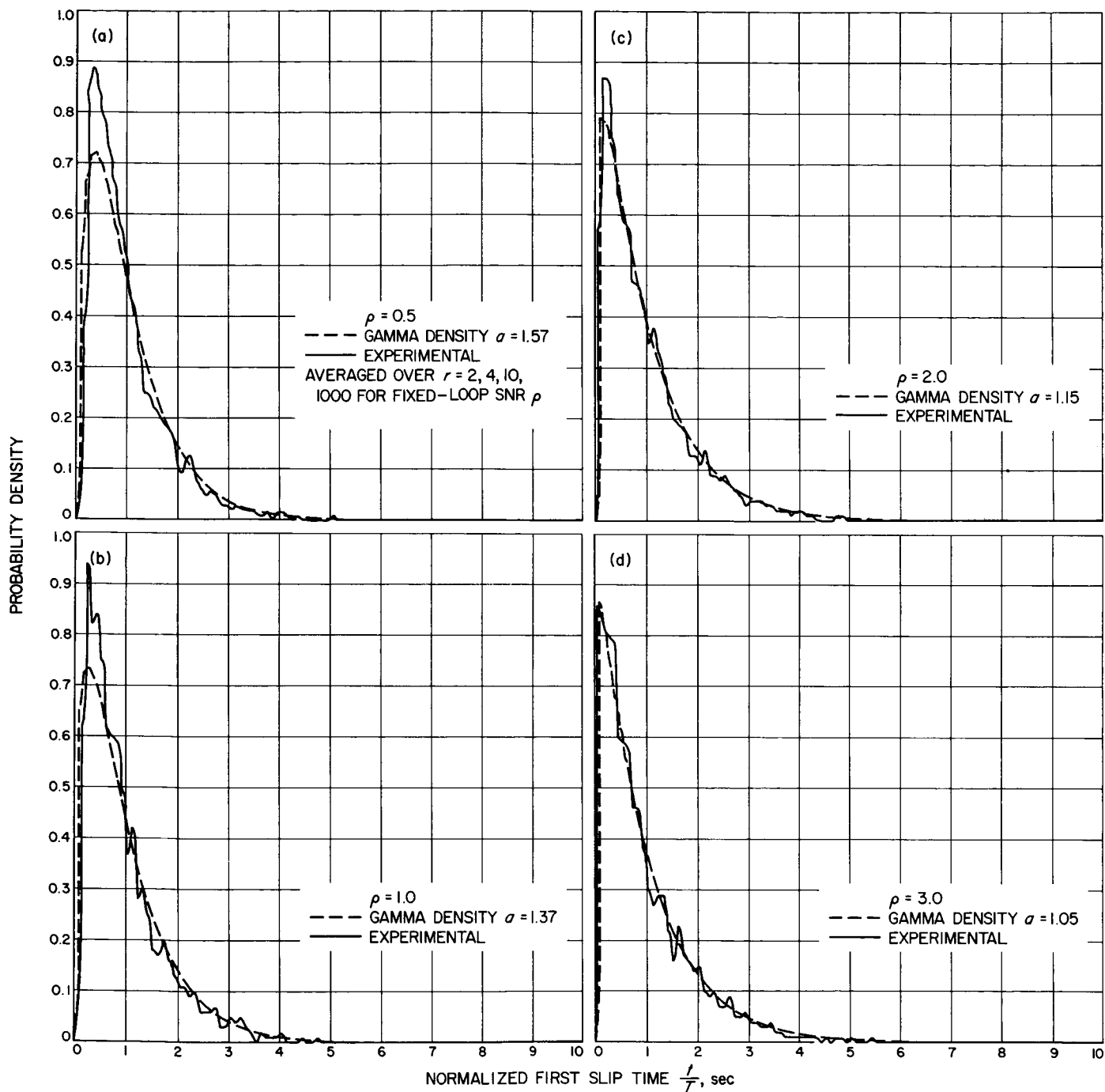


Fig. 28. Probability density of first-slip time of second-order phase-locked loop

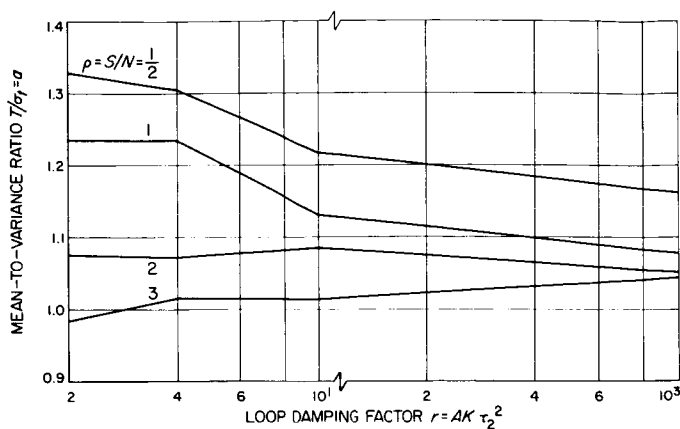


Fig. 29. Variation of average loss of lock time to standard deviation T/σ as a function of damping factor $r = AK\tau_2^2$ for various SNRs, ρ

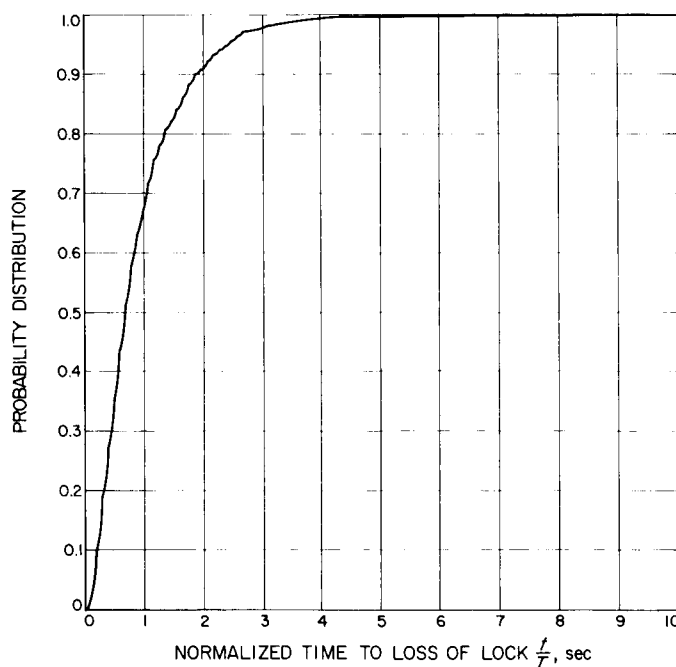


Fig. 30. Probability distribution of first-slip time t_{wL} of second-order loop

K. Ultra-Stable Oscillators: Hydrogen Maser Frequency Standard, R. Sydnor

1. Introduction

The internal electronics of the hydrogen masers has proved to be unreliable and virtually unrepairable. It is being redesigned and repackaged to eliminate these problems.

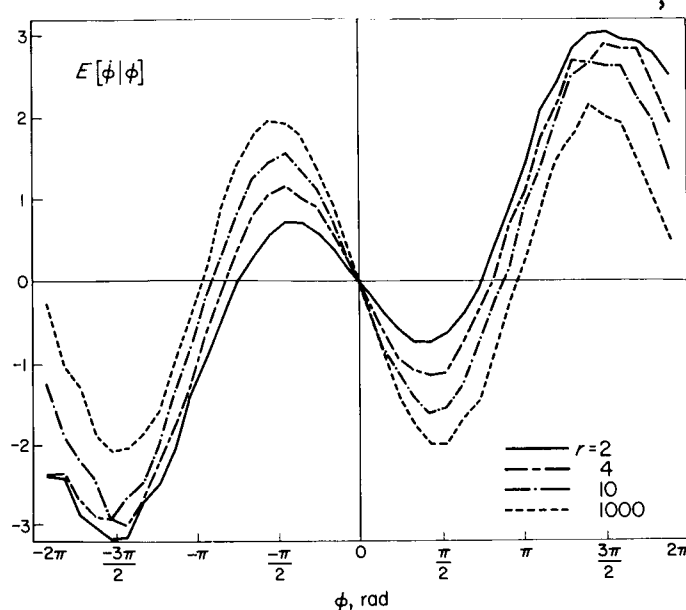


Fig. 31. Experimental plots of $\mu = E(\dot{\phi}|\phi)$ as a function of r

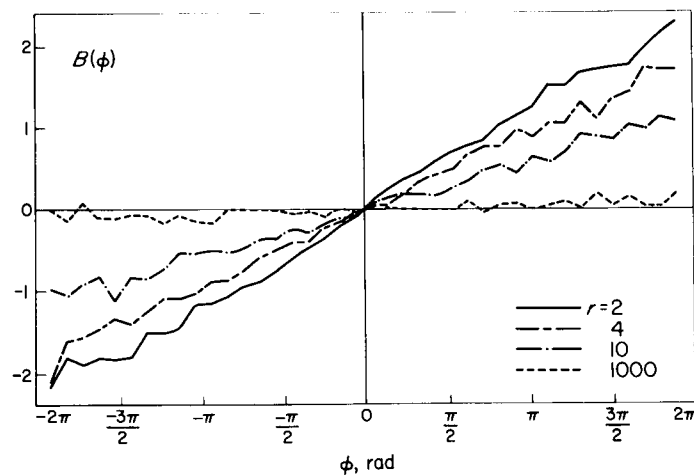


Fig. 32. $B(\phi)$ as a function of r

2. Description of Electronics System

The temperature stability of the maser cavity is of first-order importance in maintaining the maser stability. There are multiple ovens controlling the temperatures of all the nine critical components of the maser. The power supplies are used to power the electronic oven circuitry, the RF source, and the vac-ion pumps. The RF source (vacuum tube) is used to supply the RF power to dissociate the hydrogen. It supplies approximately 20 w at 225 MHz.

3. Goal of Redesign

Many of the failures encountered to date in the maser electronics have been caused by poor design. Repair of the units has been very difficult because of the packaging. For these reasons, the redesign will emphasize reliability, reparability, and ease of trouble-shooting. Insofar as is practical, commercial equipment will be used.

4. Progress in Redesign

a. General. The maser with all associated electronics (with the exception of a ruby maser amplifier, if necessary) is being housed in a rack similar to the DSIF standard. This rack is slightly deeper than the standard rack because of the shape of the maser and is constructed of heavy gauge aluminum to eliminate magnetic field problems.

All power supplies are commercial, all-silicon solid state. The voltages are the same as DSIF standard except for the high-voltage vac-ion pump supplies (5 and 10 kv) and the special regulators described below for the thermistor temperature bridges.

Commercial low-drift operational amplifiers are being used in the temperature-control system rather than temperature controlling the amplifiers as in the original system. This technique allows for improved accessibility for repair and monitoring with no degradation of performance.

b. Bridge reference voltage source. The circuit diagram for this dual regulator is shown in Fig. 33. The circuitry is conventional but, by the use of high-quality components, achieves extremely high performance.

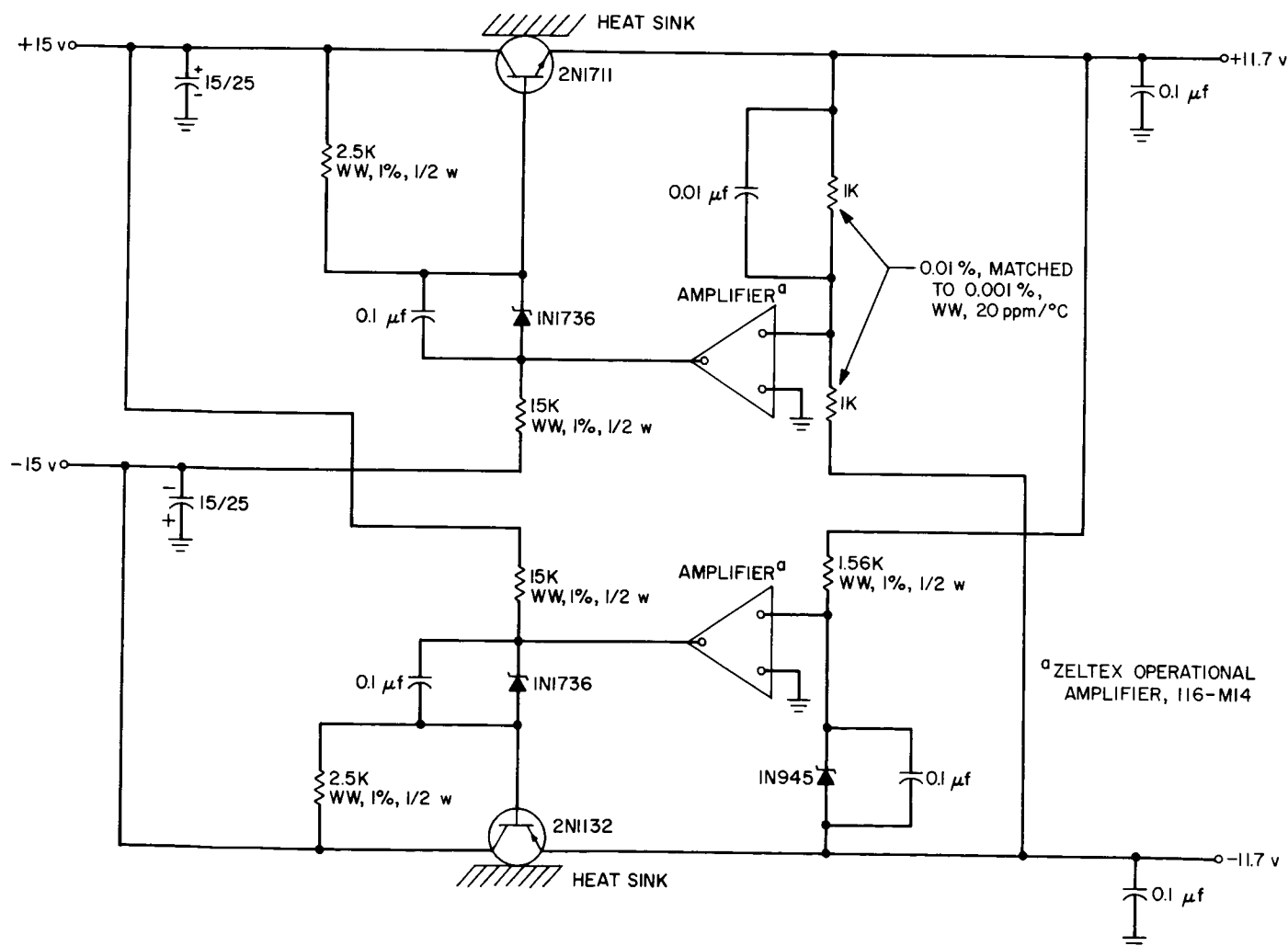


Fig. 33. Bridge reference voltage source

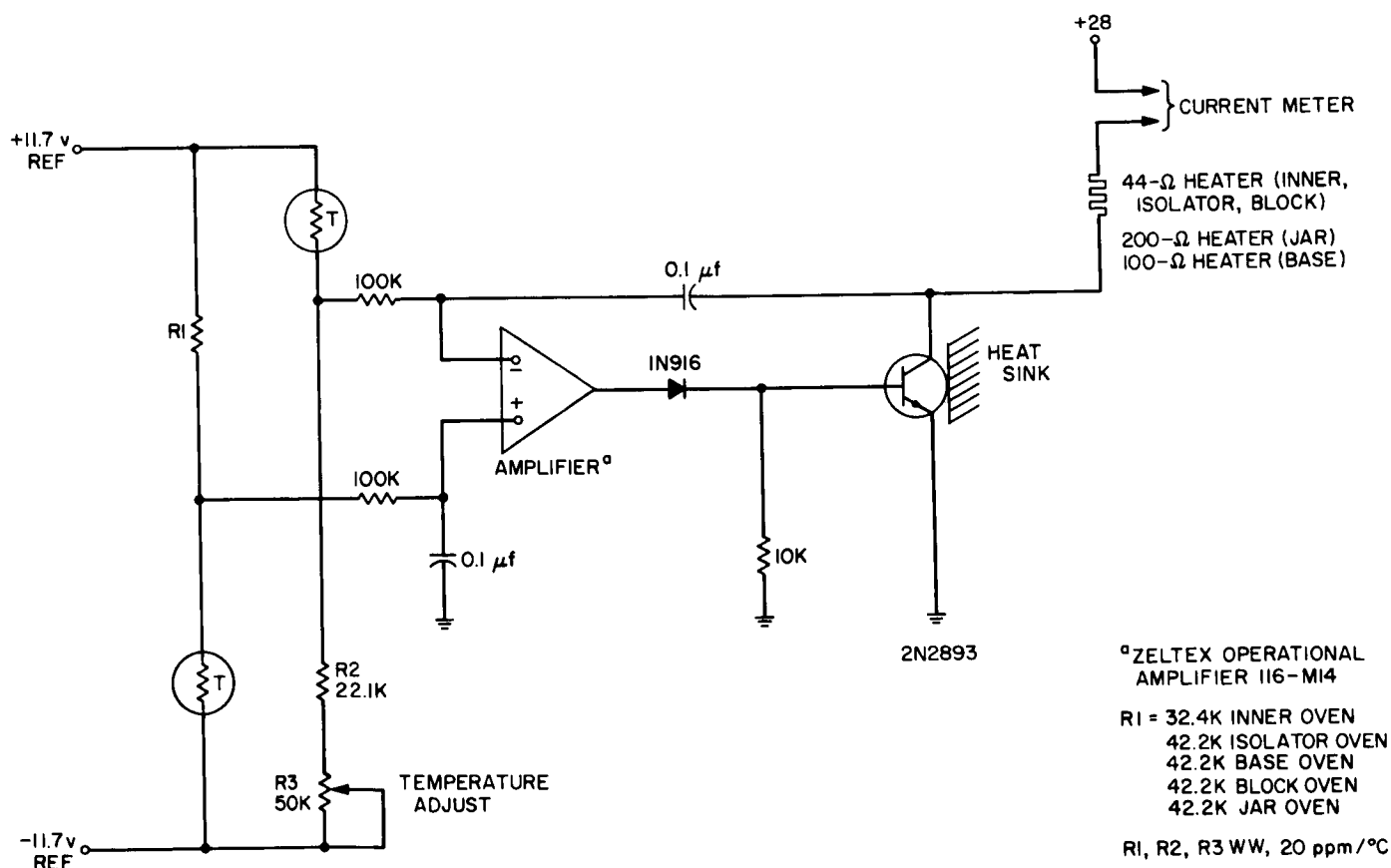
By using a state-of-the-art temperature-compensated zener diode (1N945), operational amplifiers ($5 \mu\text{V}/^\circ\text{C}$), and resistors ($20 \text{ ppm}/^\circ\text{C}$) the theoretical temperature stability is $125 \mu\text{V}/^\circ\text{C}$, i.e., $10^{-3}\%$ / $^\circ\text{C}$. The measured stability is $50 \mu\text{V}/^\circ\text{C}$, i.e., $0.4 \times 10^{-3}\%$ / $^\circ\text{C}$. The DC output impedance is $10^{-3} \Omega$. Isolation from input to output is 100 db. Hum and noise are less than $100 \mu\text{V}$ peak-to-peak, i.e., $0.8 \times 10^{-3}\%$. The supplies track within $10 \mu\text{V}$, i.e., $10^{-4}\%$ over the operating temperature range of 0 to 50°C . It is interesting to note that 90% of the instability with temperature is due to the zener diode; consequently, a simple oven controlling this element alone would improve this supply by an order of magnitude.

No further improvement in the supply is planned, however, since the sensitivity of the bridge-amplifier combinations which it powers have common mode rejection of approximately 60 db, which would produce an *apparent* drift of $50 \text{ nV}/^\circ\text{C}$ due to the power supply drift. This is negligible compared to the stability required in the system, as shown in the following.

c. Temperature controller. There are nine temperature controllers in the original system. They control the temperatures of: (1) the bell jar containing the maser cavity, (2) the neck of the bell jar, (3) the mounting base for the bell jar, (4) the inner structure surrounding the bell jar, (5) the outer structure, (6) the block within which is mounted the pirani gauge part of the pressure-control system, (7) the palladium pressure-control valve, (8) the isolator/directional coupler, and (9) the package within which are mounted the temperature-controlling amplifiers. The redesigned system will use eight temperature control circuits, eliminating (9) above in favor of improved design, insofar as inherent temperature stability of the controller is concerned.

There are three types of temperature control systems: (1) $\frac{1}{4}$ to $\frac{1}{2}$ amp (7.5 to 15 w) systems for preceding items 1, 2, 3, 4, 6, 8; (2) 6 amp (180 w) system for item 5; and the special system for pressure control in item 7.

The circuit diagram of the low-current temperature controllers is shown in Fig. 34. The thermistors used



in[†] the sensing bridge are placed on the particular item to be controlled, as is the heater winding. These thermistors are aged and selected glass bead units which have a good record of stability and reliability. At the operating temperature (40 to 50°C) the bridge sensitivity is approximately 600 $\mu\text{V}/\text{m}^\circ\text{C}$. The effects of instabilities of other parameters are summarized as follows:

Bridge resistors (20 ppm/°C)	0.20 $\mu\text{V}/\text{m}^\circ\text{C}$
Reference supply (as described in Sect. 4 b)	0.000 05 $\mu\text{V}/\text{m}^\circ\text{C}$
Operational amplifier (5 $\mu\text{V}/^\circ\text{C}$ and 1 na/°C)	0.13 $\mu\text{V}/\text{m}^\circ\text{C}$
Sum of variations	0.33 $\mu\text{V}/\text{m}^\circ\text{C}$

Thus, a 1-deg change in ambient temperature would change the temperature of the controlled element by 330/600 m°C, or 0.00055°C. A series of tests of temperature stability is being run to determine if this result is in fact achievable.

The circuit diagram of the high-current temperature controller (for the outer oven) is shown in Fig. 35. This unit is identical to the low-current controller described above, except for the additional high-current booster transistor.

The pressure-control system is shown in Fig. 36. The thermistor pirani gauge is cooled by the hydrogen gas in the system at a rate dependent on the density of gas molecules, i.e., the gas pressure. The resulting resistance change is sensed by amplifier A1 as a voltage change which is used to control the temperature of the palladium valve. The rate of flow of hydrogen through the valve is controlled by the valve temperature so that the pressure inside the system as measured by the pirani gauge is held constant. In order to adjust the pressure, the heating power to the pirani gauge bridge supplied by the constant current amplifier A2 and inverting amplifier A3 is adjusted with potentiometer R2. The additional amplifier A4 is used to monitor the bridge unbalance, and thus indicate changes in pressure. At the normal operating

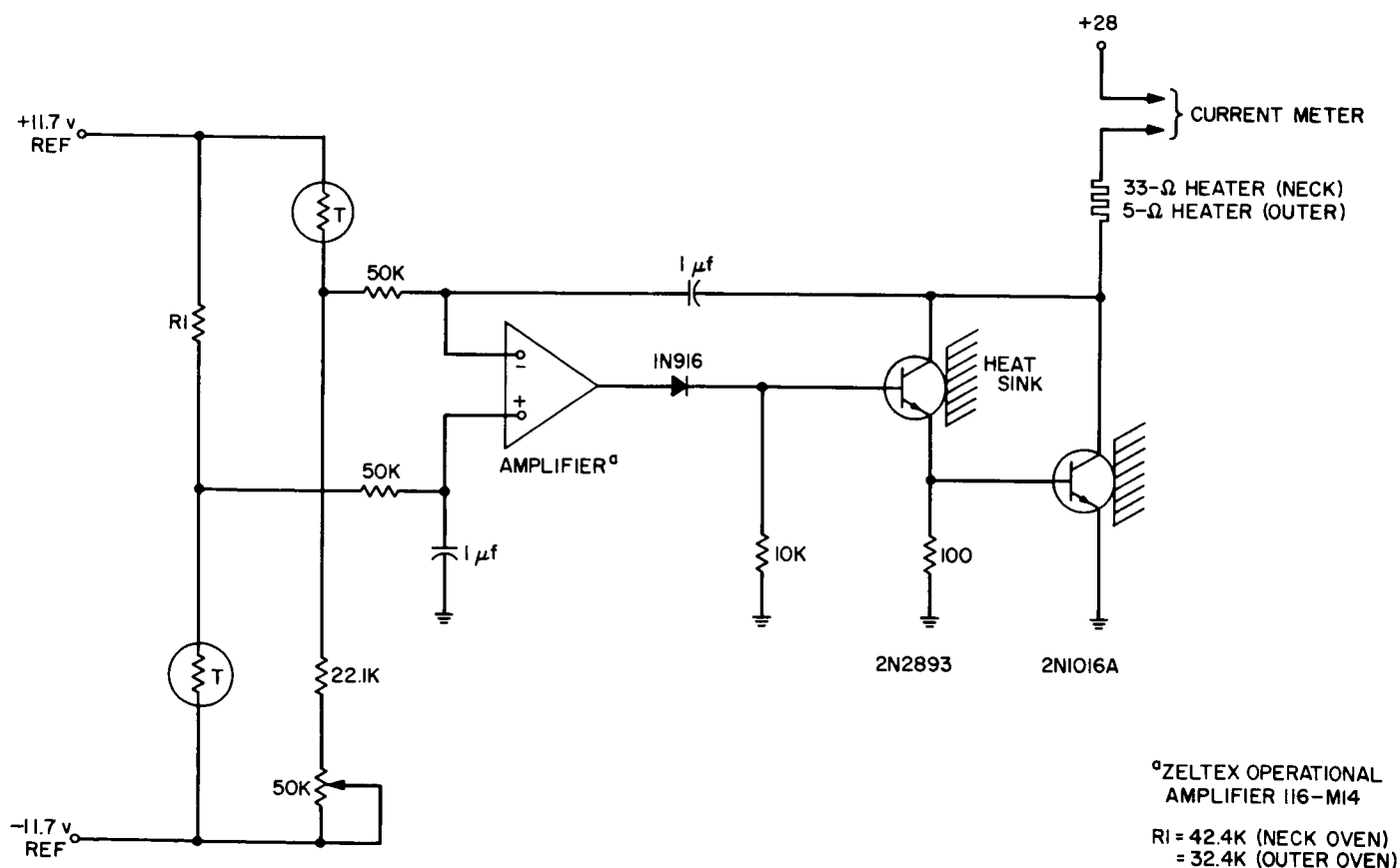


Fig. 35. High-current temperature controller

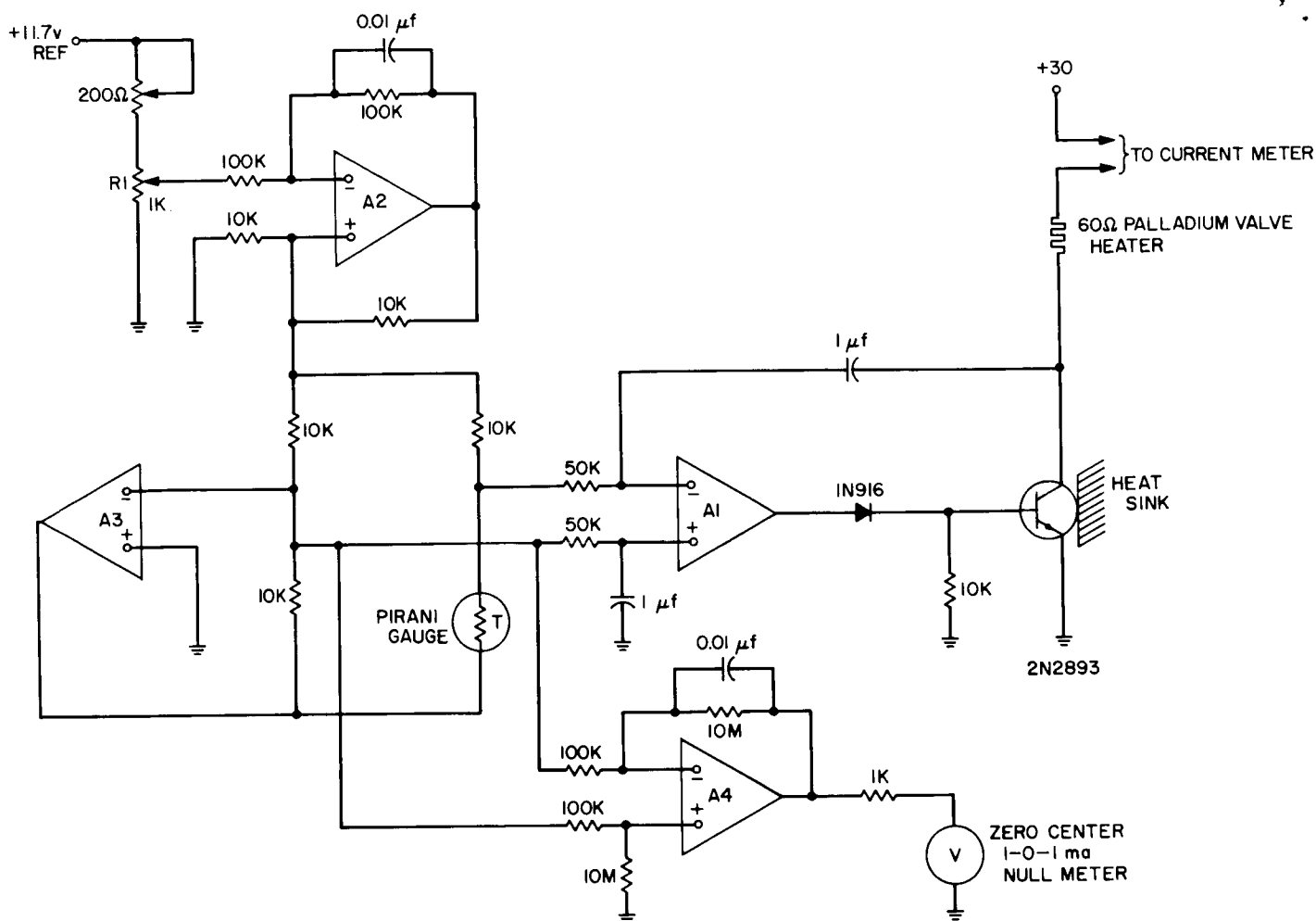


Fig. 36. Pressure-control system

pressure of approximately $60 \mu\text{m}$ of Hg this system should hold the pressure to within $0.02 \mu\text{m}$ of Hg. Since the maser, when properly tuned, does not change frequency when pressure is varied, such a pressure change has no effect. If the maser is mistuned by as much as 10×10^{-13} , such a pressure change would change the frequency 10×10^{-17} , which is negligible compared to other effects. This circuit is an improvement over the original in that the stability is improved by approximately one order of magnitude and the recovery time is shortened by an order of magnitude, thus allowing the tuning to be performed in a much shorter time.

5. Conclusion

New circuitry for the critical control systems of the maser has been designed. The performance of the maser should be somewhat better with the new circuitry. Main-

tainability and reliability have been stressed in order that a field-operable maser may be tested.

L. Frequency Generation and Control: A Digital Frequency and Phase Meter, W. F. Gillmore, Jr.

1. Introduction

The problem considered here is the measuring of the frequency of a pair of sinusoidal voltages and the phase difference between them.

The frequency of each sine wave is considerably less than 1 Hz, and its amplitude is less than 1 v. Most frequency meters and phase meters are not able to measure signals of such low frequency. Special equipment for these measurements is complicated and costly.

A new method which has been developed uses a digital computer to make the frequency and phase measurements. It is designed to give the best possible accuracy for any amount of data which is available. Error due to noise in the data is minimized as much as possible.

2. Method of Computation

Fundamentally, the method used is very simple. First the two signals are sampled and read into the computer. Then the computer fits a sine wave to each set of data by the method of least squares. Frequency and phase are found directly from each of the fitted sine waves. Mathematical details are given below.

Suppose the desired sine wave approximation has the form

$$c_1 \cos \omega t + c_2 \sin \omega t + c_3 \quad (1)$$

where c_1 , c_2 , c_3 , and ω are constants to be determined. The RMS value of the approximation error is denoted by E in

$$\varepsilon = E^2 = \frac{1}{N} \sum_{k=1}^N R_k^2 = \frac{1}{N} \sum_{k=1}^N [y_k - c_1 \cos \omega t_k - c_2 \sin \omega t_k - c_3]^2 \quad (2)$$

Summation index k runs over all N of the data points y_k which are sampled at equally spaced times t_k . The quantity in brackets is called the residual at point k and can be denoted by R_k , as shown. Special values of c_1 , c_2 , c_3 , and ω can be found which minimize E in Eq. (2).

Frequently, a reasonably good approximate value of ω is available and it can be used to advantage. With ω fixed, the three constants c_1 , c_2 and c_3 can be found from the three simultaneous linear equations.

$$\begin{aligned} \sum_{k=1}^N R_k \cos \omega t_k &= 0 \\ \sum_{k=1}^N R_k \sin \omega t_k &= 0 \\ \sum_{k=1}^N R_k &= 0 \end{aligned} \quad (3)$$

These equations come from setting the derivatives of E^2 with respect to c_1 , c_2 and c_3 , respectively, equal to zero.

Values found in this way give the best fit sine wave having a frequency ω .

To further improve the approximation found from Eqs. (3) it is also necessary to adjust the value of ω slightly. This is most easily done by expanding four equations containing c_1 , c_2 , c_3 and ω in a Taylor series about the values found from Eqs. (3). For simplicity, terms higher than first order may be dropped. In matrix form the resulting simultaneous equations are written as

$$\begin{pmatrix} A_{11} & A_{12} & A_{13} & A_{14} \\ A_{21} & A_{22} & A_{23} & A_{24} \\ A_{31} & A_{32} & A_{33} & A_{34} \\ A_{41} & A_{42} & A_{43} & A_{44} \end{pmatrix} \begin{pmatrix} \Delta c_1 \\ \Delta c_2 \\ \Delta c_3 \\ \Delta \omega \end{pmatrix} = \begin{pmatrix} A_{15} \\ A_{25} \\ A_{35} \\ A_{45} \end{pmatrix} \quad (4)$$

Improved values of c_1 , c_2 , c_3 and ω are found by adding the correction terms Δc_1 , Δc_2 , Δc_3 , and $\Delta \omega$ from Eq. (4) to the previous values. Further improvement can be obtained by repeatedly applying correction terms from Eq. (4) and using the last corrected values of c_1 , c_2 , c_3 , and ω to determine the A_{ij} matrix elements at each step. This defines an iterative scheme which might be described as Newton's method in four dimensions.

Matrix elements A_{ij} in Eq. (4) can be expressed in terms of the residuals R_k of Eq. (2). Since Eq. (4) is a symmetrical matrix, it has only fourteen different elements. These are given in Eqs. (5).

$$\begin{aligned} A_{11} &= \frac{1}{2} N \frac{\partial^2 \varepsilon}{\partial c_1^2} = \sum_{k=1}^N \cos^2 \omega t_k \\ A_{12} &= A_{21} = \frac{1}{2} N \frac{\partial^2 \varepsilon}{\partial c_1 \partial c_2} = \sum_{k=1}^N \cos \omega t_k \sin \omega t_k \\ A_{13} &= A_{31} = \frac{1}{2} N \frac{\partial^2 \varepsilon}{\partial c_1 \partial c_3} = \sum_{k=1}^N \cos \omega t_k \\ A_{14} &= A_{41} = \frac{1}{2} N \frac{\partial^2 \varepsilon}{\partial c_1 \partial \omega} = \sum_{k=1}^N \\ &\quad \times [R_k \sin \omega t_k - \cos \omega t_k (c_1 \sin \omega t_k - c_2 \cos \omega t_k)] t_k \end{aligned}$$

$$A_{15} = -\frac{1}{2}N \frac{\partial \epsilon}{\partial c_1} = \sum_{k=1}^N R_k \cos \omega t_k$$

$$A_{22} = \frac{1}{2}N \frac{\partial^2 \epsilon}{\partial c_2^2} = \sum_{k=1}^N \sin^2 \omega t_k$$

$$A_{23} = A_{32} = \frac{1}{2}N \frac{\partial^2 \epsilon}{\partial c_2 \partial c_3} = \sum_{k=1}^N \sin \omega t_k$$

$$A_{24} = A_{42} = \frac{1}{2}N \frac{\partial^2 \epsilon}{\partial c_2 \partial \omega} = \sum_{k=1}^N \left[-R_k \cos \omega t_k - \sin \omega t_k \right. \\ \left. \times (c_1 \sin \omega t_k - c_2 \cos \omega t_k) \right] t_k$$

$$A_{25} = -\frac{1}{2}N \frac{\partial \epsilon}{\partial c_2} = \sum_{k=1}^N R_k \sin \omega t_k$$

$$A_{33} = \frac{1}{2}N \frac{\partial^2 \epsilon}{\partial c_3^2} = \sum_{k=1}^N 1 = N$$

$$A_{34} = A_{43} = \frac{1}{2}N \frac{\partial^2 \epsilon}{\partial c_3 \partial \omega} = - \sum_{k=1}^N \\ \times [c_1 \sin \omega t_k - c_2 \cos \omega t_k] t_k$$

$$A_{35} = -\frac{1}{2}N \frac{\partial \epsilon}{\partial c_3} = \sum_{k=1}^N R_k$$

$$A_{44} = \frac{1}{2}N \frac{\partial^2 \epsilon}{\partial \omega^2} = \sum_{k=1}^N \left[R_k (c_1 \cos \omega t_k + c_2 \sin \omega t_k) \right. \\ \left. + (c_1 \sin \omega t_k - c_2 \cos \omega t_k)^2 \right] t_k^2$$

$$A_{45} = -\frac{1}{2}N \frac{\partial \epsilon}{\partial \omega} = - \sum_{k=1}^N R_k [c_1 \sin \omega t_k - c_2 \cos \omega t_k] t_k$$

(5)

It can be shown that the linear simultaneous Eqs (4) minimize the error in Eq. (2) by setting each of the derivatives of E^2 with respect to c_1 , c_2 , c_3 , and ω equal to zero respectively.

The main reason for using the iterative method for fitting the sine wave to the data is to avoid the necessity for solving nonlinear equations. Eqs. (4) and (5) are easy to program on a digital computer, and they converge to the answer rapidly when the starting values are good. Since arbitrarily assigned starting values, such as zero, usually give poor results, the initial values found from Eq. (3) are essential. When ω is not known, it is best to try a few values in Eq. (2) and begin iterating with the one showing the least error. Values of c_1 , c_2 , and c_3 can be found from Eqs. (3) for each of the ω values tested.

An interesting mathematical similarity exists between the starting Eqs. (3) and the iterating Eq. (4). If one makes the substitutions

$$A_{15} = \sum_{k=1}^N y_k \cos \omega t_k$$

$$A_{25} = \sum_{k=1}^N y_k \sin \omega t_k$$

$$A_{35} = \sum_{k=1}^N y_k$$

$$A_{14} = A_{41} = A_{24} = A_{42} = A_{34} = A_{43} = 0$$

$$A_{44} = 1$$

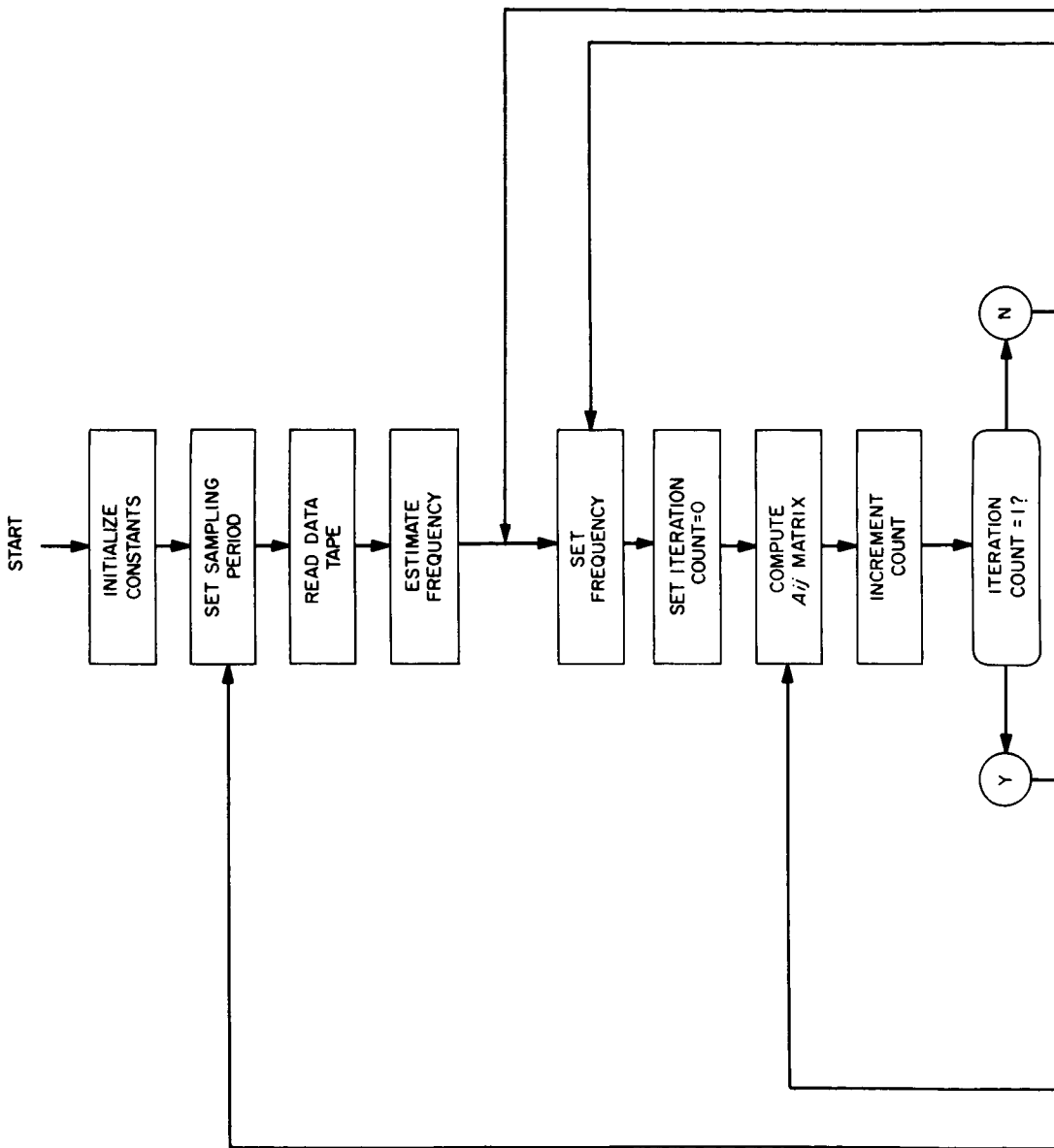
$$A_{45} = \omega$$

(6)

then a solution of Eq. (4) will give c_1 , c_2 , c_3 , and ω — exactly the same values which come from solving Eqs. (3). This similarity can be exploited to simplify the task of programming the computer.

Iterations may be terminated when the correction terms become insignificant, provided that the error is not unreasonably large. When the error remains very large, it often means that the value of frequency being used is faulty. In this case, it is best to start over again with a better estimate of the frequency.

There are two worthwhile advantages that come from using the method of least squares. First, errors in the final results due to any type of noise in the data are minimized.



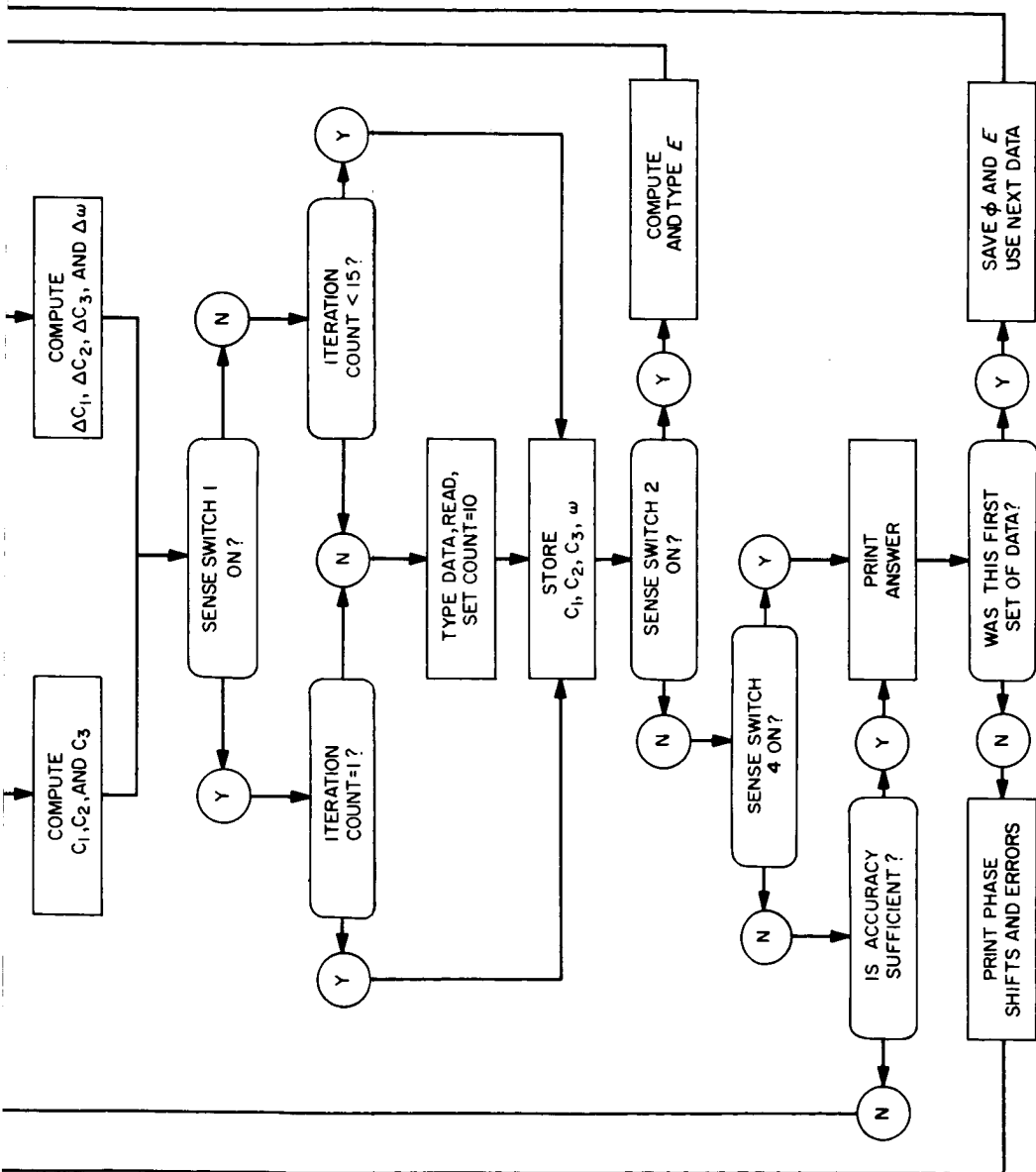


Fig. 37. Block diagram of digital frequency and phase meter program

Second, an answer can be obtained with very little data. Crude answers have even been obtained with less than a full cycle of a noisy waveform. The next section describes the operation of a computer program which carries out the above calculations.

3. Operation of the Computer Program

Input data is available to the computer system in the form of two analog voltages. These voltages are sampled periodically to 11-bit accuracy under control of the computer. In order to maintain constant spacing the sampling is synchronized externally with a frequency standard. This removes any uncertainty in the sampling period due to the variable execution time required for certain parts of the program.

Final answers are printed out by the program on three lines. The first and second lines give the results for the first and second analog voltages, respectively. These answers are in the form

$$y = c_3 + D \cos(\omega t + \phi) \quad (7)$$

Since constants D and ϕ are defined as

$$D = (c_1^2 + c_2^2)^{1/2} \quad \phi = -\tan^{-1} \frac{c_2}{c_1} \quad (8)$$

the expression in Eq. (7) is equivalent to that in Eq. (1).

Four useful constants are given on the last line. The first two are the phase shifts in degrees at frequency ω corresponding to half the sampling period and to the difference in phase between the two analog voltages. Next the two errors are given to indicate how well the approximations on lines one and two matched the analog signals. At the extreme right of the three lines are given the frequency of the two voltages and the average frequency, respectively.

A flow chart showing the operation of the program is given in Fig. 37. As soon as the program is loaded into the computer, it asks for the sampling period. After this has been typed, the data is read in. As the data is being read, the computer counts zero crossings. A rough estimate of the frequency is typed out after the last pair of samples has been checked. At this point the frequency which is to be used for starting the iterative calculations must be typed.

There is a simple method available for checking any value of frequency. First, sense switch 1 is set. Then, when the computer stops, the frequency to be checked is typed. This frequency is used to find c_1 , c_2 , c_3 and the RMS error E . The computer types E and then waits for the next value of frequency to be typed. After a few frequencies have been tried in this manner, the one producing the least error E can be selected as a suitable starting value. If sense switch 1 is reset to its normal off position when this frequency is typed, the computer will begin iterating with this as a starting value.

Normally, about eight iterations are enough to compute the final answer. If the error is still too large after fifteen iterations, the program will stop and ask for help. Two lines are typed. The first lists c_1 , c_2 , c_3 , ω and E , while the second lists Δc_1 , Δc_2 , Δc_3 , $\Delta \omega$, and the determinant of the system of simultaneous Eqs. (4). At this point corrected values of c_1 , c_2 , c_3 , and ω may be typed in and the computer will resume seeking the answer. Setting sense switch 2 has the same effect as exceeding 15 iterations in forcing the computer to stop for help.

It is possible for the data to be so bad that a sine wave cannot be fitted to it. When this occurs, nothing can be done to help the program reduce the error E . In order to print out the current value of all the constants and proceed to the next case, it is merely necessary to set sense switch 4.

Any machine having Fortran capability can run the program described above. Originally, the system was set up with a PB-250 and M-III Multiverter simultaneously sampling and punching out the samples on paper tape. This data tape was read by the main computer program described above on another computer, the SDS-920 or SDS-930. It was convenient to do this because it made the best use of available computer time. As it stands, the system can handle up to 1200 samples of each analog waveform.

The PB-250 sampling program is extremely easy to use. It starts when letter T is typed and stops when the breakpoint switch is depressed. The equipment can be left unattended, except possibly for changing reels of paper tape.

4. Results and Conclusions

In general, the accuracy which can be obtained with this digital frequency and phase meter system depends upon the noise which is present in the original waveform. Perfect data can give up to eight significant figures on each of the output quantities. Longer data runs tend to give

greater accuracy when the frequency and phase are steady.

A typical data run of a few hundred samples will give three or four significant figures on frequency and phase. It will require between six and ten iterations, depending upon the accuracy of the starting values. Each iteration will take 10 to 15 sec on an SDS-920 or 1 to 2 sec on an SDS-930 computer.

The method described here is superior to many others for measuring frequency and phase. It uses computer equipment which is already available and does not require elaborate and expensive frequency and phase meters. It also makes the maximum use of all available data. By the method of least squares one is assured of getting the best possible result with whatever amount of noise is present in any given number of samples.

M. Frequency Generation and Control: *Mariner Venus 67* Ranging, G. U. Barbani

1. Introduction

With the coming of a ranging measurement using the *Mariner Venus 67* spacecraft signals and the DSIF standard receiver, supplemental RF equipment is required. This report will confine itself to the development of two such modules, and will depict important mechanical alterations and electronic performance. A new mechanical module design has been initiated to adapt DSIF configuration to meet R&D module performance requirements.

A $\times 2$ frequency multiplier and a $\div 2$ frequency divider have been developed to meet the needs of the hardware portion of this experiment.

The objective in this effort is to implement the *Mariner Venus 67* ranging experiment as described in SPS 37-42, Vol. III, p. 71. The functional block diagram, as it appears in SPS 37-42, Vol. III, p. 72, has been further subdivided into three sides. This report will be limited to Side III — the 1.0-MHz loop and frequency synthesizer subsystem.

The development of the two mentioned RF modules has been subjected to a stringent set of electronic and environmental requirements. For simplicity, the data presented will appear in tabular form, dual graphs, etc.

2. Description

Figs. 38 and 39 show the internal construction (covers are removed) typical of both the $\times 2$ frequency multiplier

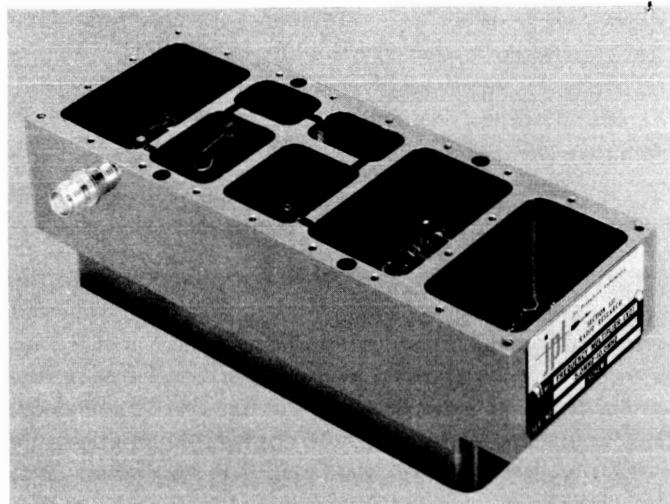


Fig. 38. Top view of $\times 2$ frequency multiplier (5 to 10 MHz)

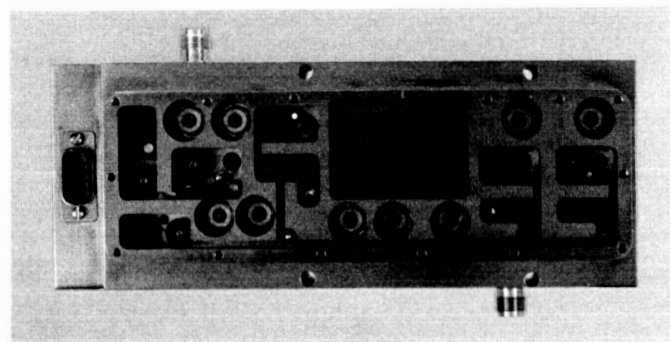


Fig. 39. Bottom view of $\div 2$ frequency divider (1.0 to 0.5 MHz)

(5 MHz $\times 2$) and the $\div 2$ frequency divider (1.0 MHz/2). The external dimensions are the same as the standard DSIF module and are interchangeable in any DSN RF system.

The gold-plated, cavity-type construction employed is a carry-over from the R&D configuration (SPS 37-27, Vol. III, p. 92). The conventional feedthroughs in the signal and power paths have been replaced by slots and channels, thus eliminating access holes and plugs. Both modules have low RFI leakage, excellent isolation, and good thermal stability.

The frequency generation process for both modules appears in Fig. 40. The circuits used are input impedance matching, limiter-amplifiers, synchronous oscillator, crystal filter, and low-noise transistor amplifiers. There are no special components such as matched pairs, selected values,

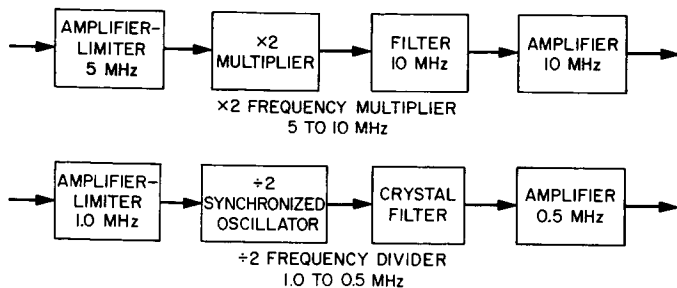


Fig. 40. Block diagram of typical frequency generation

or critical tuning elements. The electronic measurements taken include an input impedance measurement, limiting characteristics, power supply variations, isolation, harmonic distortion, stability, spurious signals, noise density, RFI leakage, and a temperature test.

The input impedance was measured from the +3 dbm level to +13 dbm. Fig. 41 shows the impedance values and the VSWR limits as a function of input level.

The limiting curves of Fig. 42 show the dynamic range of each module. The $\times 2$ frequency multiplier demonstrates a flat response of about 10 db while the $\div 2$ frequency divider drops off quickly. This is caused by the lack of RF drive for the synchronous oscillator. Since this module is in the reference channel, it is desirable to have strong synchronization to its internal oscillator.

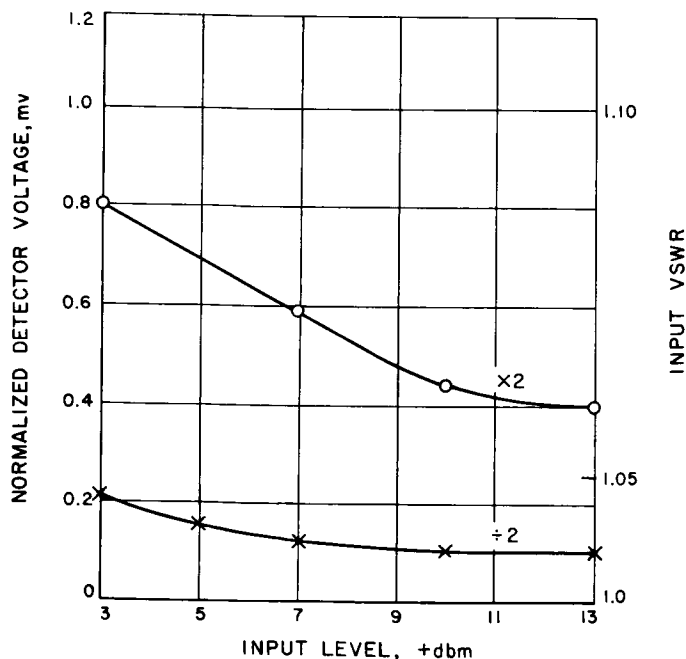


Fig. 41. Input impedance versus input level

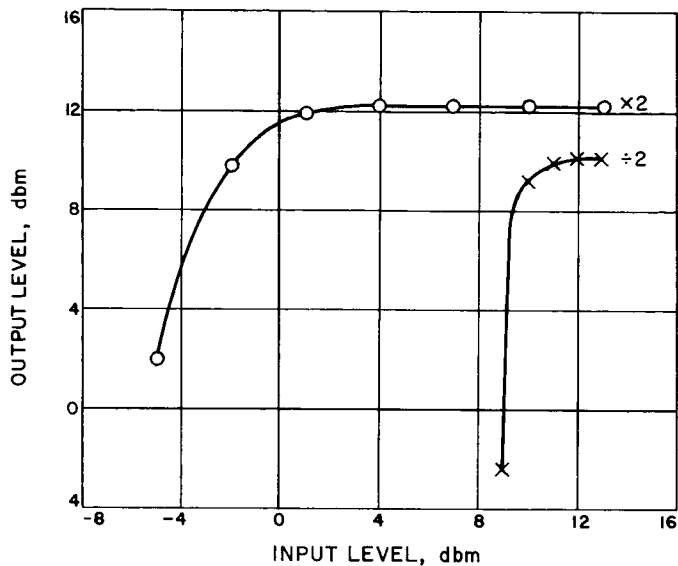


Fig. 42. Limiting characteristics

No extraneous oscillations are induced by any combination of loads, opens, or shorts on the input and output terminals. There is no evidence of any spurious signals in the band from 0.15 to 31 MHz.

The RFI leakage was checked at the input and output terminals, the power line, and all external mechanical junctions for the prime frequencies of both modules.

The modules were subjected to a temperature environment from 0 to 50°C versus output level. Fig. 43 demonstrates the behavior of each. No thermal runaway

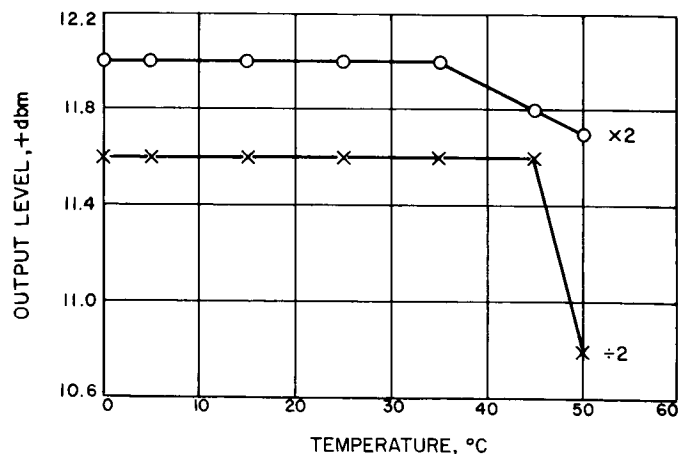


Fig. 43. Environmental conditions

was observed. Other performance data of interest can be located on Table 9.

Table 9. Performance data

Module	Isolation output to input, db	RF leakage, μ v	Noise density, dbm/Hz	Harmonic distortion, %	Power supply variation of $\pm 5\%$, ΔE_0 , dbm	Power drain, w
$\times 2$	> 60	< 0.5	-132	3.40	+0.20 -0.70	0.172
$\div 2$	> 60	< 1.0	-131.7	2.56	+0.50 -0.60	0.102

3. Summary

This has been the first in a series of modules of this type that is designed to meet the DSIF configuration without any sacrifice of performance or compatibility. Based on performance data, it appears that R&D specifications can be met in this configuration.

N. Time-Synchronization System, W. S. Baumgartner, J. R. Smith, M. F. Easterling, R. E. Arnold, E. R. Sato, M. Kron, R. C. Coffin, W. L. Martin, and R. F. Emerson

1. Introduction, W. S. Baumgartner

The DSN stations located around the world are each equipped with a rubidium frequency standard and counting circuits which together provide all frequency, time interval, and time-of-day signals used in the stations. The frequency standards are such that they provide adequate accuracy and stability for the frequency and time-interval signals. However, there is a drift in time of day due to slight frequency inaccuracies of from less than one to approximately 6 μ sec per day. This, plus a certain number of failures, makes it necessary to reset the time of day from the counting circuits occasionally. This process is known as time synchronization, and the objective is to have the time of day at each station the same as that at some master station, e.g., Goldstone DSCC or the National Bureau of Standards. In the past, time transmissions from WWV have been used, and the times of day at the several stations have generally been maintained to agree with one another to within a few milliseconds. The difficulty in obtaining closer agreement is, of course, due to the variable transmission time of radio waves over distances of several thousand miles.

The tracking data requirements for present and future flight projects include a requirement for the time of day

at the several DSN stations to agree to within a few tens of microseconds or less. Since the present methods of time synchronization cannot achieve this, a time-synchronization project has been organized to determine the exact requirements and to devise a system which will meet those requirements.

Ref. 17 investigates the effects of time-synchronization errors and determines that for 1 sec of error the coordinates of a lunar mission near encounter will be in error by 25 km. Ref. 18 establishes the error in lunar gravitational field occasioned by clock resynchronization errors of ± 5 msec. It is shown that for selenodesy studies this error must be reduced by two orders of magnitude, or to 50 μ sec. Ref. 19 shows the effectiveness of simultaneous two-station tracking data in reducing the total tracking time required for a prescribed precision on selenodesy experiments. For instance, the mission requirement on the term C_{30} can be met in 7 hr instead of 31 hr, and the science requirement on C_{20} can be met in 1 mo instead of 1 yr. This two-station data is not acceptable without appreciably better time synchronization than the 5 msec now available. Ref. 20 further investigates the effects of timing bias and shows the effect of a 5 msec bias to be a full magnitude above the visible data noise. These studies clearly demonstrate the requirement for time synchronization throughout the DSN to 20 μ sec and preferably to 5 μ sec. Four major systems for more accurate synchronization were investigated, and it was decided to use coded Moon bounce signals. The other three systems considered, and the reasons they were not selected, will be discussed briefly.

One of the technically most promising methods is the use of the standard DSN ranging system with a spacecraft appropriately equipped. Using this method, a DSN synchronization was accomplished with *Lunar Orbiter I*. A closure of better than 5 μ sec was obtained. At this time, DSS-12 led DSS-41 by 1288 μ sec, and DSS-61 led DSS-12 by 267 μ sec. This is substantially outside the acceptable tolerances. To accomplish this it is required that a spacecraft be in view and that it be available to the DSN for 1 to 2 hr each day. This is considered administratively impossible. At best, only occasional synchronization could be accomplished rather than on a daily schedule as required. An additional disadvantage is that the entire station, including the major antenna, is tied up during the operation. For these reasons, the use of ranging was not considered feasible.

The use of transportable standards has been proposed and tried. Ref. 21 reports on a 6-day trip through the DSN

stations when synchronization was made by a transportable clock. A closure of 0.8 μ sec was produced, which is acceptable. However, the cost is prohibitive and administrative problems are too complex for frequent DSN-wide trips; consequently daily checks cannot be made.

The use of VLF (from 15 to 60 KHz) signals from NBS has been widely studied and is in limited use. VLF signals do not suffer from multiple path problems as do HF signals, and under strong signal conditions accuracies of 10 μ sec are possible. A 20- μ sec diurnal shift occurs on the VLF signal but is repeatable and known. Good VLF signals are received at the Goldstone DSCC; fair VLF signals are received in Australia; but, to date, no useable signal has been received at Madrid. VLF is not sufficiently developed at this time to be reliable for the DSN and has the additional disadvantage of not being entirely under DSN administrative control.

Coded Moon-bounce signals meet all requirements for a satisfactory time-synchronization system. Accuracies of ± 5 μ sec can be obtained; the system is entirely independent of the main station and antenna; the cost is low, operation is semi-automatic; calibration can be provided daily; and the system is entirely under DSN control. An experimental system is now in fabrication, using the existing 10-kw X-band transmitter at the Venus DSS and two receiving systems. The first receiver will be installed at the Echo DSS about seven miles from the transmitter at the Venus DSS in January 1967. The Venus DSS's clock will be used on this receiver via the microwave link, and the system will be checked and calibrated for internal delays. The receiver will then be moved to JPL, and synchronization of a local clock will be demonstrated with checks against the Venus DSS clock via the microwave link. Upon completion of this experiment the receiver will be reinstalled at Echo DSS, and in April 1967 a second receiver will be installed at Canberra. It is planned to demonstrate synchronization over this range in May 1967.

2. System description, J. R. Smith

The experimental precision time-synchronization equipment now being fabricated is a bistatic X-band CW range-gated radar. The transmitted signal is biphase-modulated with a pseudorandom (PN) code, and the received signal is correlated with the same code delayed in time. The two-level autocorrelation function that characterizes the pseudorandom code ensures that energy is detected only when the round trip transit time of the signal from the transmitter to the target and back to the

receiver is equal to the time difference between the code transmitted and the code used at the receiver.

The position of the range gate relative to a radar target is a function of the round-trip distance to the target and the time displacement of the receiver local code model relative to the transmitted code. In the precision time-synchronization experiment, the target is the Moon, the position of which is assumed to be known. (Recent experience with *Lunar Orbiter 1* indicates that the lunar ephemeris may have errors as large as 1 km. This could cause a timing measurement error of about 8 μ sec if the ephemeris error is not removed. A receiver in the vicinity of the transmitter will permit corrections for this and other possible errors.) The phase of the receiver local code is controlled by the receiving station clock. The transmitted code is referenced to the transmitting station clock so that the range gate is positioned ahead of the front surface of the Moon. The range gate is then moved by 1 μ sec (of two-way range) each second until it is positioned somewhat behind the front surface of the Moon. The receiver begins to detect power when the range gate reaches the front surface of the Moon, but since the position of the range gate depends upon the time difference in the two codes (which, in turn, depends upon the difference in the two clocks), the time of day at which signal is first received is a function of the difference between the clocks at the two stations, changing by 1 sec for each microsecond of clock displacement. If the receiving station clock is 10 μ sec behind the transmitting station clock, the range gate will be 10 μ sec beyond where it would be if the clocks were in exact synchronism; and, since the gate is being moved 1 μ sec/sec, it will reach the Moon 10 sec sooner than it would if the clocks were synchronized.

The output of the receiver is recorded on a stripchart recorder along with a timing track containing 1-min and 1-sec marks. The code is controlled at the transmitter so that signals will first appear at the receiver 30 sec after the minute if the two stations' clocks are exactly synchronized. Thus, by locating the 30-sec mark and counting the number of 1-sec marks to the time of appearance of the signal in the receiver, the clock synchronization error can be determined.

An operational time-synchronization system would consist of one transmitting station located at the Goldstone DSCC and one receiving station at each of the other station complexes. The time-synchronization signals can be sent to only one receiver at a time, and then only when the Moon is in view at both the Goldstone DSCC

and the receiving station. In order to service all receiving stations, and to avoid confusion, time-synchronization signals would be sent to a given station on a regular schedule whenever the Moon is in common view. For example, signals might be sent to Madrid DSCC during the thirteenth, twenty-third, etc., minute of each hour that the Moon is above the horizon at both Madrid and Goldstone DSCC.

Since the time-synchronization system can function at a given receiving station only when the Moon is simultaneously in view at that station and the transmitting station, the duration of the common view periods is of much interest and has been examined in some detail. All deep space communications complexes will have common view periods with the Goldstone DSCC of an hour or more duration on most days. However, at the Madrid DSCC and the Johannesburg DSS, there will be several days each month on which the common view period is less than 10 min—at least for the next few years. The duration of the monthly minimum view period for these stations varies with a 19-yr period with the minimum occurring currently.

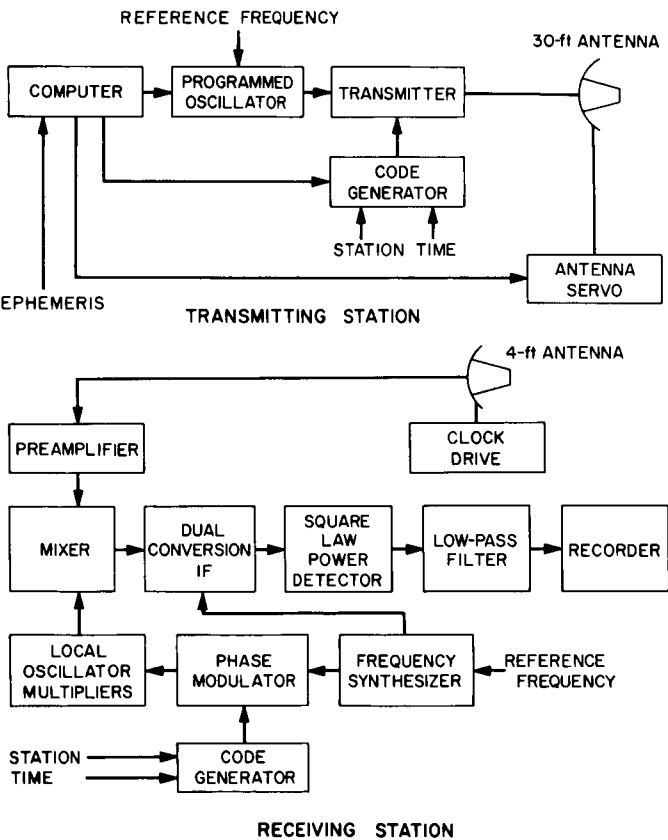


Fig. 44. Block diagram of transmitting and receiving stations

The equipment used is relatively straightforward (Fig. 44). A computer is used to control the transmitting station. Using the lunar ephemeris as an input, this computer determines the transmitter frequency required to place the received signal inside the 10-Hz receiver bandwidth, points the antenna at the Moon, and appropriately manipulates the transmitter code generator.

The receiving antenna is equipped with a variable rate clock drive which keeps it pointed at the Moon throughout a pass. The tunnel diode preamplifier used in the receiver provides for an over-all system temperature of about 670°K. The local oscillator is biphase-modulated by the local code model so that correlation, as well as conversion to the first IF, takes place in the first mixer. All frequencies required in the receiver are derived from a precision frequency reference provided by the station frequency and timing subsystem, so the receiver tuning is fixed at a frequency determined by the station rubidium standard. A square law detector is used so that the receiver output is proportional to the received signal power, and a narrow band (1/10 Hz) low-pass filter is used ahead of the recorder to reduce the jitter in recording.

The initial experiments are designed to:

- (1) Establish the accuracy of the lunar ephemeris, both with respect to range and range rate.

Table 10. Precision time-synchronization experiment equipment specifications

Transmitting station	
Transmitter frequency	8450.1 ± required doppler offset
Transmitter power	10 kw ^a
Transmitter frequency control	Programmed oscillator
Carrier suppression	>45 db
Code period	2.047 msec
Code digit length	10 µsec
Station controller	SDS 910 computer
Transmitter frequency	
Antenna pointing	
Coder control	
Antenna	30-ft parabola, AZ/EL mount
Receiving station	
Receive frequency	8450.1 MHz
Receiver bandwidth	10 Hz
Noise figure	6 db
Antenna	4-ft parabola, HA/DEC mount
^a To be increased to 25 kw during the experiment.	

- (2) Establish the feasibility of controlling the transmitter frequency, antenna pointing, and coder control to sufficient accuracy, with a single computer.
- (3) Verify the link analysis.
- (4) Establish over-all system capability of precisely measuring the time difference between two clocks widely spaced geographically.

3. System analysis, M. F. Easterling

In this section, the power received in a range-gated CW radar with the Moon as a target is calculated, and an expression useful in computing the expected performance of a time synchronization system for the DSIF is derived.

To be most useful in system trade-off studies, the radar equation will be formulated in a particular way. The power intercepted by the Moon P_I is

$$P_I = P_T G_T A_M \frac{1}{4\pi r^2}$$

where

P_T is the transmitted power,

G_T is the gain of transmitting antenna,

A_M is the cross-sectional area of the Moon, and
 r is the range.

If the area of the Moon is written explicitly, the expression becomes:

$$P_I = P_T G_T \frac{\pi R^2}{4\pi r^2}$$

in which the ratio $R^2/4r^2$ can be considered as a transmission loss. The equation then becomes

$$P_I = P_T G_T L_T$$

where $L_T = R^2/4r^2$ and R is the radius of the Moon.

The power returned to the radar can be given by the standard range equation if an efficiency factor is included for the Moon. This expression is

$$P_R = E P_I G_M G_R \frac{\lambda^2}{(4\pi)^2 r^2}$$

where

E is the efficiency factor,

G_M is the gain of the Moon,

G_R is the gain of the receiving antenna, and

$\frac{\lambda^2}{(4\pi)^2 r^2}$ is the space loss (L_S).

For purposes of analysis, the Moon will be considered as an isotropic radiator ($G_M = 1$) and the reflectivity, directivity, scattering law, and the effects of the range gate function are included in the efficiency factor. The efficiency factor will have the form

$$E = \eta \rho F_{RG}$$

where

η is the reflectivity,

ρ is the directivity, and

F_{RG} is the factor that includes the effects of both the scattering law and the range gate.

For the moon, the product of $\eta \rho$ may be taken as 0.075. The derivation of F_{RG} is the main point of this section.

Detailed radar examination of the Moon shows that all parts of the disk are not equally effective in returning power to the radar receiver. To describe this, we note that the effectiveness is a function of the distance from the center of the disk; that is, all parts of a ring concentric about the center of the disk are equally effective. The effectiveness could be described as a function of the radius from the center of the disk, but it is usually described in terms of the angle at the center of the Moon which the radius to the ring subtends. The function which describes the effectiveness is defined over a range of angles from θ to $\pi/2$ and is termed the normalized scattering law. The normalization makes it a density function such that

$$\int_0^{\pi/2} S(\theta) d\theta = 1$$

where

$S(\theta)$ is the normalized scattering law, and

θ is the angle at the center of the Moon.

Thus, if the radar is not range-gated, power is returned from the whole disk, and the efficiency factor becomes

$$E = \eta \rho \times 1.$$

From Muhleman, the normalized scattering law for the Moon is

$$S(\theta) = \frac{2\alpha^2 \cos \theta}{(\sin \theta + \alpha \cos \theta)^3}$$

in which α is a frequency-dependent term that is 0.35 for X-band.

That the range gate effectiveness is also described by a density function is shown by the following argument. Suppose that there were a gate which would admit the power reflected from the entire Moon but no power from either closer or farther away. Such a function would be a constant from $r-R$ to r (assuming that the range is to the center of the Moon) and zero elsewhere. Then

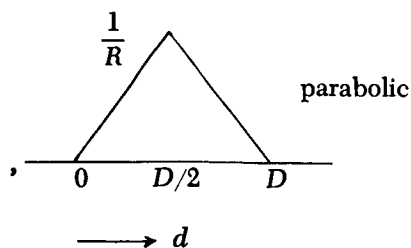
$$S(\theta) P(d) = 1$$

which is descriptive rather than rigorous since the two functions have different arguments. The proper value for $P(d)$ is $1/R$ and

$$\int_{r-R}^r \frac{1}{R} dr = 1.$$

To convolve the normalized scattering law and the range gate function requires that the variable be changed in one of them; we choose to change in the range gate function. This, in turn, requires the actual function.

If a PN range code is used for range gating, the range gate function is the autocorrelation function squared with the $1/R$ normalizing factor. The function looks like:



$$P(d) = \frac{1}{R} \frac{d^2}{(D/2)^2} \quad 0 \leq d \leq D/2$$

$$P(d) = \frac{1}{R} \frac{(D-d)^2}{(D/2)^2} \quad D/2 \leq d \leq D$$

where the gate width D is given by

$$D = \text{speed of light} \times \text{digit period}.$$

The variable may be changed by using the geometry of the Moon as shown in Fig. 45.

Assume that the gate starts at the face of the Moon. Then,

$$\begin{aligned} d &= R - R \cos \theta \\ &= R(1 - \cos \theta). \end{aligned}$$

For very small angles,

$$\begin{aligned} d &= R \left(1 - 1 + \frac{\theta^2}{2} \right) \\ &= R \frac{\theta^2}{2}, \end{aligned}$$

and $dd = R \theta d \theta$.

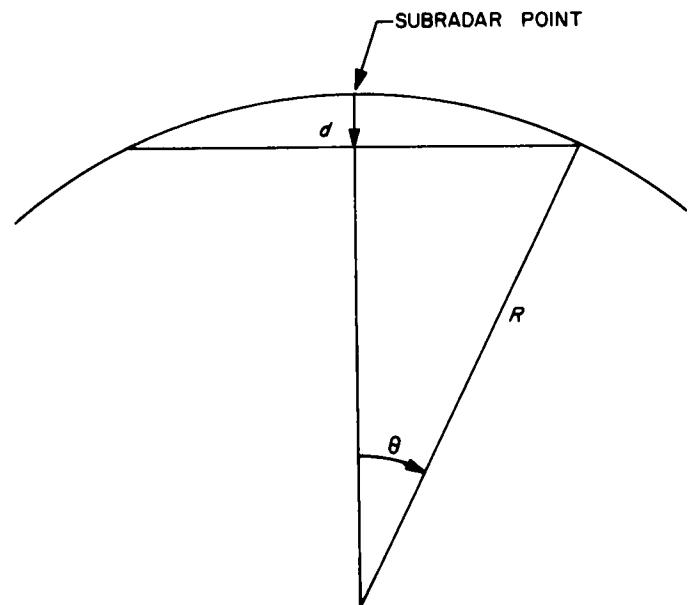


Fig. 45. Cross-section of Moon showing scattering-law geometry

If Φ is the angle corresponding to D ,

$$D = \frac{R\Phi^2}{2}, \text{ or}$$

$$\Phi = (2D/R)^{1/2}.$$

If ψ is the angle corresponding to $D/2$,

$$D/2 = R\psi^2/2, \text{ or}$$

$$\psi = (D/R)^{1/2} = \Phi/(2)^{1/2}.$$

From these expressions and the definition of the normalized scattering law may be obtained

$$F_{RG} = \int_0^{\Phi/(2)^{1/2}} \frac{2\alpha^2 \cos \theta}{(\sin \theta + \alpha \cos \theta)^3} \frac{4\theta^5}{\Phi^4} d\theta \\ + \int_{\Phi/(2)^{1/2}}^{\pi} \frac{2\alpha^2 \cos \theta}{(\sin \theta + \alpha \cos \theta)^3} \\ \times \frac{4}{\Phi^4} (\theta^5 - 2\theta^3 \Phi^2 + \theta \Phi^4) d\theta.$$

Because only small angles are to be considered, the trigonometric functions can be simplified. Also, the first term of the second integral can be combined with the first. The result is

$$F_{RG} = \frac{8\alpha^2}{\Phi^4} \int_0^{\pi} \frac{\theta^5 d\theta}{(\theta + \alpha)^3} + 8\alpha^2 \int_{\Phi/(2)^{1/2}}^{\pi} \frac{\theta}{(\theta + \alpha)^3} \\ - \frac{2\theta^3}{\Phi^2 (\theta + \alpha)^3} d\theta.$$

This expression can be integrated in closed form, but the results lead to difficulties in computation because of taking small differences of several pairs of large numbers. If the integrands are converted to power series and integrated term-by-term, the results are:

$$F_{RG} = \frac{8\Phi^2}{\alpha} \left\{ 0.04166 - 0.0518 \frac{\Phi}{\alpha} + 0.125 \frac{\Phi^2}{\alpha^2} - 0.1529 \frac{\Phi^3}{\alpha^3} \right. \\ \left. + 0.1718 \frac{\Phi^4}{\alpha^4} - 0.5598 \frac{\Phi^5}{\alpha^5} + 3.164 \frac{\Phi^6}{\alpha^6} + \dots \right\}$$

in which the coefficients are given in decimal form for ease of computation. The values of F_{RG} for 10- and 1- μ sec digit periods are 2.829×10^{-3} (-25.5 db) and 3.092×10^{-4} (-35.1 db), respectively.

For computational purposes, it is convenient to write the over-all radar equation as

$$P_R = P_T G_T L_T G_M (\eta \rho F_{RG}) L_S$$

Using this formula, the expected system performance can be calculated.

Parameter		Timing system
P_T	10 kw ^a	+70.0 dbm
G_T	30 ft	+56.0 dbm
L_T		-52.9 db
G_M		0.0 db
G_R	4 ft	+38.5 db
$\eta \rho$		-11.3 db
F_{RG}	10 μ sec	-25.5 db
L_S		-223.3 db
P_R		-148.5 dbm
K		-198.6 dbm sec/deg
T	670°K	+28.3 db/deg
B		+10.0 db/sec
P_N		-160.3 dbm
SNR		+11.8 db

^aThis is to be increased to 25 kw during the experiment.

The radar receiver heterodynes the received signal to some low frequency and passes it through a bandpass filter, a square law detector, and a smoothing filter to a stripchart recorder. In assessing the performance of the system, we are interested in two things: one is the deflection of the chart pen when the gate is fully on the Moon relative to the deflection when the gate is fully off the Moon, and the second is the jitter of the pen as a fraction of its deflection.

To compute the first part of the performance, note that the pen deflection is proportional to the power in the bandwidth of the filter preceding the detector. When the gate is entirely off the Moon, the power is the noise power only. When the gate is fully on the Moon, the power is the sum of the signal and the noise powers. Since in our cases the signal is much larger than the

noise, the ratio of the deflections is approximately the signal-to-noise ratio. From the above figures, the deflection will be about 15 times as much when the gate is fully on the Moon as when the gate is fully off the Moon.

The power spectrum of the detector output has both a DC component and an AC component which, in the vicinity of zero frequency, has a density

$$N = BN_0^2 + 2P_R N_0$$

where

B is the predetection bandwidth, and

N_0 is the predetection noise spectral density.

The variance of the voltage at the output of the smoothing filter is

$$\sigma^2 = bN$$

where b is the bandwidth of the smoothing filter. Since P_R is very much larger than BN_0

$$\sigma^2 \approx 2bP_R N_0.$$

The ratio of the pen deflection when the gate is fully on the Moon to the RMS jitter is

$$\begin{aligned} \text{ratio} &= \frac{P_R}{\sigma} \\ &= \frac{P_R}{(2bP_R N_0)^{1/2}} \\ &= \left(\frac{P_R}{2bN_0} \right)^{1/2}. \end{aligned}$$

In the system under consideration this ratio is for a $1/10$ cps bandwidth smoothing filter, 55 to 1.

4. Equipment,⁵ R. E. Arnold, E. R. Caro, T. Sato, M. Kron, R. C. Coffin, W. L. Martin, and R. F. Emerson

a. Transmitter. The transmitter to be used during the precision time-synchronization experiment is essentially the 10-kw X-band transmitter that was used for the former lunar radar mapping experiment (SPS 37-35, Vol. III, "Lunar Radar X-Band Transmitter," p. 65). The

⁵Transmitter reported by R. E. Arnold; antenna and receiver converter by E. R. Caro and T. Sato; receiving antenna mount by M. Kron; receiver by R. C. Coffin; coders by W. L. Martin; and programming by R. F. Emerson.

requirements for the bistatic radar are less stringent than for the monostatic radar. The 30-ft antenna will be used for transmitting only; no output waveguide switching will be necessary, except for occasional RF output power calibration using the RF water load.

Since the bistatic radar's operating frequency of 8450.1 MHz is only slightly above the former monostatic radar's 8448-MHz frequency, no new equipment will be required. The only changes will be the retuning of klystrons.

The RF block diagram for the X-band transmitter as used for the lunar mapping experiment is shown in Fig. 46. The X240 multiplier-exciter chain will operate unchanged. The VA401 and VA849 klystrons will be retuned as noted below.

The RF bandpass and power output characteristics of the transmitter RF components are shown in Table 11 with the VA849 final amplifier klystron and the VA401 exciter-driver klystron (SPS 37-34, Vol. III, "X-Band Lunar Radar Transmitter," p. 57) returned to ensure optimum performance at the 8450.1-MHz center frequency. The X240 exciter-multiplier chain's high-end bandpass characteristics will be marginally adequate without retuning.

b. Antenna and receiver converter. The RF assembly, shown in Fig. 47, consists of the antenna feed and a pedestal-mounted package containing the microwave amplifier, mixer, and local oscillator (LO) multiplier stages. Its purpose is to collect the signal reflected from

Table 11. X-Band transmitter bandpass and power output characteristics

RF Component	Output power		Tuning range ^a MHz	Bandpass	
	For experiment	Maximum rated power		-1 db, MHz	-3 db, MHz
VA849, Final amplifier klystron (efficiency-tuned)	10 kw	25 kw	8448 ± 30	+11 -12	+22 -14
VA401, Exciter-driver klystron	10 w	30 w	8448 ± 10	+7.0 -6.9	+9.7 -9.2
Exciter X240 multiplier chain (referenced to X-band output)	11 mw	11 mw	8448	+13 -16	+27 -32
^a Manufacturer's data.					

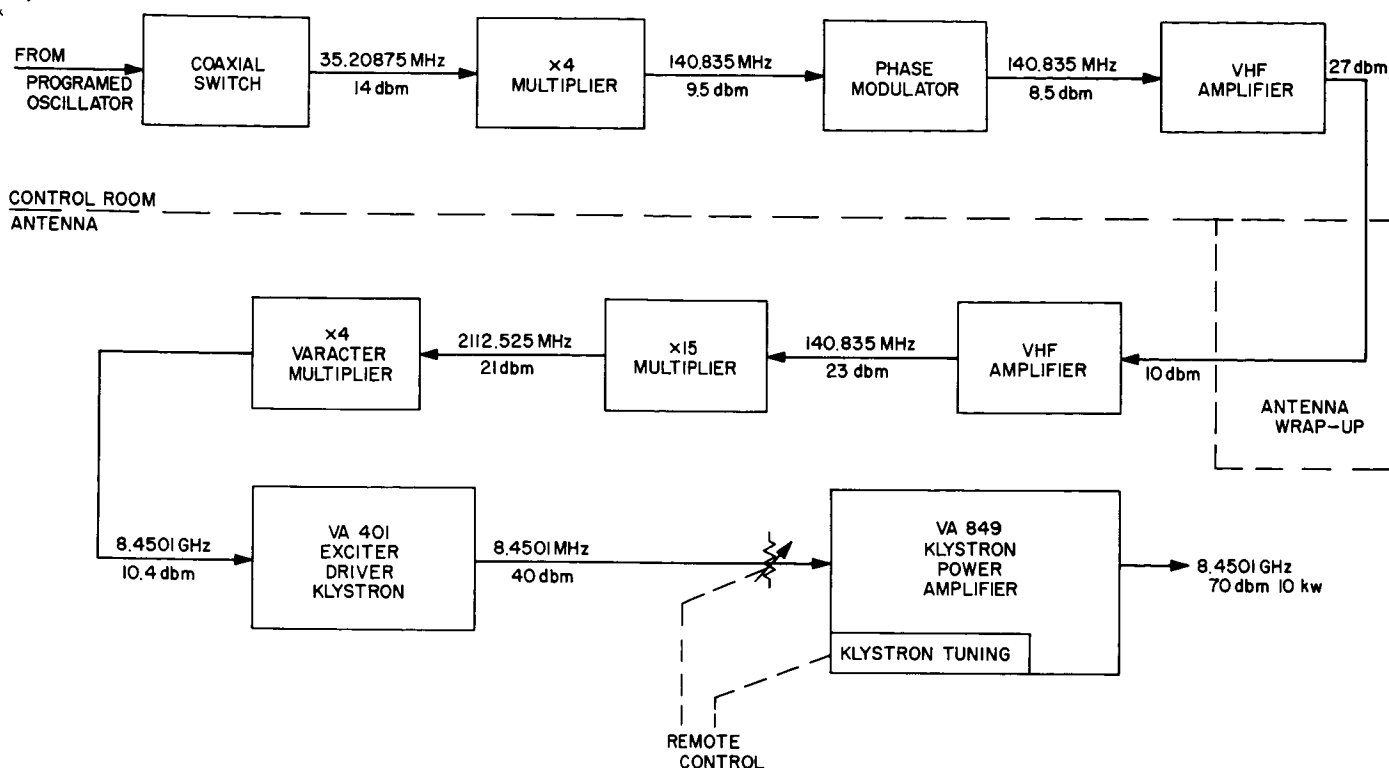


Fig. 46. X-Band transmitter system block diagram

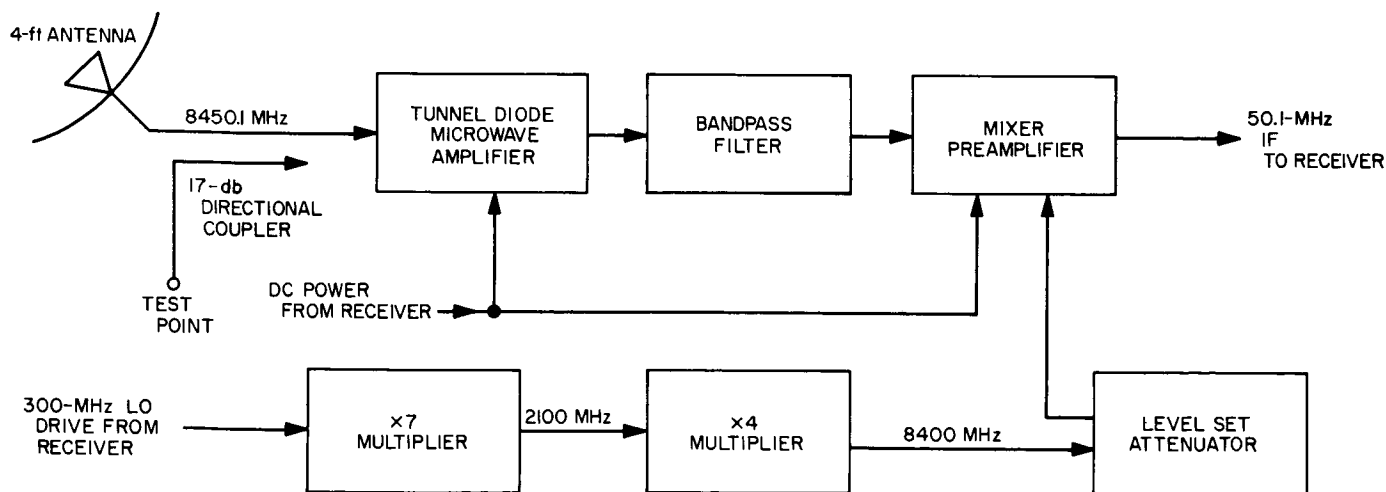


Fig. 47. Block diagram of RF assembly

the Moon, amplify and mix it with the modulated LO signal generated by the receiver, and produce the IF signal used by the receiver system.

Expected performance of the RF system is to provide 48 db RF to IF gain with a noise figure of about 5.2 db referenced to the input of the tunnel diode ampli-

fier. Nominal bandwidth will be 12 MHz at the signal frequency of 8450 MHz.

Antenna. The antenna system consists of a modified commercial 4-ft-D reflector and antenna feed. An antenna gain of 37 db is expected with a nominal beamwidth of 2 deg of arc at the operating frequency of 8450 MHz.

The feed will have the capability of accepting either circular or linear polarization and is manually switched.

Directional coupler. A 17-db crossguide directional coupler is used as a test point. A gas tube may be applied at this point to inject noise to measure the system noise figure with either an automatic meter or manually. Test signals may also be applied to the entire receiving system at this point.

Microwave amplifier. A tunnel diode amplifier is used as the microwave amplifier. A gain of 18 db with a noise figure of 5 db has been achieved at 8450 MHz. Input voltage required is +15 v dc and will be obtained from the receiver system.

Bandpass filter. A bandpass filter is used as the pre-selector and is tunable from 8000 to 8500 MHz with a nominal 3-db bandwidth of 15 MHz. Maximum insertion loss of the filter is 1.25 db.

Mixer-preamplifier. The mixer-preamplifier has a noise figure of 9 db at 8450 MHz. The RF to IF gain is 31 db with a bandwidth of 12 MHz. The output frequency is 50 MHz. All solid-state electronics is used in the IF amplifier section and requires -15 v dc, which is obtained from the receiver system.

Multipliers. The last two stages of frequency multiplication in the LO chain will consist of a step-recovery diode $\times 7$ module and a varactor $\times 4$ unit. The $\times 7$ unit will be a retuned version of a $\times 8$ DSIF module (SPS 37-41, Vol. III, pp. 99-101). The $\times 4$ unit is currently under development and will consist basically of a varactor diode mounted in a waveguide mount which will include an output bandpass filter tuned to 8400 MHz. An LO level-set attenuator will allow adjustment of the LO drive to the mixer for optimum noise figure of the mixer-preamplifier subassembly.

c. Receiving antenna mount. The functional requirements of the antenna mount were established so that an internal design specification could be developed that would afford versatility, minimum size and weight, and adaptability to unlimited changes in site locations and latitude angles. In order to establish the HA drive design philosophy, the nautical almanac was perused to establish the changes in lunar rate throughout the year. Since the Moon's rate of travel varied over a range of approximately 0.952 to 0.975 rev/day, relative to the Earth, an adjustable drive system was necessary.

Several alternatives were considered, such as a fixed synchronous rate with the operator running and stopping the drive for discrete intervals according to the Moon's rate for that particular day and time. Another device considered was an adjustable pulley or sheave design that could be manually adjusted, thus also attaining the required rate variations. However, in order to maintain versatility and eliminate the need for calibration at each site, a drive design commonly used on radio-astronomy mounts was selected. The drive consists of a synchronous motor driving through a differential and gear train (Fig. 48). Another input to the differential is made with a small AC motor that has a speed variation capability of approximately 20% of its base speed. In this manner, the variable speed motor adds or subtracts revolutions through the differential.

It is now feasible to calibrate each antenna mount at assembly by the use of a chart that will indicate the antenna rate relative to a potentiometer setting on the control box. Therefore, it will only be necessary for the operator to compute the Moon's rate for that precise day and time.

In addition to the two drive motors discussed, a slew motor has also been incorporated and operates through a clutch system that disengages the tracking drives. The HA drive system allows variable speed drive between 6 hr east and 6 hr west.

The base pedestal has been designed as a truncated trapezoid which, in addition to being a structural member, also houses the HA drive equipment in a weather-tight compartment. The design of the base pedestal is not affected by changes in latitude angles. A lower transition base bolted to the base pedestal allows compensation for various site locations, thus making the mount universal and affording lower production costs (Fig. 49).

The design of the declination axis structure was predicated upon reducing the moment arm to a minimum for stress considerations and upon reducing the over-all height and weight of the entire assembly. Since a moderate-sized bull gear was necessary, the gear itself became the support structure, thus providing a direct load path to the polar shaft and bearings.

The declination drive consists of a manually operated worm and worm wheel. Two friction-type locking devices are provided in addition to the self-locking properties of the worm gear set, and they maintain the desired declination setting. Declination travel capability is 30 deg

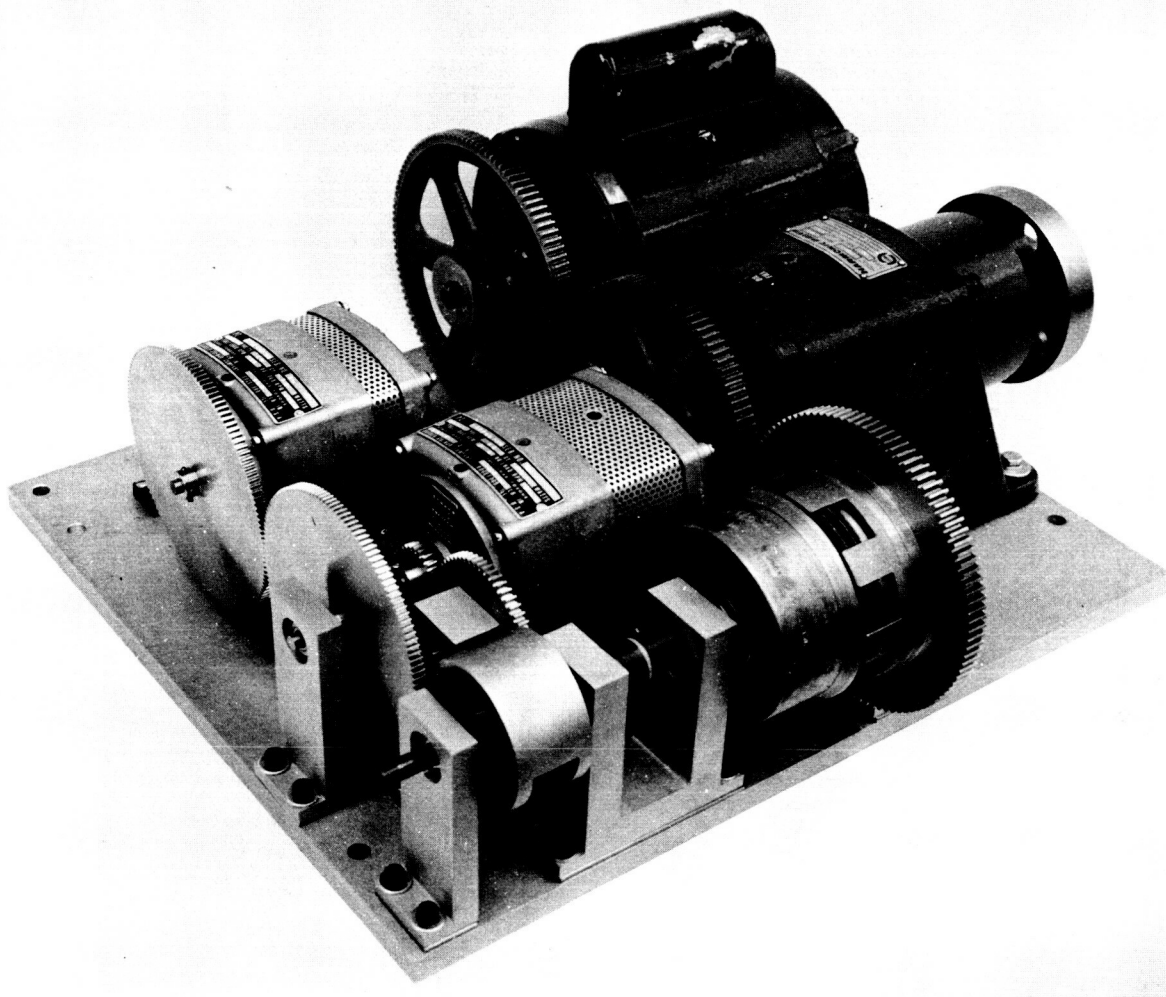


Fig. 48. Antenna drive train (prototype configuration)

south of the celestial equator to 30 deg north, and position indication is provided by a protractor-type scale.

The transition member that mounts the reflector to the declination axis was designed to resist torsion, since the reflector assumes an infinite number of positions. In addition to being a structural member, it also serves as a housing for RF components mounted directly behind the vertex of the parabola.

d. Receiver. A block diagram of the control room portion of the time-synchronization receiver is shown in Fig. 50. It is an open-loop, fixed-tuned, narrow band (10 Hz), double conversion receiver. The first conversion is from the X-band receive frequency of 8450.1 to 50.1 MHz, and the second conversion is to 100 KHz. The IF frequencies of 50.1 and 100 KHz have been chosen,

keeping in mind the design objective of simplicity in the local oscillator synthesis as well as the problem of spurious responses. Also considered in the initial design phase of the time synchronization receiver was the possibility of adapting existing module design for use in this application; and, as will be shown later, several modules used in this receiver are adaptations of existing modules. The gain of the receiver is sufficient to amplify the front-end noise (system noise temperature $\approx 670^\circ\text{K}$) to a level of -18 dbm at the input of the squarer. The squarer has a 40-db dynamic range; the -18 dbm level is 31 db below the upper limit.

The control room portion of the receiver consists of five modules, a stripchart recorder, an RMS voltmeter, and the associated power supplies. All reference frequencies used in the receiver are generated from the

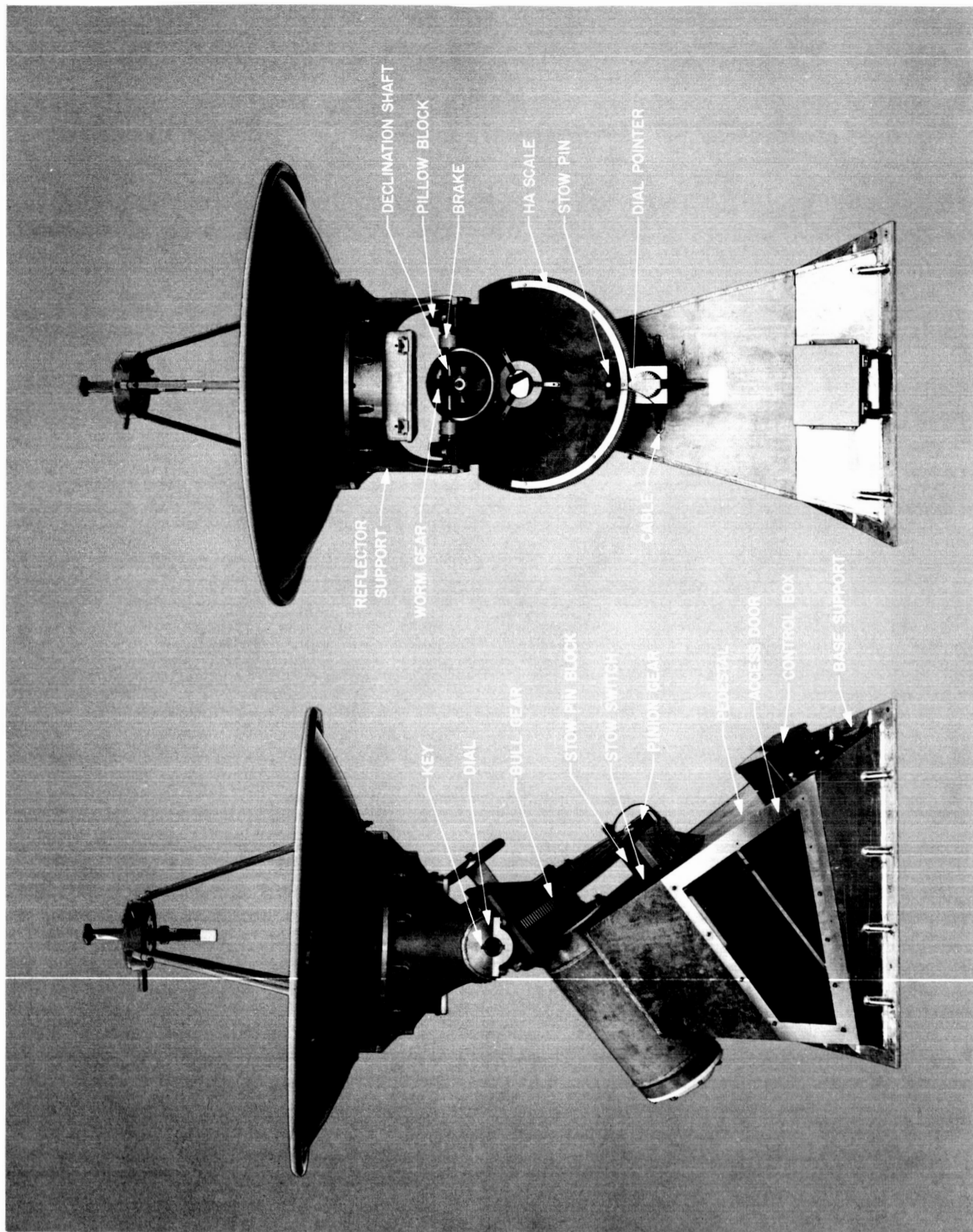


Fig. 49. Antenna mount (prototype configuration)

5-MHz output of the frequency and timing subsystem (FTS). The first multiplier in the local oscillator chain multiplies by 30, but it also provides an output at 50 MHz ($\times 10$) for the second mixer. It has 50- Ω input impedance, requires 10-dbm nominal input signal, and provides 10-dbm nominal outputs at both 50 and 150 MHz.

The second unit in the local oscillator chain is the phase modulator and VHF amplifier. The modulator is a solid-state, varactor diode version of the modulator used in the Venus DSS's S-band receiver and exciter. It is capable of producing a 45-dB carrier null. Three stages of amplification follow the modulator, thereby providing an output signal level of +23 dBm. The 3-dB bandwidth of the modulator/amplifier combination is approximately 12 MHz.

The next module in the local oscillator chain is a $\times 2$ frequency multiplier. This unit consists of a transistor-amplifier-multiplier followed by a power amplifier boosting the output level to $\frac{1}{2}$ w. Harmonic distortion is less than 5%, and the spurious signals are all greater than 40 dB down from the 300-MHz output. In the system, an isolator is employed after the $\times 2$ multiplier in order to minimize reflection problems.

Turning our consideration from the reference channel to the signal channel, we find a 50.1-MHz bandpass amplifier. This unit is a modified DSIF unit. The crystal filter

used to determine the 40-KHz bandwidth has been changed from 50 to 50.1 MHz. The second module in the RF signal section of the receiver, the 50.1-MHz IF amplifier and mixer, is also a modified DSIF module. The mixer portion of this module is modified to accommodate the 100-KHz difference frequency. The IF amplifier and mixer module has the capability of adjustable gain control, but this feature will not be used in this application, the gain being set to maximum.

The module following the second mixer is a 100-KHz bandpass amplifier having a bandwidth of ten Hz. This module was originally designed for use in the *Mariner* Venus 67 ranging experiment. It has a gain of either 20 or 40 dB and provides two output terminals. The gain of this module will be set to 40 dB. One output of the 100-KHz bandpass amplifier will drive a true RMS voltmeter which will facilitate initial tests by providing an instantaneous indication of the output signal power, whereas the output of the squarer will provide an indication delayed by the time constant of the lowpass filter.

The squarer and lowpass filter module is an adaptation of a previously used module. It consists of a crystal square-law detector followed by an operational amplifier. Feedback is used around the operational amplifier to produce the desired lowpass characteristic. Power detection by this means was chosen, based upon the requirements of dynamic range, stability, and repeatability.

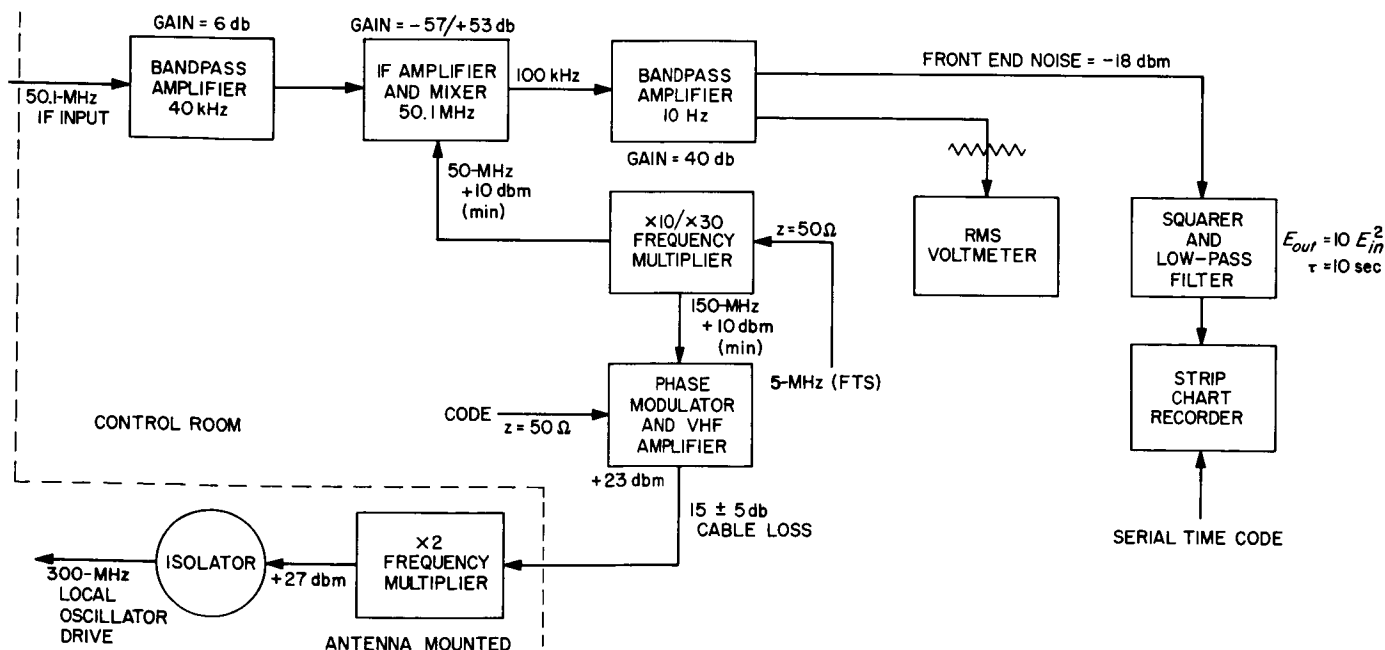


Fig. 50. X-Band time-synchronization receiver

The control room portion of the time-synchronization receiver will occupy about 18 in. of standard 19-in. rack space. The modules described above, with the exception of the $\times 2$ frequency multiplier, will be mounted in a 7-in. drawer. The $\times 2$ multiplier is mounted, with the microwave section of the receiver, in a box at the base of the receiving antenna. The RMS voltmeter and stripchart recorder are both $\frac{1}{2}$ -rack units and are mounted side by side above the drawer. Below the drawer are the three power supplies, which are $\frac{1}{3}$ -rack units, and supply voltages of +15, -15, and +28 v.

The time-synchronization receiver will have very few operator controls. There will be, of course, the controls associated with the voltmeter and recorder. But the only control on the receiver itself, will be the set screw necessary for adjustment of the modulation index. This control will not appear on the front panel of the receiver but will be concealed beneath an access hole on the phase modulator and the VHF amplifier module. Because of the dynamic range of the units involved, it is felt at this time that control of the receiver gain will not be necessary, though it would be relatively simple to add this capability at a later date.

Calibration of the receiver will be achieved by taking advantage of natural sources wherever possible. For example, correct operation of the receiver may be verified by comparing the output reading when the antenna is pointed at the cold sky to that when it is pointed at the Sun. An estimated 1-db increase in noise level should be detected in this case.

e. Coders. The coders for the precision time-synchronization experiment are constructed of Division 33 standard digital modules. Each coder generates a pseudorandom binary sequence of length 2047. The digit period of the code is 10 μ sec and is derived from the precision frequencies supplied from the frequency and timing subsystem.

The pseudorandom sequence is added modulo two (exclusive) or to a sequence of alternating ones and zeros. This process effectively complements every other digit of the code and, since the code contains an odd number of digits, effectively inverts the modified code sequence on alternate repetitions of the code. Thus, on the average, there is an equal number of ones and zeros in the code. Without this feature, the maximum carrier suppression that could be achieved at the transmitter would be approximately 33 db; whereas, with this system, 45 to 50 db can be achieved.

At the receiver, the code is automatically restarted at a particular phase once each minute. In the process of restarting the code, the code output is turned off during the first second of each minute.

At the transmitter the coder is fully controlled by the computer. Normally, the computer turns off the coder for a short time each minute, so that an unmodulated carrier arrives at the receiver during the first second of that minute when, simultaneously, timing information will be sent to that receiving station. Since the receiver coder is also off during that second, a very useful test signal is provided at the receiver.

The computer at the transmitting station can shift the phase of the transmitted code relative to the station clock so as to place the range gate at the required location and move it in the required manner.

6. Programming, R. F. Emerson

The controllable frequency-generating device for driving the transmitter is under construction, and the software necessary to control the frequency-generating device, the coders, and the transmitting site antenna are being developed. The software must operate in one machine, performing each of its three functions simultaneously (Fig. 51).

The frequency-generating equipment selected for driving the transmitter is essentially identical to the Mod V programmed oscillator (SPS 37-39, Vol. III, pp. 77-79) installed at the Mars DSS for use on the *Mariner* Sun-occultation experiment. The only changes in this equipment are those that were found necessary during the operation of the equipment located at the Mars DSS.

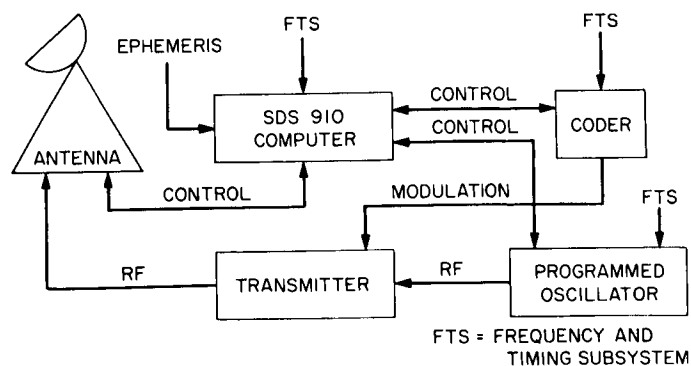


Fig. 51. Time-synchronization project control configuration

In brief, the programmed oscillator consists of a frequency synthesizer, special digital logic for interfacing the frequency synthesizer to the computer, special digital equipment for interfacing between the FTS and the digital computer, auxiliary power supplies, and control panels.

As was stated above, three separate areas must be included in the software package required for the control of the time-synchronization transmitting equipment. This section will describe first the general philosophy of the programming technique, followed by the ephemeris input and calculation program and the interface with the FTS, two areas which are common to all three requirements. This will be followed by a description of the special requirements for each of the three subsystems to be controlled by the same computer (e.g., the frequency-generating equipment).

The computer selected for the control of the subsystems is an SDS 910 with 8,000 words of memory, 16 interrupts, and typewriter and papertape I/O. This hardware configuration places the following constraints on the programming philosophy: (1) All control subprograms must run under interrupt demand, (2) ephemeris information must be entered by the papertape reader, (3) only a minimum of computer-to-operator communication can be included, (4) routines entered as the result of interrupts cannot use programmed operators, and (5) all program parts must be segmented into sections of running time less than 100 msec.

Based on the above constraints a program is being written which will, when initially entered, request of the operator the day and month. It will use this information to search a paper tape and pull from it the necessary constants to be used for the generation of ephemeris data. From this point on, the operation of the program progresses in a natural sequence, requesting of the peripheral devices certain information and returning with appropriate commands.

Internally, the following sequence of operations will occur. After an interrupt, an interrupt routine will be entered which will perform a minimum amount of operations. These operations will include real-time data acquisition, real-time control, and link setup operations. All other calculations will be accomplished in these linked routines. In Fig. 52, a block diagram of the program, the blocks labeled R1, R2, R53, etc., are program segments which are switched into the program as required by the

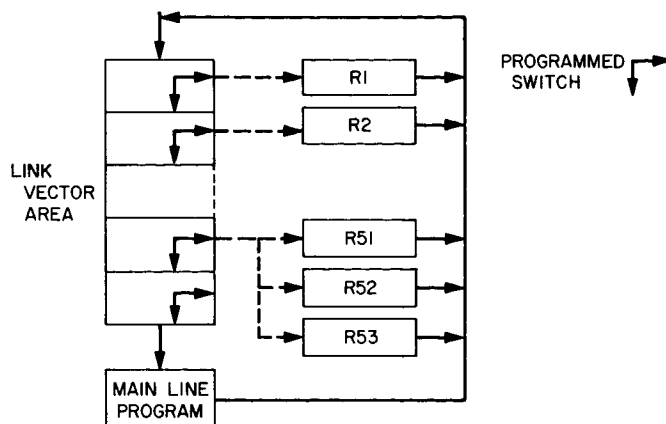


Fig. 52. Link vector concept

programmed switches in the link vector area. There is an implied priority level associated with each segment. At the completion of a linked routine, two things may happen: (1) if additional calculations are required because of the length of the program, a second link will be set up and control transferred to the head of the link vector area; (2) if no further calculations are required in this portion of the program, this level of the link vector area of the program will be cleared and control transferred to the head of the link vector area.

In addition to the calculations done on demand by the interrupt routines, there is a small amount of processing to be done on a main-line basis. Since the priority of this effort is lowest, it is placed at the end of the link vector area.

The generation of specific points of the ephemeris is accomplished by a routine called POLY. This routine accepts polynomial constants and evaluates a Chebyshev Polynomial. Requests for this subroutine are generated by all three subsystem control programs at intervals which are specific to each. The constants for each subsystem control program are located in separate areas of core, and the results of each evaluation are placed in communication cells for that subprogram.

The station time is entered into the control system via a subsystem of the programmed oscillator which formats and converts the FTS signals into the proper form for the computer. A set of 1-sec and ½-sec interrupt routines operate on the above hardware. Their function is to check the validity of the station time with reference to the computer time and to update the internal clock cells used by each subprogram.

The special programs which control the frequency generation subsystem read the present status of this equipment under interrupt command, compare the status with that required by the ephemeris, and send appropriate error-correcting signals to the equipment.

The heart of this particular subprogram is a computer-evaluated difference equation representing the control function required for a rate servo.

The package of programs which control the antenna pointing subsystem accepts the ephemeris data and converts it from HA-DEC to AZ-EL antenna coordinates, adds the refraction term, compares this reference position with the actual antenna position, and sends error-correcting commands to the antenna servo system. Because of the speed of the control operation, the servo is treated as a position servo.

The control of the coder involves two separate operations each minute. First, it is necessary to restart the coder so that the output will be in the proper phase at the receiving site. This requires that rapid offsetting be done by the coder control program. The second activity of the coder control program involves the sweeping of the range gate over $\pm 30 \mu\text{sec}$ in range so that the receiving station

may acquire the front face of the Moon at a time which is proportional to the time offset between the transmitter and receiver clocks.

Other routines are included in the program package which provide operator assistance during a mission. These are primarily concerned with the display of control information and other selected data.

During the initial phases of operation, a portion of the program accepts commands from the operator which specify the day to be used for the ephemeris calculations.

An additional common routine is used for the reporting of the error conditions which may arise during the normal operation of the control equipment.

An important result of this software development is the integration of three separate control programs into one. Previously, control software has been limited to one function per computer, resulting in a proliferation of "single-minded" computers. The project demonstrates that a computer can keep more than one task in operation without confusion. This requires additional computing time overhead, but the over-all cost effectiveness is increased.

References

1. Stelzried, C. T., et al., "A Precision DC Potentiometer Microwave Insertion Loss Test Set," *IEEE Transactions on Instrumentation and Measurement*, Vol. IM-15, No. 3, September 1966, p. 98.
2. Ginzton, E. L., "Microwave Measurements," McGraw Hill Book Co., 1957, p. 413.
3. Beatty, R. W., "Mismatch Errors in the Measurement of Ultra-high Frequency and Microwave Variable Attenuators," *Journal of Research of the National Bureau of Standards*, Vol. 52, No. 1, January, 1954, Eq. 8 of p. 8.
4. Hogg, D. C., and Semplak, R. A., "The Effect of Rain and Water Vapor on Sky Noise at Centimeter Wavelengths," *Bell System Technical Journal*, Vol. 40, September 1961, pp. 1331-1348.
5. *Handbook of Chemistry and Physics*, 37th edition, Chemical Rubber Publishing Co.
6. Feldman, N. E., "Estimates of Communication System Degradation Due to Rain," Rand Corporation, October 1964.
7. Holzer, W., "Atmospheric Attenuation in Satellite Communications," *The Microwave Journal*, Vol. VIII, No. 3, March 1965, pp. 119-125.
8. *Handbook of Geophysics*, United States Air Force, MacMillan Co., 1960.

References (contd)

9. Tausworthe, R. C., "The Theory and Practical Design of Phase-Locked Receivers," Technical Report 32-819, Jet Propulsion Laboratory, Pasadena, California, February 1966.
10. *Handbook of Mathematical Functions*, National Bureau of Standards, Vol. AMS-55, April 1966.
11. Viterbi, A. J., "Phase Locked Loop Dynamics in the Presence of Noise by Fokker-Planck Techniques," *Proceedings of IEEE*, Vol. 51, No. 12, December 1963, pp. 1737-1753.
12. Tausworthe, R. C., "Cycle Slipping in Phase Locked Loops," Space Programs Summary 37-41, Vol. IV, Jet Propulsion Laboratory, Pasadena, California, October 31, 1966.
13. Tausworthe, Robert C., "Random Numbers Generated by Linear Recurrence, Modulo 2," *Mathematics of Computation*, Vol. XIX, No. 90, April 1965, pp. 201-208.
14. Box, G. E. P., and Mueller, M. E., "A Note on the Generation of Random Normal Deviates," *Annals of Mathematical Statistics*, Vol. 29, 1958, pp. 610-611.
15. Todd, J., et al., *Survey of Numerical Analysis*, McGraw-Hill Book Co., New York, N.Y., 1962, pp. 314-326.
16. Papoulis, A., *Probability, Random Variables, and Stochastic Processes*, McGraw-Hill Book Co., New York, N.Y., 1965, pp. 103-104.
17. Trask, D. W., and Muller, P. M., "DSIF Two-Way Doppler Inherent Accuracy Limitations," SPS 37-39, Vol. III, pp. 7-16, May 31, 1966.
18. Tolson, R. H., "How Station Clock Resynchronization Influences the Orbit Determination Process," interoffice report, Jet Propulsion Laboratory, Pasadena, California, May 16, 1966.
19. Lorell, J., "Ranging Data Importance to Selenodesy Experiment," IOM 312.1-6JL to M. S. Johnson, Jet Propulsion Laboratory, Pasadena, California, March 23, 1966.
20. Sjogren, W. L., "Two-Way Doppler Data Sensitivity to Relative Station Timing When Tracking a *Lunar Orbiter*," IOM 312.3-464 to J. Brenkle, Jet Propulsion Laboratory, Pasadena, California, January 25, 1966.
21. Curtright, J., "Trip Report (Transportable Clock)," interoffice memo to D. McClure, Jet Propulsion Laboratory, Pasadena, California, October 3, 1966.

IV. Communications Development Engineering

A. High Power Transmitter Development:

400-kw Klystron, C. P. Wiggins

1. Summary

A 400-kw klystron is under development by a contractor for future use in the DSN. The prototype tubes will be tunable over the range of 2.320–2.455 GHz, but the design is such that it can be scaled to produce tubes for operation at the DSN frequency (2.1 GHz) or at other lower frequencies. The design is being verified, and fabrication and assembly of the first tube is in process.

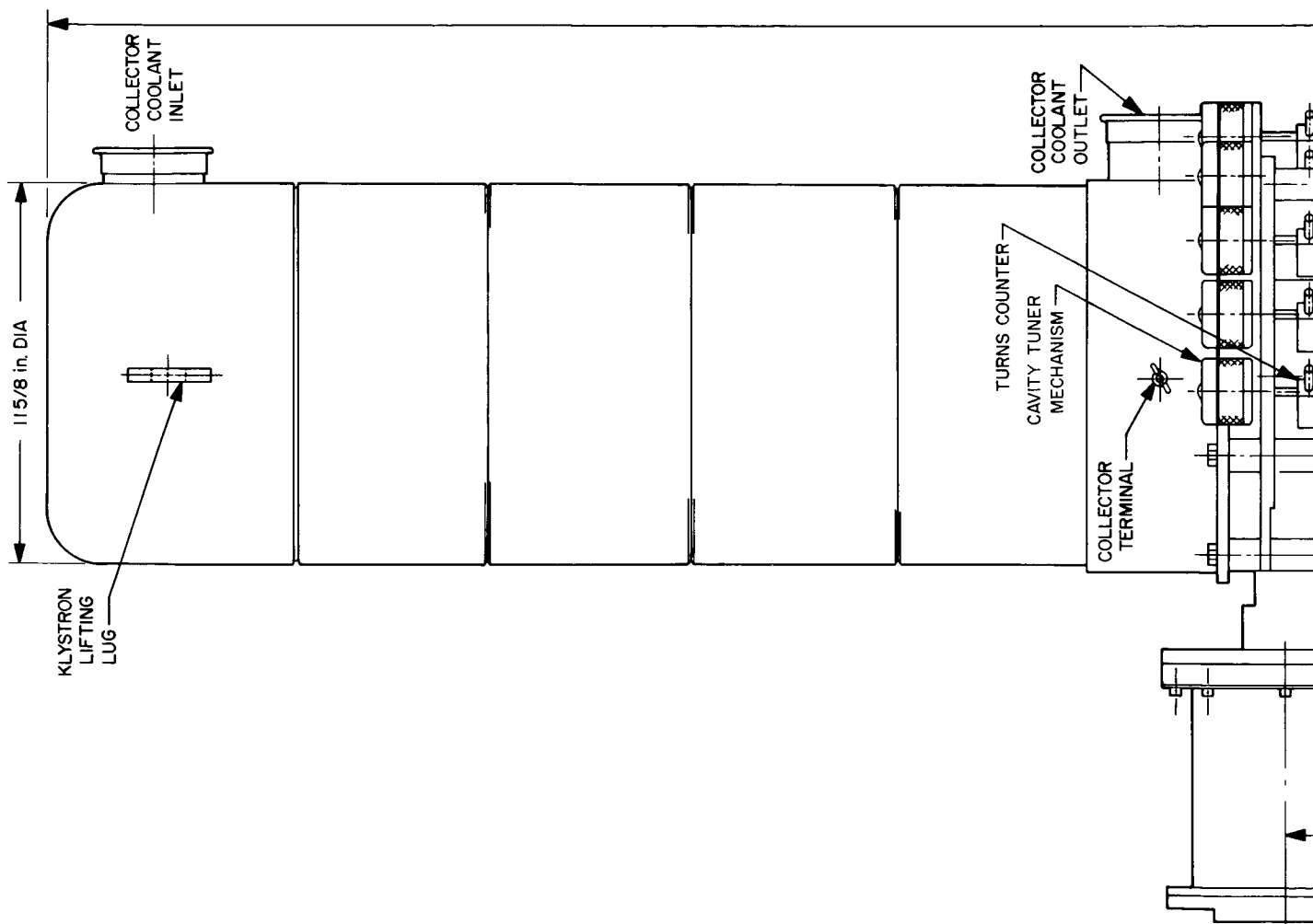
2. Description of Klystron

The klystron is shown in Fig. 1. The focus magnet and socket tank are cut away to illustrate the electron gun and body of the tube. The cathode of the klystron will be at –65 kv and will be oil-immersed to reduce the length of the cathode insulator and to improve the cooling of the electron gun. The filament power supply must be insulated for this high voltage, since one side of the filament is connected to the cathode. This supply is included in the socket tank, below the cathode, thus utilizing the same insulating and cooling oil and eliminating the need for high voltage bushings.

The klystron specifications are:

Power output:	400 kw (nominal)
Gain:	53 db
Beam voltage:	65,000 DC
DC beam power:	1 Mw
Cooling water flow:	300 gpm
Gross weight: (including magnet and tank)	1100 lb
Overall height:	80¼ in.

Prior to fabricating parts for the klystron, a significant number of models was tested in order to evaluate the design. A full-scale model of the electron gun was tested in the beam analyzer with excellent results. The beam exhibited low scalloping and good laminarity. Thermal tests of the tuner were set up in a vacuum using the tuner paddle as the plate of a high power diode. Cooling water was run through the paddle, which absorbed 2 kw (the expected power dissipation) without incident. Analysis of these data shows that the tuner can safely absorb 10 kw, which allows a safety factor of five. Brass models of the cavities have been operated with a pulse to observe their



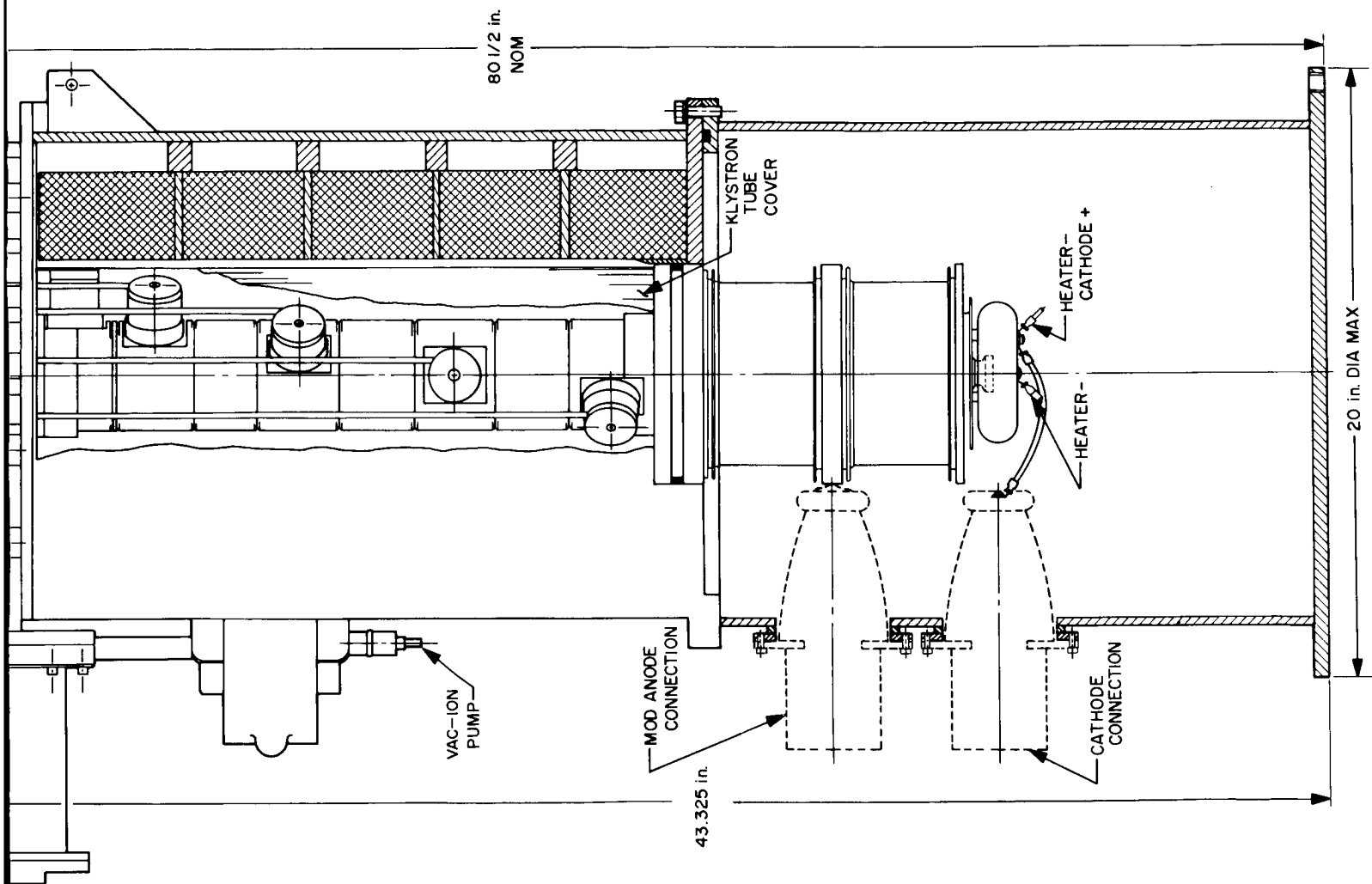


Fig. 1. 400-kw klystron

characteristics. As a result of extensive RF window studies in J-band guide at 8.0 GHz, for the Department of Defense, the beryllium oxide window that was originally proposed as an alternate will be used. Scaling the results of this study shows that the S-band window can handle at least 1.2 Mw of RF energy.

3. Status

Fabrication and assembly of the first tube is in process. The collector (Fig. 2) has been assembled, and it is vacuum tight. The electron gun (Fig. 3) is shown cold-stacked for testing prior to brazing. The RF body will be stacked and cold-tested as an assembly, both before and after brazing. The RF window is being fabricated and will be cold-tested soon. The focus magnet and socket tank are being subcontracted.

The klystron is scheduled for testing in mid-February 1967 and shipment is scheduled for March. The contractor has received a 500-kw RF water load which will be used to absorb the power output from the tube.

Design and fabrication of a transmitter to utilize the 400-kw klystron is proceeding. RF loads and waveguide switches have been ordered. Material for increasing the DC power supply voltage to 70 kv from 55 kv is on order or on hand.

Following receipt of the klystron, it will be subjected to extensive testing at the high power facility of the Goldstone Venus station, using the new transmitter. It is expected that the new transmitting system can be placed into service on the 85-ft diameter antenna at the Goldstone Venus station during the third quarter of 1967.

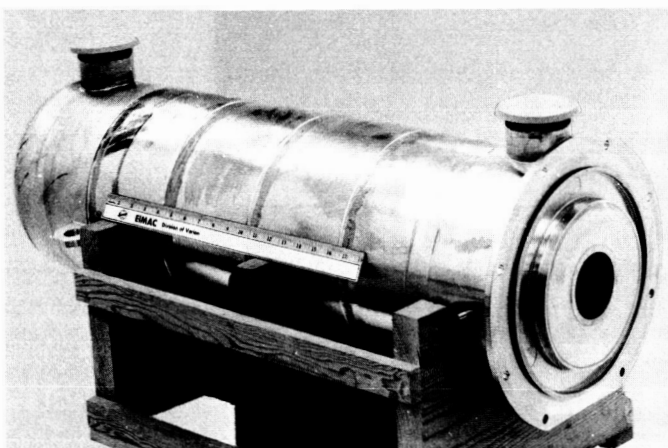


Fig. 2. Collector assembly, 400-kw klystron

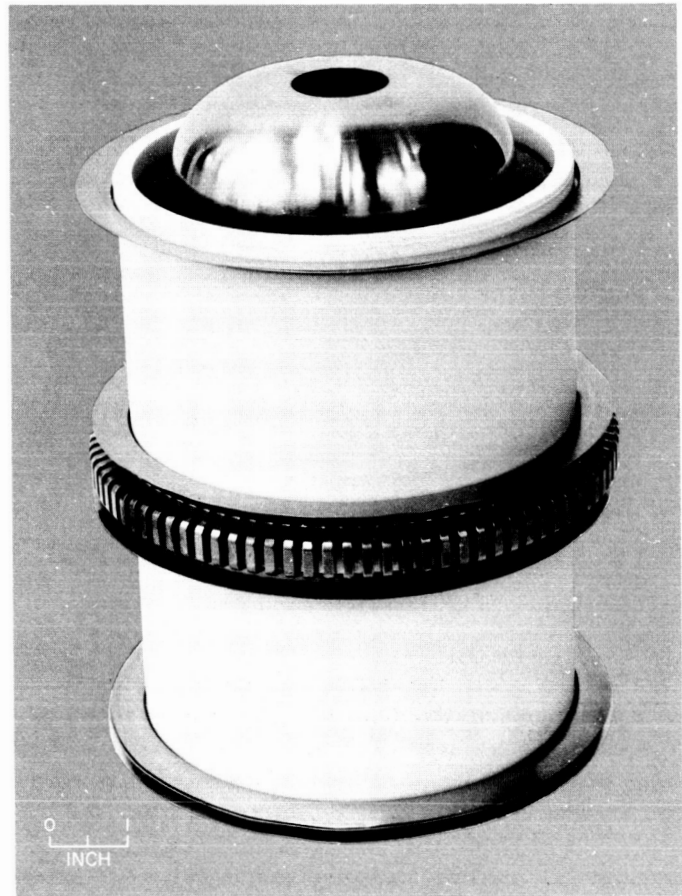


Fig. 3. Electron gun for 400-kw klystron

B. High Power Transmitter Development:

A Controlled 20-kw Power Source, E. J. Finnegan

The development of a universal controllable power source to be used on the 400-kw klystron focus magnet power supply and on a 500-kw (or larger) alternator exciter is in process. Supplies of this type now installed use three-phase, adjustable autotransformers for voltage control, but at 20 kw these are prohibitive in size and weight. The use of SCR's for control of these power supplies eliminates the requirement for autotransformers with significant savings in size and weight, faster response, and improved over-all efficiency.

In SPS 37-40, Vol. III, p. 82, a power supply was described that used the SCR's in the DC bridge. This approach was adequate for small power supplies but would prove to be too bulky for large supplies, which should have commutating reactors in series with each SCR to insure their proper control under all types of loads. Therefore, in designing a large unit, the SCR's were used on the AC side, thus controlling the primary power

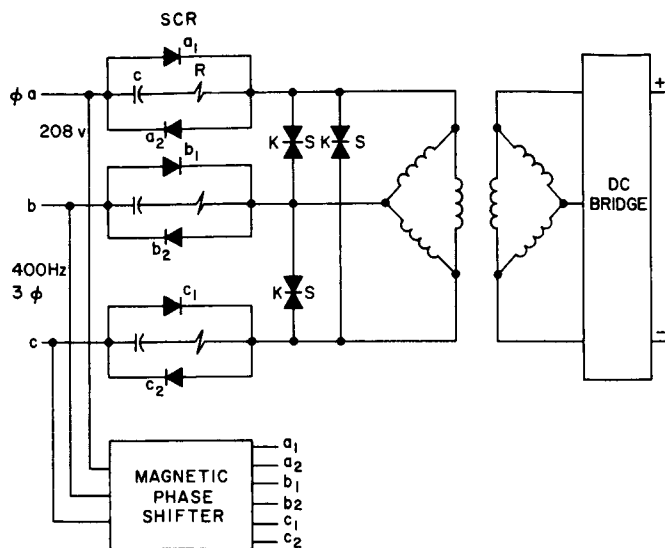


Fig. 4. 20-kw controller

(Fig. 4). To adjust the output voltage from 0 to 100%, SCR's were connected for full wave control (opposed). The capacitor and resistor shunting the SCR's give transient protection along with the klip-sels (transient protective devices) in Fig. 4. If 100% control is not needed, an SCR and diode may be connected opposed, which simplifies the circuitry and gives automatic protection to the SCR as the diode shunts inverse voltages.

A magnetic amplifier was chosen as a phase shifter because it gives smoother control of the SCR's than other techniques. Also, other windings on the core may be used for current limiting or to transform the power supply into a constant voltage or current source. An extra winding may be employed in a closed-loop circuit for feed-back, if desired. This control unit also places $-1v$ bias on the

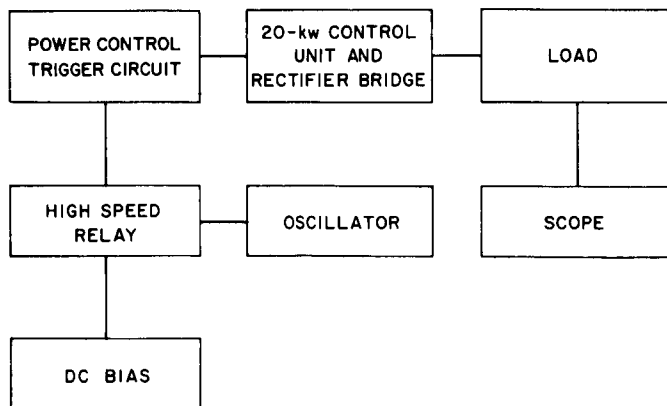


Fig. 5. 20-kw controller response time

gate to insure SCR cut-off and to prevent spurious triggering.

Due to limitations of 400-Hz power in the laboratory, the control unit has not yet been tested to its full capability. However, the unit has been tested to 8 kw and operated satisfactorily. Fig. 5 shows how the equipment was connected to measure the response time. The trigger circuits were gated on and off at the rate of approximately 2 Hz, which loaded the power supply from zero to 30 amp. As can be seen from Fig. 6, the response time of the trigger circuits and power controller and bridge is approximately 8 ms. The ripple on the pulse is due to the lack of sufficient DC filtering, which will be added.

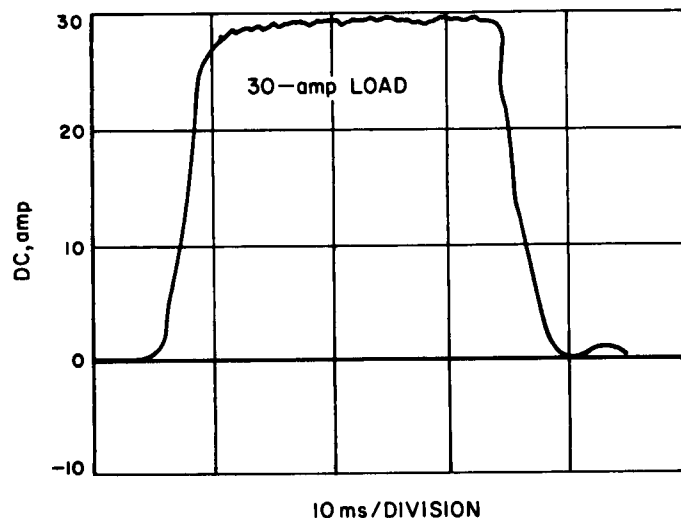


Fig. 6. Response time of SCR power controller

C. 100-kHz Module Development, R. B. Crow

1. Introduction

A new family of 100-kHz modules consisting of: a 100-kHz IF amplifier; a 100-kHz phase shifter; and a 100-kHz coherent amplitude detector has been developed. A limiting phase detector and a distribution amplifier are currently under development.

100 kHz was chosen as the IF to allow construction of narrow-band crystal filters in the IF amplifier. A noise bandwidth of 10 Hz is the narrowest crystal filter presently available.

The 100-Hz module family was originally developed to allow narrow-band carrier tracking loops and angle pointing systems to be built. Presently, three new systems

are using these modules: The X-band time synchronization receiver (SPS 37-43, Vol. III), *Mariner Venus 67* ranging experiment (SPS 37-42, Vol. III, pp. 1-5), and a "mission-independent" telemetry system.

The reduction in predetection bandwidth will eventually allow a carrier loop bandwidth of a fraction of a hertz, thus increasing the receiver threshold. To meet the more stringent requirements created by increasing the system threshold, a new set of design specifications has been incorporated into the modules discussed here.

2. 100-kHz IF Amplifier

The 100-kHz IF amplifier has two outputs, capable of linear operation up to ± 13 dbm with greater than 40-db isolation between outputs. The amplifier gain is continuously adjustable from 20- to 40-db. The crystal filter used in the amplifier is easily removed and is presently available in noise bandwidths of 10, 100, 1000, 2000, and 4000 Hz.

The phase shift for a 0 to 50°C temperature change for the amplifier and the filter is listed in Table 1.

Table 1. Phase shift vs 50° C temperature change

Amplifier only	Phase shift for bandpass filter corrected for amplifier phase shift			
	10 Hz	100 Hz	1 kHz	2 kHz
+4°	-5°	-16°	-1°	+8°

The amplifier noise figure is 4 db at a gain of 40 db and 5 db at a gain of 20 db. RFI leakage on the power line and plate-to-plate leakage is $< 1 \mu\text{V}$.

The chassis is a machined, gold-plated cavity-type conforming to the DSN standard configuration and using standard DSIF supply voltages. Fig. 7 shows the chassis and components of the IF amplifier with a crystal bandpass filter installed.

A grounded gate field effect transistor (FET) with high transconductance was chosen as the input stage to assure a low noise figure and low harmonic distortion (Figs. 8 and 9). The common gate configuration was chosen since the input impedance of the FET is approximately $1/g_m$, which for the T1XS35 is $50 \pm 5 \Omega$, providing a $\text{VSWR} < 1.1$ in the circuit. This input match had little

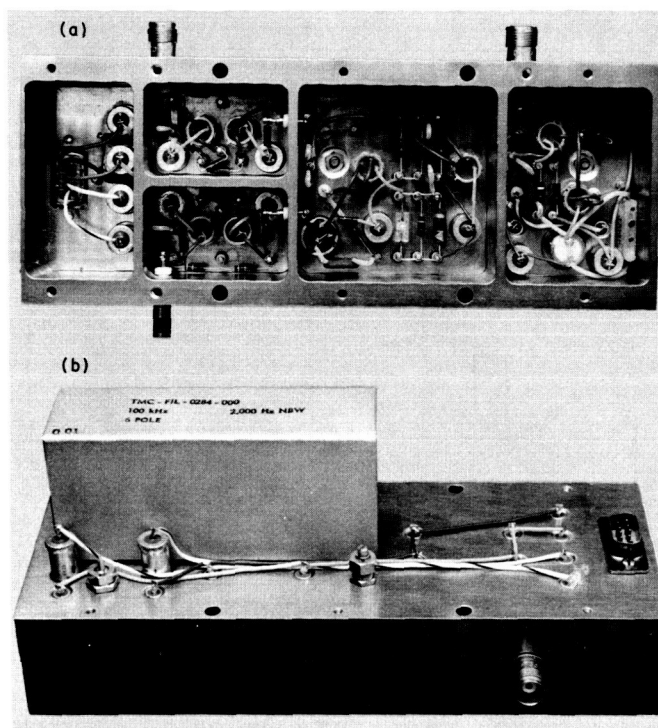


Fig. 7. (a) 100-kHz IF amplifier interior; (b) 100-kHz IF amplifier exterior

circuit loss and did not use the large inductors required at 100 kHz to secure a low loss input circuit

The emitter follower was required to furnish the proper impedance match for the crystal bandpass filter. The common source FET amplifier was used to maintain a low noise figure. The emitter follower was used after the common source amplifier as an impedance matcher and to assure adequate isolation between outputs. The complementary emitter followers were selected for their temperature stability and linearity.

3. 100-kHz Coherent Amplitude Detector

The coherent amplitude detector has been designed to provide a nominal sensitivity of 10 v/rad at maximum input level of ± 13 dbm with a harmonic distortion of less than 2%. The signal and reference balance are 40 db below the nominal output level over a dynamic range of 40 db.

The signal input circuit uses a common source field effect transistor as an input amplifier for low noise and low harmonic distortion (Fig. 10). An emitter follower was used to drive the low impedance diode bridge.

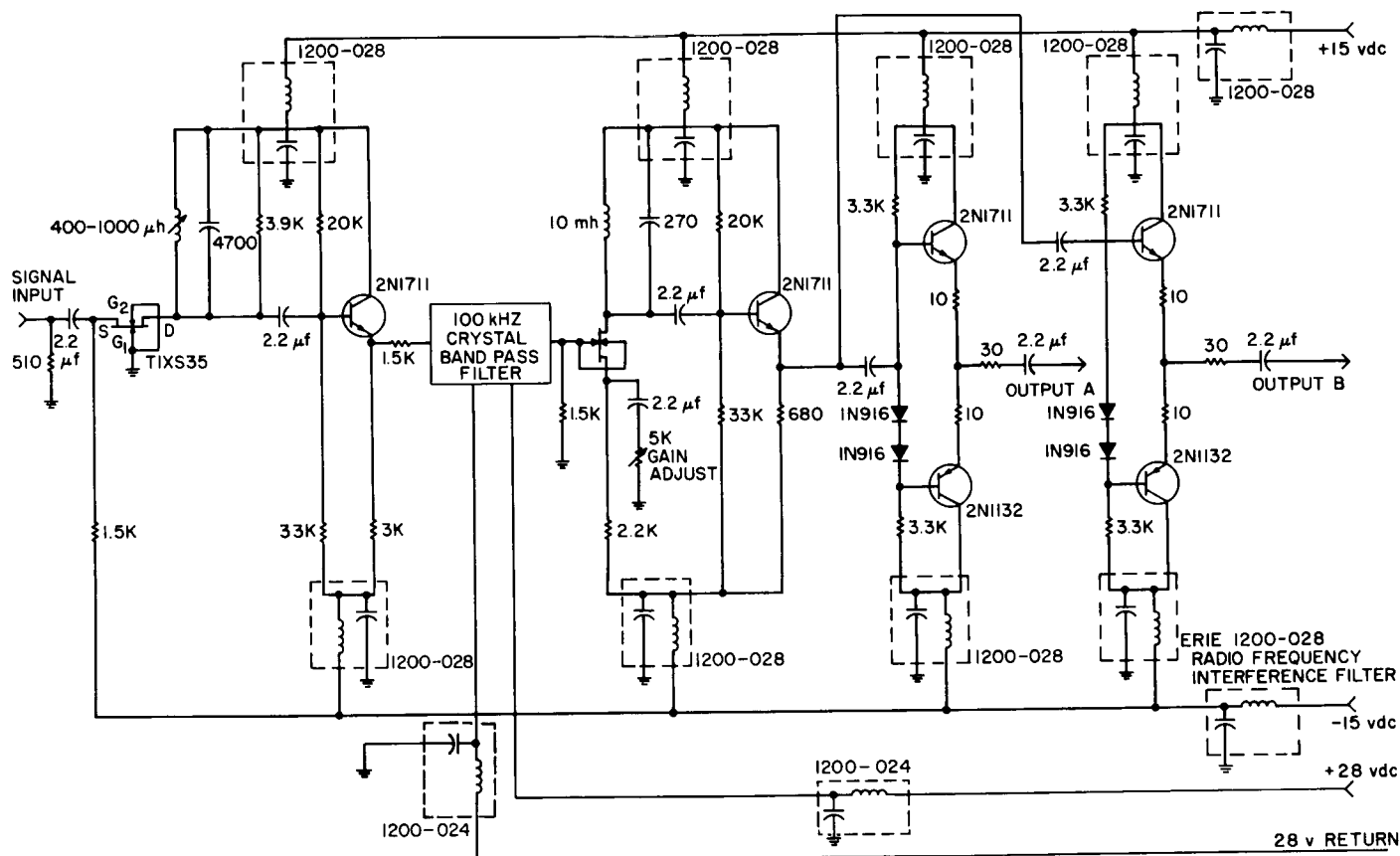


Fig. 8. Schematic for 100-kHz IF amplifier

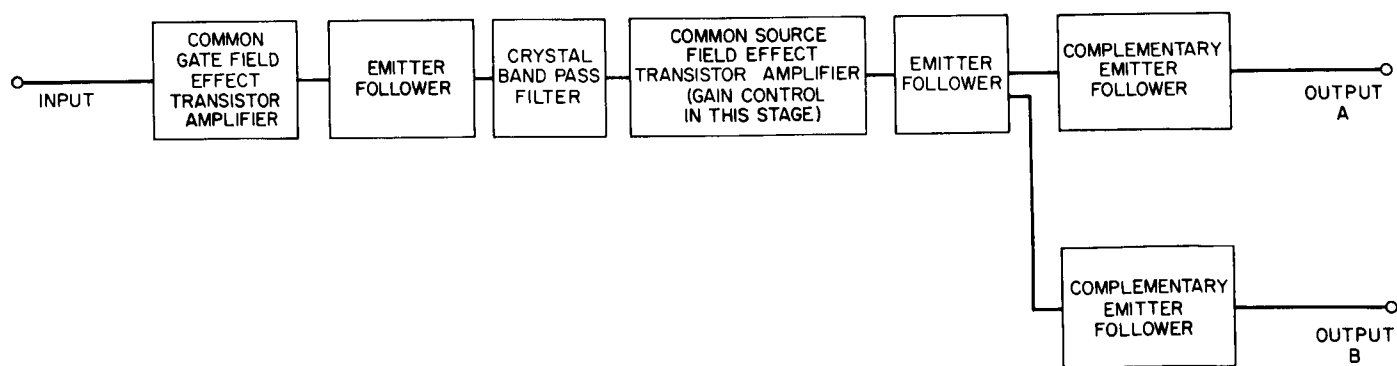


Fig. 9. Block diagram for 100-kHz IF amplifier

Reference balance as a function of reference power input and temperature variation required that diode limiting be used. It was found that excellent limiting could be obtained by using hot carrier diodes and linear amplifiers. A complementary emitter follower was used to provide adequate undistorted reference to the low impedance diode bridge. The output of the diode bridge is amplified in a chopper stabilized operational amplifier. The sensitivity can be adjusted to be exactly the required 10 v/rad.

The low impedance diode quad-detector and associated DC amplifier have shown excellent balance, linearity, and distortion characteristics. The low impedance also makes the unit much easier to reproduce and adjust. However, a dual approach using a high impedance, high output detector will also be followed to evaluate both types.

4. 100-kHz Phase Shifter

The 100-kHz phase shifter was designed to produce an undistorted reference signal whose phase can be accurately adjusted.

The output signal limiting characteristic (Fig. 11) indicates that the output is constant for an input variation of at least +3 to +13 dbm. A measured phase shift linearity of 1° P-P was observed with a harmonic distortion less than 2%. The change in phase shift over the 0 to +50°C temperature range is 5°C maximum with a corresponding 0.5-db change in output power.

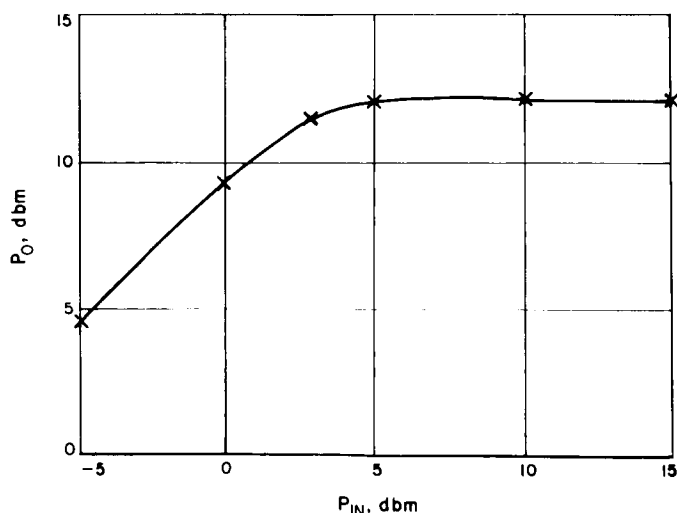


Fig. 11. Limiting characteristics for 100-kHz phase shifter

The common source FET was used as an input circuit to allow low harmonic distortion (Fig. 12). Complementary emitter followers were used to provide a low impedance, undistorted input into the phase transducer. The second FET was used to provide a high input impedance and low noise characteristics. This was required since the phase transducer has a 30-db insertion loss and is sensitive to output circuit loading. Diode limiting was used to provide the temperature stable output limiting characteristic.

Additional development and testing in the laboratory and in the three systems listed above will continue for the five types of modules. Progress will be reported in subsequent SPS articles.

D. Mariner IV Subcarrier Signal Evaluation Near Threshold, N. A. Burow

A simple comparison technique for measuring *Mariner IV* subcarrier signal-to-noise ratios (SNR) at, and somewhat below, *Mariner* telemetry threshold has been implemented. The primary objective of the technique was to determine the *Mariner IV* subcarrier SNR for passes late in the mission, several months after Martian encounter. At the time (and subsequently) *Mariner IV* was transmitting on its low-gain antenna. As a result the signal received on Earth was substantially below its "design threshold" level. Measurement of the subcarrier SNR under this condition is interesting because it gives an assessment of system and equipment performance in regions not normally used for operation in the usual sense.

It was found that the recorded signal was characterized by a ratio of modulation energy per bit to noise spectral density of 4.2 db. At this level the theoretical bit error rate is 0.03. The telemetry users, observing the processed data, had estimated its error rate as roughly 0.12. The difference is due to degraded ground system performance at the nonstandard signal levels.

The *Mariner IV* subcarrier was recorded (using FM tape recording techniques) at DSS 14, the 210-ft-antenna station, and sent to JPL for evaluation. An estimate of the subcarrier SNR was obtained by playing the recorded signal through a telemetry demodulator with an SNR estimator device (SNORE)¹ installed (Fig. 13). Direct use

¹See SPS 37-27, Vol. IV, pp. 169-184, for a discussion of the SNORE system. Analysis of system performance has been carried out by D. Boyd of JPL Section 336 in a technical memorandum soon to be published in the SPS, Vol. IV.

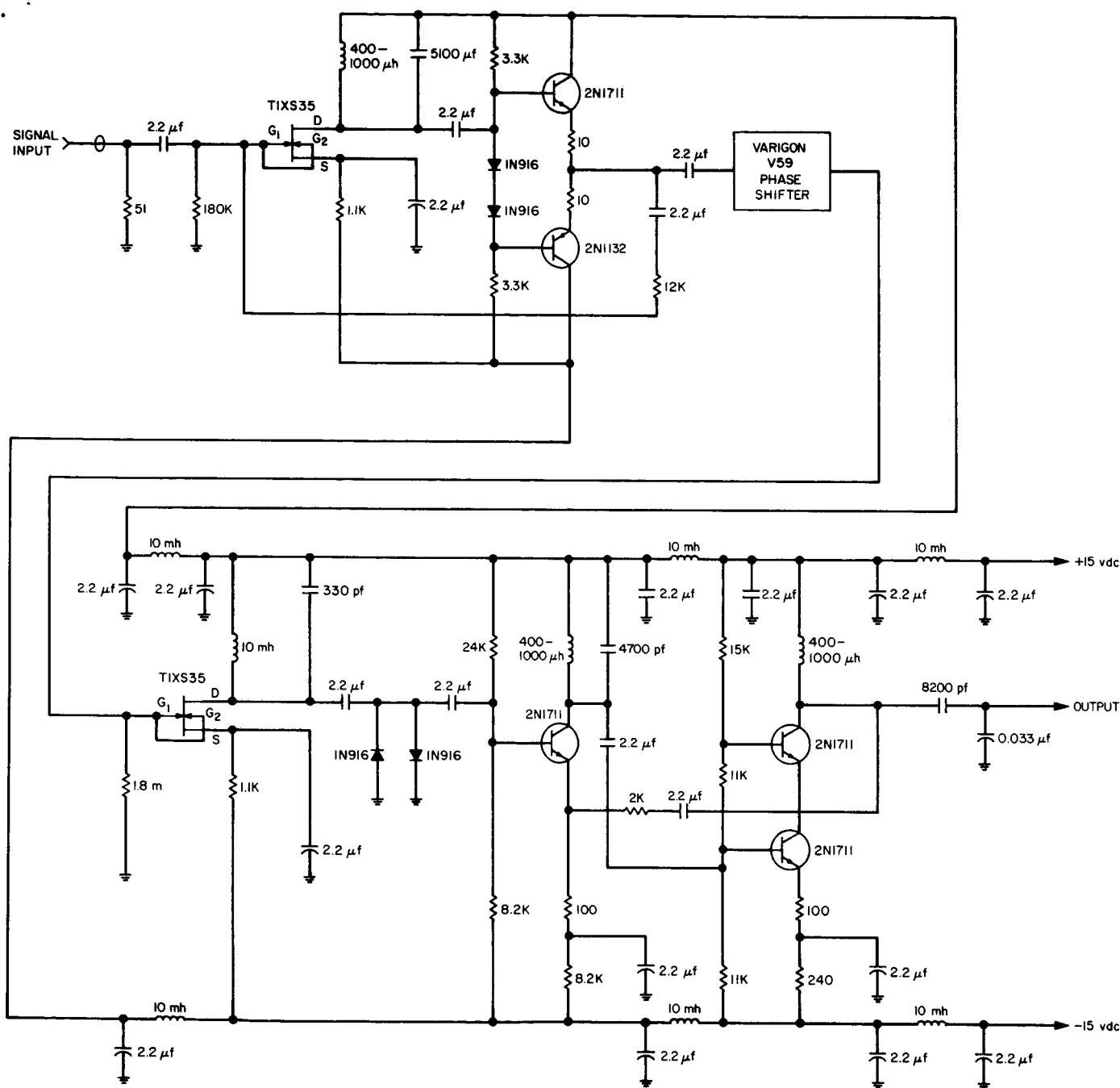


Fig. 12. Schematic for 100-kHz phase shifter

of the SNORE on the *Mariner IV* data was not possible, due to its low SNR. Instead, the SNORE output derived from the recorded *Mariner IV* subcarrier signal was compared with that obtained for a signal of known SNR. The SNR of this known input was adjusted until the output of the SNORE was the same with either signal. The *Mariner IV* subcarrier SNR was then equal to that of the known input (+4.2 db).

The SNORE measures the ratio of modulation energy per bit to noise spectral density,

$$P_m T / N_0$$

In the above equation, P_m is the modulation power, T is the bit period, and N_0 is the noise spectral density. In

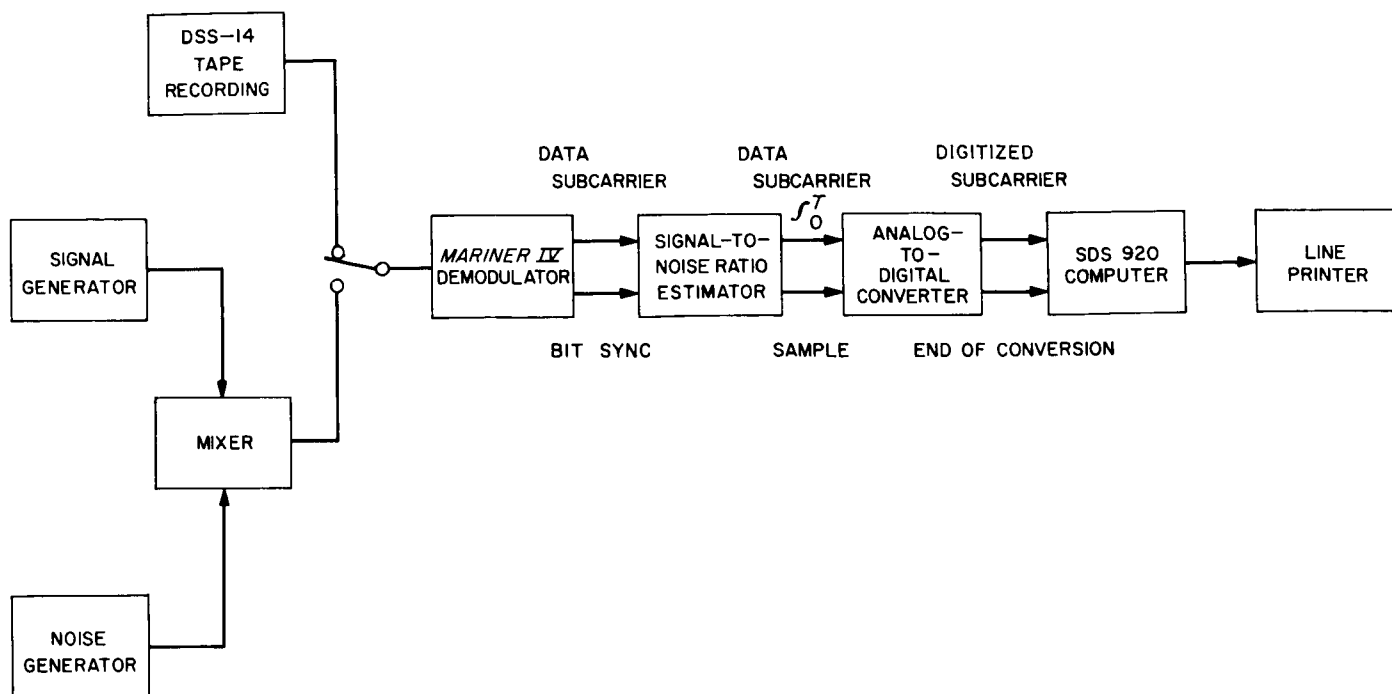


Fig. 13. SNR subcarrier estimating technique

making this measurement, the SNORE assumes that the phase jitter in the demodulator data loop is small. If this is not the case, a direct measurement of $P_m T/N_0$ cannot be made. Phase jitter in the demodulator data loop for the recorded *Mariner IV* signal was quite high, the loop being out of lock nearly one-third of the time. Therefore, the estimate of $P_m T/N_0$ by the SNORE of +1.45 db was erroneous. To find the correct value for $P_m T/N_0$, a known signal from a *Mariner C* simulator was mixed in a calibrated mixer with noise of a known spectral density and adjusted until the output of the SNORE was the same as it had been when using the *Mariner IV* data (+1.45 db). $P_m T/N_0$ at this point was +4.2 db, as measured in the mixer. This is 2.7 db below the design threshold of the demodulator.²

The SNORE unit provides an output of the data subcarrier, phase detected and integrated over $\frac{1}{2}$ of a bit period and sampled at bit sync time. The data samples are digitized and processed by an SDS 920 computer. The computer program (written by J. Gillis of the Bendix Field Engineering Corporation at Goldstone) computes the data subcarrier mean (\bar{x}) using the form

$$\bar{x} = \frac{1}{n} \sum_{i=1}^n x_i$$

in which $n = 1000$, and the x_i are samples of the integrated subcarrier phase.

The variance (σ^2) is computed using the form

$$\begin{aligned} \sigma^2 &= \frac{1}{n-1} \left[\sum_{i=1}^n (x_i - \bar{x})^2 \right] \\ &= \frac{1}{n-1} \left[\sum_{i=1}^n (x_i)^2 - \frac{1}{n} \left(\sum_{i=1}^n x_i \right)^2 \right] \end{aligned}$$

The data subcarrier SNR is determined using

$$\text{SNR} = \frac{\bar{x}}{\sigma}$$

The signal modulation energy per data bit to noise spectral density ratio $P_m T/N_0$ is computed using the form

$$P_m T/N_0 = 20 [\log_{10} (\text{SNR})] + K$$

where K is proportional to the integration time constant.

²JPL functional specification MC-4-310A, "Functional Specification, *Mariner C* Flight Equipment, Telecommunications System," December 10, 1963.

For a given $P_m T/N_0$ the theoretical channel bit error rate P_e can be determined and turns out to be an error function of the SNR. For a $P_m T/N_0$ of 4.2 db the theoretical P_e is 0.03. The observed 0.12 bit error rate is explained by the degradation of the demodulator performance due to the large amount of phase jitter in the data loop. A subjective verification of the 4.2-db figure was obtained by comparing spectrum plots from the taped *Mariner IV*

signal and the known (signal + noise) signal from the mixer.

At present, the limiting point of this technique has not been determined. The technique worked well at the 4.2-db level discussed above and was noted to give consistent outputs at somewhat lower levels (3.2- to 4.2-db range).

V. Facility Engineering and Operations

A. Flight Project Support, J. Orbison

1. Lunar Orbiter Project

The *Lunar Orbiter II* spacecraft was launched on November 6, 1966, from Cape Kennedy, Florida. The first acquisition by the Echo DSS (DSS 12) took place on November 7, 1966, during the first pass; the midcourse maneuver sequence was performed on November 8, during the second pass. Deboost for the initial lunar orbit began at 20:00:15 GMT and ended at 20:40:00 GMT; the first occultation occurred at 21:10:28 GMT.

The spacecraft remained in the initial high orbit until the tenth pass on November 16, when previously stored commands from Robledo, Spain (DSS 61) were executed by a command from DSS 12, and the photographic low orbit was achieved. Picture-taking began immediately after a stable orbit was confirmed, and the first picture readout at DSS 12 was recorded during the first orbit of the twelfth pass on November 18. Picture readouts were recorded until pass 28 on December 7. During pass 30, the spacecraft was boosted into a higher orbit, and tracking on an extended mission continued until the end of the year.

2. Pioneer Project

a. Pioneer VI. The *Pioneer VI* spacecraft completed its first year in space on December 16, 1966, and continues to be tracked by the Mars DSS (DSS 14) 210-ft antenna. Multimission telemetry and command processing is provided by the Echo DSS. On December 13, during pass 363, the spacecraft was tracked to operationally test the master equatorial (ME) antenna pointing system. During pass 371, on December 21, a special track was performed by the Echo DSS to update the tracking data analysis, using the receiver, servo, tracking data handling, and digital instrumentation subsystems.

b. Pioneer VII. Tracking of the *Pioneer VII* spacecraft returned to the Pioneer DSS with pass 78, November 3, with the Echo DSS providing telemetry and command processing from the Pioneer ground operational equipment (GOE). Although committed to the *Lunar Orbiter II* mission, the Echo DSS continued *Pioneer VII* multimission support through pass 117, December 13. A transmitter malfunction at the Pioneer DSS during pass 117 was covered by the Echo DSS transmitter during the last hour of tracking, permitting the transmission of two

commands to the spacecraft. With pass 118, the Echo DSS reassumed the prime tracking of the *Pioneer VII*, in addition to the *Lunar Orbiter II* tracking.

3. Mariner Mars 1964 Project

The *Mariner IV* spacecraft completed its second operational year in space on November 27, 1966. The tracking continues to be performed by the Mars DSS, using the experimental maser mounted in a cone modified from an 85-ft antenna unit and mated to the 210-ft antenna on a special adapter section. The experimental receiver installed in the alidade control room, with the maser, is used exclusively in the *Mariner IV* tracking, in conjunction with the normal DSIF S-band antenna drive. Resulting telemetry is microwaved to the Venus DSS for certain experiments involving a bistatic arrangement of the two stations.

4. Surveyor Project

Preparations for the *Surveyor C* mission are in progress at the Pioneer DSS, concurrent with the DSN system operational testing of the equipment in the MSFN wing. Two major tests—an on-site data processing and an SFOF/DSS 11 simulation—were performed. The latter was a simulation of midcourse and spacecraft maneuver anomalies. Both were used for operational testing of equipment and for personnel training.

Contact with the *Surveyor I* spacecraft took place on November 8, 1966, during the sixth lunar day after the landing on June 1, 1966. A total of 566 commands were transmitted from the Pioneer DSS to the spacecraft; however, no additional pictures were received. Spacecraft telemetry was recorded during the contact and forwarded to JPL for processing.

B. Facility Construction and Equipment Installation, J. Orbison

1. Echo Deep Space Station

The Tiefert Peak commercial power line construction was completed in December, with the power change-over scheduled for January 1967. Construction was difficult because of the roughness of the terrain (SPS 37-42, Vol. III, p. 89) requiring men and materials to be airlifted to the site. A helicopter was used to lift and place the 1900-lb poles (Fig. 1) and to string the cable from a special cable reel hung below the aircraft (Fig. 2).



Fig. 1. Tiefert Peak pole line installation

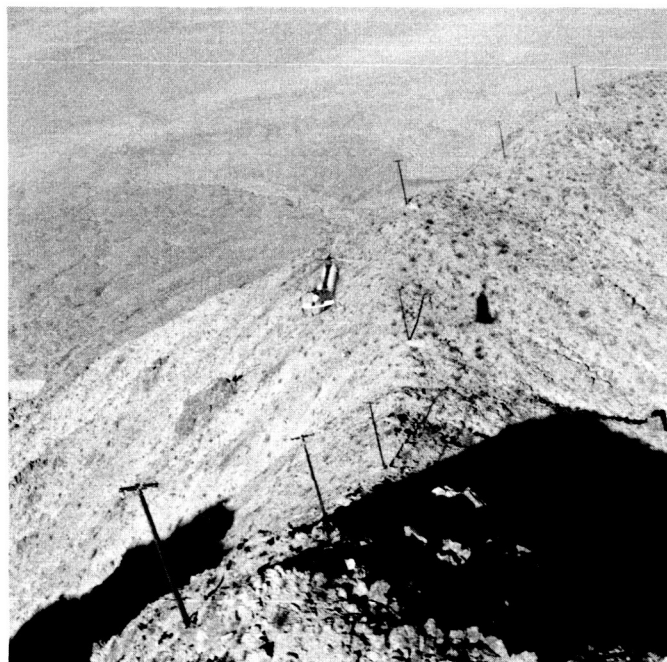


Fig. 2. Tiefert Peak power line cable installation

The multiple mission support recording (MMSR) analog instrumentation subsystem was operationally tested for power-on and internal tests before shipment to the Johannesburg DSS. Fig. 3 illustrates the MMSR area (right) and its relationship to the Echo DSS standard DSIF control area (left). Except for building arrangements, the area illustrated is similar to the equipment rack layouts at all DSS locations.

2. Pioneer Deep Space Station

The installation of the underground primary power distribution is complete. Additional switch equipment has been temporarily installed, awaiting completion of the generator installation scheduled for early 1967. Currently, the station is using commercial power with a diesel generator backup for emergency use (SPS 37-38, Vol. III, p. 85).

Operational testing of the equipment in the MSFN wing is in progress. Final installation testing was performed using a NASA target airplane flying a prescribed course to determine antenna pointing and control-room equipment operation. Boresight testing of the acquisition-aid antenna took place in December. Inter-site interface testing between the MSFN Apollo Station and the Pioneer DSS is essentially completed.

Installation of the multiple mission support area (MMSA) continues. Currently installed are the telemetry and command data transfer racks, and one of a pair of computers for the telemetry and command processing II (TCP II) subsystem. Interfaces between the MMSA/TCP II and the *Surveyor* GOE are undergoing operational testing. The TCP II equipment for the Tidbinbilla DSS 42 was operationally tested before shipment in December.

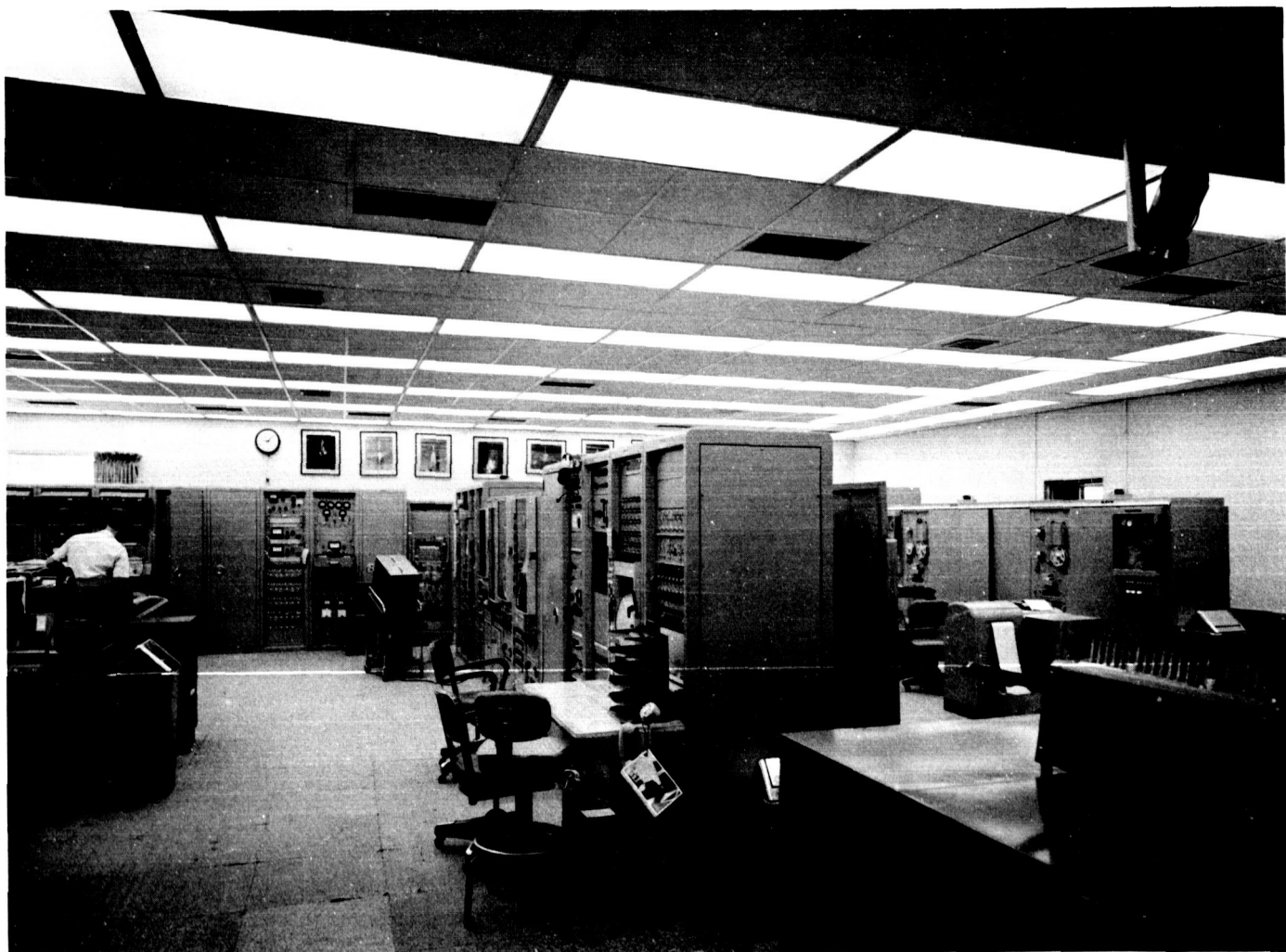


Fig. 3. Echo DSS control room and multiple mission support area

Preparation for the *Mariner Venus 67* mission is in progress. Currently installed in Building G-1, Room 9, are the read-write-verify command equipment and ground telemetry equipment racks (Fig. 4). Power-on and internal subsystem tests have been performed.

3. Mars Deep Space Station

Installation of the DSIF S-band equipment continues concurrent with tracking commitments for *Mariner IV* and *Pioneer VI*. Station personnel are assisting JPL engineers with the continuing alignment testing of the hydrostatic bearing assembly. Calibration of the master equatorial (ME) and the independent reference structure (IRS) is being performed using a series of star tracks and the *Pioneer VI* spacecraft. Equipment for the antenna pointing subsystem is receiving operational testing in preparation for use with the ME and IRS subsystems.

C. DSIF Station Control and Data Equipment,

W. Frey, R. Flanders, G. Jenkins, A. Burke, and H. Baugh

The DSIF station control and data equipment (SCDE) was introduced in SPS 37-41, Vol. III, and continued in SPS 37-42, Vol. III. This article presents the status of this equipment as of December 1966.

1. Antenna Pointing Subsystem

The Mars DSS (DSS 14) is the first DSIF station to be equipped with the Phase I antenna pointing subsystem (APS I), where it has been installed and is now operational. Beginning in June 1967, the remaining stations will be provided with the APS I. Until this time, all stations, with the exception of the Mars DSS, will continue to use the interim APS.

The APS I provides increased flexibility and capabilities over the existing interim APS. The functional capabilities of APS I are described in detail in SPS 37-38, Vol. III, pp. 74-76. The APS I is presently being used at the Mars DSS to provide tracking support for (1) *Pioneer VI* and *Mariner IV* flight projects, (2) Venus planetary radar experiments, and (3) Mars DSS antenna pointing calibrations.

2. Digital Instrumentation Subsystem, Phase II

The digital instrumentation subsystem, Phase II (DIS II) implementation is proceeding, with procurement of the prototype DIS II currently in process. Upon completion, the existing DIS I (composed of an SDS 910 computer, SDS 920 computer, associated peripheral equipment, data gathering elements, and recording apparatus) will be returned to the manufacturer for updating to the DIS II configuration.

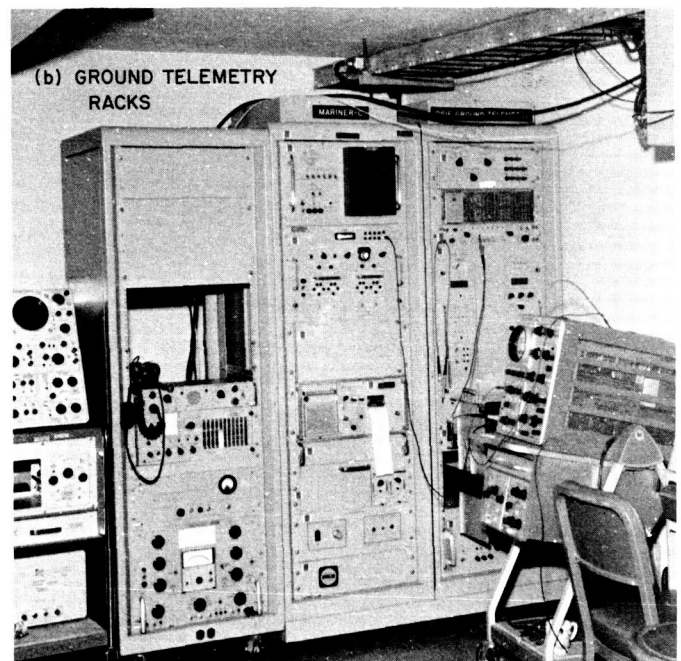
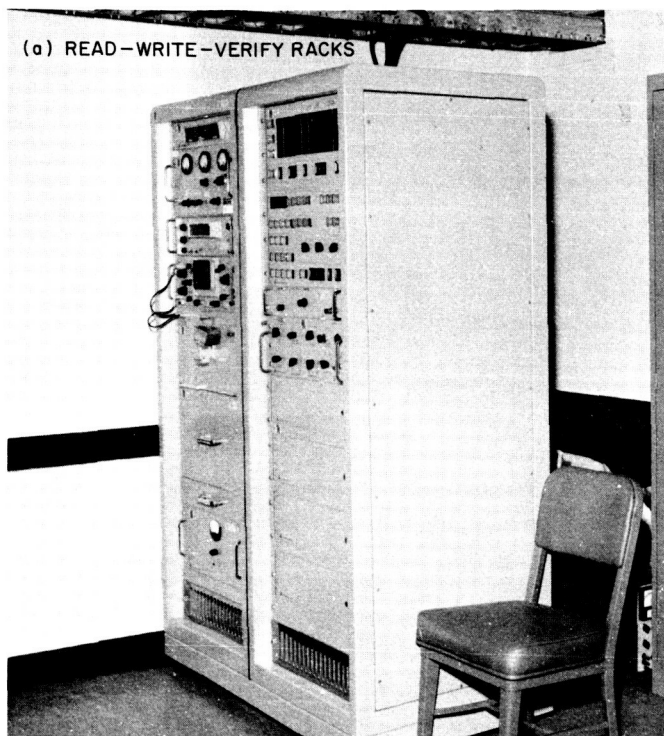


Fig. 4. *Mariner Venus 67* read-write-verify command equipment and ground telemetry equipment

The DIS II will use the existing SDS 920 computer, peripheral equipment, magnetic tape recorders, and data gathering elements. To this complement of equipment will be added a communications buffer with teletype and high-speed data capability, Y-buffer, interrupt arming chassis, Y-buffer interlace cartridge loading magnetic tape transport, and memory expansion.

Delivery of the DIS II prototype is scheduled for the third quarter of 1967. Procurement of a DIS II for each of five stations has been initiated, with delivery scheduled for 1967, following prototype evaluation.

Documentation for the DIS II is to be consolidated with that for the APS I and the telemetry command processor (TCP) to take advantage of elements common to all subsystems. Procurement of this material (composed of operation and maintenance manuals and drawings) is in process to assure delivery simultaneously with, or shortly after, delivery of the hardware portion. The DSIF Phase I monitor program is being prepared, with completion also scheduled to coincide with the installation and check-out of the actual subsystems.

3. Telemetry and Command Processors, Phase II

The telemetry and command processors, Phase II (TCP II) are the major assemblies in the telemetry and command data handling subsystem, Phase II (TCD II). A description of the TCP II has been presented in SPS 37-38, Vol. III, pp. 76-77. During this reporting period, three SDS 920 computers have been delivered to Goldstone. These units have been checked out and shipped to DSS 42, 61, and 11, respectively. The TCP II-A configurations at these stations will be changed to the full TCP II configuration as specified in Table 2, p.128, SPS 37-41, Vol. III.

4. Station Control and Monitor Console

The station control and monitor console subsystem, Phase I (SMC I) will provide each station manager a facility for the display and control of station performance at a central location. Furthermore, the SMC displays information to indicate nonstandard system or subsystem performance. SMC II calls for added functions as follows: (1) displaying selected station parameters, (2) an English-text printout of station performance and status, (3) system alarm monitoring under control of the DIS to indicate station failures, and (4) a teletype page printer. SMC I is complete except for the countdown clock, which is scheduled for delivery by October 1967.

SMC II development is under way and delivery of the prototype x-y plotter is scheduled for February 1967. This unit is scheduled to undergo thorough evaluation at both JPL and Goldstone prior to procurement of follow-on units. The plotter is intended to display actual data versus predicted performance data. The program alarm and control panel is undergoing an extensive redesign which will incorporate an audible alarm and use JPL Hi-Rel digital modules in lieu of the original commercial circuit boards. The first unit should be operational by June 1967. Implementation of the program alarm and control panel is planned for five stations in the fiscal year of 1967.

Page printers and line printers are in the requisition phase at the time of this writing and delivery to five stations is planned for the first quarter of the 1968 fiscal year.

5. Frequency and Timing Subsystem, Phase II

The final block diagram and the functional specification for the frequency and timing subsystem, Phase II (FTS II) have been prepared.

Deliveries of screened components needed for digital module fabrication are somewhat behind schedule, and some additional difficulties have been experienced in the evaluation of the rubidium frequency standards. Since this will delay the prototype fabrication, the overall project is being reexamined to present a more precise and realistic schedule.

D. Venus DSS Operations, M. A. Gregg,

E. B. Jackson, and A. L. Price

1. Experimental Activities

During the period of October 15 through December 12, 1966, the Venus DSS was primarily engaged in bistatic (with the Mars DSS) planetary radar experiments and in reception from and transmission to the *Mariner IV* spacecraft. Additionally, the 85-ft AZ-EL antenna was used for radio source evaluation at both S- and X-band (2388 and 8448 MHz, respectively). Utilization of the 85-ft antenna at X-band was made possible by the construction and installation of a standard Cassegrain feed cone equipped with a traveling wave maser (TWM) and associated closed-cycle refrigerator (CCR), two follow-up receivers, and various waveguide switches, terminations, signal sources, etc., as required for operation and evaluation. The 30-ft AZ-EL antenna was used for 22- to 23-GHz radiometer observations of Venus. The major station activities are summarized in Table 1.

**Table 1. Summary of Venus DSS activities
(October 15–December 12, 1966)**

Activity	Hours	Percent
Primary experiments		
Planetary radar (Venus bistatic)	33	2.33
X-band performance evaluation (85-ft AZ-EL)	528	37.29
Secondary experiments		
Radio source temperature calibration (S- and X-band)	60	4.24
Passive Venus observation (22–23 GHz)	310	21.89
Mariner experiments		
Transmission, reception, and testing (including time required to change Cassegrain feed cone)	36	2.54
Testing, calibration, construction, and maintenance	354	25.00
Holidays and scheduled nonoperating time	95	6.71
Total	1416	100.00

2. Subsystem Performance

a. Receiving systems. During this period, the Mod IV receiver was used in its bistatic configuration for the reception of signals from the *Mariner* spacecraft and the Venus planetary experiments. As is normal for this mode of operation, signals from the appropriate Mars DSS receiver are fed, via the microwave link, into the 455-kHz portion of the Mod IV receiver.

The Venus DSS R&D 2388-MHz receiver was used during this period for source temperature measurements. Operation of the programmed local oscillator (PLO) remained good throughout this period; however, only the radio frequency portion was used. No failures occurred in the central frequency synthesizer (CFS) and the operation was normal.

b. 100-kw transmitter. During this period, the R&D transmitter has operated 167.1 filament hours and 104.5 beam hours for the Venus bistatic radar experiments. Some failures were experienced because of the reflected power coupler load termination (resulting in high reflected power trip-offs), and some were due to low coolant water flow in the high voltage rectifier. These were repaired by replacement of the load terminations and by increasing the coolant flow to the rectifiers.

c. Mariner 100-kw transmitter. During this period, the *Mariner* transmitter has operated 29.2 filament hours and

15.1 beam hours. Failure of a relay in the GE Limit-Amp control panel to the motor generator caused a two-hour delay at the beginning of a track on the *Mariner* spacecraft on October 31.

3. System Improvements

a. Data systems. During the evaluation of the 85-ft antenna's performance at X-band, on-site antenna patterns are produced by the SDS 930 computer from receiver automatic gain control (AGC) voltages developed as the antenna scans across the signal source. The data system records, on punched tape, the azimuth, elevation, time, and AGC voltage during a data run. These data tapes are read by the SDS 930 computer, along with data on AGC voltage, as a function of relative received power. The computer then plots a curve of AGC voltage versus relative received power, as well as tabular data showing data points from which the curve was internally fitted. It also plots antenna patterns in either azimuth or elevation, as desired.

b. Receiving systems. To provide phase-locked reception at X-band frequencies in the 85-ft-diameter antenna, the 8448- to 30-MHz converter and power supply were removed from the 30-ft-diameter antenna and installed in the X-band Cassegrain feed cone for the 85-ft antenna. Existing control and signal cabling was used for the operation of the X-band receiver. The control room junction box for the X-band system was modified to be compatible with the cabling from either the 30- or the 85-ft antenna.

The output from the converter is fed into the 30-MHz portion of the Mod IV receiver. Phase-locked operation can be accomplished using either the special 455-kHz loop or the normal loop. The PLO is used to center the free-running signal input, 8448 MHz, within the pass-band of the receiver. The developed AGC voltage is routed to a voltage-to-frequency converter. The output of the converter is then recorded by the data system.

As the tracking schedule permits, all of the Mod IV interconnecting cables are being examined for wear or damage, and all defective units will be replaced.

c. Transmitting systems. A new air-break switch was installed on top of the 1-MW motor generator to enable the output of the motor generator to be disconnected from the vacuum relays in the high voltage vault. Thus, without turning off the motor generator set, maximum personnel safety is assured. This also speeds up repair of failures in the rectifier system or components.

E. Systems Reliability and Availability Study for SFOF Power Design, D. C. Card

1. Introduction

As in other system designs, the design of the power system for the SFOF must take into consideration the fact that the elements of the system are unreliable (experience failures). System failure and unavailability during unscheduled down periods can often be translated into loss (e.g., cost in mission dollars). This loss must be traded-off against the cost of improving the system reliability; generally, the trade-off criterion is to minimize some function of these combined costs.

This article summarizes a study that was performed to provide a rational basis for reliability design of the SFOF power system. Briefly, the steps involved are: (1) the estimation of reliability/availability parameters from historical data and design specifications; (2) estimation of the reliability/availability of certain system configurations; (3) development of a cost (loss) function; and (4) analysis of minimum-cost configurations, after the choice of suitable performance criteria and the estimation of total reliability of the system being supported by the power system.

2. Estimation of Mean Time Between Failures

It is assumed that a system such as the primary power supply for the SFOF (commercial power to the JPL substation) has failures that are occurrences of a random variable X , described by the exponential probability density function *pdf*,

$$f(x; \lambda) = \lambda e^{-\lambda x}, \quad x \geq 0, \quad \lambda > 0$$

$$= 0, \quad \text{otherwise}$$

where λ is the parameter of the *pdf*; $\lambda = 1/\theta$, and θ = mean time to failure. The estimation problem, in this case, is to find a lower bound for θ such that there is a 95% confidence that the actual (population) value of θ is not less than this lower bound.

The maximum likelihood estimate of θ , θ^* (a point estimate) is

$$\theta^* = T/r$$

where

T = accumulated time in operation for the system

r = number of failures occurring in the interval over which T is measured

For r failures, the probability density function of θ^* is given as

$$f_r(x) = \frac{\lambda}{(r-1)!} (\lambda x)^{r-1} e^{-\lambda x}, \quad x \geq 0$$

$$= 0, \quad \text{otherwise}$$

which is the *gamma probability law*.

The χ^2 probability law is given by

$$f(y) = \frac{1}{2^{n/2} \sigma^n \Gamma(n/2)} y^{(n/2)-1} e^{-y/(2\sigma^2)}, \quad y > 0$$

with n degrees of freedom. It is noted that by making the substitutions $r = n/2$, $\lambda = 1/(2\sigma^2)$ into the gamma probability law, the χ^2 law is obtained.

In order to arrive at the required interval estimate, make the change of variable $x = 2r\theta^*/\theta = 2T/\theta$ in the gamma *pdf* for θ^* . This results in

$$f_r\left(\frac{2T}{\theta}\right) = \frac{1}{2^r \sigma^{2r} \Gamma(r)} \left(\frac{2T}{\theta}\right)^{r-1} e^{-(2T/\theta)/(1/2\sigma^2)}$$

Therefore, $2T/\theta$ is distributed as χ^2 with $2r$ degrees of freedom. It follows that a one-sided $100(1 - \alpha)\%$ confidence interval for θ is given by

$$\theta > \frac{2T}{\chi_a^2}$$

where χ_a^2 is the upper α percentage point for χ^2 with $2r$ degrees of freedom.

The data that were presented give $T = 7$ years, $r = 11$ failures; therefore, with the tabulated value, $\chi_{5\%, 22df}^2 = 33.9$, $\theta > 0.41$ year, with 95% confidence ($\lambda = 1/\theta < 2.4$ failures per year is the corresponding average failure rate interval).

3.1 Estimation of Mean Repair Time

The system is a *maintained* system; i.e., when a failure occurs, the system is returned to operation by repair (or replacement). It is of interest to know the distribution of repair times in order to make statements about system availability. It is also important to know the distribution, since there are certain critical system *down* times which affect mission success.

It is assumed that repair time is a random variable, Z , which is also described by the exponential probability law,

$$f(z; \mu) = \mu e^{-\mu z}, \quad z \geq 0, \quad \mu > 0 \\ = 0, \quad \text{otherwise}$$

with the parameter μ ($\mu \triangleq$ average repair rate; $m = 1/\mu \triangleq$ mean repair time). In the maintained system, there are dual processes of operation and repair; hence, both processes are treated formally in the same fashion.

Again, as in Section 2, the maximum likelihood estimate of m , m^* , is given by

$$m^* = W/r$$

where W is the accumulated time of the system in the repair state.

Also, for r terminations of the repair state, the probability density function of m^* is given by

$$f_r(z) = \frac{\mu}{(r-1)!} (\mu z)^{r-1} e^{-\mu z}, \quad z \geq 0 \\ = 0, \quad \text{otherwise}$$

After changing variable $z = 2W/m$, the distribution is given by

$$f_r\left(\frac{2W}{m}\right) = \frac{1}{2^r \sigma^{2r} \Gamma(r)} \left(\frac{2W}{m}\right)^{r-1} e^{-(2W/m)(1/2\sigma^2)}$$

Therefore, $2W/m$ is also distributed as χ^2 with $2r$ degrees of freedom.

In the case of repair, it is of interest to know the two-sided $100(1-\alpha)\%$ confidence interval, which is given by

$$\frac{2W}{\chi_{a/2}^2} < m < \frac{2W}{\chi_{(1-a/2)}^2}$$

with $2r$ degrees of freedom.

The repair time data for the eleven failures are: one of 45 min, one of 2 min, nine of 0.5 min or less. For an upper bound, $W = 51.5$ min. For $2r = 22$ degrees of freedom, and 95% confidence,

$$\chi_{a/2}^2 \simeq 37.0, \quad \chi_{(1-a/2)}^2 \simeq 12.1 \\ 2W \simeq 103 \text{ min}$$

Therefore, $2.8 \text{ min} < m < 8.5 \text{ min}$. The seemingly wide dispersion between upper and lower bound of the interval is due to the small sample.

It should be mentioned that no data were available concerning the precision of measurement of the observed repair times. Since nothing is known about the precision, it will be assumed that the value chosen for W is fairly conservative.

4. Reliability and Availability of a Single Maintained System

The single maintained system has associated with it the parameters λ , the average failure rate, and μ , the average repair rate. For a system having the failure and repair variables described by the exponential probability law, it is well known that, in an interval T , the probability of at least one failure is

$$P_F[t \leq T] = \int_0^T \lambda e^{-\lambda x} dx = 1 - e^{-\lambda T}$$

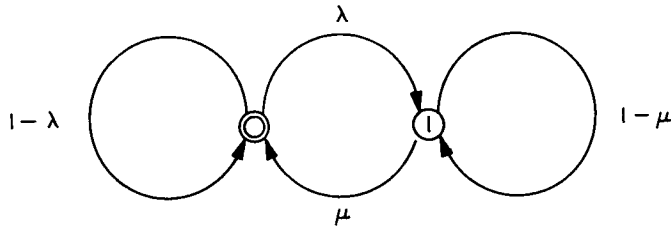
and the probability of no failure (success) is

$$P_S[t \leq T] = 1 - P_F[t \leq T] = e^{-\lambda T}$$

Similar probability functions give the probabilities for repair in an interval $[0, W]$.

The method of Markov processes is useful for the description of a single maintained system. In the case of a single mode of failure, the system has two possible states; i.e., the operating state, and the failed (or *down*) state.

A simple graph model of such a system is



where the states are

0 = operating

1 = down

If state 0 is occupied at time t , there is a probability $\lambda\Delta t + O(\Delta t)$ of a transition to state 1 in $(t, t + \Delta t)$, independent of occurrences prior to t ; if state 1 is occupied at t , there is the constant probability of transition $\mu\Delta t + O(\Delta t)$, to state 0 in $(t, t + \Delta t)$. The transition matrix \mathbf{P} can be written

$$\mathbf{P} = \begin{bmatrix} 0 & 1 \\ 1 & \lambda\Delta t \\ (1 - \lambda\Delta t) & \mu\Delta t \\ (1 - \mu\Delta t) & 0 \end{bmatrix}$$

Denoting by p_0, p_1 the probabilities of being in states 0 or 1, respectively, the differential equations of the process can be formed directly:

$$p_0(t + \Delta t) = p_0(t)(1 - \lambda\Delta t) + p_1(t)\mu\Delta t + O(\Delta t)$$

$$p_1(t + \Delta t) = p_0(t)\lambda\Delta t + p_1(t)(1 - \mu\Delta t) + O(\Delta t)$$

Then by transposing terms, dividing by Δt , and taking the limit as $\Delta t \rightarrow 0$:

$$\frac{dp_0(t)}{dt} = -\lambda p_0(t) + \mu p_1(t)$$

$$\frac{dp_1(t)}{dt} = \lambda p_0(t) - \mu p_1(t)$$

These equations are most simply solved by Laplace transform methods; namely, denoting $\mathcal{L}[p_i(t)] \triangleq p_i(s)$,

$$sp_0(s) - p_0(0) + \lambda p_0(s) - \mu p_1(s) = 0$$

and

$$sp_1(s) - p_1(0) - \lambda p_0(s) + \mu p_1(s) = 0$$

Denote by $\mathbf{p}(t), \mathbf{p}(s)$, etc., the row vectors $\mathbf{p}(t) = (p_0(t), p_1(t))$, etc., and let

$$\mathbf{P} = \begin{bmatrix} 1 - \lambda & \lambda \\ \mu & 1 - \mu \end{bmatrix}$$

Then, the solution to the equations is given by

$$\mathbf{p}(s) = \mathbf{p}(0) [(s + 1)\mathbf{I} - \mathbf{P}]^{-1}$$

where \mathbf{I} is the identity matrix. Then, $\mathbf{P}(t)$ is the matrix of the inverse transform of $[(s + 1)\mathbf{I} - \mathbf{P}]^{-1}$; i.e.,

$$\mathbf{P}(t) = \mathcal{L}^{-1}\{[(s + 1)\mathbf{I} - \mathbf{P}]^{-1}\}$$

The elements of $[(s + 1)\mathbf{I} - \mathbf{P}]^{-1}$ are found by partial fraction expansions. For $\mathbf{P}(t)$, we can write

$$\mathbf{P}(t) = \begin{bmatrix} \frac{\mu}{\lambda + \mu} & \frac{\lambda}{\lambda + \mu} \\ \frac{\mu}{\lambda + \mu} & \frac{\lambda}{\lambda + \mu} \end{bmatrix} + e^{-(\lambda + \mu)t} \begin{bmatrix} \frac{\lambda}{\lambda + \mu} & \frac{-\lambda}{\lambda + \mu} \\ \frac{-\mu}{\lambda + \mu} & \frac{\mu}{\lambda + \mu} \end{bmatrix}$$

Therefore, for any time t ,

$$\mathbf{p}(t) = \mathbf{p}(0)\mathbf{P}(t) \quad (1)$$

Furthermore, the steady-state (stationary) transition matrix is

$$\lim_{t \rightarrow \infty} \mathbf{P}(t) \triangleq \mathbf{P}(\infty) = \begin{bmatrix} \frac{\mu}{\lambda + \mu} & \frac{\lambda}{\lambda + \mu} \\ \frac{\mu}{\lambda + \mu} & \frac{\lambda}{\lambda + \mu} \end{bmatrix}$$

Since there are two possible initial vectors (*a posteriori*), namely, $\mathbf{p}(0) = (1, 0)$ or $\mathbf{p}(0) = (0, 1)$, it follows that the stationary probability vector is

$$\mathbf{p}(\infty) = \left(\frac{\mu}{\lambda + \mu}, \frac{\lambda}{\lambda + \mu} \right)$$

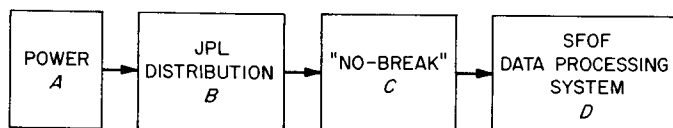
The stationary probability vector has the operations interpretation that, long after the system has been started, the probabilities of finding it in states 0 or 1 are given by the components of $p(\infty)$.

The solution satisfying initial conditions for Eq. (1) can be written directly in component form as

$$\left. \begin{aligned} p_0(t) &= \frac{\mu}{\lambda + \mu} + \left[p_0(0) - \frac{\mu}{\lambda + \mu} \right] e^{-(\lambda + \mu)t} \\ p_1(t) &= \frac{\lambda}{\lambda + \mu} + \left[p_1(0) - \frac{\lambda}{\lambda + \mu} \right] e^{-(\lambda + \mu)t} \end{aligned} \right\} \quad (2)$$

These equations are useful for computing the reliability and availability of the system.

Consider the reliability of the following system over various time intervals (i.e., the probability of continuous operation)



where

A = primary power source

B = JPL transmission from the power source to the user

C = on-line "no-break" system which provides inertia sufficient to regulate surges and "small" drop-outs

D = essential data processing and auxiliary areas for mission support

Of interest is the reliability of A; for simplicity, it is assumed that B, C, and D are sufficiently more reliable than A, that they meet operational criteria (actually, this assumption is not true for B, but on the basis of design specifications and testing data supplied for C and D, it is good for the remainder of the system). The probability of success for A in an interval $[0, T]$ is

$$P[S; t \leq T] = e^{-\lambda T}$$

where λ is evaluated in Section 2. Changing scale for λ to hr^{-1} , it is found that, with 95% confidence,

$$\lambda < 0.00028 \text{ hr}^{-1}$$

Table 2 gives 95% confidence level $P[S]$ corresponding to the tabulated length of time intervals.

Table 2. Success probabilities, 95 % confidence

$T, \text{ hr}$	$P[S] > p$
3	0.999
12	0.997
24	0.993
72	0.98
288	0.92

A partially backed-up (redundant) power concept would provide emergency power to the actual support subsystems, but not to such heavy-load utilities as air-conditioning. In such a case, the computer systems would continue to operate for 15 to 30 min before overheating will cause automatic shutdown; probabilities of the primary source being down for greater intervals can be calculated. The probability of being "renewed" in the interval $[0, T]$ is

$$P[R; t \leq T] = 1 - e^{-\mu T}$$

In this case, the critical value of the average repair rate is the upper bound of the 95% confidence interval; changing scale to hr^{-1} : $\mu > 7.04 \text{ hr}^{-1}$, with 95% confidence. Table 3 shows the values associated with the two critical times.

Table 3. Recovery probability in time $[0, T]$, 95 % confidence

$T, \text{ hr}$	$P[R] > p$
0.25	0.83
0.5	0.97

The development for a single-element, two-state system can be generalized to several elements; indeed, some of the possible generalizations will be required for computing system reliabilities in the backed-up system configurations. As an example, consider a system which has two elements, A (λ_1, μ_1) and B (λ_2, μ_2), operating in parallel redundant fashion. Sufficient repair facilities are available so that the repair of one element never depends upon

the repair of the other. Let the operational state for A be denoted thus, and the down state be denoted \bar{A} ; similarly for B. We can then write the state transition matrix for a "small" interval $(t, t + \Delta t)$ as

$$\mathbf{P}(t, t + \Delta t) = \begin{matrix} & \begin{matrix} AB & \bar{A}B & A\bar{B} & \bar{A}\bar{B} \end{matrix} \\ \begin{matrix} AB \\ \bar{A}B \\ A\bar{B} \\ \bar{A}\bar{B} \end{matrix} & \begin{bmatrix} 1 - (\lambda_1 + \lambda_2) \Delta t & \lambda_1 \Delta t & \lambda_2 \Delta t & 0 \\ \mu_1 \Delta t & 1 - (\lambda_2 + \mu_1) \Delta t & 0 & \lambda_2 \Delta t \\ \mu_2 \Delta t & 0 & 1 - (\lambda_1 + \mu_2) \Delta t & \lambda_1 \Delta t \\ 0 & \mu_2 \Delta t & \mu_1 \Delta t & 1 - (\mu_1 + \mu_2) \Delta t \end{bmatrix} \end{matrix}$$

To find the reliability of such a system, the failure state $\bar{A}\bar{B}$ is made an absorbing state, and the equations are solved for the probability that the system will not reach an absorbing state in the interval of interest $[0, T]$. Thus, the row corresponding to $\bar{A}\bar{B}$ in $\mathbf{P}(t, t + \Delta t)$ is replaced by $(0, 0, 0, 1)$, to yield the matrix $\mathbf{P}^*(t, t + \Delta t)$. From this matrix, we find the system of differential equations $(d/dt) \mathbf{p}(t) = \mathbf{A} \mathbf{p}(t)$. From this, the Laplace transforms of the system, $\hat{\mathbf{p}}(s) = \mathcal{L}[\mathbf{p}(t)]$, are found:

$$\hat{\mathbf{p}}(s) = \mathbf{p}(0) [s\mathbf{I} - \mathbf{A}]^{-1}$$

This system is solved, and the inverse transform

$$\mathcal{L}^{-1}[\hat{\mathbf{p}}(s)] = \mathbf{p}(t)$$

gives the required vector $\mathbf{p}(t)$, which may be evaluated at T . The reliability of the system in $[0, T]$ is

$$R(T) = 1 - p_{\bar{A}\bar{B}}(T)$$

The development of the loss function, and the subsequent power system evaluation will be dealt with in a subsequent issue of this volume.

VI. Operations Programming

A. SFOF Conversion Project: *Surveyor* and *Lunar Orbiter* Mission-Dependent Software, H. Alcorn

1. Introduction

The software system for the *Lunar Orbiter* and *Surveyor* Projects consists of an integrated system of computer programs for the SDS 920, IBM 7044, and IBM 7094 computers. Of these, the IBM 7044 computer functions as an input/output processor in the Space Flight Operations Facility (SFOF) data processing system. The software system which operates in the IBM 7044 computer consists of both mission-independent and mission-dependent programming. It is the purpose of this article to describe the mission-dependent or project-oriented portion of this system for *Surveyor* and *Lunar Orbiter* Projects as implemented under the SFOF conversion project. Also described is the overall implementation plan and schedule.

2. *Surveyor* System Interface with Mission-Independent System

There are two areas of interface between the *Surveyor* system and the mission-independent system. The first is

the data transfer interface in which the data are moved into the *Surveyor* system from the independent system, and also from the *Surveyor* system back to the independent system.

All data passing into the mission-dependent system from the mission-independent system come through three system buffers:

1. Telemetry processing system buffer (TPSB).
2. Telemetry (teletype) data buffer (TELB).
3. Command confirmation buffer (COMB).

Data output from the *Surveyor* system to the mission-independent system are through both a system buffer and a mission-independent subroutine. All telemetry data are output, by the *Surveyor* system, to the telemetry data buffer (TLMB) where they are available for output on the bulk printers or plotters. Confirmed commands and data alarms, which are to be displayed immediately upon the bulk printers, are output via a mission-independent printer subroutine. The *Surveyor* alarm status printout and the coefficient verification printout are also output via the printer subroutine.

The second interface between the *Surveyor* system and the mission-independent system is the control interface. Control can be differentiated into three separate areas.

1. Program and overlay-subroutine movement from auxiliary memory to overlay memory.
2. Program execution.
3. User requests.

Control areas 1 and 2 can almost be considered as one area, since a program is not brought into overlay memory unless it is going to be executed. The mission-independent system determines when a mission-dependent program is to be executed.

The criterion for the execution of the *Surveyor* telemetry processing program (STEP), the *Surveyor* communications processor program (SCPP), and the command confirmation printout program (SCMP), is the presence of data in the following buffers: buffer TPSB for program STEP, buffer TELB for program SCPP, and buffer COMB for program SCMP. The other two *Surveyor* system programs, *Surveyor* alarm status printout and the *Surveyor* calibration verification, are called into overlay and executed by a request from a user's area via a message composer input. The *Surveyor* alarm update subprocessor (M30S) operates as a direct result of a message composer request. It does not, however, run as a program in the mission-dependent overlay area of core, but as a portion (subprocessor) of the mission-independent message checking and disposal subroutine.

When it has been determined that a program is to be executed, the name of that program is put into a program-execution queue list. When the program name arrives at the top of the queue, the mission-independent system moves it from the auxiliary memory into the mission-dependent overlay area along with the needed mission-dependent subroutines. The *Surveyor* program is then given control, upon which it runs to completion. Control is then given back to the mission-independent system.

The third control type, user requests, are input to the *Surveyor* system via a message composer or card reader. These messages are processed by the *Surveyor* software routines which are a part of the mission-independent message checking and disposal subroutine. The action taken as a result of the message depends upon the message control word.

Fig. 1 diagrams the data flow through the mission-independent system, and to and from the *Surveyor* system. Rectangular boxes represent data buffers, and hexagonal boxes represent the mission-independent programs that move the data through the system. The *Surveyor* system is symbolized by the large rectangular box in the middle of the figure. The message subprocessors of the *Surveyor* system are shown as running within and under the control of the mission-independent subroutine (MCDS).

3. *Surveyor* Software System

The *Surveyor* spacecraft mission-dependent system is responsible for processing the *Surveyor* spacecraft telemetry data in the IBM 7044 input-output-control computer. This responsibility includes:

1. Decommultiplexing and identifying the telemetry data from the communications processor (CP).
2. Recognizing data mode changes and decommultiplexing, identifying, and synchronizing the data by frame according to the mode.
3. Time-tagging the data.
4. Categorizing the data for output into frames or subframes.
5. Checking specified data for out-of-limit conditions (alarming).
6. Placing the processed data into mission-independent output buffers for bulk printer, teleprinter, and plotter displays.
7. Displaying the confirmed spacecraft commands on the SC 3070 bulk printers as they are received from the DSS.

The *Surveyor* mission-dependent program performs the above tasks within the framework of the mission-independent program system. Some portions of the tasks, in fact, are performed by the mission-independent programs, since these tasks are basically the same for all missions. Among these tasks are: control of the administrative typewriters, bulk printers and plotters, transmission of spacecraft commands from the shared disk to the communications processor (CP), logging all incoming data on tape and disk, controlling which telemetry data channel the mission-dependent program will receive data from for processing, and control of the execution of the mission-dependent program.

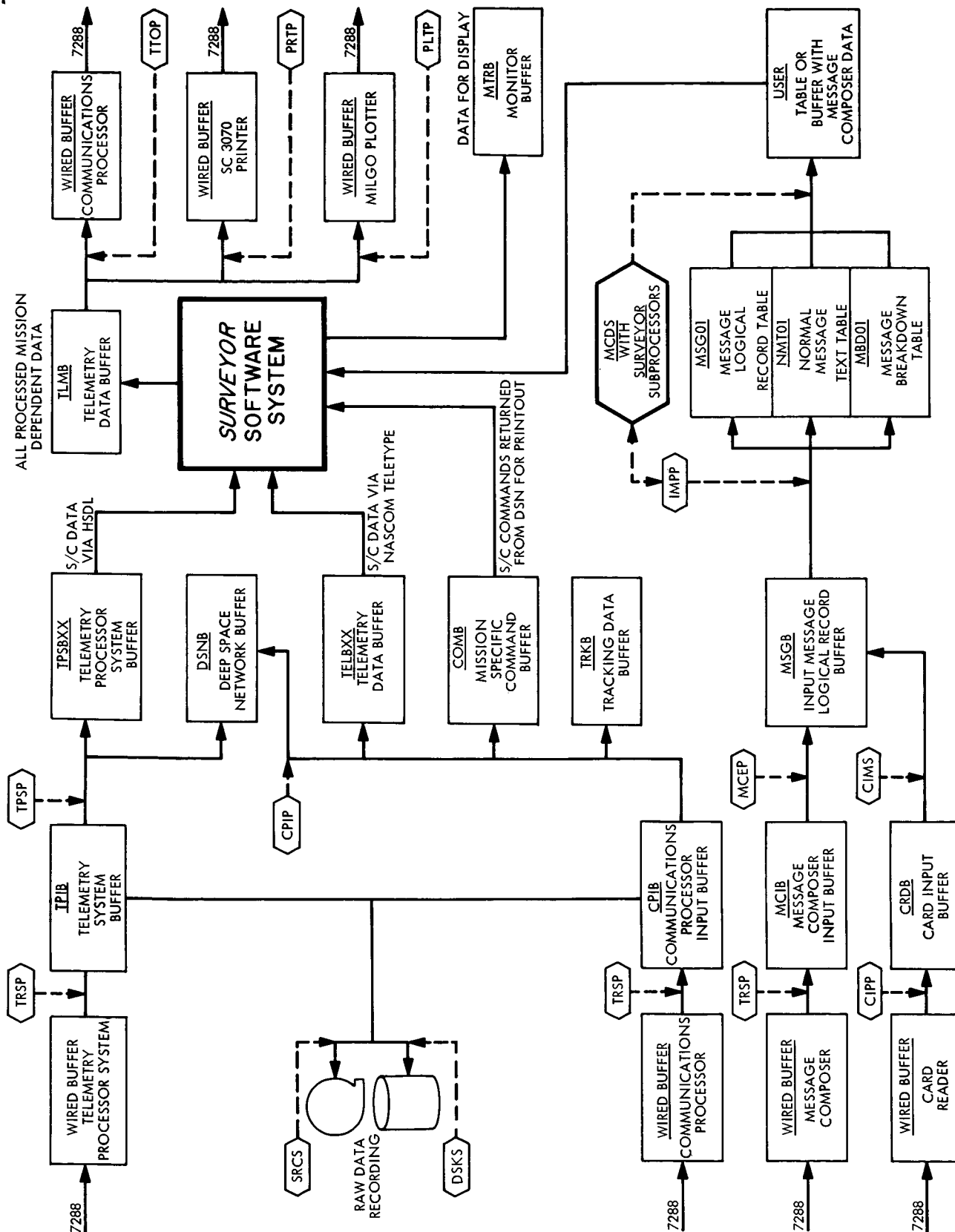


Fig. 1. IBM 7044R computer software system data flow

The mission-dependent program operates in overlay memory; that is, the program is stored on bulk-storage drums and is brought into the core memory by the mission-independent system whenever there is *Surveyor* telemetry data to be processed. The advantage of the overlay memory scheme is that it allows more than one program to operate in the same core memory area.

The *Surveyor* program system is made up of a number of programs and overlay subroutines. When telemetry data are transmitted via high-speed data lines and pre-processed in the SFOF telemetry system, the *Surveyor* telemetry processing program is brought into memory with its related overlay subroutines, and is executed. When telemetry data are transmitted from the site via teletype lines through the communications processor, the *Surveyor* communications processor program (SCPP) is brought into overlay memory with its related overlay subroutines and executed. Fig. 2 is a simplified block diagram of the *Surveyor* mission-dependent processing system. It should be noted that all programs and overlay subroutines operate in overlay memory, while all *Surveyor* tables are stored in permanent memory. Program STEP does not occupy the overlay memory at the same time as program SCPP. Since the same overlay subroutines are used by both programs, they must be brought into overlay memory whenever either program is run.

a. Telemetry data input processor. The two methods of transmitting telemetry data from the DSN site to the SFOF are via the high-speed data link (HSDL) and teletype lines. The *Surveyor* telemetry data, when transmitted over the high-speed data link, are input to the telemetry processing system prior to input to the IBM 7044 computer. The telemetry processing system decommutates and identifies the spacecraft telemetry data prior to input to the IBM 7044 computer. The telemetry processing program STEP receives the data from the telemetry processing system via the IBM 7044 computer mission-independent system.

Program STEP performs the following functions on the telemetry data:

1. Separates the data into frames and subframes by observing the frame sync words.
2. Time-tags each frame and subframe of data.
3. Parity-checks each datum.
4. Formats the data into a format suitable for the output buffers of the mission-independent system.
5. Recognizes data mode changes.

6. Counts the number of words in each frame and sub-frame to insure that the frame size is correct.
7. Controls the execution of the *Surveyor* alarm processor overlay subroutine and the *Surveyor* output and calibration subroutine.
8. Sends alarm messages to the DPCC whenever there appears to be a problem in the *Surveyor* telemetry data stream.

When the *Surveyor* telemetry data are transmitted to the SFOF via teletype lines, they are input to the communications processor and then to the IBM 7044 computer. The teletype-telemetry program for *Surveyor* (SCPP) receives the teletype data via the mission-independent system. The data have not been decommutated or time-tagged prior to their input to program SCPP. The functions of this program are, therefore, to decommutate and identify the data, in addition to performing the same tasks as are performed by program STEP. The teletype data stream contains a time frame every 5 min of operation. It is, therefore, necessary for program SCPP to extrapolate the time from frame to frame during the 5-min period in order to time tag each frame of telemetry data with a reasonably accurate time.

b. Data alarm processing and status-light updating. The *Surveyor* alarm processor overlay subroutine (SAPS) carries out the data alarm processing, and the spacecraft performance analysis area (SPAA) status-light processing for both HSDL-telemetry data and teletype-telemetry data.

The *Surveyor* system has the capability of monitoring up to 50 digitally-coded analog telemetry data values. Each alarmed datum is checked against a high and low limit, and if the datum is out of limits, an alarm message is printed out on a bulk printer in the spacecraft performance-analysis area. The alarm message bypasses the printer queue list so that the message is printed immediately.

The 13 digital status words are interrogated to determine whenever any of the digital status bits change state. When this happens, the engineering term of the changed bit and its new state (1 or 0) is output on the SC 3070 bulk printer.

Each of the 24 status lights in the user areas is assigned to a particular digital status bit. At the present time, there are 19 different patterns of these assigned bits. The

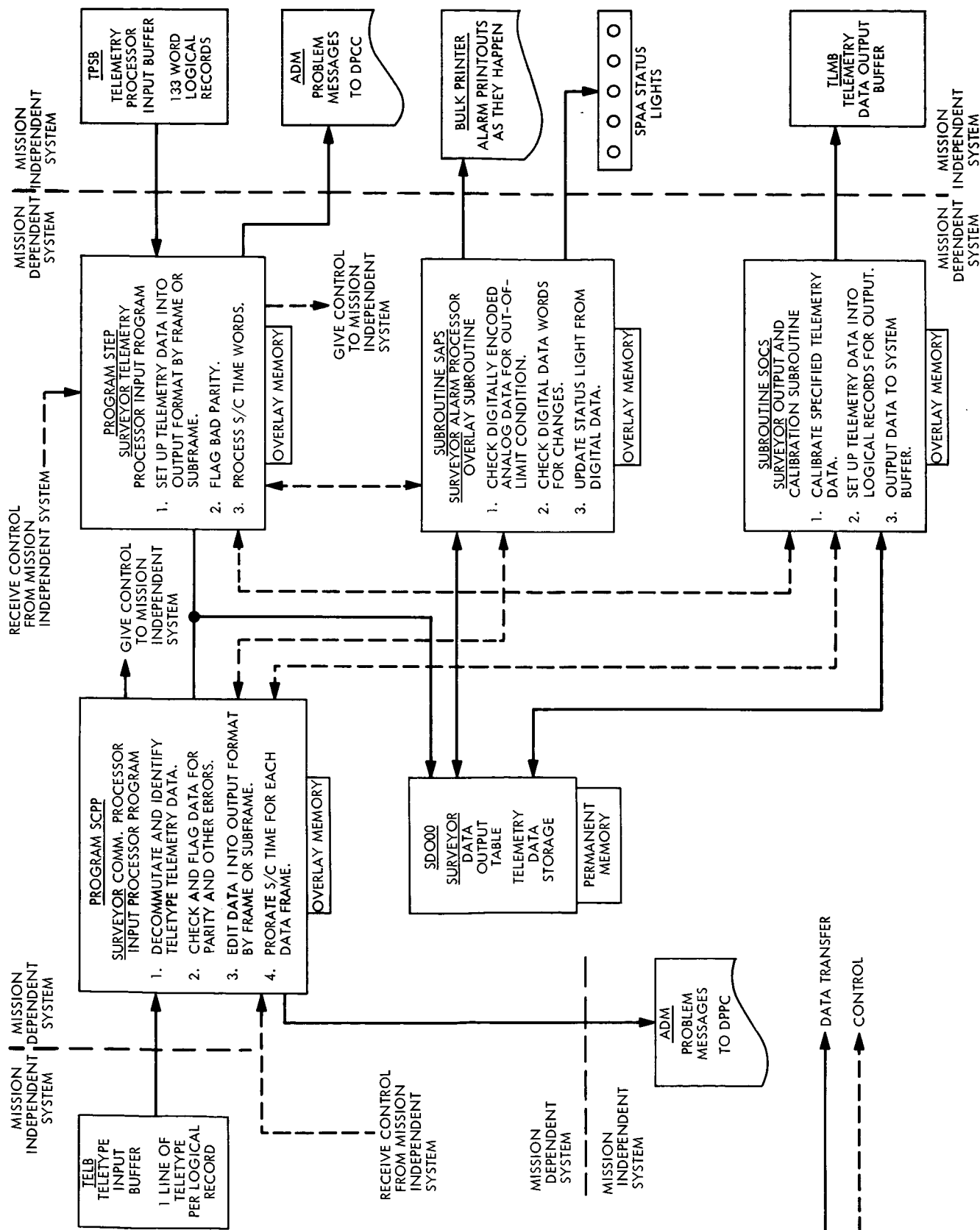


Fig. 2. Surveyor telemetry data processing system

particular pattern that is used is a function of the incoming telemetry data mode. The user area, however, can choose any one of the 19 status-light patterns by a message composer input message. When the data mode changes again, however, the status-light pattern for the new mode is automatically assigned.

The data alarms can be changed whenever necessary by inputting to the computer a message via the message composer or the card reader. The type of changes that can be made are:

1. Enable or disable a particular alarm.
2. Enable or disable all alarms.
3. Add new alarms (up to a maximum of 50).
4. Delete alarms.
5. Change the limits of a particular alarm.

The *Surveyor* alarms, their limits, and other pertinent facts about them can be printed on the bulk printer. This status printout is done by the *Surveyor* alarm status printout program (SASP). The printout can be obtained by a request to the message composer in the user area that program SASP be run. A block diagram of the data alarming and status light update system is shown in Fig. 3.

c. Telemetry data calibration and output processing. The telemetry data are calibrated and set up for output back to the mission-independent system, by an overlay subroutine called *Surveyor* output and calibration overlay subroutine (SOCS). This subroutine makes the required calibration on certain of the telemetry data and the TV-ID data. Both the original raw and the resultant calibrated data are prepared for output to the mission-independent buffer. The calibration function of the telemetry data contains a prespecified calibration voltage. This calibration value can be changed from the area via the message composer. The calibration value must be specified in raw counts.

The *Surveyor* telemetry data are output to a mission-independent buffer in logical records. Each logical record contains a time word and a portion or all of the telemetry data from a frame of data. Since all of the telemetry data in a frame must be available for output by print or plot, and because of the design of the mission-independent print and plot programs, there can be no

duplicate data types within a logical record that are output to the system buffer. This means that, for data frames which contain a number of data types that appear more than once, there are a number of logical records made up from each of the frames of data. The number of logical records is equal to the number of times the most frequent data type appears within the frame. The overlay subroutine outputs these logical records to the system telemetry data output buffer so that they are available for print and plot requests.

d. Command processing. The function of the *Surveyor* mission-dependent system in the area of spacecraft commands is to print only the confirmed commands on the specified bulk printers as they are received in the IBM 7044 computer. The returned commands are stored by the mission-independent system into a system buffer. Whenever this buffer contains data, the *Surveyor* command processor program (SCMP) is brought into overlay memory and executed.

Program SCMP receives the data from the system buffer, extracts the confirmed commands, and formats them into a readable print format. The format contains the time that the command was executed, spacecraft number, deep space station (DSS) number, and the command number, and magnitude if any. This information is printed immediately on the specified printer, breaking into the current material that is being printed.

The confirmed commands can be output on as many as six SC 3070 bulk printers at one time. The particular printers that are used can be specified by a real time input to the system via a message composer.

The mission-independent system performs the other IBM 7044 computer spacecraft command functions, such as receiving the commands from the shared disk, adding the correct teletype headers, and outputting the commands to the CP. The mission-independent system also receives the verified commands from the CP and stores them on the shared disk.

e. System initialization and verification. The *Surveyor* mission-dependent table initialization is performed by subprocessors that operate within, and under the control of, the mission-independent initialization program. This program is run either in the IBM 7094 or in the IBM 7044 computer, thus providing the capability of initialization of the system from either computer.

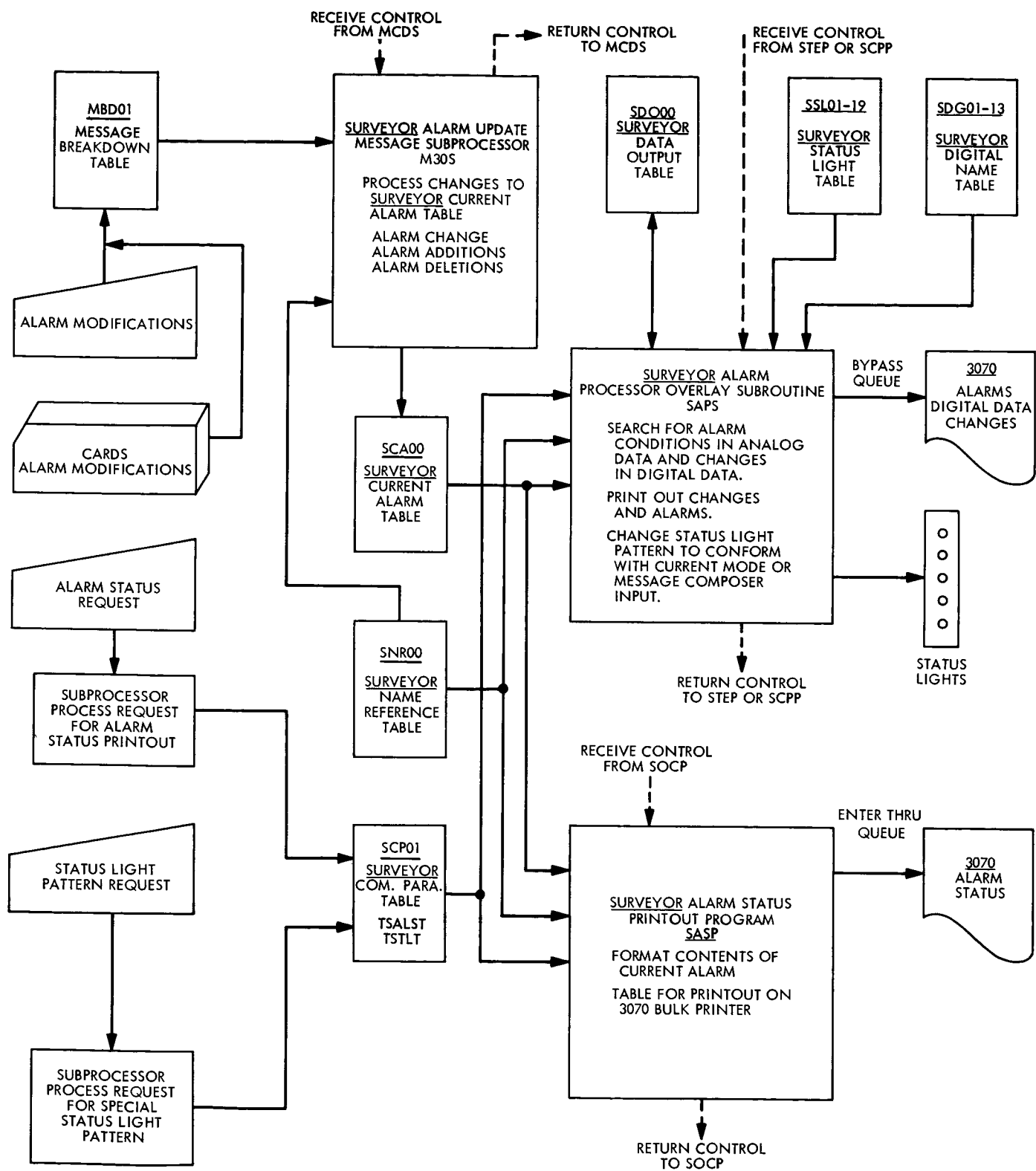


Fig. 3. Surveyor alarming system

The following parameters of the *Surveyor* system are initialized:

1. Alarms.
2. Data names and related items, i.e., exponents.
3. Engineering coefficient verification high and low check values.
4. Engineering coefficients.¹
5. Plot formats.¹
6. Print formats.¹

The information for these parameters is inserted on punched cards, and the subprocessor converts this information to specified system tables, which are stored on disk and magnetic tape when the IBM 7094 computer is used for the initialization process, or is stored on drum and magnetic tape when the IBM 7044 computer is used for initialization. Each initialization package is uniquely identified with its own identification number.

The engineering coefficients are verified by converting two unique check numbers from raw counts to engineering units for each *Surveyor* digitally-encoded analog datum. The *Surveyor* calibration verification program (SCVP) is called into overlay memory to perform this verification function whenever required by a user area request via a message composer input. The program prints the unique check values, conversion results, and coefficients of the conversion function for each datum. The program has the additional capability of printing the above-described format for a single telemetry datum, as specified by a request from the user area, or displaying only the *Surveyor* coefficients without the check values.

4. Lunar Orbiter Interface with Mission-Independent System

The areas of interface between the *Lunar Orbiter* system and the mission-independent (MI) system are as follows:

1. Data transfer interface, in which data are moved from the MI system to the *Lunar Orbiter* system.
2. Data transfer interface, in which data are moved from the *Lunar Orbiter* system to the MI system.

¹The task of defining and writing the subprocessor routines to initialize these parameters is the responsibility of the mission-independent project, since its programs and subroutines use this information.

3. Control interface, in which the mission-independent system moves *Lunar Orbiter* program overlay from the overlay storage media to overlay core storage, transfers control to the *Lunar Orbiter* system for program execution, and receives control back from the *Lunar Orbiter* system.
4. Subprocessor interfaces required for processing *Lunar Orbiter* specific initialization cards and message composer requests.

Telemetry data are transferred from the mission-independent system to the *Lunar Orbiter* system by means of the system buffers, TPSB and TELB. The data are extracted from these buffers by means of the mission-independent routine (BPES). Command verification messages are transferred from the mission-independent system to the *Lunar Orbiter* system by means of the system buffers (COMB). The data are extracted from these buffers by means of the mission-independent routine (BPES).

Telemetry data are transferred from the *Lunar Orbiter* system to the mission-independent system by means of the system buffers (TLMB). The data are placed in these buffers by means of the mission-independent routine (BPSS). Command data for transmission to the communications processor (CP) are transferred from the *Lunar Orbiter* system to the mission-independent system by means of the mission-independent routine (CPOS). *Lunar Orbiter* specific displays for the SC 3070 printers are output via the mission-independent routine (PRTS). *Lunar Orbiter* specific displays for the teleprinter are output via the mission-independent routine (CPOS). Administrative messages for display on the administrative printers are output via the mission-independent routine (ADMS).

When it is determined that a *Lunar Orbiter* program needs to be executed, the name of that program is inserted into a program-execution queue list. When the program name arrives at the top of the queue, the mission-independent system moves the program from the overlay media into the *Lunar Orbiter* overlay area along with required subroutines. Control is then transferred to the *Lunar Orbiter* program which runs to completion. The *Lunar Orbiter* program then returns control to the mission-independent system. The criteria for the execution of the *Lunar Orbiter* telemetry processor program (LTPP) are the presence of telemetry data in system buffers TPSB or TELB. The criterion for the execution of

the *Lunar Orbiter* command program is a message-composer request for the transmission of a command data file. The criterion for the execution of the *Lunar Orbiter* display program (LDSP) is a message-composer request for a *Lunar Orbiter* specific display.

Subprocessors required for processing *Lunar Orbiter* specific message composer requests function under the control of the mission-independent program (IMPP). As such, the subprocessors function in the mission-independent overlay core storage area. They receive control from program IMPP and return control to program IMPP.

Subprocessors required for processing *Lunar Orbiter* specific initialization cards function under the control of the mission-independent program, INTP. The subprocessors receive control from program INTP and return control to program INTP. Note that program INTP operates as a separate computer program and does not function as part of the real-time IBM 7044 computer data-processing system.

Fig. 4 diagrams the data flow through the mission-independent system to the *Lunar Orbiter* system and from the *Lunar Orbiter* system to the mission-independent system. Rectangular boxes represent data buffers, and hexagonal boxes represent the mission-independent programs that move the data through the system. The subprocessors required for processing *Lunar Orbiter* specific message-composer requests are shown as part of the mission-independent subroutine MCDS.

5. General Description of the *Lunar Orbiter* System

While most, if not all, of the basic capabilities of the IBM 7044 computer hardware and software are needed for the proper exercise of *Lunar Orbiter* mission control, the *Lunar Orbiter* project has established specific requirements in the following areas:

1. Real-time processing (i.e., identification routing, decommutation, and conversion) of incoming telemetry data when received via HSDL, or one or two teletype lines.
2. Real-time display of an incoming telemetry data stream in raw form (i.e., before processing) as received via HSDL or teletype.
3. Real-time display of selected measurements, after decommutation, either in raw data counts or in engineering units.

4. Real-time monitoring of selected measurements for out-of-tolerance conditions and the issuing of appropriate alarm messages when such conditions occur.
5. Controlling of the transmission of spacecraft command messages from the SFOF to deep space stations (DSS) and verifying the correctness of such transmissions.

In conjunction with the mission-independent system, the *Lunar Orbiter* system meets these specific requirements. The *Lunar Orbiter* system, per se, is composed of a telemetry processor, a command processor, a display processor for mission-dependent displays, message composer subprocessors and associated tables and buffers. Fig. 5 is a simplified block diagram of the *Lunar Orbiter* system. For the most part, programs and subroutines operate in overlay memory while tables and buffers occupy permanent core. A brief description of the processors that make up the *Lunar Orbiter* system follows.

a. Telemetry processor. The telemetry processor is made up of *Lunar Orbiter* telemetry processor program (LTPP) with the following associated subroutines: *Lunar Orbiter* message block subroutine (LMBS), *Lunar Orbiter* decommutation subroutine (LDCS), and *Lunar Orbiter* alarm subroutine (LALS). In general, the telemetry processor performs the following functions:

1. Receives the telemetry data from the mission-independent system.
2. Assembles the telemetry data stream into complete telemetry frames.
3. Recognizes changes in the source of the telemetry data stream and changes in the edit-table mode.
4. Decommutates the telemetry frame into time-tagged, identified measurement values.
5. Limit-tests designated telemetry measurements and issues alarm messages as required.
6. Makes the identified measurement values available to the mission-independent system for display purposes.
7. When transmission is via high-speed data line (HSDL), makes the unprocessed telemetry data stream available for display purposes when requested by message composer requests.

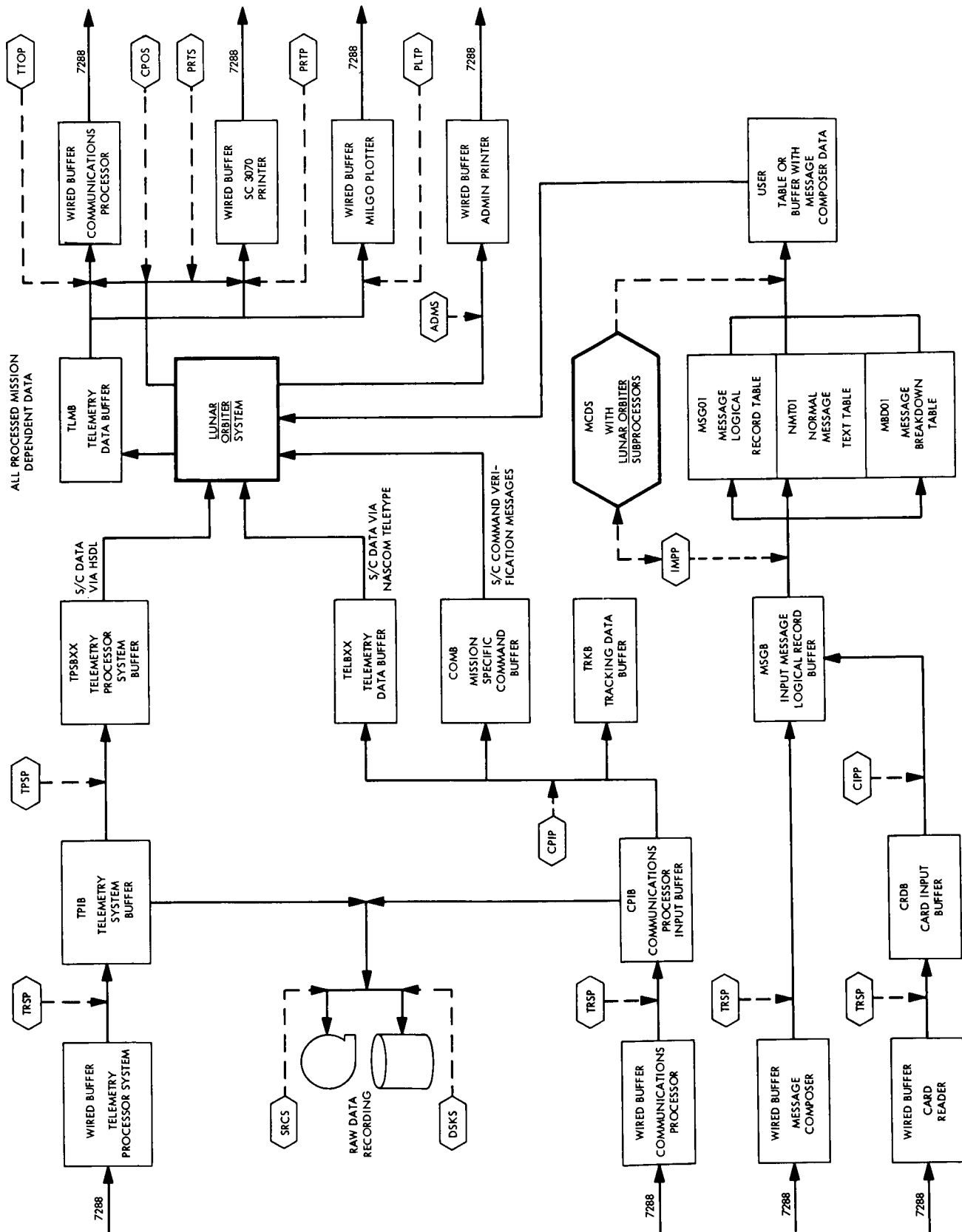


Fig. 4. Lunar Orbiter IBM 7044R computer software system data flow

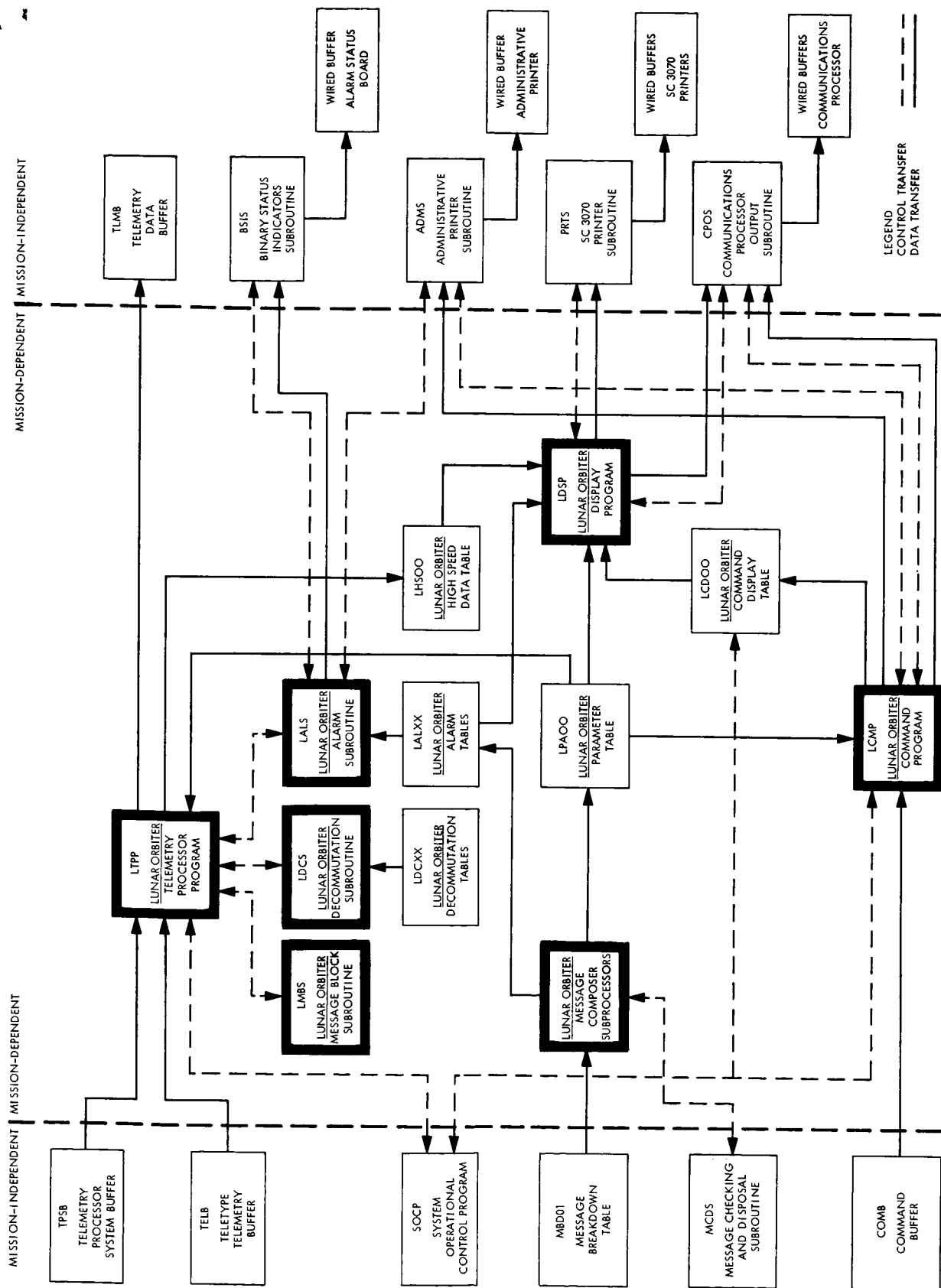


Fig. 5. Lunar Orbiter telemetry data processing system

b. Command processor. The command processor is made up of the *Lunar Orbiter* command program (LCMP). In general, the command processor performs the following functions:

1. When directed by message-composer request, obtains the teletype file from disk.
2. Identifies the teletype data file as being command data and insures that the command file has been verified by the user.
3. Checks the format of each segment of a command data file before that segment is transmitted.
4. Causes each segment of a command data file to be transmitted to a DSS on the basis of a message-composer request from the user or the receipt of a verification message from the DSS.
5. Causes each segment transmitted to be displayed on the administrative printers and to be made available for display by teleprinter.

c. Display processor for mission-dependent displays. The display processor for mission-dependent displays is made up of the *Lunar Orbiter* display program (LDSP). In general, the display processor performs the following functions:

1. When directed by message-composer request, causes the unprocessed telemetry data as transmitted via a high-speed data line to be displayed on the specified SC 3070 printer.
2. When directed by message-composer request, causes the alarm table to be displayed on the specified SC 3070 printer.
3. When directed by message-composer request, causes the command file currently being transmitted from the SFOF to a DSS to be displayed on the specified teleprinter.
4. When directed by message-composer request, stops the mission-dependent display on the specified SC 3070 printer or the specified teleprinter.

d. Message-composer subprocessors. The message-composer subprocessors function under the control of the mission-independent system input message processor program (IMPP). The *Lunar Orbiter* system has four

message-composer subprocessors which perform the following functions:

1. Effect the designated changes to the *Lunar Orbiter* alarm tables specified by the message-composer request.
2. Process all message-composer requests related to the transmission of command data files from the SFOF to a DSS.
3. Process all message-composer requests related to mission-dependent processing of the telemetry data.
4. Process all message-composer requests related to mission-dependent displays.

6. Implementation Plan

The development of the MD programming task is being accomplished within an assigned project task group. This task group was established when the functional requirements were first specified. A task group leader (TGL) was chosen to carry out all functions and bear all responsibilities of the task.

a. Major milestones. On the basis of the functional requirements, the TGL set the major planning milestones (Fig 6). The major milestones are:

1. Request for programming (RFP)—written by each project to specify the requirements for processing of mission-oriented data.
2. Preliminary software system design (SSD)—accomplished by project task group to specify how the RFP would be implemented in programming terms.
3. Design review (DR)—conducted by a committee of software experts and project representatives.
4. Acceptance tests (AT)—test-verifies the integrity of the entire IBM 7044 computer software system before delivery to projects.

b. Documentation plan. Following is a list and description of the documents which are required to be published for the SFOF conversion project for both *Surveyor* and *Lunar Orbiter* projects.

1. *Software system design document*—describes the overall software system design and the programming interfaces which must be adhered to.
2. *Program detail design document*—contains a detailed description of each program and subroutine

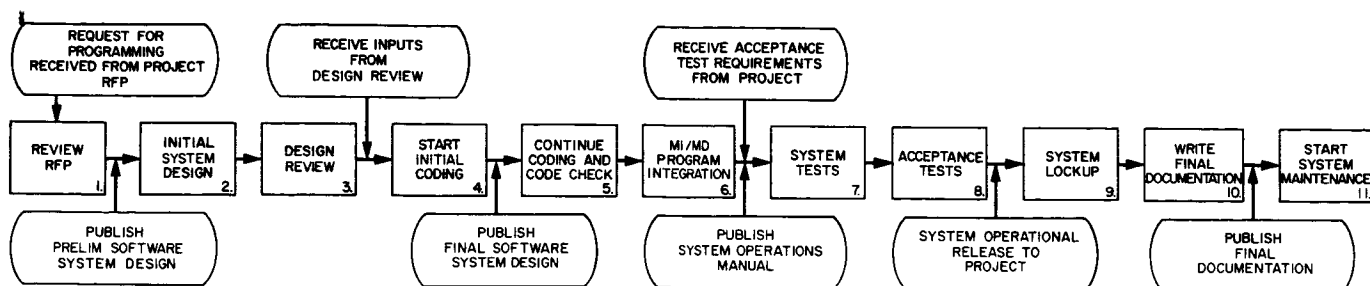


Fig. 6. IBM 7044R computer mission-dependent software milestones

and the associated data control tables/buffers. It includes a detailed flowchart of each program and subroutine.

3. *System operations manual*—contains the details for generating and operating the system programs. It describes options within the program, parameter formats, and various mechanisms for inputting those parameters.

4. *Final documentation*—compiles all existing documentation for the software. At this stage, all documentation is brought up-to-date.

c. *Schedule or status.* The *Surveyor* system has progressed through the various phases shown as milestones 1–5 in Fig. 6. At the present time some of the programs are in the MI/MD integration phase while others are in the final stages of code checking. The status of the individual programs is shown in Fig. 7.

The *Lunar Orbiter* system has progressed through the phases shown as milestones 1–4 in Fig. 6. At the present time, some of the programs are in the implementation

PROGRAM / SUBROUTINE NAME	DESIGNED	CODED	INTEGRATED INTO SYSTEM	90% CHECKOUT
STEP				
SCPP				
SAPS				
SASP				
SALARM				
SOCS				
SCVP				
SCMP				
SUNS				
MD MESSAGE PROCESSORS				
SUTS				

Fig. 7. *Surveyor* IBM 7044R computer software program status

PROGRAM / SUBROUTINE NAME	DESIGNED	CODED	INTEGRATED INTO SYSTEM	90% CHECKOUT
LTPP			02-27-67	03-27-67
LMBS			02-27-67	03-27-67
LDCS			02-27-67	03-27-67
LALS			02-27-67	03-27-67
LDSP			02-27-67	03-27-67
LCMP			03-13-67	04-03-67
MD MESSAGE PROCESSORS			03-13-67	04-03-67

Fig. 8. *Lunar Orbiter* IBM 7044R computer software program status

phase. The status of the individual programs is shown in Fig. 8.

7. Summary

This report describes the SFOF conversion project with its two project interfaces—*Surveyor* and *Lunar Orbiter*. The two software systems, their division into specific modules of coding, and the mission-independent interfaces are discussed. Finally, the project implementation plan is described, delineating the major milestones, the documentation to be written, and the status of the two software systems.

B. DSIF Monitoring Programming: Interim Version (IMP), I. Urban

1. Introduction

A computer program has been written to fulfill an immediate need for monitoring certain DSIF functions and to serve as a pilot model for future monitoring designs. As such, the program, designated interim monitoring program (IMP) was conceived and implemented to provide quick station status displays with a minimal amount of long range planning and also to aid in developing the DSN Phase I monitoring system. IMP was

coded for an SDS 920 with 8K memory and operates in the digital instrumentation subsystem (DIS).

2. Description

The program interrogates or receives information from other subsystems or devices and converts, summarizes, displays, and logs this data. Basically, three types of data are monitored in this way:

1. Station operating configuration status.
2. Signal strength or AGC data.
3. Doppler data.

The station operating configuration can be described as the status of a series of switches (approximately 75) associated with the microwave and receiver subsystem. The status of these switches can be determined by the program at any time, using the 1-pps interrupt available from the frequency and timing subsystem and the parallel I/O facilities of the SDS 920 computer. The program interrogates these switches every second, logs on magnetic tape, compares this input status with a predefined configuration, and generates a typewriter message describing the differences, if any.

Signal-strength monitoring is accomplished by sampling AGC data once per second via an analog-to-digital converter, which is part of the DIS. If the receiver is in lock, the sample is converted to dbm using calibration curves previously input via typewriter or paper tape. A running mean and standard deviation is computed over a selected time interval, which is then available for typewriter display. All AGC data samples are logged on magnetic tape.

Doppler monitoring requires doppler predicts available from a magnetic tape. The program accepts doppler data at a rate of 1-6 samples/min, using the interrupt generated by the tracking data handling subsystem. Besides logging on magnetic tape, the program will compute the 1-second doppler count, the residuals (the difference between predicted and actual count), and the mean and standard deviation of these residuals over a selected time interval. A typewriter message with this information is generated once each minute.

3. Status

IMP is in general use at most of the DSIF stations. It has stimulated many suggestions from station personnel for improvements and additions, and, in this way,

it has served one of its major purposes. Its replacement, the DSIF phase 1 monitor is under development.

C. Antenna-Pointing Subsystem Phase 1 Computer Program For 210-Ft Antennas, R. Rovello

1. Purpose

The purpose of the antenna-pointing subsystem (APS) program is to provide the 210-ft antenna sites with the capability of pointing the tracking antenna and the master equatorial (ME) unit with an SDS 910 computer.

The APS program adds the following capabilities to the DSIF:

1. Improved spacecraft-acquisition time.
2. Ability to generate angle-search patterns for spacecraft acquisition.
3. Tracking, when received signal strength is too low for auto-track operations.
4. Programmed corrections to eliminate antenna structural and radio boresight shift pointing errors.
5. More flexibility and precision in control of antenna movement.

2. Program Functions

The program computes ephemeris from parameter inputs and provides position error signals via a digital-to-analog converter to the error assembly of the antenna/ME mechanical subsystem. Updating the errors is accomplished by computing the ephemeris in local hour-angle (LHA) and declination (DEC) for the ME unit and converting these to azimuth (AZ) and elevation (EL) for the antenna. The computer reads the angle encoders to determine the present position of the antenna and ME, and calculates the servo errors using the calculated ephemeris and the encoder readings.

Associated with the computer program is an operator panel, from which the operator may enter various parameters and subsystem changes which determine the program function.

These inputs are processed in order of priority, and internal corrections or changes are made accordingly. A typewritten log of each subsystem change is maintained by the program with the date and time of each entry.

The operator may also select various parameters for display at the panel such as time, Greenwich hour-angle of Aries, antenna/ME commanded positions, antenna/ME errors and antenna/ME offsets.

In addition to the functions mentioned above, the program performs internal tests, when time permits, to ensure that the computer is functioning properly. It performs read/write memory diagnostics and also checks the instructions for proper execution.

3. Modes of Operation

The program has four tracking modes (modes 1 to 4) and an idle or wait mode (mode 0). In the wait mode, the program environment is initialized, zero errors are sent to the servos, and the program awaits a selection of one of the tracking modes. When in a tracking mode, rate and position offsets may be entered to modify antenna/ME positions. Search patterns may be generated in modes 1, 2 and 3 to assist in "target" acquisition.

The four tracking modes are as follows:

1. Mode 1 is the star track mode and is used mainly for calibration purposes. The program accepts panel inputs of right ascension (RA) and DEC and updates the servo system at a sidereal rate.
2. Mode 2 is the planetary/spacecraft mode. In this mode, the operator enters three sets of RA and DEC. The entered coordinates (of the object to be tracked) are for 0 hr GMT of the first day of the track, the second day of the track, and the day after the track. Lagrange's interpolation formula is used to compute hourly points, and a linear interpolation is then performed between the hourly points to compute the ephemeris.
3. Mode 3 is the paper tape drive mode. The antenna and ME are positioned using the ephemeris read from paper tape. The coordinates on paper tape are in LHA and DEC and are time-tagged. Checks are performed on the data read to ensure that the format is valid and that the data do not exceed certain limits. The valid data are used to generate the servo errors that position the 210-ft antenna and ME.
4. Mode 4 is used for antenna calibration. The program accepts coordinates in AZ and/or EL or LHA and/or DEC. The program drives the antenna and ME to the selected position at a maximum rate.

4. Software Characteristics

The program is written in "Symbol" assembly language and occupies approximately 5,000 (decimal) words of its 8K memory. The program uses standard SDS-programmed operators for functions such as sin, cos, square root, \tan^{-1} , multiply and divide.

5. Program Accuracy

All angles are carried in the computer in $\text{deg} \times 10^3$ with the binary scaling at bit 20. All computations are performed in fixed-point single-precision arithmetic except the coordinate conversion from LHA/DEC to AZ/EL (and vice versa) which is performed in floating-point double-precision arithmetic.

6. Status

The program is currently in operation at the Mars Station at Goldstone. Acceptance by the DSIF digital systems development section is expected shortly.

D. PDP-7 Symbolic Assembler (BLAP), P. Poulson

1. Introduction

BLAP is a two-pass symbolic assembly program for the PDP-4 and PDP-7 computers with a 4K core memory. The program accepts programmer symbolic code in a standard card format from magnetic tape, converts to machine code, and prints and punches the binary results. Programs written for other PDP assemblers cannot be directly assembled with BLAP. However, in most cases, only minor changes are needed to do so. This program was written to be compatible with the machine and peripheral equipment in the telemetry processing station (TPS) which employs PDP-7 computers with magnetic tape units and on-line printers. However, an attempt is being made to create a single version that is usable for all PDP-4 and PDP-7 computers now in use at JPL.

2. Description

BLAP was developed and assembled using its own language. The current version uses 1280 locations for logic and about 2700 locations for tables and buffers. The tables for symbols, literals, and mnemonic codes may easily be expanded for use on machines with larger than 4K memories. Operational options to inhibit either listed or punched output have been provided. All control is accomplished through the accumulator switches.

The total assembly process is accomplished in two passes by reading through the symbolic program twice. Processing in the first pass consists of storing all symbol definitions, processing certain pseudo-operational codes, and calculating the current instruction counter. The second pass, using information saved by the first pass, will convert all codes, symbols, and numbers to binary, punch the binary or object program on paper tape, and list the results of the assembly on the on-line printer or on magnetic tape. Errors will be indicated on the assembly listing.

All symbolic input is from magnetic tape, in standard IBM magnetic-tape BCD code, with a bit density of 556 bpi. Each pass is terminated by reading an EOF or an "END" pseudo instruction, which will cause the input tape to rewind.

The object program is standard 8-level binary punched paper tape in read-in mode (RIM) format, which is the standard Digital Equipment Corp. (DEC) loader format. The tape is easily read as it is in one-to-one correspondence to the loaded memory image.

The assembly listing consists of the classical side-by-side compilation of input symbolics and resulting object code converted to octal. Error indicators appear as single-character codes printed at the far left margin. An alphabetized symbol table is listed at the conclusion of the assembly listing. Additional capabilities are as follows:

1. Symbol table capacity up to 600 6-character symbols.
2. Literal table capacity up to 300.
3. Decimal and octal conversion.
4. Symbolic literals.
5. IBM-type pseudo operation codes.
6. Recognition of up to 130 mnemonic codes, including the EAE (extended arithmetic element codes).
7. BCD-to-binary conversion.

3. Status

The assembler program is currently operational in DSN, and several programs for *Surveyor* and *Mariner 67* have been coded for BLAP. No further additions or changes are contemplated, other than those necessary to adapt to other existing machine configurations.

E. Bit-String Data Processing Procedure, M. Seamons

1. Introduction

This article describes a programming technique which is particularly appropriate for the orderly manipulation of data in computer core storage wherein information must be stored, referenced, and accessed by the bit. The method has been implemented in assembly language for the CDC 3000 series computer.

2. General Problem Area

In a number of data processing programming applications, data input to a program often consists of a serial string of bits which make up a logical record or frame of information. The data frame is N bits in length, although frequently N may not be an integral multiple of the computer word length in bits. Hardware or operational considerations may dictate that input of the N -bit string be broken into a time-wise series of inputs of K -bit ($K < N$) substrings which may not be of equal length. Further processing of the data generally involves assembly of the bits or pieces of data into a logical contiguous record, inspection/verification of the integrity of the frame, translation or restructuring of parts of the frame, and finally, disassembly and output of all or part of the frame. This processing generally requires referencing subfields of the data where the most or least significant bits of a subfield do not generally "reside" at either a computer word or byte boundary. Most computer addressing schemes are limited to word-wise or, at best, byte-wise addressing. Referencing a logical subfield which physically "resides" across word or byte boundaries presents a complex programming problem to the computer programmer. Solution of this type of data-handling problem demands a tedious trade-off between core storage requirements and complicated, error-prone bookkeeping logic.

The programming method described here offers an approach which minimizes the core storage requirements and simplifies, or at least eases, the complexity of the logic necessary to manipulate and process data files of this form.

3. Method

The method is an extension of the circular word buffer or sequential-queue programming concept. A circular word buffer consists of a defined block of core storage with three system registers associated with each block.

One register defines the size of the block (number of words) allocated to data storage. Two registers are pointers, an input pointer which specifies or points to the next word in the data block which is available for use as storage of new information, and an output pointer which points to the last word committed to data storage. Data flow through the buffer is normally on a first-in-first-out basis. The buffer is circular in the sense that the first data word of a logical data string may occupy the last physical word of the defined block, and the last data word may occupy the first physical word.

The circular bit buffer technique is based on the same concept with the system pointers referencing specific bit positions, and the buffer size register specifying the data block size in bits. Fig. 9 depicts a storage layout for a buffer.

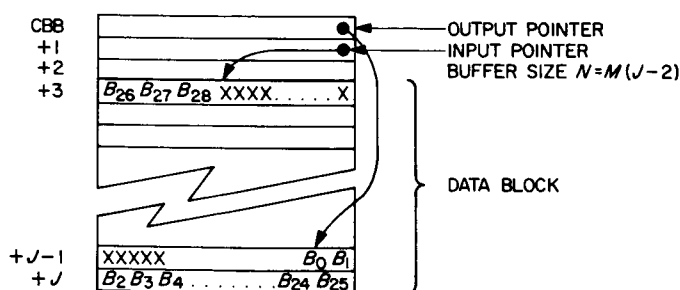


Fig. 9. Storage buffer layout

The B_n symbols in Fig. 9 denote a data string 29 bits in length as might be stored in a 24-bit word memory buffer; the X's denote uncommitted bit positions. To initialize the buffer for input the pointers are set to zero, or equal modulo N . As data is input to the buffer, it is stored bit by bit starting at the bit position specified by the input pointer. The data string forms a bit-chain which snakes from one memory word to the next until the chain wraps around to the beginning word of the buffer. Output of data from the buffer requires merely copying the appropriate words in the buffer, then updating the output pointer to reflect the change and uncommit that segment of the buffer. The beginning and end of a string are defined completely by the system pointers; no flag bits within the data block are required. The output function is mechanized such that an output bit string is either left or right justified.

4. Use and Characteristics

The mechanism for manipulation of data through or within the buffer is centralized in a set of storage and

pointer bookkeeping subroutines. The subroutine set has the following functional points of entry from the outside: ATTACH, DETACH, EXTRACT, REPLACE and COUNT. Each entry specifies, via an input parameter K , the number of bits to be involved in a data transaction. K ranges from 1 bit up to the machine word size in bits M .

The basic set of subroutines (or entry points) provides the capability detailed below:

1. ATTACH: Attach K bits specified as input or new data at the end of a data string existing in the buffer then advance the input pointer by K modulo N (N being the buffer size).
2. DETACH: Extract the K oldest bits in the buffer (if any) and update the output pointer, again modulo N .
3. REPLACE: Effectively erase the K "old" bits and insert K "new" bits starting at a specified bit position.
4. EXTRACT: Copy (return to the external user) the K bits in the buffer starting at a specified bit position without alteration of buffer data or pointers.
5. COUNT: Determine the number of committed bit positions in the buffer of N bits.

As written, the bookkeeping mechanism consists of 8 subroutines including the 5 which are cited as entry points. The total subroutine package required 87 instructions to implement on a specific computer. The technique, while not as operationally efficient as straight-line, task-specific coding, offers a generality which reduces implementation and check-out time for bit manipulation programs. As written, the subroutine package can be used as a system facility to service any number of circular bit buffers concurrently.

The advantages offered by this technique are summarized as follows:

1. It provides a procedure for pseudo-addressing of core storage to the bit level.
2. It permits maximum use of storage required for buffering serial bit string data. The defined data block appears to the user as a contiguous bit storage area even though a logical data string may physically start at the last bit position and wrap around past the first bit position of a buffer.

3. The circular buffer technique tends to minimize the number of data moves required to assemble, process and disassemble bit strings.
4. A single bookkeeping package can accommodate the manipulation of data through any number of buffers (of the same or different size) concurrently.
5. If the bit transaction parameter K is equal to the computer word size, then the technique reduces to the standard circular word buffer procedure.

As is strongly suggested in the general problem area description, this programming technique evolved as a by-product from PCM telemetry data processing studies and was developed to support DSN programming activities.

F. Symbolic Tape Update Program, Truman Cox

1. Introduction

This program allows the user to put a symbolic program, or any deck of Hollerith cards, onto a magnetic tape, and to make any revisions to the "deck" of card images on the tape. This permits large programs to be kept in a convenient form and altered as necessary, without the need of handling a large and time-consuming card deck.

2. Description

The program reads an original card deck and writes equivalent card images onto magnetic tape in BCD. In columns 73-80 of each card image (on tape), a label, designated by the user, and sequence number is written by the program. The sequence increment is also designated by the user. An IBM-compatible, end-of-file mark is written after the last card image.

With a "deck" of card images on tape, the tape can be altered in any way a physical card deck can be altered, by inserting, deleting, and/or replacing card images. This control is handled by the card reader. A new tape is written with a new label and sequence numbers with all the alterations specified by the control cards. An end-of-file mark is written after the last card image, and operating instructions and explicit error messages are output on the typewriter.

3. Program Requirements

The symbolic tape update program can be used on any SDS 900 series computer with card reader and two magnetic tape units and requires only 904 core-memory storage locations. A self-loading paper tape is also available. No programmed operators are required. The program was written to support DSN computer programming activities.